

Doctoral Dissertation
Doctoral Program in Metrology (31.st cycle)

Modeling of the hysteresis losses of magnetic nanostructures for hyperthermia applications

Riccardo Ferrero
* * * * * *

Supervisors
Dr. A. Manzin, Supervisor
Dr. O. Bottauscio, Co-supervisor

Doctoral Examination Committee:
Prof. L. Buda-Prejbeanu, Referee, Grenoble Institute of Technology
Prof. M. D'Aquino, Referee, Università degli Studi di Napoli Parthenope
Prof. L. Dupré, Ghent University
Prof. L. Gozzelino, Politecnico di Torino
Prof. C. Ragusa, Politecnico di Torino

Politecnico di Torino
July 11, 2019

I hereby declare that, the contents and organisation of this dissertation constitute my own original work and does not compromise in any way the rights of third parties, including those relating to the security of personal data.

. . . . . .

Riccardo Ferrero
Turin, July 11, 2019

Summary

In this thesis we present a detailed parametric analysis of permalloy nanostructures with variable shape (disk, cylinder and sphere) and size, for possible application in magnetically mediated hyperthermia, exploiting hysteresis losses for the heat release. Hyperthermia is a promising therapy for the cure of cancer, able to enhance the effect of already available therapies such as chemotherapy and radiotherapy, using a localized source of heat to increase the temperature of diseased tissues. In the case of magnetic hyperthermia, superparamagnetic iron oxide nanoparticles are typically used to increase the temperature of diseased tissues, when excited by alternating magnetic fields (with a frequency from 50 kHz to 1 MHz). However, they present a medium heating efficiency, requiring the injection of large quantity of material to obtain therapeutic effects, at the cost of potential toxicity.

In this framework, we aim at individuating more efficient heat mediators, focusing on multi-domain ferromagnetic nanostructures, which have recently attracted strong interest, due to the potential improvement of heating efficiency via hysteresis losses. The study is performed by means of in house developed micromagnetic codes, which are able to efficiently solve the Landau-Lifshitz-Gilbert (LLG) equation in 3D domains. In particular, we have implemented both a 3D solver for the modelling of 3D-shape nanostructures as well as a 2.5D solver for the simulation of thin-film like nanostructures randomly distributed in a 3D space. The solvers, which adopt a geometric time integration scheme for the integration of the LLG equation, are both written in CUDA Fortran to leverage the high parallelization performance offered by Graphical Processing Units.

By means of micromagnetic modelling, we have performed an extensive investigation of the influence of geometrical properties (shape and size) on the amount of heat generated via hysteresis losses. We have also obtained useful information on remanence magnetization configuration and on its implications in aggregation phenomena. Third, we have explored magnetization reversal process and determined saturation fields, which are required to obtain major hysteresis loops and thus maximize hysteresis losses. Regarding this last aspect, caution has been paid to not exceed acceptable biophysical limits for the maximum applicable field at a given frequency.

The attention is first focused on disk-shaped nanostructures, for which we present a detailed comparison between micromagnetic simulations and experimental results on samples arranged in both 2D array (intermediate production phase) and free-standing

(in solution). Subsequently, we study the magnetization reversal process and the hysteresis properties of permalloy nanocylinders (diameter between 150 nm and 600 nm, thickness from 30 nm up to 150 nm) and permalloy nanospheres (size between 100 nm and 300 nm), to compare the relative heating performances of different nanostructures. Focusing on disk-shaped nanostructures, we also analyze the influence on the loss generation of the state of aggregation, concentration and spatial distribution. In particular, by means of the 2.5D micromagnetic code we investigate the hysteretic behavior of permalloy nanodisks randomly oriented in a 3D medium, analyzing the effects of magnetostatic interactions and variations in the orientation with respect to the applied field. This analysis has been conducted to have a more precise estimate of the heat delivery during hyperthermia treatment, trying to mimic the stochastic dispersion of nanomaterials in a tissue or in a biological fluid.
Finally, as an alternative use of magnetic nanostructures, we have studied the nucleation and control of vortex state, for possible applications in non-volatile magnetic random access memories (MRAMs). In particular, we have investigated bi-component magnetic nanodisks as potential storage systems, where the information unit is represented by vortex chirality (magnetization rotational direction).

Contents

List of Tables

List of Figures

Chapter 1

Introduction

Magnetism intrigued humanity from ancient time, but only in the last few centuries proper theories for describing this phenomena were developed. Nowadays, ferromagnetic materials are widespread and used in a variety of applications of everyday life. At a large scale, we can found them in electromechanical systems, like electromagnets, electric motors, generators and transformers. Down to the microscopic scale, they have been used as memory supports for almost 70 years. The development of techniques that allow us to control the matter at ever smaller scale opened new scenarios, new challenges and new applications. In parallel, it introduced the need to understand and predict the behaviour of magnetic materials at a very fine scale.

For example, since its initial development in the 50s, magnetic storage is one of the technological areas where the greatest improvement was obtained, and, nowadays, it can greatly benefits from the development of magnetic nanostructures. Another field that is interested in the behaviour of ferromagnetic materials at the nanoscale level is nanomedicine. In this area, ferromagnetic materials can find a wide variety of applications: imaging, sensing, biotracing, drug delivery and tumor therapies. Regarding this last topic, which is one of the main challenges of the 21st century, many progresses were made but we are still far from the end. To pursue better and better therapies, magnetic nanoparticles can play an active role. The development of techniques as the

nano-chemotherapy, or the *magnetically mediated hyperthermia*, showed the potential to considerably improve the chances of treating tumors.
A large amount of research is now aimed to gain a deeper understanding of the ferromagnetic properties of nanomaterials, in order to develop high performing and optimized nanostructures for the aforementioned applications. In the following sections, we will focus on magnetically mediated hyperthermia, explaining the idea behind such therapy, the limitations of actual thermotherapies and how magnetic nanostructures can help overcoming these limitations. We then discuss the challenging aspects of the development of new and optimized nanoparticles for this kind of therapy. We also highlight that the development of nanostructures with specific topological properties like nanodisks, here studied for hyperthermia therapies, may find application in other sectors such as magnetic recording.

1.1 Overwiev of hyperthermia therapy

Hyperthermia can refer to a condition where the tissues reach a temperature above the normal one, in general from 42° to 45° C. These temperatures induce a series of physiological responses in the cells and in the tissues themselves. In the middle of 1970s, a large number of studies began the evaluation of the effects of hyperthermia on cancer tissues, showing that: the threshold temperature for heat induced apoptosis is lower for cancer cells if compared to normal ones; hyperthermia induces an increase in the response of the immune system increasing the tumor antigen expression; it inhibits the DNA repair process in cancer cells and the tumor vascular endothelial growth factor [1–3]. Hence, it developed the idea to exploit the effect of the increase in temperature to enhance traditional cancer therapy. For example, radiotherapy, which causes cell death by damaging DNA, can receive great benefit from the reduction of the DNA repair process,induced by the rise in temperature [4, 5].
The first studies on multi modal therapies using hyperthermia began in the early 1980s

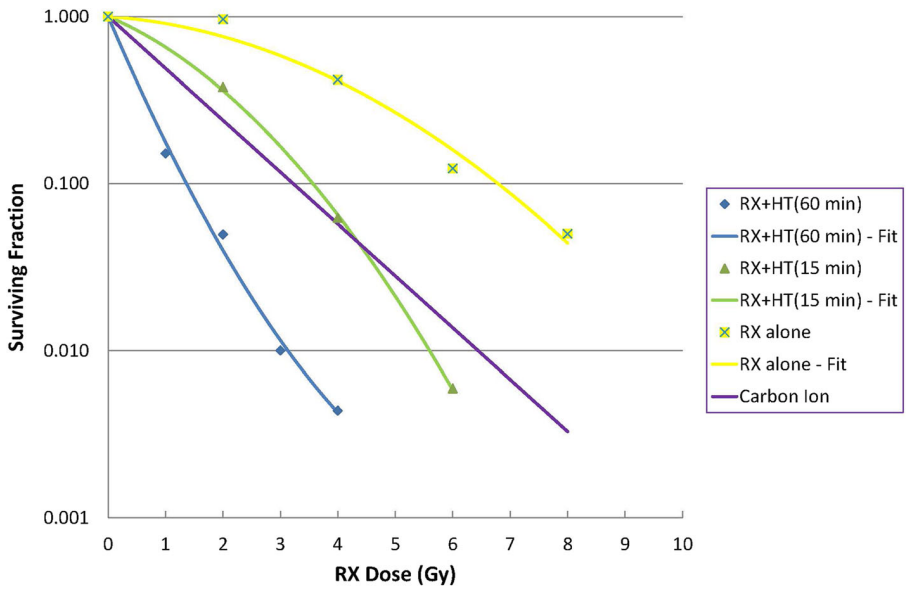

Figure 1.1: Surviving fraction of cancer cells after different treatments (Hyperthermia + Radiotherapy, Radiotherapy alone, Carbon Ions) as function of the radiation dose [5].

[3], showing promising results. As reported in [5], for example, the use of thermo-radiotherapy can provide the same surviving fraction of cancerous cells after the treatment using a radiation dose four times lower than radiotherapy alone (see Fig. 1.1).

Recently, many studies have confirmed that a rise in the temperature T of the tumor cells can improve chemotherapy or radiotherapy efficacy due to cellular alteration ($T = 42 - 45$ ℃) or, in the case of thermo-ablation, can directly lead to cell death ($T > 46$ ℃), even in treatments lasting only a few minutes [6–12].

Thermotherapies can be classified on the basis of the scale of the heated region: local hyperthermia, regional hyperthermia, and whole-body hyperthermia. Through the years, a wide range of techniques was developed for the heat generation: high-intensity focused ultrasound, radiofrequency radiation, microwave radiation, laser application, to name some of them. Typically, when using electromagnetic energy, hyperthermia is performed at high frequencies (13 MHz to 430 MHz depending on tumor depth) with phased-array antennas placed outside the body. On the other hand, microwaves (915 MHz or 2.45 GHz) are applied in thermal ablation through interstitial antennas placed

inside the tumor. The variety of techniques and modalities of heating allow us the development of therapies suitable for the treatment of different kinds of cancer, comprising local heating for superficial or solid tumors, regional heating for deep-seated tumors in the pelvis or abdomen, and whole-body heating for metastatic cancer that has spread throughout the body.

One of the main technical challenges, which has to be considered during treatment, is the thermal dosimetry. It is proved that a close relationship exists between the thermal dose of hyperthermia combined with radio- or chemo-therapy and the treatment response [13]. Unfortunately, the tissue temperature regulation is a difficult phenomenon to be controlled. The temperature of a tissue can depend on a lot of factors, including the physical properties of the specific tissue and the physiological response of the body. Moreover, the monitoring and measurement of temperature, in the case of deep seated tumor, is an invasive procedure.

In the case of localized hyperthermia, another issue is the effective control of the heat deposition. To achieve the desired therapeutic efficacy, the temperature increase must effectively involve the Region Of Interest (ROI) of the tumor, and possibly be limited to the only ROI. Thanks to the development of nanotechnologies, in the last two decades a lot of attention has been paid to the application of a new technique for hyperthermia: magnetically mediated hyperthermia. This technique, which uses magnetic nanoparticles exposed to ac magnetic fields as heat mediators, has proven to be promising in guaranteeing a more targeted and uniform heat generation.

1.2 Magnetically mediated hyperthermia

Both hyperthermia and thermal ablation proved their safety and efficacy in several clinical trials [14]. However, both techniques suffer from poor reproducibility and control of the temperature distribution obtained into the tumor in the different clinical conditions. Recent research is thus devoted to the development of personalized protocols

[15], to the understanding of the different physical phenomena associated with heating [16], and to the improvement of heating uniformity and target specificity while minimizing invasiveness. With reference to this last issue, a promising route is represented by thermotherapies mediated by magnetic nanostructures. In magnetically mediated hyperthermia, magnetic nanostructures are injected into the tumor and then excited by an alternating magnetic field, with a given frequency that typically ranges from 10 kHz to 1.2 MHz. This leads to a localized release of heat and to a consequent increment of the target tissue temperature.

Typically, superparamagnetic iron oxide nanoparticles (SPIONs) are used in experimental trials on magnetically mediated hyperthermia, showing promising outcomes [17–21], and being able to reach the target temperature in a localized region. Three independent mechanisms result in thermal energy, namely Néel relaxation, Brownian relaxation and hysteresis [22–24]. Their contribution strongly depends on the size, shape, magnetocrystalline anisotropy and degree of aggregation of the nanostructures. Also eddy current generation can concur to thermal energy production, but in a negligible way for the frequency range typically considered [24]. One of the main limitations of magnetic hyperthermia is the medium heating efficiency of the currently used magnetic nanostructures, which have to be injected in large quantity to obtain therapeutic effects, at the cost of potential toxicity [20].

Coated SPIONs are considered promising candidates for hyperthermia applications, because of good biocompatibility and weak tendency to agglomeration [25, 26]. Moreover, they are already approved by regulatory offices for medical trials, since by now they are employed for other biomedical treatments. However, their heating efficiency is limited, since thermal energy comes from size-dependent Néel and Brownian relaxation, with negligible hysteresis loss contribution. In a tumor tissue, Brownian relaxation is practically inhibited due to nanoparticle immobilization, apart from a small oscillation allowed by tissue elasticity [27]. A similar behaviour is also found in the cellular environment, where Brownian losses are not present, due to nanoparticle attachment to

the cellular membrane or confinement within endosomes [28]. Studies on iron-oxide nanoparticle size (5-22 nm) have shown that, for a diameter of 10 nm, Néel losses reach their maximum and then their relative heating contribution starts reducing as diameter increases. The emerging single-domain ferromagnetic behaviour leads to an increase in hysteresis losses, which overcome Néel losses for nanoparticle dimensions higher than 15-20 nm[29, 30].

Both single- and multi-domain ferromagnetic nanostructures have recently attracted strong interest, because of the potential improvement of heating efficiency due to hysteresis. Different strategies have been adopted to tune hysteresis properties (hysteresis loop size and shape) with the aim of increasing the relative heating contribution. A possible way is to use materials with high saturation magnetization and/or high uniaxial magneto-crystalline anisotropy, such as cobalt or cobalt-zinc ferrites.[28, 31–36].Another strategy consists in modifying nanostructure geometry, introducing shape anisotropies; promising results have been obtained by using magnetite nanorods with 250/50 nm aspect ratio [37], magnetite, maghemite or cobalt ferrite nanocubes [38–40] and octahedral magnetite nanoparticles [41].]. Nanostructure geometry can strongly affect the magnetization reversal process and thus the remanence magnetic state, which should be characterized by negligible moment to reduce magnetostatic interactions and agglomeration effects. To this aim, special attention has been given to nanodisks, nanorings and nanotubes, which exhibit magnetic vortex configuration at remanence and thus very small remanence moment [42–46]. They are able to preserve some of the advantages of SPIONs (reduced aggregation and good colloidal stability), allowing at the same time to obtain large hysteresis losses.

1.2.1 Biological limitations on the ac magnetic field

In general, hysteresis losses can be augmented by increasing the amplitude H_a of the applied field up to saturation conditions and its frequency f. However, when a patient is exposed to an alternating magnetic field, parameters H_a and f should be

controlled to avoid the undesirable induction of eddy currents in the body, which can cause the occurrence of hot-spots, leading to possible discomfort and tissue damage. To limit these effects, restrictions are imposed on the product $H_a \times f$. An upper value of 4.85×10^8 $\mathrm{Am^{-1}s^{-1}}$, known as the Atkinson-Brezovich limit [47], was first assumed as an acceptable threshold to avoid intolerable resistive heating. A less rigid criterion, $H_a \times f \leq 5 \times 10^9$ $\mathrm{Am^{-1}s^{-1}}$, was successively proposed [48]. Good tolerability was documented during one of the first clinical trials on magnetic hyperthermia, performed on patients with different tumor types (glioblastoma multiforme, sarcoma, ovarian, rectal or prostate carcinoma), which were exposed to a magnetic field of 100 kHz, with amplitude variable between 2.5 kA/m and 18 kA/m [49, 50]. In silico and in vivo analyses demonstrated the possibility of overcoming the threshold of 5×10^9 $\mathrm{Am^{-1}s^{-1}}$ of more than one order of magnitude, maintaining eddy current effects below safe and tolerable limits [51]. As an example, breast and pancreatic tumors in mice were successfully treated with SPIONs exposed to magnetic fields with $H_a = 15.4$ kA/m and $f = 435$ kHz [52].

These problems can be overcome with a careful design of both nanostructures and magnetic field applicators. This could be achieved by developing nanostructures with higher hysteresis losses without increasing the saturation field, therefore allowing higher excitation frequency without exceeding the biological thresholds. Another solution can be the development of focused field generators, thus limiting the development of undesired eddy currents or hot spots.

1.2.2 Design and optimization of magnetic nanostructures

In this thesis, we focus the attention on ferromagnetic nanostructures, for which the main heating contribution comes from hysteresis losses. The optimization process for magnetic hyperhermia application is not an easy task, since one has to consider multiple constraints. For example, since we are interested in the hysteresis losses, it is fundamental to estimate the minimum field necessary to reach the irreversible jumps of

the hysteresis loop, in order to obtain a sufficiently large loop area and thus achieve a good heating efficiency. As previously mentioned, because of biological limitations on the product $H_a \times f$, the selection of the field amplitude has also impact on the choice of the working frequency. If saturation conditions can not be reached due to biophysical limits to the applicable fields, large hysteresis losses could be still obtained by properly tuning the irreversible jumps via nanostructure shape and size modification.

In this thesis, we present a modelling analysis of permalloy ($Ni_{80}Fe_{20}$) nanostructures with variable shape (disk, cylinder and sphere), for possible application in magnetically mediated hyperthermia. A parametric study is performed by varying aspect ratio and size (up to some hundreds of nanometers), with the aim of finding the optimal conditions for the maximization of the specific heating capabilities with tolerable fields. Hysteresis losses, which are the main heating contribution for the considered magnetic nanostructures, are calculated by integrating the Landau-Lifshitz-Gilbert (LLG) equation [53], with the inclusion of thermal noise effects.

The attention is mainly focused on disk-shaped permalloy nanostructures, for which we present a detailed comparison between experimental and numerical results. Moreover, we perform a parametric analysis varying the nanodisk diameter in the range 100-800 nm and the thickness in the range 15-30 nm, to find the optimal geometrical properties for the maximization of the specific heating capabilities.We also study the magnetization reversal process and the hysteresis properties of permalloy nanocylinders (diameter between 150 nm and 600 nm, thickness from 30 nm up to 150 nm) and permalloy nanospheres (size between 100 nm and 300 nm). We analyze hysteresis losses, remanent magnetization state and quasi-saturation conditions, as a function of size and shape. The aim is to find the optimal geometrical properties, which guarantee at the same time energy release maximization, negligible magnetic remanence and fulfilment of the biophysical constraint on $H_a \times f$, within the typical range of variation of f.

Focusing on permalloy nanodisks, which seem to be very promising for hyperthermia application, we explore the influence of other factors, such as the angle of orientation

of the applied field with respect to the nanodisk surface, the magnetostatic interactions between disks and the local concentration, to obtain a more reliable estimation of the heating performance in a realistic hyperthermia setup. In the analysis, we also consider the effect of temperature.

In Table 1.1 we resumed part of our bibliographic investigation, to compare our results with the specific loss power of other nanostructures studied in the literature. As can be seen in the table, for studies conducted in phantoms or tissue-mimicking materials, the values of the amplitude and frequency of the applied field exceed the biological constraints discussed before. In vivo or in vitro studies present data in terms of heat generated in the tissues, but, especially for in vivo studies, a precise estimate of the quantity or concentration of magnetic material deposited in the tissues is difficult to obtain. This makes a direct comparison of the heating efficiency of the different nanostructures not an easy task.

1.2.3 Hypertermia applicators

The other fundamental building block for the development of successful hyperthermia treatment is the engineering of magnetic field applicators optimized for this kind of treatment. One of the most advanced study in this field was carried out by the Charité Medical School Berlin in cooperation with MagForce Applications GmbH, a company specialized in the production of magnetic fluids, and MFH Hyperthermiesysteme GmbH, which developed the magnetic applicator. The system was designed for magnetic fluids made of nanosized iron oxide particles consisting of magnetite (Fe_3O_4) or maghemite (γFe_2O_3). The device named MFH® 300F is capable of generating a field at a frequency of 100kHz with a variable amplitude between 12 kA/m and 18 kA/m [54]. To the best of our knowledge, this is actually the only commercially available system developed for magnetically mediated hyperthermia on human patients.

For what concerns in vitro or in vivo testing, researchers tend to use in house built

applicators, using a wide range of fields and frequencies. This fact makes direct comparison between different sources quite challenging. MagneTherm™ system developed by NanoTherics offers an interesting setup for in vitro studies [55–57], proposing different fixed frequency coils, and fields up to 40 kA/m. In studies on animal models [44, 58], we often find self developed hyperthermia applicators.

As the research is moving from SPIONs to novel ferromagnetic nanostructures, without a previous knowledge of the hysteretic behavior of this new heat mediators, the evaluation of their heating performance is not straightforward. For example, the used field parameters may not be suitable to achieve the maximum heating efficiency of the nanostructures. This kind of studies, therefore, is useful not only in the individuation of optimized nanostructures for hyperthermia, but also in the engineering of suitable field applicators, for both in vitro and in vivo applications.

Author	Structure	Material	Dimension	Freq kHz	Hmax kA/m	SAR W/g metal	ILP Hm^2/g	Specific Loss kJ/m^3 metal	Specific Loss kJ/m^3 @given concentration	Measurement type	concentration mg/cm3
Yang 2015	Nanodisk	Fe3O4	t 26 nm, d 225 nm	488	47.8	5000	0.0044843	51.2295082	0.00102459	Water	0.1
Yang 2015	SuperparaNP	Fe3O4	d 11.2 nm	488	47.8	500	0.0004484	5.12295082	0.000102459	Water	0.1
Yang 2015	FerromagNP	Fe3O4	d 58.7 nm	488	47.8	2000	0.0017937	20.49180328	0.000409836	Water	0.1
Yang 2015	Nanodisk	Fe3O4	t 26 nm, d 225 nm	488	31.8	3000	0.0060792	30.73770492	0.000614754	Water	0.1
Yang 2015	SuperparaNP	Fe3O4	d 11.2 nm	488	31.8	420	0.0008511	4.303278689	8.60656E-05	Water	0.1
Yang 2015	FerromagNP	Fe3O4	d 58.7 nm	488	31.8	1200	0.0024317	12.29508197	0.000245902	Water	0.1
Yang 2015	Nanodisk	Fe3O4	t 26 nm, d 225 nm	488	15	500	0.0045537	5.12295082	0.000102459	Water	0.1
Yang 2015	SuperparaNP	Fe3O4	d 11.2 nm	488	15	420	0.0038251	4.303278689	8.60656E-05	Water	0.1
Yang 2015	FerromagNP	Fe3O4	d 58.7 nm	488	15	2000	0.0182149	20.49180328	0.000409836	Water	0.1
Yang 2015	Nanodisk	Fe3O4	t 26 nm, d 225 nm	488	47.8	2820	0.0025291	28.89344262	0.000577869	Gel	0.1
Liu2015 chin Phys B	Nanoring	Fe3O4	N. A.	400	16	375	0.0036621	4.6875	N. A.	suspension	0.05-0.15
Liu2015 chin Phys B	Resovist Magnetite–Fe3O4/ Maghemite–Fe2O3	Fe3O4	7.5 nm	400	16	10	9.766E-05	0.125	N. A.	suspension	0.05-0.15
Liu2015 chin Phys B	Nanorig	Fe3O4	N. A.	400	32	1400	0.003418	17.5	N. A.	suspension	0.05-0.15
Liu2015 chin Phys B	Resovist Magnetite–Fe3O4/ Maghemite–Fe2O3	Fe3O4	7.5 nm	400	32	75	0.0001831	0.9375	N. A.	suspension	0.05-0.15
Liu2015 chin Phys B	Nanorig	Fe3O4	N. A.	400	48	2400	0.0026042	30	N. A.	suspension	0.05-0.15
Liu2015 chin Phys B	Resovist Magnetite–Fe3O4/ Maghemite–Fe2O3	Fe3O4	7.5 nm	400	48	125	0.0001356	1.5625	N. A.	suspension	0.05-0.15
Liu2015 chin Phys B	Nanorig	Fe3O4	N. A.	400	64	3000	0.0018311	37.5	N. A.	suspension	0.05-0.15
Liu2015 chin Phys B	Resovist Magnetite–Fe3O4/ Maghemite–Fe2O3	Fe3O4	7.5 nm	400	64	250	0.0001526	3.125	N. A.	suspension	0.05-0.15
Liu2015 chin Phys B	Nanodisk	Fe3O4	N. A.	N. A.	N. A.	4925	N. A.	N. A.	N. A.	water	0.05-0.15
Liu2015 chin Phys B	Nanodisk	Fe3O4	N. A.	N. A.	N. A.	2818	N. A.	N. A.	N. A.	gel	0.05-0.15
Liu2015 chin Phys B	Nanodisk	Fe3O4	N. A.	488	70	4659	0.0019484	47.73565574	N. A.	computed water	0.05-0.15
Liu2015 chin Phys B	Nanodisk	Fe3O4	N. A.	488	70	3017	0.0012617	30.91188525	N. A.	computed gel	0.05-0.15
Liu2015 adma	Nanoring	Fe3O4	rext 70 nm t 50 nm rint 42 nm	400	35	2213	0.0045163	27.6625	N. A.	water	N. A.
Liu2015 adma	Nanoring	Fe3O4	rext 70 nm t 50 nm rint 42 nm	400	56	2346	0.0018702	29.325	N. A.	gel	N. A.
Liu2015 adma	Resovist Magnetite–Fe3O4/ Maghemite–Fe2O3	Fe3O4	7.5 nm	400	35	104	0.0002122	1.3	N. A.	topo	N. A.

Table 1.1: Table resuming part of the bibliographic investigation performed. We report the author of the study, the kind of nanostructures studied and the significative parameters, for the comparison of our results with the specific loss power of other nanostructures.

Author	Structure	Material	Dimension	Freq kHz	Hmax kA/m	SAR W/g metal	ILP Hm^2/g	Specific Loss kJ/m^3 metal	Specific Loss kJ/m^3 @given concentration	Measurement type	concentration mg/cm3
Liu2015 adma	Nanoring	Fe3O4	rext 70 nm t 50 nm rint 42 nm	37.5	32	215.65	0.0056159	28.75333333	0.0017252	topo	0.3
Liu2015 adma	Nanoring	Fe3O4	rext 70 nm t 50 nm rint 42 nm	400	45.7	2300	0.0027532	28.75	0.00115	water	0.2
Liu2015 adma	Nanoring	Fe3O4	rext 70 nm t 50 nm rint 42 nm	400	45.7	2300	0.0027532	28.75	0.000575	water	0.1
Liu2015 adma	Nanoring	Fe3O4	rext 70 nm t 50 nm rint 42 nm	400	45.7	2300	0.0027532	28.75	0.0002875	water	0.05
Liu2015 adma	Resovist Magnetite–Fe3O4/ Maghemite–Fe2O3	Fe3O4	7.5 nm	400	45.7	190	0.0002274	2.375	0.000095	water	0.2
Liu2015 adma	Resovist Magnetite–Fe3O4/ Maghemite–Fe2O3	Fe3O4	7.5 nm	400	45.7	190	0.0002274	2.375	0.0000475	water	0.1
Liu2015 adma	Resovist Magnetite–Fe3O4/ Maghemite–Fe2O3	Fe3O4	7.5 nm	400	45.7	190	0.0002274	2.375	0.00002375	water	0.05
Vitol 2012	Nanodisk	Fe3O4	d=1000 t=60	332	11.2	121.6	0.0029198	1.831325301	0	water	N. A.
Vitol 2012	nanoparticle	Fe3O4	10	300	15.2	120	0.0017313	2	N. A.	N. A.	N. A.
Kim2010	Nanodisk (Mechanical Destruction)	Ni20Fe80	d=1000 t=60	N. A.	N. A.	N. A.	N. A.	N. A.	N. A.	N. A.	N. A.
Simeonidis 2016	Nanorod	Fe3O4	300 60	210	12	10	0.0003307	0.238095238	0.000238095	Water	5
Simeonidis 2016	Nanorod	Fe3O4	300 60	765	24	759	0.0017225	4.960784314	0.005952941	gel Agar	6
Simeonidis 2016	Nanorod	Fe3O4	300 60	765	24	759	0.0017225	4.960784314	0.004960784	Water	5
Liu2012	nanoparticle	Fe3O4	9 nm coating 1	400	27	367	0.0012586	4.5875	0.00045875	Water	0.5
Liu2012	nanoparticle	Fe3O4	9 nm coating 2	400	27	332	0.0011385	4.15	0.000415	Water	0.5
Liu2012	nanoparticle	Fe3O4	9 nm coating 3	400	27	267	0.0009156	3.3375	0.00033375	Water	0.5
Liu2012	nanoparticle	Fe3O4	19 nm coating 1	400	27	930	0.0031893	11.625	0.0011625	Water	0.5
Liu2012	nanoparticle	Fe3O4	19 nm coating 2	400	27	686	0.0023525	8.575	0.0008575	Water	0.5
Liu2012	nanoparticle	Fe3O4	19 nm coating 3	400	27	**535**	0.0018347	6.6875	0.00066875	Water	0.5
MingMa 2013	Hexa nanoplates	Fe3O4	d 150-200 t 10	175	0.1	253.7	144.97143	7.248571429	0.001304743	Water	0.9
MingMa 2013	Hexa nanoplates	Fe3O4	d 150-200 t 10	175	0.1	253.7	144.97143	7.248571429	0.002609486	Water	1.8
jones 2011	Embeddded Microsphere	gFe2O3		53	40	**0.08	N. A.	9.309541779	0.001609057	coniglio (rene)	0.84
jones 2011	Embeddded Microsphere	gFe2O3		53	40	**0.147	N. A.	9.579518491	0.002956642	coniglio (rene)	1.5
jones 2011	Embeddded Microsphere	gFe2O3		53	40	**0.173	N. A.	9.394879245	0.003479585	coniglio (rene)	1.8
jones 2011	Embeddded Microsphere	gFe2O3		53	40	**0.161	N. A.	9.257517869	0.003238226	coniglio (rene)	1.7
						**W/g of tissue					
Johannsen2007	MAGForce	Fe3O4		100	4.4	0.09	4.649E-05	0.123828922	0.0009414	Prostate cancer	38.01212121
Our Disk				10	50	29.20560748	0.0011682	25	0.000876168		0.3

1.3 A panoramic view of other application of nanostructures

Magnetic nanostructures, with peculiar magnetization configurations, such as the permalloy nanodisks we studied for hyperthermia, attracted a lot of interest and are widely studied for their potential application in many different sectors. A lot of analyses, conducted experimentally with Magnetic Force Microscopy (MFM) and magnetometry as well as theoretically with the support of micromagnetic numerical models, are performed to study closed magnetization configurations, including the out-of-plane vortex state showed by ferromagnetic nanodisks. This configuration is of particular interest for its topological stability and because it minimizes the nanostructure stray field. Other than the application we showed, many other fields can benefit from this property, like high-density magnetic recording.

In the last decade, special attention has been paid to the nucleation and control of vortex state in magnetic nanostructures, for possible applications in non-volatile magnetic random access memories (MRAMs). The magnetization vortex configuration is interesting for the magnetic recording because the chirality and polarity of the vortex can be used as 0 or 1 bit indicators. The combination of the two informations can allow us the construction of logic elements similar to what is now found in the NAND flash Multi Level Cell (MLC) of modern Solid State Disks (SSDs): each cell has four possible readable states corresponding to the 2-bit strings 00, 01, 10 and 11. Moreover, the reduced stray field of the vortex magnetization configuration permits to have closely packed nanostructures with relatively small interactions.

In the following, we report a brief resume on the development of magnetic recording technologies, to better understand the potentiality and advantages that nanostructures presenting a vortex remanent state may introduce in this field. Despite the development of new supports for data storage such has SSDs using NAND flash, which allowed much

higher I/O speed, the data density of magnetic recording is still a welcome trade off, especially when the cost per terabyte of data and the longevity of the support is factored. In modern hard disks, data are recorded magnetizing a thin film of ferromagnetic material. Sequential changes in the direction of magnetization represent binary data bits. A single bit involves the magnetization of a certain number of ferromagnetic grains weakly interacting. Today, the demand pushing for always increasing data density is rapidly approaching the physical limit of magnetic nanostructures known as the *magnetic recording trilemma*. Three main aspects contribute to the limitation imposed to the development of magnetic recording: the grain size of which each bit cell is made, the grain magnetic strength and the ability of the head to write the bit cell. In order to increase the area density of stored information, namely the number of bits per square centimeter, one can: reduce the size of the single grain, however this size is bounded below by the superparamagnetic regime, or reduce the number of grains necessary to record a single bit, which however would reduce the Signal to Noise Ratio). This last aspect can be overcome using materials with stronger magnetization thus increasing the grain strength, which however is limited by the ability of the head to overcome the coercive field in order to write the bit. Today, the areal density reached is 1Tb/inch^2. To go beyond this limit, many different technical strategies are under development, such as heat assisted magnetic recording (HAMR), and microwave assisted magnetic recording (MAMR) or bit patterned magnetic recording (BPMR) [59].The first technique (HAMR) tries to overcome the problem of writing bits with high coercivity, heating the region to be written, therefore temporary lowering the coercive field of the grain to allow the data recording. The second one (MAMR) tries to solve the same problem assisting magnetization reversal in the media by using a microwave oscillator. In BPMR the idea is to overcome the superparamagnetic limit by fabricating nano-islands composed of strongly exchange coupled grains. In the case of BPMR, micromagnetic studies allow us to optimize the size and distribution of the magnetic units as well as understand the effect of magnetostatic interaction on the switching field distribution in the patterned

media and coercive field of the bits.

Alongside to memory storage and hard disks, Random Access Memory (RAM) rapidly developed in the last decades. Today the main technology for the production of RAM is based on semiconductors, but the idea of random access memory based on magnetoresistive effects dates back to 1960s [60].Despite showing some concrete advantages over semiconductors technology, such as non-volatility, many issues have to be addressed before magnetoresistive elements could replace semiconductors. Research interest for Magnetoresistive Random Access Memory (MRAM) grown again in the late 2000s thanks to the discover of Giant Magneto Resistance and Magnetic Tunnel Junction phenomena, whose application to magnetic sensors opened new possibility for the development of MRAMs [61, 62].

The ability to permanently store data of MRAMs depends on the hysteresis properties of ferromagnets, while the reading is done through the magnetoresistive properties of the material. On a very basic level, a MRAM cell can be described as a magnetic device presenting two magnetic stable states that correspond to the 0 or 1 bit. The reading of the information is performed measuring the resistance of the cell that depends on the magnetization state [63]. A MRAM chip is therefore an array of magnetoresistive cells integrated with a circuit able to singularly address each memory element. The main advantages of MRAM compared to traditional solutions are [64]:

- Non-volatility;
- Fast I/O operations;
- High density;
- Low power consumption once the data is written;
- Very long write endurance;
- Radiation hardness.

The main drawbacks of this type of memory is due to writing technologies. When MRAMs were initially developed, the writing procedure was performed with field induced magnetic switching, using high current injection. In general, high currents generate a lot of heat due to Joule losses, thus limiting the data density, and causing high power consumption. Moreover, with this technology also nearby cells are affected by the magnetic field generated by the current pulse, further limiting the achievable data density.

The problem of magnetic recording, as an alternative application field of magnetic nanodisks, is also explored in this thesis. In particular, in the last chapter we will propose a study of bi-component (iron-permalloy) nanodisks in both single and 2D array arrangement, as potential storage systems where the information unit is represented by vortex chirality (magnetization rotational direction). We focus on 300 nm diameter nanodisks made of a permalloy lens and an iron crescent, with variable location of the permalloy-iron interface. Through an extensive micromagnetic modelling analysis, we demonstrate the possibility of tuning, via the application of a magnetic field parallel to the interface, the nucleation of vortex (always occurring in permalloy region), its motion up to the expulsion site and its chirality. Moreover, we find that the vortex stability is preserved over a wide field range also for highly packed nanodisks, due to the reduced effects of inter-disk magnetostatic coupling.

This study on vortex chirality control may find application, in the aforementioned problem of magnetic recording. In the specific case of MRAMs, for example, the information could be read by monitoring variations in the magnetoresistivity due to changes in the relative chirality of the magnetization.

1.4 Outline of the thesis

The thesis, which was carried out at the Istituto Nazionale di Ricerca Metrologica (INRIM), in Torino, is divided in three parts: in the first one (Chapters 2 to 4) the micromagnetic theory underlying our investigation of magnetic nanostructures is presented, together with the numerical tools developed to magnetization their reversal processes and hysteresis losses. In the second part (Chapters 5 and 6) we focus on the applications of micromagnetism to the optimization of magnetic nanostructures for magnetically mediated hyperthermia therapies. In the last part, we show how magnetic nanostructures with vortex magnetization configuration are of interest in data storage application (Chapter 7).

1. The first chapter, which is concluded by this list, introduces the topic of the Thesis.

2. In the second chapter we report the theoretical model of micromagnetism, which is used in the thesis.

3. The third chapter describes the development and peculiarities of the 3D micromagnetic numerical solver implemented to analyze the hysteresis losses of nanostructures with three-dimensional shape.

4. In the fourth chapter we describe the development and peculiarities of an optimized 2.5D micromagnetic numerical solver, implemented to analyze the hysteresis of thin-film nanostructures randomly distributed in a 3D space. This solver was developed to study the effects of concentration and variable orientation with respect to the applied field of ensembles of magnetic nanodisks, mutually interacting in a 3D medium.

5. In the fifth chapter the results of a study focusing on permalloy nanostructures of different sizes and shapes (disk, cylinder, sphere) are presented, providing indication on which combination of parameters is more suitable for magnetically mediated hyperthermia applications.

6. The sixth chapter summarizes the main results obtained on the optimization of permalloy nanodisks, considering the effects of concentration (magnetostatic interactions) and variable orientation with the applied field.

7. The seventh chapter presents an analysis on bi-material (iron-permalloy) nanodisks, showing how the shape anisotropy introduced by the material interface affects the chirality of the vortex and its motion inside the disk.

References

[1] W. Rao, Z.-S. Deng, and J. Liu. "A Review of Hyperthermia Combined With Radiotherapy/Chemotherapy on Malignant Tumors". In: *Critical Reviews™ in Biomedical Engineering* 38.1 (2010), pp. 101–116. ISSN: 0278-940X. DOI: 10.1615/CritRev/BiomedEng.v38.i1.80.

[2] J. L. R. Roti. "Introduction: Radiosensitization by hyperthermia". In: *International Journal of Hyperthermia* 20.2 (2004), pp. 109–114. ISSN: 0265-6736. DOI: 10.1080/0265673032000173898.

[3] M. Mallory et al. "Therapeutic hyperthermia: The old, the new, and the upcoming". In: *Critical Reviews in Oncology/Hematology* 97.2015 (Jan. 2016), pp. 56–64. ISSN: 10408428. DOI: 10.1016/j.critrevonc.2015.08.003.

[4] K. A. Leopold et al. "Preoperative hyperthermia and radiation for soft tissue sarcomas: Advantage of two vs one hyperthermia treatments per week". In: *International Journal of Radiation Oncology*Biology*Physics* 16.1 (Jan. 1989), pp. 107–115. ISSN: 03603016. DOI: 10.1016/0360-3016(89)90017-5.

[5] G. Borasi et al. "Fast and high temperature hyperthermia coupled with radiotherapy as a possible new treatment for glioblastoma". In: *Journal of Therapeutic Ultrasound* 4.1 (Dec. 2016), p. 32. ISSN: 20505736. DOI: 10.1186/s40349-016-0078-3.

[6] K. Mahmoudi et al. “Magnetic hyperthermia therapy for the treatment of glioblastoma: a review of the therapy’s history, efficacy and application in humans”. In: *Int. J. Hyperth.* 34.8 (2018), pp. 1316–1328. DOI: 10.1080/02656736.2018.1430867.

[7] S. Spirou et al. “Magnetic Hyperthermia and Radiation Therapy: Radiobiological Principles and Current Practice †”. In: *Nanomaterials* 8.6 (2018), p. 401. ISSN: 2079-4991. DOI: 10.3390/nano8060401.

[8] D. Chang et al. “Biologically Targeted Magnetic Hyperthermia: Potential and Limitations”. In: *Front. Pharmacol.* 9 (2018), p. 831. ISSN: 1663-9812. DOI: 10.3389/fphar.2018.00831.

[9] A. Hervault and N. T. K. Thanh. “Magnetic nanoparticle-based therapeutic agents for thermo-chemotherapy treatment of cancer”. In: *Nanoscale* 6 (20 2014), pp. 11553–11573. DOI: 10.1039/C4NR03482A.

[10] M. Bañobre-López, A. Teijeiro, and J. Rivas. “Magnetic nanoparticle-based hyperthermia for cancer treatment”. In: *Reports Pract. Oncol. Radiother.* 18.6 (2013), pp. 397–400. ISSN: 15071367. DOI: 10.1016/j.rpor.2013.09.011.

[11] T. Kobayashi. “Cancer hyperthermia using magnetic nanoparticles”. In: *Biotechnol. J.* 6.11 (2011), pp. 1342–1347. ISSN: 18606768. DOI: 10.1002/biot.201100045.

[12] C. Tapeinos et al. “Stimuli-responsive lipid-based magnetic nanovectors increase apoptosis in glioblastoma cells through synergic intracellular hyperthermia and chemotherapy”. In: *Nanoscale* 11 (1 2019), pp. 72–88. DOI: 10.1039/C8NR05520C.

[13] D. E. Thrall. “Thermal Dose Is Related to Duration of Local Control in Canine Sarcomas Treated with Thermoradiotherapy”. In: *Clinical Cancer Research* 11.14 (July 2005), pp. 5206–5214. ISSN: 1078-0432. DOI: 10.1158/1078-0432.CCR-05-0091.

[14] E. S. Glazer and S. A. Curley. "The Ongoing History of Thermal Therapy for Cancer". In: *Surg. Oncol. Clin. N. Am.* 20.2 (2011), pp. 229–235. ISSN: 10553207. DOI: 10.1016/j.soc.2010.11.001.

[15] H. P. Kok et al. "Current state of the art of regional hyperthermia treatment planning: a review". In: *Radiation Oncology* 10.1 (Sept. 2015), p. 196. ISSN: 1748-717X. DOI: 10.1186/s13014-015-0503-8.

[16] V. Lopresto, R. Pinto, and M. Cavagnaro. "Experimental characterisation of the thermal lesion induced by microwave ablation". In: *Int. J. Hyperth.* 30.2 (2014), pp. 110–118. ISSN: 14645157. DOI: 10.3109/02656736.2013.879744.

[17] Z. Hedayatnasab, F. Abnisa, and W. M. A. W. Daud. "Review on magnetic nanoparticles for magnetic nanofluid hyperthermia application". In: *Materials and Design* 123 (2017), pp. 174–196. ISSN: 0264-1275. DOI: 10.1016/j.matdes.2017.03.036.

[18] E. A. Périgo et al. "Fundamentals and advances in magnetic hyperthermia". In: *Applied Physics Reviews* 2.4 (2015), p. 041302. DOI: 10.1063/1.4935688.

[19] S. Dutz and R. Hergt. "Magnetic particle hyperthermia - A promising tumour therapy?" In: *Nanotechnology* 25.45 (2014), p. 452001. ISSN: 13616528. DOI: 10.1088/0957-4484/25/45/452001.

[20] L. H. Reddy et al. "Magnetic nanoparticles: Design and characterization, toxicity and biocompatibility, pharmaceutical and biomedical applications". In: *Chem. Rev.* 112.11 (2012), pp. 5818–5878. ISSN: 00092665. DOI: 10.1021/cr300068p.

[21] C. S. Kumar and F. Mohammad. "Magnetic nanomaterials for hyperthermia-based therapy and controlled drug delivery". In: *Adv. Drug Deliv. Rev.* 63.9 (2011), pp. 789–808. ISSN: 0169409X. DOI: 10.1016/j.addr.2011.03.008.

[22] A. E. Deatsch and B. A. Evans. "Heating efficiency in magnetic nanoparticle hyperthermia". In: *J. Magn. Magn. Mater.* 354 (2014), pp. 163–172. ISSN: 03048853. DOI: 10.1016/j.jmmm.2013.11.006.

[23] G. Vallejo-Fernandez et al. “Mechanisms of hyperthermia in magnetic nanoparticles”. In: *J. Phys. D. Appl. Phys.* 46.31 (2013), p. 312001. ISSN: 00223727. DOI: 10.1088/0022-3727/46/31/312001.

[24] A. J. Giustini et al. “Magnetic nanoparticle hyperthermia in cancer treatment”. In: *Nano Life* 01.01n02 (Mar. 2010), pp. 17–32. ISSN: 1793-9844. DOI: 10.1142/S1793984410000067.

[25] S. Laurent et al. “Magnetic fluid hyperthermia: Focus on superparamagnetic iron oxide nanoparticles”. In: *Adv. Colloid Interface Sci.* 166.1-2 (2011), pp. 8–23. ISSN: 00018686. DOI: 10.1016/j.cis.2011.04.003.

[26] T. Neuberger et al. “Superparamagnetic nanoparticles for biomedical applications: Possibilities and limitations of a new drug delivery system”. In: *J. Magn. Magn. Mater.* 293.1 (2005), pp. 483–496. ISSN: 03048853. DOI: 10.1016/j.jmmm.2005.01.064.

[27] S. Dutz et al. “Magnetic multicore nanoparticles for hyperthermia-influence of particle immobilization in tumour tissue on magnetic properties”. In: *Nanotechnology* 22.26 (2011). ISSN: 09574484. DOI: 10.1088/0957-4484/22/26/265102.

[28] R. Di Corato et al. “Magnetic hyperthermia efficiency in the cellular environment fordifferent nanoparticle designs”. In: *Biomaterials* 35.24 (2014), pp. 6400–6411. ISSN: 18785905. DOI: 10.1016/j.biomaterials.2014.04.036.

[29] K. D. Bakoglidis et al. “Size-dependent mechanisms in AC magnetic hyperthermia response of iron-oxide nanoparticles”. In: *IEEE Trans. Magn.* 48.4 (2012), pp. 1320–1323. ISSN: 00189464. DOI: 10.1109/TMAG.2011.2173474.

[30] M. Jeun et al. “Physical limits of pure superparamagnetic Fe3O4 nanoparticles for a local hyperthermia agent in nanomedicine”. In: *Appl. Phys. Lett.* 100.9 (2012), pp. 3–7. ISSN: 00036951. DOI: 10.1063/1.3689751.

[31] S. Hatamie et al. “Heat transfer of PEGylated cobalt ferrite nanofluids for magnetic fluid hyperthermia therapy: In vitro cellular study”. In: *J. Magn. Magn. Mater.* 462 (2018), pp. 185–194. ISSN: 0304-8853. DOI: 10.1016/j.jmmm.2018.05.020.

[32] T. Yadavalli et al. “Magnetic hyperthermia heating of cobalt ferrite nanoparticles prepared by low temperature ferrous sulfate based method”. In: *AIP Advances* 6.5 (2016), p. 055904. DOI: 10.1063/1.4942951.

[33] E. Kita et al. “Ferromagnetic nanoparticles for magnetic hyperthermia and thermoablation therapy”. In: *J. Phys. D. Appl. Phys.* 43.47 (2010). ISSN: 00223727. DOI: 10.1088/0022-3727/43/47/474011.

[34] W. Zhang et al. “Novel nanoparticles with Cr3+ substituted ferrite for self-regulating temperature hyperthermia”. In: *Nanoscale* 9 (37 2017), pp. 13929–13937. DOI: 10.1039/C7NR02356A.

[35] V. Mameli et al. “Studying the effect of Zn-substitution on the magnetic and hyperthermic properties of cobalt ferrite nanoparticles”. In: *Nanoscale* 8.19 (2016), pp. 10124–10137. ISSN: 20403372. DOI: 10.1039/c6nr01303a.

[36] C. Gómez-Polo et al. “Tailoring the structural and magnetic properties of Co-Zn nanosized ferrites for hyperthermia applications”. In: *J. Magn. Magn. Mater.* 465.March (2018), pp. 211–219. ISSN: 03048853. DOI: 10.1016/j.jmmm.2018.05.051.

[37] K. Simeonidis et al. “In-situ particles reorientation during magnetic hyperthermia application: Shape matters twice”. In: *Sci. Rep.* 6.October (2016), pp. 1–11. ISSN: 20452322. DOI: 10.1038/srep38382.

[38] N. A. Usov, M. S. Nesmeyanov, and V. P. Tarasov. “Magnetic vortices as efficient nano heaters in magnetic nanoparticle hyperthermia”. In: *Sci. Rep.* 8.1 (2018), pp. 1–9. ISSN: 20452322. DOI: 10.1038/s41598-017-18162-8.

[39] C. Martinez-Boubeta et al. “Learning from nature to improve the heat generation of iron-oxide nanoparticles for magnetic hyperthermia applications”. In: *Sci. Rep.* 3.May 2014 (2013). ISSN: 20452322. DOI: 10.1038/srep01652.

[40] D. Cabrera et al. “Unraveling viscosity effects on the hysteresis losses of magnetic nanocubes”. In: *Nanoscale* 9.16 (2017), pp. 5094–5101. ISSN: 2040-3364. DOI: 10.1039/C7NR00810D.

[41] Y. Lv et al. “Size dependent magnetic hyperthermia of octahedral Fe3O4 nanoparticles”. In: *RSC Adv.* 5.94 (2015), pp. 76764–76771. ISSN: 2046-2069. DOI: 10.1039/C5RA12558H.

[42] Z. Nemati et al. “Superparamagnetic iron oxide nanodiscs for hyperthermia therapy: Does size matter?” In: *J. Alloys Compd.* 714 (2017), pp. 709–714. ISSN: 09258388. DOI: 10.1016/j.jallcom.2017.04.211.

[43] Y. Yang et al. “Orientation Mediated Enhancement on Magnetic Hyperthermia of Fe3O4 Nanodisc”. In: *Advanced Functional Materials* 25.5 (2015), pp. 812–820. DOI: 10.1002/adfm.201402764.

[44] X. L. Liu et al. “Magnetic Vortex Nanorings: A New Class of Hyperthermia Agent for Highly Efficient in Vivo Regression of Tumors”. In: *Adv. Mater.* 27.11 (2015), pp. 1939–1944. ISSN: 15214095. DOI: 10.1002/adma.201405036.

[45] X. L. Liu et al. “Novel magnetic vortex nanorings/nanodiscs: Synthesis and theranostic applications”. In: *Chinese Phys. B* 24.12 (2015). ISSN: 16741056. DOI: 10.1088/1674-1056/24/12/127505.

[46] D. F. Gutierrez-Guzman et al. “Hyperthermia in low aspect-ratio magnetic nanotubes for biomedical applications”. In: *Appl. Phys. Lett.* 110.13 (2017). ISSN: 00036951. DOI: 10.1063/1.4979165.

[47] W. J. Atkinson, I. A. Brezovich, and D. P. Chakraborty. “Usable Frequencies in Hyperthermia with Thermal Seeds”. In: *IEEE Trans. Biomed. Eng.* BME-31.1 (1984), pp. 70–75. ISSN: 15582531. DOI: 10.1109/TBME.1984.325372.

[48] R. Hergt and S. Dutz. "Magnetic particle hyperthermia-biophysical limitations of a visionary tumour therapy". In: *J. Magn. Magn. Mater.* 311.1 SPEC. ISS. (2007), pp. 187–192. ISSN: 03048853. DOI: 10.1016/j.jmmm.2006.10.1156.

[49] P. Wust et al. "Magnetic nanoparticles for interstitial thermotherapy - Feasibility, tolerance and achieved temperatures". In: *Int. J. Hyperth.* 22.8 (2006), pp. 673–685. ISSN: 02656736. DOI: 10.1080/02656730601106037.

[50] K. Maier-Hauff et al. "Intracranial thermotherapy using magnetic nanoparticles combined with external beam radiotherapy: Results of a feasibility study on patients with glioblastoma multiforme". In: *J. Neurooncol.* 81.1 (2007), pp. 53–60. ISSN: 0167594X. DOI: 10.1007/s11060-006-9195-0.

[51] M. Angelakeris. "Magnetic nanoparticles: A multifunctional vehicle for modern theranostics". In: *Biochim. Biophys. Acta - Gen. Subj.* 1861.6 (2017), pp. 1642–1651. ISSN: 18728006. DOI: 10.1016/j.bbagen.2017.02.022.

[52] S. Kossatz et al. "High therapeutic efficiency of magnetic hyperthermia in xenograft models achieved with moderate temperature dosages in the tumor area". In: *Pharm. Res.* 31.12 (2014), pp. 3274–3288. ISSN: 1573904X. DOI: 10.1007/s11095-014-1417-0.

[53] O. Bottauscio and A. Manzin. "Parallelized micromagnetic solver for the efficient simulation of large patterned magnetic nanostructures". In: *J. Appl. Phys.* 115.17 (2014), p. 17D122. DOI: 10.1063/1.4862379.

[54] U. Gneveckow et al. "Description and characterization of the novel hyperthermia- and thermoablation-system MFH®300F for clinical magnetic fluid hyperthermia". In: *Med. Phys.* 31.6 (2004), pp. 1444–1451. ISSN: 00942405. DOI: 10.1118/1.1748629.

[55] A. P. Khandhar et al. "Enhancing cancer therapeutics using size-optimized magnetic fluid hyperthermia". In: *J. Appl. Phys.* 111.7 (2012), pp. 2012–2015. ISSN: 00218979. DOI: 10.1063/1.3671427.

[56] G. Kandasamy et al. “Functionalized Hydrophilic Superparamagnetic Iron Oxide Nanoparticles for Magnetic Fluid Hyperthermia Application in Liver Cancer Treatment”. In: *ACS Omega* 3.4 (2018), pp. 3991–4005. ISSN: 24701343. DOI: 10.1021/acsomega.8b00207.

[57] C. Yadel et al. “Hyperthermia Efficiency of Magnetic Nanoparticles in Dense Aggregates of Cerium Oxide/Iron Oxide Nanoparticles”. In: *Appl. Sci.* 8.8 (2018), p. 1241. DOI: 10.3390/app8081241.

[58] S. K. Jones and J. G. Winter. “Experimental examination of a targeted hyperthermia system using inductively heated ferromagnetic microspheres in rabbit kidney”. In: *Phys. Med. Biol.* 46.2 (Feb. 2001), pp. 385–398. ISSN: 0031-9155. DOI: 10.1088/0031-9155/46/2/308.

[59] Y. Shiroishi et al. “Future options for HDD storage”. In: *IEEE Trans. Magn.* Vol. 45. 10. 2009, pp. 3816–3822. ISBN: 0018-9464. DOI: 10.1109/TMAG.2009.2024879.

[60] J. I. Raffel and T. S. Crowther. “A Proposal for an Associative Memory Using Magnetic Films”. In: *IEEE Transactions on Electronic Computers* EC-13.5 (1964), p. 611. DOI: 10.1109/PGEC.1964.263736.

[61] G. Varvaro and F. Casoli, eds. *Ultra-High-Density Magnetic Recording*. Pan Stanford, Mar. 2016. ISBN: 978-981-4669-58-0. DOI: 10.1201/b20044.

[62] S. Bhatti et al. “Spintronics based random access memory: a review”. In: *Mater. Today* 20.9 (Nov. 2017), pp. 530–548. ISSN: 13697021. DOI: 10.1016/j.mattod.2017.07.007.

[63] R. Hertel. “Vortex states à la carte”. In: *Nat. Nanotechnol.* 8.5 (May 2013), pp. 318–320. ISSN: 1748-3387. DOI: 10.1038/nnano.2013.81.

[64] J. M. Slaughter et al. “Fundamentals of MRAM technology”. In: *J. Supercond.* 15.1 (2002), pp. 19–25. DOI: 10.1023/A:1014018925270.

Chapter 2

Micromagnetic theory

In this chapter we will introduce the theoretical aspects used in the thesis. The theoretical framework, which enables us to describe magnetization processes at nanoscale level, is *micromagnetism*. In our case, the micromagnetic study of nanostructures allows us to understand which parameters mainly influence the hysteretic behavior of nanostructures and thus their heating properties and, through a parametric analysis, to identify the best candidates as heating mediators for hyperthermia. As we will see in the last chapter, another potential application is the study of the possibility to control the magnetization state of nanostructures for applications in high-density magnetic storage.

2.1 Micromagnetism

Micromagnetism is a continuum theory of ferromagnetism that describes magnetization processes at sub-micrometer length scales. It was first formalized by William Fuller Brown in 1963 [1]. Generally, a ferromagnetic material can be defined as a material that can show a spontaneous magnetization, independently from the presence of an external magnetic field. For long time it was supposed that ferromagnetic materials were not homogeneously magnetized; finally, experiments conducted at the beginning

of the 20^{th} century by Bitter [2], followed by many others, confirmed the existence of magnetic domains and domain walls theorized by Weiss in 1907 [3]. Nevertheless, Maxwell's macroscopic theory of electromagnetism alone was not able to describe the presence of magnetic domains. During the 1950s, quantum theory developments were able to shed light on the quantum mechanics origin of magnetic moments and their interaction. However, the difference between quantum mechanics length scale and magnetic domain length scale is too large to explain the magnetization behavior in this intermediate scale level.

Micromagnetism bridges the discrete quantum scale and the continuous macroscopic scale, describing magnetization processes in terms of microscopic continuous quantities, taking into account quantum mechanic effects and explaining the experimental findings. In 1935, Landau and Lifshitz [4] posed the base of micromagnetism, introducing a continuous expression for quantum mechanical exchange energy, introducing the idea of *domain pattern* as the magnetization configuration able to minimize the magnetostatic energy.

2.2 Micromagnetic free energy

Micromagnetism characterizes the state of a ferromagnetic object Ω by means of its free energy and describes this state in terms of the continuous magnetization vector field $\mathbf{M}$, which is defined as

$$\mathbf{M}(\mathbf{r}, t) = \frac{\sum_j^N \boldsymbol{\mu}_j}{dV}, \tag{2.1}$$

where the elementary volume dV with position $\mathbf{r} \in \Omega$ is large enough to contain an elevated number N of atomistic magnetic moments $\boldsymbol{\mu}_j, j = 1, ..., N$, and small enough to guarantee continuity. $\mathbf{M}$ is associated with the net magnetic moment of dV ($\mathbf{M}dV$). Magnetization in a given volume dV is also constant in amplitude and can be written as

$$\mathbf{M}(\mathbf{r}, t) = M_S \mathbf{m}(\mathbf{r}, t), \tag{2.2}$$

where the saturation magnetization M_S is a property of the material. This is in agreement with the quantum mechanics theory, which prescribes that each atomistic magnetic moment has a constant amplitude but a changing orientation.
Different physical interactions are present in a ferromagnetic material involving different spatial scales and to each interaction is associated an energy contribution. Micromagnetic theory studies the magnetization state in terms of minimization of the magnetic Gibb's free energy of the material. In the following sub-sections we will present the different contributing energy terms, namely the exchange energy (describing short-range interactions of quantum mechanics origin), the magneto-crystalline anisotropy energy (associated with the properties of the crystal lattice), the magnetostatic or shape anisotropy energy (describing long-range interactions) and the Zeeman energy (due to external applied fields). Other contributions include the thermal energy (associated with thermal noise) and the magneto-elastic or magnetostriction energy (due to the stress anisotropy effects). The last term is here considered negligible.

2.2.1 Exchange energy

In this sub-section we will discuss the exchange interaction in ferromagnetic materials. Since this kind of phenomenon strongly depends on spin-spin interaction, it is generally studied within the quantum mechanics framework. At the atomic scale, the exchange interaction tends to align neighboring spins, favoring the formation of uniformly magnetized regions, known as *magnetic domains*. The first continuum derivation of the exchange energy is due to Landau and Lifshitz [4] developing the initial works of Bloch [5] and Heisenberg [6]. Let us introduce a cubic lattice of atomic moments; the continuum expression for the exchange energy term can be derived from the homogenization of the Heisenberg exchange Hamiltonian [6]:

$$\hat{\mathcal{H}}_{ex} = -2 \sum_{i \neq j} J_{ij}(\mathbf{r}_{ij}) \mathbf{S}_i(\mathbf{r}_i) \cdot \mathbf{S}_j(\mathbf{r}_j) \tag{2.3}$$

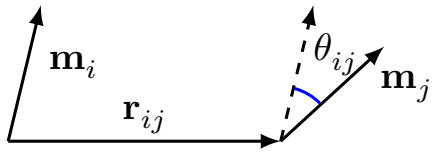

Figure 2.1: Two adjacent moments with the geometrical quantities that describe their relative positions.

with $J_{ij}(\mathbf{r}_{ij})$ describing exchange interaction between atomic spin moments $\mathbf{S}_i$ and $\mathbf{S}_j$ at positions $\mathbf{r}_i$ and $\mathbf{r}_j$. The generic atomic spin moments $\mathbf{S}_i$ can be written as $S\mathbf{m}_i$, where $\mathbf{m}_i$ is the unit vector parallel to $\mathbf{S}_i$. From a theoretical point of view the Hamiltonian describes the interaction between all the spins in the material, however this is relevant only over very short distances, therefore it is sufficient to consider only the interaction with the closest neighbors to a specific atom. Thus, the exchange energy density for one atom can be write as:

$$\phi_{ex}(\mathbf{r}_i) = -\frac{2J_0S^2}{V_{atom}}\sum_{i\neq j}^{\nu}\mathbf{m}_i\cdot\mathbf{m}_j. \tag{2.4}$$

where ν is the number of *nearest neighbors* of the atom at position $\mathbf{r}_i$, V_{atom} is the atom volume and J_0 is the nearest neighbor exchange integral. Since $\mathbf{m}_i$ and $\mathbf{m}_j$ are both unit vectors for all i and j, the scalar product $\mathbf{m}_i\cdot\mathbf{m}_j$ is only a function of the angle θ_{ij} between $\mathbf{m}_i$ and $\mathbf{m}_j$ (Fig. 2.1). This function can be rewritten as:

$$\phi_{ex}(\mathbf{r}_i) = -\frac{2J_0S^2}{V_{atom}}\sum_{i\neq j}^{\nu}\cos(\theta_{ij}). \tag{2.5}$$

Under the assumption that the angle between neighboring spins θ_{ij} is very small it is possible to introduce the Taylor's series expansion of the cosine of the angle θ_{ij}. Moreover, if the small angle approximation $|\theta_{ij}| \approx |\mathbf{m}_i - \mathbf{m}_j|$ is verified, the scalar product is recast as:

$$\sum_{i\neq j}^{\nu}\cos(\theta_{ij}) \approx \sum_{i\neq j}^{\nu}\left(1-\frac{1}{2}\theta_{ij}^2\right) \approx \nu - \frac{1}{2}\sum_{i\neq j}^{\nu}|\mathbf{m}_i-\mathbf{m}_j|^2. \tag{2.6}$$

Let us suppose to be able to write the vector $\mathbf{m}_i - \mathbf{m}_j$ as a continuous function of $\mathbf{m}$, like

$$\mathbf{m}_i - \mathbf{m}_j \approx \mathbf{r}_{ij} \cdot \nabla \mathbf{m}_j \tag{2.7}$$

that can be derived from the first order Taylor's series expansion of $\mathbf{m}_i$, i.e. $\mathbf{m}_i \approx \mathbf{m}_j + \mathbf{r}_{ij} \cdot \nabla \mathbf{m}_j$. Then, Eq. (2.5) becomes

$$\phi_{ex}(\mathbf{r}_i) = -\frac{2\nu J_0 S^2}{V_{atom}} + \frac{J_0 S^2}{V_{atom}} \sum_{i \neq j}^{\nu} (\mathbf{r}_{ij} \cdot \nabla \mathbf{m})^2, \tag{2.8}$$

describing the exchange energy density around an atom of position $\mathbf{r}_i$.
For a cubic lattice of edge length a the following identities are verified

$$\sum_{i \neq j}^{\nu} x_{ij}^2 = \sum_{i \neq j}^{\nu} y_{ij}^2 = \sum_{i \neq j}^{\nu} z_{ij}^2 = \frac{1}{3} \sum_{i \neq j}^{\nu} r_{ij}^2 \tag{2.9}$$

$$\sum_{i \neq j}^{\nu} x_{ij} y_{ij} = 0 \tag{2.10}$$

$$\sum_{j \neq i}^{\nu} r_{ij}^2 = 6a^2. \tag{2.11}$$

Considering the above identities, neglecting the constant term (related to the exchange energy for a uniformly magnetized medium), and summing over the number of spins per unit volume, we obtain the expression of the exchange energy density per unit volume

$$g_{ex}(\mathbf{r}) = k_{ex} \sum_{q=1}^{3} (\nabla m_q(\mathbf{r}))^2. \tag{2.12}$$

The exchange constant k_{ex} has the following expression

$$k_{ex} = \frac{2 J_0 S^2}{a} c. \tag{2.13}$$

As denoted before, a is the lattice edge length and c is a parameter describing the number of lattice points per unit cell (e.g. c=1 for cubic primitive cells, c=2 for body centered

cubic cells and c=4 for face centered cubic cells). The passage from the quantum mechanical operator to classical quantities is done replacing the spin magnetic moments $\mathbf{S}$ in Eq. (2.3) with the magnetization vector $\mathbf{M}$ using the following relationship:

$$\mathbf{M} = M_S \mathbf{m} = \frac{g\mu_{Bohr}^2}{V_{atom}} \mathbf{S}, \tag{2.14}$$

with g being the Landé factor (~ 2 for iron). μ_{Bohr} is the Bohr magneton and it is equal to

$$\mu_{Bohr} = \frac{e\hbar}{2m_e} = 9.274 \times 10^{-24} \text{J/T}. \tag{2.15}$$

Here, m_e the mass of the electron, $\hbar$ the reduced Plank constant and e is the elementary charge. The Bohr magneton is a physical constant and the natural unit for expressing the magnetic moment of an electron caused by either its orbital or spin angular momentum. With the opportune substitutions, the exchange constant becomes

$$k_{ex} = \frac{2J_0 M_S^2 V_{atom}^2}{g^2 \mu_{Bohr}^2 a} c \tag{2.16}$$

The material constant k_{ex} is positive in the case of a ferromagnetic material, this implies that the exchange energy is minimized when the magnetic moments are parallel. The total contribution of the exchange interaction to the free energy of a magnetic body can be obtained integrating Eq. (2.12) over the ferromagnetic region Ω, obtaining:

$$G_{ex} = \int_\Omega k_{ex}[(\nabla m_x)^2 + (\nabla m_y)^2 + (\nabla m_z)^2] dV. \tag{2.17}$$

2.2.2 Magneto-crystalline anisotropy energy

It is quite common to experimentally observe anisotropic effects in ferromagnetic materials, due to the symmetries of the crystal lattice of the material. In particular,

certain ferromagnetic materials exhibit energy-favored directions, known as *easy directions*. This effect originates from quantum mechanical phenomena, namely the coupling between spin moments and electronic orbital moments, and the coupling between spin moments and the anisotropic crystal field acting on the atoms. This behavior can be taken into account, introducing a phenomenological term to the free energy functional, based on lattice symmetry considerations.

Let us consider a volume ΔV with uniform magnetization $\mathbf{M}$. We aim at describing the dependence of the anisotropy energy on the orientation of $\mathbf{M}$. The state of the system can be represented as a function of the unit vector $\mathbf{m} = \frac{\mathbf{M}}{M_S}$, identified by the cartesian components m_x, m_y, m_z and the spherical angles θ and ψ (Fig. 2.2), being respectively the polar and azimuthal angles

$$\begin{aligned} m_x &= \sin\theta\cos\psi \\ m_y &= \sin\theta\sin\psi \\ m_z &= \cos\theta \end{aligned} \quad . \tag{2.18}$$

The anisotropy energy density $\phi_{an}(\mathbf{m})$ can be expressed as a function of the angles θ and ψ, and the anisotropy energy as the integral of the energy density function over

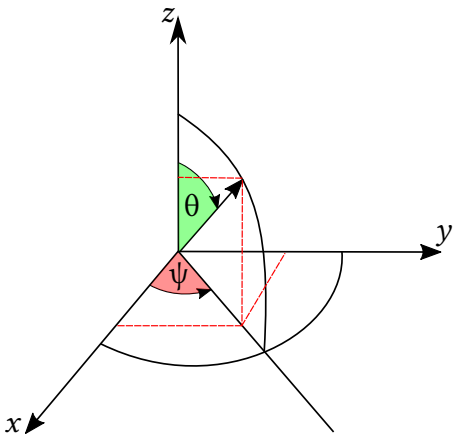

Figure 2.2: Reference system with polar and azimuthal angles.

the volume

$$G_{an} = \int_{\Omega} \phi_{an}(\mathbf{m}) dV. \tag{2.19}$$

The expression of the energy density function $\phi_{an}(\mathbf{m})$ describes the macroscopic anisotropic behavior, the minima of the function correspond to the easy axes, the saddle points correspond to the medium-hard axes and the maxima correspond to the hard axes.

Uniaxial anisotropy

One of the most common kind of anisotropy is the uniaxial anisotropy, where only one lattice direction is favored. This type of behavior can be found in cobalt or in rare earth transition metal intermetallic compounds (e.g. $SmCo_5$, $SmCo_{17}$, $Nd_2Fe_{14}B$). In this case the energy density function is rotationally symmetric with respect to the easy axis and depends only on the relative orientation of $\mathbf{m}$ with the easy axis. If, for simplicity, we suppose that the easy axis coincides with the Cartesian z axis, it is possible to write the anisotropy energy density as an even function of $m_z = \cos\theta$. With a change of variables $m_x^2 + m_y^2 = 1 - m_z^2 = 1 - \cos^2\theta = \sin^2\theta$ the expansion series becomes:

$$\phi_{an}(\mathbf{m}) = K_0 + K_1 \sin^2\theta + K_2 \sin^4\theta + K_3 \sin^6\theta + \ldots \tag{2.20}$$

where the *anisotropy constants* $K_0, K_1, K_2, \ldots$ have the dimensions of energy per unit volume. The expansion is generally truncated at the second-order term:

$$\phi_{an}(\mathbf{m}) = K_0 + K_1 \sin^2\theta \tag{2.21}$$

With this approximation the anisotropic behavior depends on the sign of K_1. From the first order derivative the critical points of the function are $0, \frac{\pi}{2}, \pi$. If $K_1 > 0$, we have two minima at $\theta = 0$ and $\theta = \pi$ corresponding to *easy axis anisotropy*. If $K_1 < 0$, we have a minimum at $\theta = \pi/2$ (xy-plane) and thus an *easy plane anisotropy*. The two

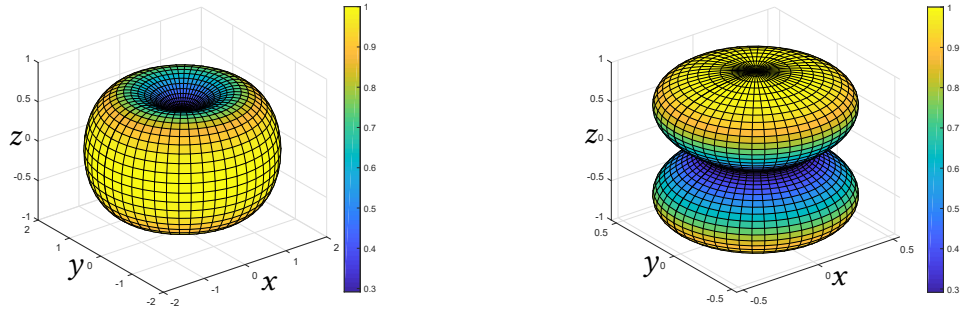

(a) ($K_1 > 0$) (b) ($K_1 < 0$)

Figure 2.3: Uniaxial anisotropy energy density function. On the left easy axis anisotropy. On the right easy plane anisotropy.

types of anisotropy are described in Fig. 2.3

The anisotropy energy, derived from the integration of Eq. (2.21) becomes:

$$G_{an}(\mathbf{m}) = \int_{\Omega} K_1[1 - (\mathbf{e}_{an}(\mathbf{r}) \cdot \mathbf{m}(\mathbf{r}))^2]dV, \tag{2.22}$$

where $\mathbf{e}_{an}$ is the easy axis unit vector and the constant K_0 is neglected.

Cubic anisotropy

Other ferromagnetic materials, such as iron and nickel, show cubic anisotropy behavior. This is mainly due to spin-lattice coupling in cubic crystals. In cartesian coordinates the anisotropy energy density function can be expressed as

$$\phi_{an}(\mathbf{m}) = K_0 + K_1(m_x^2 m_y^2 + m_y^2 m_z^2 + m_x^2 m_z^2) + K_2 m_x^2 m_y^2 m_z^2 + ... \tag{2.23}$$

where $K_0, K_1, K_2, ...$ are the anisotropy constants. Also in this case we neglect the higher order terms, i.e. $K_{i\geq 2} = 0$. If $K_1 > 0$, we have six equivalent minima along the x, y, z axes in both the positive and negative directions as illustrated by Fig. 2.4a. If $K_1 < 0$, we have eight equivalent minima along <111> directions (see Fig. 2.4b), while <110> directions are the medium-hard axes and <100> directions are the hard axes.

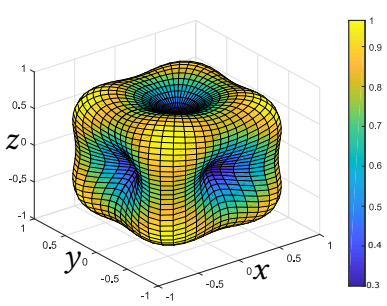

(a) ($K_1 > 0$)

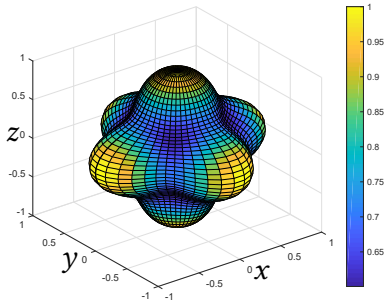

(b) ($K_1 < 0$)

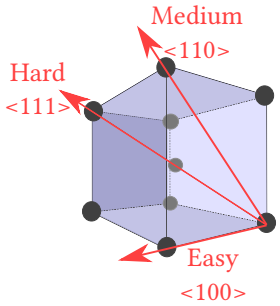

(c) Body Centered Cubic lattice

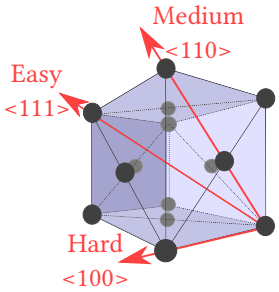

(d) Face Centered Cubic lattice

Figure 2.4: Cubic anisotropy energy density function. On the left: coordinate axes are easy directions. On the right: coordinate axes are hard directions.

2.2.3 Magnetostatic energy

The magnetostatic interaction represents how the magnetic moments interact with each other over the long distance and it is due to the shape anisotropy of the magnetized sample. To describe this interaction we introduce the magnetostatic field $\mathbf{H}_{ms}$, which depends on the contribution from the whole magnetization spatial distribution, leading to an integral term in the magnetization dynamic equations. The phenomena can be described at the macroscopic level starting from the Maxwell equations for a magnetized media, and can be derived using both the vector potential or the scalar potential, introducing the concept of magnetic charge density. In the following part we will derive $\mathbf{H}_{ms}$ using the scalar potential.

In the absence of current, the following equations are considered:

$$\begin{cases} \nabla \cdot \mathbf{B}_{ms} = 0 \\ \nabla \times \mathbf{H}_{ms} = 0. \\ \mathbf{B}_{ms} = \mu_0(\mathbf{H}_{ms} + \mathbf{M}) \end{cases} \tag{2.24}$$

From the first and third equation one can easily obtain that

$$\nabla \cdot \mathbf{H}_{ms} = -\nabla \cdot \mathbf{M} \tag{2.25}$$

while, from the second equation, it is possible to introduce a scalar potential ψ_{ms} such that $-\nabla\psi_{ms} = \mathbf{H}_{ms}$ [7]. In analogy with electrostatics, we can introduce an effective magnetic charge density, defined as $\rho_{ms} = -\nabla \cdot \mathbf{M}$, which allows us to write the following relationships

$$\begin{cases} \nabla \cdot \mathbf{H}_{ms} = -\rho_{ms} & \text{in} \quad \Omega \\ \nabla \cdot \mathbf{H}_{ms} = 0 & \text{in} \quad \Omega^c \\ \mathbf{n} \cdot [\![\mathbf{H}_{ms}]\!]_{\partial\Omega} = \mathbf{n} \cdot [\![\mathbf{M}]\!]_{\partial\Omega} \\ \mathbf{n} \times [\![\mathbf{H}_{ms}]\!]_{\partial\Omega} = \mathbf{0} \end{cases}, \tag{2.26}$$

where Ω^c represents the space external to the magnetic domain Ω. Despite magnetic charges are a fictitious abstraction of their electrical counterpart, they are a useful concept to understand how the magnetization configuration reduces the magnetostatic energy via the minimization of magnetic pole number.

The scalar potential ψ_{ms} is the solution of the Poisson's equation boundary problem:

$$\begin{cases} \nabla^2 \psi_{ms}(\mathbf{r}) = \nabla \cdot \mathbf{M}(\mathbf{r}) & \text{in} \quad \Omega, \\ \nabla^2 \psi_{ms}(\mathbf{r}) = 0 & \text{in} \quad \Omega^c \\ [\psi]_{\partial\Omega} = 0 \\ \left[\dfrac{\partial \psi}{\partial \mathbf{n}}\right]_{\partial\Omega} \end{cases} \tag{2.27}$$

which admits the following solution:

$$\psi_{ms}(\mathbf{r}) = -\frac{1}{4\pi} \int_{\Omega} \frac{\nabla' \cdot \mathbf{M}(\mathbf{r}')}{|\mathbf{r} - \mathbf{r}'|} dV' + \frac{1}{4\pi} \oint_{\partial\Omega} \frac{\mathbf{n}' \cdot \mathbf{M}(\mathbf{r}')}{|\mathbf{r} - \mathbf{r}'|} dS' \tag{2.28}$$

where

$$\sigma_M = \mathbf{n} \cdot \mathbf{M}, \tag{2.29}$$

is a *magnetic surface charge density* [7]. Using the divergence theorem the surface integral can be rewrite as a volume integral, obtaining

$$\psi_{ms}(\mathbf{r}) = \frac{1}{4\pi} \int_{\Omega} -\frac{\nabla' \cdot \mathbf{M}(\mathbf{r}')}{|\mathbf{r} - \mathbf{r}'|} + \nabla' \cdot \left(\frac{\mathbf{M}(\mathbf{r}')}{|\mathbf{r} - \mathbf{r}'|} \right) dV' \tag{2.30}$$

Tanks to this equality $\nabla \cdot (f\mathbf{v}) = f \nabla \cdot \mathbf{v} + \mathbf{v} \cdot \nabla f$, the previous equation is recast as:

$$\psi_{ms}(\mathbf{r}) = -\frac{1}{4\pi} \int_{\Omega} \nabla' \frac{1}{|\mathbf{r} - \mathbf{r}'|} \cdot \mathbf{M}(\mathbf{r}') dV' \tag{2.31}$$

Applying the gradient operator to both sides of the equation, we obtain the following expression of the magnetostatic field

$$\mathbf{H}_{ms}(\mathbf{r}) = -\frac{1}{4\pi} \nabla \int_{\Omega} \left(\nabla' \frac{1}{|\mathbf{r} - \mathbf{r}'|} \cdot \mathbf{M}(\mathbf{r}') \right) dV'. \tag{2.32}$$

The same expression can be derived from the microscopic point of view calculating the field generated by the single magnetic moments and summing their contribution over

the whole body. Analyzing the expression of the magnetostatic field in Eq. (2.32), it is trivial to notice that, apart from the linear dependence on $\mathbf{M}$, the magnetostatic field is determined uniquely by the geometrical shape of the magnetic object.
Following the similitude between magnetic and electric charges [8], the total energy of the magnetostatic field in the whole space $\mathcal{D}$ can be written as

$$\mathcal{U}_{ms} = \frac{1}{2}\mu_0 \int_{\mathcal{D}} H_{ms}^2 d\mathcal{D} \tag{2.33}$$

From Eq. (2.24) the integral can be recast as

$$\begin{aligned} \mathcal{U}_{ms} =& \frac{1}{2}\mu_0 \int_{\mathcal{D}} \mathbf{H}_{ms} \cdot \left(\frac{\mathbf{B}_{ms}}{\mu_0} - \mathbf{M} \right) d\mathcal{D} = \\ =& \frac{1}{2} \int_{\mathcal{D}} \mathbf{H}_{ms} \cdot \mathbf{B}_{ms} d\mathcal{D} - \frac{1}{2}\mu_0 \int_{\mathcal{D}} \mathbf{H}_{ms} \cdot \mathbf{M} d\mathcal{D} \end{aligned} \tag{2.34}$$

The first integral is equal to zero because $\mathbf{B}_{ms}$ is solenoidal and $\mathbf{H}_{ms}$ is irrotational. Since $\mathbf{M}$ is nonzero only inside the magnetic object, the second integral is reduced to the volume of the magnetic body Ω, leading to the following expression for the magnetostatic energy

$$G_{ms} = -\frac{1}{2}\mu_0 \int_{\Omega} \mathbf{M}(\mathbf{r}) \cdot \mathbf{H}_{ms}(\mathbf{r}) dV. \tag{2.35}$$

Therefore, the magnetostatic energy density becomes

$$\phi_{ms} = -\frac{1}{2}\mu_0 \mathbf{M} \cdot \mathbf{H}_{ms} \tag{2.36}$$

2.2.4 Zeeman energy

The presence of an external magnetic field $\mathbf{H}_a$ produces a long-rage effect on a magnetized object, therefore we introduce into the energy functional a term that is able to describe the interaction between the magnetization and the applied field.

Let us consider the force acting on a magnetic dipole with magnetic moment $\boldsymbol{\mu}$ in presence of an external field,

$$\mathbf{F}_{\text{ext}} = \mu_0 \nabla(\boldsymbol{\mu} \cdot \mathbf{H}_a). \tag{2.37}$$

This force can be seen as the negative gradient of a potential energy

$$E_a = -\mu_0 \boldsymbol{\mu} \cdot \mathbf{H}_a, \tag{2.38}$$

which is zero when the magnetic moment is aligned parallel to the applied field and reaches its maximum when the two vectors are orthogonal, thus it models the tendency of a magnetic moment to align itself to the applied field. In a magnetized body the total energy contribution is obtained performing a sum over all the local magnetic moments, thus

$$E_a = -\mu_0 \sum_i \boldsymbol{\mu}_i \cdot \mathbf{H}_a. \tag{2.39}$$

With the introduction of the micromagnetic continuum approach this energy, which is expressed in terms of discrete magnetic moments, is rewritten as the potential energy of a continuous distribution of magnetic moments under the action of an externally applied magnetic field. It results the following expressions

$$G_a = -\mu_0 \int_\Omega \mathbf{M} \cdot \mathbf{H}_a dV. \tag{2.40}$$

This term is known as the *Zeeman energy*, named after the Dutch physicist Pieter Zeeman.

2.2.5 The Gibb's free energy

It is now possible to introduce the expression of the Gibb's free energy functional as

$$\begin{aligned} G(\mathbf{M}, \mathbf{H}_a) &= G_{ex} + G_{an} + G_{ms} + G_a \\ G(\mathbf{M}, \mathbf{H}_a) &= \int_\Omega \left[k_{ex}(\nabla \mathbf{m})^2 + \phi_{an}(\mathbf{m}) - \mu_0 \frac{1}{2} \mathbf{M} \cdot \mathbf{H}_{ms} - \mu_0 \mathbf{M} \cdot \mathbf{H}_a \right] dV \end{aligned} \tag{2.41}$$

The Gibb's free energy is closely related to the Helmholtz free energy by the following equation

$$G = \underbrace{U - TS}_{\text{Helmholtz energy } F} - \mu_0 \int \mathbf{M} \cdot \mathbf{H}_a dV \tag{2.42}$$

where U is the internal energy of the system, T is the absolute temperature, S is the entropy and the integral is the interaction energy with the external field. The Gibb's free energy can be regarded as a complicated functional of the magnetization. This energy displays a multi-valley articulated landscape, which is transversed by the system when the applied field is changed. The search for the local equilibrium configurations of the magnetization spatial distribution in a body may in principle be carried out by imposing a minimum condition on the Gibb's free energy, looking for the minima of the energy landscape.

2.3 Micromagnetic equilibrium configuration

Under the assumptions of constant external field and negligible temperature effects, the system equilibrium points (metastable states) correspond to the minima of the Gibb's free energy. Using variational techniques we will study the response of the functional $G(\mathbf{M}, \mathbf{H}_a)$ to small variations $\mathbf{m} + \delta\mathbf{m}$ with the non convex constraint $\mathbf{M} = M_S\mathbf{m}$, $|\mathbf{M}| = M_S$, which thus implies $|\mathbf{m} + \delta\mathbf{m}| = 1$. In particular, we focus on the linear part of the change in the functional, namely its *first order variation.*

2.3.1 First-order variation of Gibb's free energy

The idea is to find the distribution of $\mathbf{M}$ that minimizes the Gibb's free energy, therefore we want to study the critical points of the functional, which satisfies the following relationship

$$\delta G(\mathbf{M}, \mathbf{H}_a) = 0, \tag{2.43}$$

where $\delta G(\mathbf{M}, \mathbf{H}_a)$ is the first order variation of the functional. Imposing the vanishing of the first order variation δG, for any variation $\delta\mathbf{m}$ of $\mathbf{m}$, allows us to derive the equilibrium condition of the system and consequently the equilibrium configuration of the magnetization in the body [1]. To do this task we will now analyze each term of the energy functional and introduce, one by one, their first order variation.

Exchange energy

The first order variation of Eq. (2.17) is

$$\delta G_{ex} = G_{ex}(\mathbf{m} + \delta\mathbf{m}) - G_{ex}(\mathbf{m}) = \int_\Omega 2k_{ex}\nabla\mathbf{m} \cdot \nabla\delta\mathbf{m} dV. \tag{2.44}$$

Using the vector identity

$$\mathbf{v} \cdot \nabla f = \nabla \cdot (f\mathbf{v}) - f\nabla \cdot \mathbf{v} \tag{2.45}$$

and considering

$$\nabla\mathbf{m} \cdot \nabla\delta\mathbf{m} = \nabla m_x \cdot \nabla\delta m_x + \nabla m_y \cdot \nabla\delta m_y + \nabla m_z \cdot \nabla\delta m_z \tag{2.46}$$

for the generic q^{th} component of the integral we obtain

$$\int_\Omega k_{ex}\nabla m_q \cdot \nabla\delta m_q dV = \int_\Omega \left[\nabla \cdot (\delta m_q k_{ex}\nabla m_q) - \delta m_q \nabla \cdot (k_{ex}\nabla m_q)\right] dV, \tag{2.47}$$

having assumed $f = \delta m_q$ and $\mathbf{v} = \nabla m_q$ Using the Gauss theorem it is possible to rewrite the first term of the right hand side of the last equation as a surface integral over the boundary $\partial\Omega$, resulting in

$$\int_\Omega k_{ex}\nabla m_q \cdot \nabla \delta m_q dV = \int_{\partial\Omega} \delta m_q k_{ex} \frac{\partial m_q}{\partial \mathbf{n}} dS - \int_\Omega \delta m_q \nabla \cdot (k_{ex}\nabla m_q) dV. \quad (2.48)$$

Thus the exchange contribution to the first order variation of the energy functional in Eq. (2.44) can be recast using the last reformulation of the integral term (2.48) as

$$\delta G_{ex} = -\int_\Omega 2\nabla \cdot (k_{ex}\nabla \mathbf{m}) \cdot \delta \mathbf{m} dV + \int_{\partial\Omega} \left[2k_{ex}\frac{\partial \mathbf{m}}{\partial \mathbf{n}} \cdot \delta \mathbf{m}\right] dS. \quad (2.49)$$

Anisotropy energy

The first order variation of anisotropy energy described in Eq. (2.19) can be written as:

$$\delta G_{an} = \int_\Omega \frac{\partial \phi_{an}}{\partial \mathbf{m}} \cdot \delta \mathbf{m} dV. \quad (2.50)$$

For example, in the case of uniaxial anisotropy the latter equation becomes

$$\delta G_{an} = -\int_\Omega 2K_1(\mathbf{m} \cdot \mathbf{e}_{an})\mathbf{e}_{an} \cdot \delta \mathbf{m} dV. \quad (2.51)$$

Magnetostatic energy

The first order variation of Eq. (2.35) is

$$\delta G_{ms} = -\frac{1}{2}\mu_0 \int_\Omega M_S \delta \mathbf{m} \cdot \mathbf{H}_{ms} dV - \frac{1}{2}\mu_0 \int_\Omega M_S \mathbf{m} \cdot \delta \mathbf{H}_{ms} dV. \quad (2.52)$$

Because of the reciprocity theorem [1], the two terms in the above integral are equal, therefore the equation becomes

$$\delta G_{ms} = -\mu_0 \int_\Omega M_S \mathbf{H}_{ms} \cdot \delta\mathbf{m} dV. \tag{2.53}$$

Zeeman energy

The applied magnetic field does not depend on the magnetization so the first order variation of Zeeman energy is

$$\delta G_a = -\mu_0 \int_\Omega M_S \mathbf{H}_a \cdot \delta\mathbf{m} dV. \tag{2.54}$$

2.3.2 Brown's equations and effective field

Summing the previous results, the first-order variation of the Gibb's free energy functional is written as follows

$$\begin{aligned}\delta G = -\int_\Omega \left[2\nabla \cdot (k_{ex}\nabla\mathbf{m}) - \frac{\partial \phi_{an}}{\partial \mathbf{m}} + \mu_0 M_S \mathbf{H}_{ms} + \mu_0 M_S \mathbf{H}_a\right] \cdot \delta\mathbf{m} dV + \\ + \int_{\partial\Omega} \left[2k_{ex}\frac{\partial \mathbf{m}}{\partial \mathbf{n}} \cdot \delta\mathbf{m}\right] dS.\end{aligned} \tag{2.55}$$

From here we will obtain an equation describing the equilibrium state of the problem. As stated previously $|\mathbf{m} + \delta\mathbf{m}| = 1$, therefore the most general variation of $\mathbf{m}$ is a rotation, and can be written as:

$$\delta\mathbf{m} = \mathbf{m} \times \delta\vec{\theta} \tag{2.56}$$

where $\delta\vec{\theta}$ is the vector representing the elementary rotation of an angle $\delta\theta$. Performing a substitution in Eq. (2.55) and using the following vector product identities

$$\mathbf{v}\cdot(\mathbf{w}\times\mathbf{u}) = \mathbf{u}\cdot(\mathbf{v}\times\mathbf{w}) = -\mathbf{u}\cdot(\mathbf{w}\times\mathbf{v}) \tag{2.57}$$

it is possible to obtain by imposing $\delta G = 0$

$$\begin{aligned}\delta G = \int_\Omega \mathbf{m}\times\left[2\nabla\cdot(k_{ex}\nabla\mathbf{m}) - \frac{\partial\phi_{an}}{\partial\mathbf{m}} + \mu_0 M_S\mathbf{H}_{ms} + \mu_0 M_S\mathbf{H}_a\right]\cdot\delta\vec{\theta}dV + \\ + \int_{\partial\Omega}\left[2k_{ex}\frac{\partial\mathbf{m}}{\partial\mathbf{n}}\times\mathbf{m}\right]\cdot\delta\vec{\theta}dS = 0.\end{aligned} \tag{2.58}$$

Since the elementary rotation is arbitrarily chosen, the latter equation can be equal to zero if and only if the following equations are satisfied

$$\begin{cases}\mathbf{m}\times\left[2\nabla\cdot(k_{ex}\nabla\mathbf{m}) - \dfrac{\partial\phi_{an}}{\partial\mathbf{m}} + \mu_0 M_S\mathbf{H}_{ms} + \mu_0 M_S\mathbf{H}_a\right] = \mathbf{0} \\ \left[2k_{ex}\dfrac{\partial\mathbf{m}}{\partial\mathbf{n}}\times\mathbf{m}\right]_{\partial\Omega} = \mathbf{0}\end{cases} \tag{2.59}$$

The second equation of the system $\frac{\partial\mathbf{m}}{\partial\mathbf{n}}\times\mathbf{m}$ implies that $\frac{\partial\mathbf{m}}{\partial\mathbf{n}} = 0$ on the surface of the body. Since the two vectors are always orthogonal, the vector product can only vanish if the normal derivative of $\mathbf{m}$ is identically equal to zero. Opportunely regrouping the constants in the first equation of the system allows us to obtain in the right hand side of the vector product the expression of the *effective field*

$$\mathbf{H}_{\mathit{eff}} = \frac{2}{\mu_0 M_S}\nabla\cdot(k_{ex}\nabla\mathbf{m}) - \frac{1}{\mu_0 M_S}\frac{\partial\phi_{an}}{\partial\mathbf{m}} + \mathbf{H}_{ms} + \mathbf{H}_a \tag{2.60}$$

Here the two first terms represent how the exchange and anisotropy interactions act respectively on the magnetization as two magnetic fields:

$$\mathbf{H}_{ex} = \frac{2}{\mu_0 M_S} \nabla \cdot (k_{ex} \nabla \mathbf{m}), \tag{2.61}$$

$$\mathbf{H}_{an} = -\frac{1}{\mu_0 M_S} \frac{\partial \phi_{an}}{\partial \mathbf{m}}. \tag{2.62}$$

The quantity

$$l_{ex} = \sqrt{\frac{2k_{ex}}{\mu_0 M_S^2}} \tag{2.63}$$

is the *exchange length*, which gives a measure of the distance at which the exchange interaction is prevalent. This parameter is generally in the order of $5 \div 10$ nm, thus one can reasonably expect that around that spatial scale the magnetization is uniform. This aspect has to be taken into account in the spatial discretization of the problem for the numerical integration of magnetization equation, since generally one of the assumptions is that the magnetization is uniform in each mesh element. Therefore, the size of each discretization element should not be larger than the exchange length to correctly represents the physics of the problem.

It is now possible to rewrite Eq. 2.59 as

$$\begin{cases} \mu_0 M_S \mathbf{m} \times \mathbf{H}_{\mathit{eff}} = \mathbf{0} \\ \left. \dfrac{\partial \mathbf{m}}{\partial \mathbf{n}} \right|_{\partial\Omega} = \mathbf{0} \end{cases} \tag{2.64}$$

which are known as the *Brown's equations*.

The solution of this system of equations allows us to find the equilibrium configuration of the magnetization within a magnetic body. The first Brown's equation is strongly non linear since $\mathbf{H}_{\mathit{eff}}$ has a strong integro-differential dependence on the magnetization vector field $\mathbf{m}$. To properly describe the system it is necessary to take into account its dynamics too. In the following section we will derive the equation to evaluate the time

behavior of the system.

2.4 Magnetization dynamics and the Landau-Lifshitz-Gilbert equation

The theory described before allows us to study the equilibrium configuration of a magnetic body, but does not give us any information on the time evolution of the system towards a new minimum energy point when the applied field changes. We will now introduce the dynamic model proposed by Landau and Lifshitz in 1935 [4], further developed by Gilbert [9] in 1955.

2.4.1 Gyromagnetic precession

We start introducing the gyromagnetic precession of spin magnetic moment. From quantum mechanics we know that the spin magnetic moment can be expressed as a function of the angular momentum of electrons, following the relation

$$\boldsymbol{\mu} = -\gamma \mathbf{L} \tag{2.65}$$

where γ is the absolute value of the gyromagnetic ratio, which expresses the proportionality between the two moments and has an absolute value of $1.76 \times 10^{11} \mathrm{radT}^{-1}\mathrm{s}^{-1}$. In particular:

$$\gamma = \frac{ge}{2m_e} = \frac{g\mu_B}{\hbar} \tag{2.66}$$

where $g \sim 2$ is the Landé splitting factor, $e = 1.6 \times 10^{-19}\mathrm{C}$ is the elementary charge and $m_e = 9.1 \times 10^{-31}\mathrm{kg}$ is the electron mass. As for the second cardinal equation of motion $d\mathbf{L}/dt = \tau$ (assuming that the polo speed is zero), one can write:

$$\frac{d\mathbf{L}}{dt} = \mu_0 \boldsymbol{\mu} \times \mathbf{H} \tag{2.67}$$

expressing the relation between the torque exerted by the field on the magnetic moment $\tau = \mu_0 \boldsymbol{\mu} \times \mathbf{H}$ and the rate of change of the angular moment. From Eq. (2.65) it is possible to derive the equation describing the precession of the spin magnetic moment around the field

$$\frac{d\boldsymbol{\mu}}{dt} = -\mu_0 \gamma \boldsymbol{\mu} \times \mathbf{H} \tag{2.68}$$

with frequency

$$f_l = \mu_0 \frac{\gamma H}{2\pi} \tag{2.69}$$

known as the *Larmor frequency* or precession frequency.

Let us now consider an elementary volume dV, for each magnetic moment $\boldsymbol{\mu}_j$ in the volume we can rewrite Eq. (2.68) as

$$\frac{d\boldsymbol{\mu}_j}{dt} = -\mu_0 \gamma \boldsymbol{\mu}_j \times \mathbf{H} \tag{2.70}$$

and under the hypothesis of spatially uniform field $\mathbf{H}$ we can derive the volume average of the previous equation

$$\frac{1}{dV} \frac{d \sum_j \boldsymbol{\mu}_j}{dt} = -\mu_0 \gamma \frac{\sum_j \boldsymbol{\mu}_j}{dV} \times \mathbf{H}. \tag{2.71}$$

Recalling the definition of magnetization $\mathbf{M}$ we provided in Section 2.2, from the last equation we obtain the continuum gyromagnetic precession model, namely

$$\frac{\partial \mathbf{M}}{\partial t} = -\mu_0 \gamma \mathbf{M} \times \mathbf{H}. \tag{2.72}$$

2.4.2 Landau-Lifshitz equation

In 1935 Landau and Lifshitz proposed a first model for the processional motion of magnetization. Starting from continuum precession model described by Eq. (2.72), the

quantum mechanics and anisotropy effects are taken in account through a phenomenological approach by means of the *effective field* $\mathbf{H}_{eff}$, which is described in Eq. (2.60), leading to the following equation:

$$\frac{\partial \mathbf{M}}{\partial t} = -\gamma_L \mathbf{M} \times \mathbf{H}_{eff}, \tag{2.73}$$

where γ_L is the gyromagnetic ratio according to the precessional motion definition provided by Landau and Lifshitz as $\mu_0\gamma$. This formulation is equivalent to the first Brown's equation when the rate of change of the magnetization vanishes $\frac{\partial \mathbf{M}}{\partial t} = 0$, and the same boundary condition applies, that is $\frac{\partial \mathbf{M}}{\partial \mathbf{n}}\big|_{\partial\Omega} = \mathbf{0}$. The Landau-Lifshitz equation, as the precessional model it comes from, is a conservative Hamiltonian equation. However, we know, from experimental observation, that dissipative processes take place in magnetization dynamics. Atomic-level dynamics involves interactions between magnetization, electrons and phonons. Magnetization damping can occur through energy transfer from an electron's spin to itinerant electrons, lattice vibrations, spin waves, magnons impurities [10]. In order to take into account these effects, Landau and Lifshitz introduced

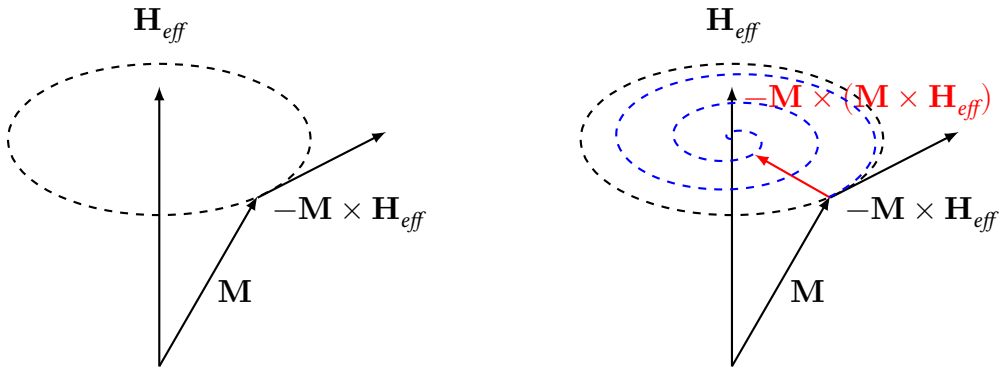

Figure 2.5: (a) Scheme of magnetization precession motion as described by Eq. (2.73) in absence of dissipative term. (b) Scheme of dampened magnetization precession motion as described by Eq. (2.74).

in the equation 2.73 a dissipative term , which drives the magnetization towards the

direction of $\mathbf{H}_{eff}$. Specifically

$$\frac{\partial \mathbf{M}}{\partial t} = -\gamma_L \mathbf{M} \times \mathbf{H}_{eff} - \frac{\lambda}{M_S} \mathbf{M} \times (\mathbf{M} \times \mathbf{H}_{eff}). \tag{2.74}$$

In the above equation $\lambda > 0$ is a phenomenological parameter that depends on the properties of the magnetic material. The additional term preserves the non convex constraint on the magnetization, since, by its vector product definition, it always acts orthogonally to the magnetization. Its damping role is well illustrated by the comparison of the schemes in Fig. 2.5.

2.4.3 Landau-Lifshitz-Gilbert equation

In 1955 Gilbert [9] proposed an alternative approach for the inclusion of the dissipative phenomena in the precession equation. Gilbert, applying a Lagrangian approach to the gyromagnetic equation of magnetization (2.73), introduced the phenomenological damping as a "viscous force" proportional to the time derivative of the magnetization, i.e.

$$\frac{\alpha}{M_S} \mathbf{M} \times \frac{\partial \mathbf{M}}{\partial t}. \tag{2.75}$$

Adding this term is equivalent to the introduction of a torque produced by a field equal to:

$$-\frac{\alpha}{\gamma M_S} \frac{\partial \mathbf{M}}{\partial t}. \tag{2.76}$$

Also in this case, the formulation of the damping term is able to preserve the magnetization amplitude. The parameter α, known as the *Gilbert damping constant*, is adimensional and its value ranges between $0.001 \div 0.01$. We can now write the Landau-Lifshitz-Gilbert (LLG) equation:

$$\frac{\partial \mathbf{M}}{\partial t} = -\gamma_G \mathbf{M} \times \mathbf{H}_{eff} + \frac{\alpha}{M_S} \mathbf{M} \times \frac{\partial \mathbf{M}}{\partial t}. \tag{2.77}$$

In the following part we will show how to obtain the Landau-Lifshitz equation from the LLG equation and we will discuss the differences between the two. An external product is applied to Eq. (2.77), multiplying both sides by $\mathbf{M}$. The equation thus becomes

$$\mathbf{M} \times \frac{\partial \mathbf{M}}{\partial t} = -\gamma_G \mathbf{M} \times (\mathbf{M} \times \mathbf{H}_{\mathit{eff}}) + \mathbf{M} \times \left(\frac{\alpha}{M_S} \mathbf{M} \times \frac{\partial \mathbf{M}}{\partial t} \right). \tag{2.78}$$

Recurring to the vector triple product formula $\mathbf{a} \times (\mathbf{b} \times \mathbf{c}) = \mathbf{b}(\mathbf{a} \cdot \mathbf{c}) - \mathbf{c}(\mathbf{a} \cdot \mathbf{b})$ and since $\mathbf{M} \cdot \frac{\partial \mathbf{M}}{\partial t} = 0$, the last equation is rewritten as:

$$\mathbf{M} \times \frac{\partial \mathbf{M}}{\partial t} = -\gamma_G \mathbf{M} \times (\mathbf{M} \times \mathbf{H}_{\mathit{eff}}) - \alpha M_S \frac{\partial \mathbf{M}}{\partial t}. \tag{2.79}$$

We can now take the LLG equation (2.77) and substitute in the last term the expression we just introduced, obtaining

$$\frac{\partial \mathbf{M}}{\partial t} = -\gamma_G \mathbf{M} \times \mathbf{H}_{\mathit{eff}} - \frac{\gamma_G \alpha}{M_S} \mathbf{M} \times (\mathbf{M} \times \mathbf{H}_{\mathit{eff}}) - \alpha^2 \frac{\partial \mathbf{M}}{\partial t}. \tag{2.80}$$

Bringing the last right hand side term of the equation on the left side and dividing the equation by $(1+\alpha^2)$, it is possible to derive the Landau-Lifshitz equation in the Gilbert's form:

$$\frac{\partial \mathbf{M}}{\partial t} = -\frac{\gamma_G}{(1+\alpha^2)} \mathbf{M} \times \mathbf{H}_{\mathit{eff}} - \frac{\gamma_G \alpha}{(1+\alpha^2) M_S} \mathbf{M} \times (\mathbf{M} \times \mathbf{H}_{\mathit{eff}}), \tag{2.81}$$

where

$$\gamma_L = \frac{\gamma_G}{(1+\alpha^2)}, \quad \lambda = \frac{\gamma_G \alpha}{(1+\alpha^2) M_S} \tag{2.82}$$

are the coefficients of the Landau-Lifshitz (LL) equation. The equations (2.74) and (2.81) are equivalent from a mathematical point of view, but they describe two different physics. Taking a closer look, they behave in the same way only in the case of pure precession without damping ($\alpha, \lambda \to 0$). As pointed out by Mallinson [11] and Kikuchi [12] in the

case of infinite damping ($\alpha, \lambda \to \infty$) they have two different behaviors, i.e.

$$\begin{aligned} \lambda \to \infty \quad &\text{LL equation} \quad \frac{\partial \mathbf{M}}{\partial t} \to \infty \\ \alpha \to \infty \quad &\text{LLG equation} \quad \frac{\partial \mathbf{M}}{\partial t} \to 0 \end{aligned} \tag{2.83}$$

Since, for very large damping, we expect that the motion is very slow, we can say that the LLG formulation is better suited to describe the physics of the problem. In the following chapter, we will refer to the magnetization dynamics equation in the LLG form, indicating for conciseness γ_G as γ.

For completeness we include also the normalized LLG equation, since it is often useful to have an equation expressed in dimensionless units. We introduce the normalized quantity

$$\mathbf{m} = \frac{\mathbf{M}}{M_S}, \quad \mathbf{h}_{\mathit{eff}} = \frac{\mathbf{H}_{\mathit{eff}}}{M_S}. \tag{2.84}$$

The normalized LLG equation is obtained dividing both sides of Eq. (2.81) by γM_S^2 and measuring the time in units of $(\gamma M_S)^{-1}$. These operations lead to

$$\frac{\partial \mathbf{m}}{\partial t} = -\frac{1}{(1+\alpha^2)} \mathbf{m} \times \mathbf{h}_{\mathit{eff}} - \frac{\alpha}{(1+\alpha^2)} \mathbf{m} \times (\mathbf{m} \times \mathbf{h}_{\mathit{eff}}). \tag{2.85}$$

The expression of $\mathbf{H}_{\mathit{eff}}$ in Eq. (2.60) can be renormalized by same normalizing the different field terms, therefore the normalized version of the effective field becomes:

$$\mathbf{h}_{\mathit{eff}} = \frac{2}{\mu_0 M_S^2} \nabla \cdot (k_{ex} \nabla \mathbf{m}) - \frac{1}{\mu_0 M_S^2} \frac{\partial \phi_{an}}{\partial \mathbf{m}} + \mathbf{h}_{ms} + \mathbf{h}_a. \tag{2.86}$$

2.4.4 Properties of magnetization dynamics

Let us now briefly recap the properties of the Landau-Lifshitz-Gilbert equation.

Conservation of magnetization amplitude

Taking the normalized LLG equation (2.85) and applying the scalar product by $\mathbf{m}$ to both sides of the equation, we can rewrite the left side as the derivative of the square of the module of $\mathbf{m}$, while the right side becomes identically equal to zero because of the orthogonality.

$$\frac{d}{dt}\left(\frac{1}{2}|\mathbf{m}|^2\right) = 0. \tag{2.87}$$

therefore

$$\forall t_1, t_2 \in \mathbb{R}^+ \text{ and } \mathbf{r} \in \Omega \; |\mathbf{m}(t_1, \mathbf{r})| = |\mathbf{m}(t_2, \mathbf{r})|. \tag{2.88}$$

This means that any magnetization motion, at a given location $\mathbf{r}$, evolves on the unit sphere. In Chapter 3 we will see how this property influences the choice of time integration methods.

Lyapunov structure

Taking the normalized LLG equation (2.85), we can rewrite it in the following form:

$$\frac{\partial \mathbf{m}}{\partial t} = -\mathbf{m} \times \left(\mathbf{h}_{\mathit{eff}} - \alpha \frac{\partial \mathbf{m}}{\partial t}\right). \tag{2.89}$$

If we apply the scalar product by $(\mathbf{h}_{\mathit{eff}} - \alpha \frac{\partial \mathbf{m}}{\partial t})$ to both sides of the equation, the right hand side term vanishes because of the orthogonality and we obtain

$$\frac{\partial \mathbf{m}}{\partial t} \cdot \left(\mathbf{h}_{\mathit{eff}} - \alpha \frac{\partial \mathbf{m}}{\partial t}\right) = 0 \tag{2.90}$$

Introducing now the following expression for the time derivative of the free energy g

$$\frac{dg}{dt} = \int_\Omega \left(\frac{\delta g}{\delta \mathbf{m}} \cdot \frac{\partial \mathbf{m}}{\partial t} + \frac{\delta g}{\delta \mathbf{h}_a} \cdot \frac{\partial \mathbf{h}_a}{\partial t}\right) dv = \int_\Omega \left(-\mathbf{h}_{\mathit{eff}} \cdot \frac{\partial \mathbf{m}}{\partial t} - \mathbf{m} \cdot \frac{\partial \mathbf{h}_a}{\partial t}\right) dv \tag{2.91}$$

using the result in Eq. (2.90) we obtain

$$\frac{dg}{dt} = -\int_{\Omega} \alpha \left| \frac{\partial \mathbf{m}}{\partial t} \right|^2 dv - \int_{\Omega} \mathbf{m} \cdot \frac{\partial \mathbf{h}_a}{\partial t} dv \tag{2.92}$$

This is an energy balance equation for magnetization dynamics. Since $\alpha > 0$ the first integral will always be positive, therefore when the applied field is constant $\left(\frac{\partial \mathbf{h}_a}{\partial t} = 0\right)$, the derivative of g can only be negative or zero, thus we can conclude that the free energy is a non-increasing function of time. Moreover if α is also equal to zero then the energy is constant. This is referred as the *Lyapunov structure* of the LLG equation [13, 14].

2.5 Stochastic LLG equation: inclusion of thermal effect

The theory presented until now does not consider the effects of temperature, therefore it does not include in the model the effects of the thermal noise on the magnetization dynamics. The study of thermal fluctuations becomes more and more relevant as the size of the magnetic body reduces. In fact, thermal effects, which tend to destabilize the magnetization configuration, potentially overcoming energy barriers and moving the system into the basin of attraction of a different energy minimum, are more evident when the objects are small. This property is confirmed, for example, by the transition to the superparamegnetic behavior of ferromagnetic objects with dimensions lower than a critical size. This problem is relevant, for example, in the study of magnetic recording. To increase the capacity of magnetic memories one of the main strategy is to increase the information density, thus shrinking the magnetic bits. The information units are now approaching a size where the effect of thermal noise can be large enough to cause a reversal of magnetization, therefore causing a bit switch from 0 to 1 or vice-versa, corrupting the stored information. Looking at our main application in hyperthermia

therapy, the thermal fluctuations can ease the switch between mangetization states, changing the hysteresis loop, and reducing the value of saturating field.

The introduction of thermal effects requires a modified stochastic version of LLG equation, which will be described in this section. The treatment of stochastic PDEs would require a deeper analysis and the introduction of theories related to Wiener processes and stochastic calculus, but this is not the scope of this thesis, therefore we provide only few details. For a proper analysis of stochastic PDEs we suggest to read references [15, 16].

The most common way to introduce the effects of thermal noise in LLG equation, it is to include, as a stochastic noise contribution with precise stochastic property, a thermal field $\mathbf{H}_{th}$ in Eq. (2.81), which becomes

$$\frac{\partial \mathbf{M}}{\partial t} = -\frac{\gamma}{(1+\alpha^2)}[\mathbf{M} \times (\mathbf{H}_{\mathit{det}} + \mathbf{H}_{th})] - \frac{\gamma\alpha}{(1+\alpha^2)}\mathbf{M} \times [\mathbf{M} \times (\mathbf{H}_{\mathit{det}} + \mathbf{H}_{th})]. \quad (2.93)$$

Initially introduced by Brown [1], in this equation, $\mathbf{H}_{\mathit{det}}$ correspond to the effective field $\mathbf{H}_{\mathit{eff}}$ of the original LLG equation, representing the deterministic part, while $\mathbf{H}_{th}$ is the stochastic Langevin term. Its components are assumed to be uncorrelated in space and time [17],and have

$$\langle \mathbf{H}_{th}(\mathbf{r}, t) \rangle = 0 \quad (2.94)$$

$$\left\langle H^i_{th}(\mathbf{r}, t) \cdot H^j_{th}(\mathbf{r}', t') \right\rangle = 2D\delta_{ij}\delta(t - t')\delta(\mathbf{r} - \mathbf{r}') \quad (2.95)$$

where $\langle , \rangle$ denotes the average, $i, j = x, y, z$ are the cartesian components and D is the amplitude of the thermal fluctuation according to the fluctuation-dissipation theorem, which is assumed to have the following expression

$$D = \alpha k_B T / \gamma \mu_0 M_S \Delta V \quad (2.96)$$

where T is the absolute temperature, k_B is the Boltzmann constant and ΔV is the cell size in the discretized problem [18]. This term, when solving the LLG equation, introduces a Wiener process, which requires to be treated inside the framework of stochastic calculus. For an in depth analysis on the choice of appropriate numerical methods we suggest reading the works of Berkov [19, 20]

References

[1] W. F. Brown. *Micromagnetics*. Interscience tracts on physics and astronomy. Interscience Publishers, 1963.

[2] F. Bitter. "On Inhomogeneities in the Magnetization of Ferromagnetic Materials". In: *Phys. Rev.* 38.10 (Nov. 1931), pp. 1903–1905. ISSN: 0031-899X. DOI: 10.1103/PhysRev.38.1903.

[3] P. Weiss. "L'hypothèse du champ moléculaire et la propriété ferromagnétique". In: *J. Phys. Théorique Appliquée* 6.1 (1907), pp. 661–690. ISSN: 0368-3893. DOI: 10.1051/jphystap:019070060066100.

[4] L. Landau and E. Lifshitz. "On the Theory of the Dispersion of Magnetic Permeability in Ferromagnetic Bodies". In: *Phys. Zeitsch. der Sow.* 169.14 (1935), pp. 14–22. ISSN: 0018-9464. DOI: 10.1109/TMAG.2004.836740.

[5] F. Bloch. "Zur Theorie des Austauschproblems und der Remanenzerscheinung der Ferromagnetika". In: *Zeitschrift für Physik* 74.5 (May 1932), pp. 295–335. ISSN: 0044-3328. DOI: 10.1007/BF01337791.

[6] W. Heisenberg. "Zur Theorie der Magnetostriktion und der Magnetisierungskurve". In: *Zeitschrift für Physik* 69.5 (May 1931), pp. 287–297. ISSN: 0044-3328. DOI: 10.1007/BF01391350.

[7] J. D. Jackson. *Classical electrodynamics*. 3rd ed. New York, NY: Wiley, 1999. ISBN: 9780471309321.

[8] S. Bobbio. *Electrodynamics of materials : forces, stresses, and energies in solids and fluids*. San Diego : Academic Press, 1999. ISBN: 0121082601.

[9] T. Gilbert. "A Lagrangian Formulation of the Gyromagnetic Equation of the Magnetization Field". In: *Phys. Rev.* 100 (1955), p. 1243.

[10] J. Stöhr and H. C. Siegmann. *Magnetism: From fundamentals to nanoscale dynamics*. Vol. 152. 2006, pp. 1–822. ISBN: 3540302824. DOI: 10.1007/978-3-540-30283-4.

[11] J. Mallinson. "On damped gyromagnetic precession". In: *IEEE Trans. Magn.* 23.4 (July 1987), pp. 2003–2004. ISSN: 0018-9464. DOI: 10.1109/TMAG.1987.1065181.

[12] R. Kikuchi. "On the Minimum of Magnetization Reversal Time". In: *J. Appl. Phys.* 27.11 (1956), pp. 1352–1357. DOI: 10.1063/1.1722262.

[13] P. Podio-Guidugli. "On dissipation mechanisms in micromagnetics". In: *Eur. Phys. J. B* 19.3 (Feb. 2001), pp. 417–424. ISSN: 1434-6028. DOI: 10.1007/s100510170318.

[14] M. D'Aquino. "Nonlinear magnetization dynamics in thin-films and nanoparticles". PhD thesis. Università degli studi di Napoli Federico II, 2004.

[15] W. Liu and M. Röckner. *Stochastic partial differential equations: an introduction*. Springer, 2015. DOI: 10.1007/978-3-319-22354-4.

[16] C. Aron et al. "Magnetization dynamics: Path-integral formalism for the stochastic Landau-Lifshitz-Gilbert equation". In: *J. Stat. Mech. Theory Exp.* 2014.9 (Sept. 2014), P09008. ISSN: 17425468. DOI: 10.1088/1742-5468/2014/09/P09008.

[17] A. Lyberatos, D. V. Berkov, and R. W. Chantrell. "A method for the numerical simulation of the thermal magnetization fluctuations in micromagnetics". In: *J. Phys. Condens. Matter* 5.47 (1993), pp. 8911–8920. ISSN: 09538984. DOI: 10.1088/0953-8984/5/47/016.

[18] E. Martinez et al. “Micromagnetic simulations with thermal noise: Physical and numerical aspects”. In: *J. Magn. Magn. Mater.* 316.2 SPEC. ISS. (2007), pp. 269–272. ISSN: 03048853. DOI: 10.1016/j.jmmm.2007.03.178.

[19] D. V. Berkov. “Magnetization Dynamics Including Thermal Fluctuations: Basic Phenomenology, Fast Remagnetization Processes and Transitions Over High-energy Barriers”. In: *Handbook of Magnetism and Advanced Magnetic Materials*. American Cancer Society, 2007. ISBN: 9780470022184. DOI: 10.1002/9780470022184.hmm204.

[20] D. Berkov, N. Gorn, and P. Görnert. “Magnetization Dynamics in Nanoparticle Systems: Numerical Simulation Using Langevin Dynamics”. In: *Physica status solidi (a)* 189.2 (2002), pp. 409–421. DOI: 10.1002/1521-396X(200202)189:2<409::AID-PSSA409>3.0.CO;2-G.

Chapter 3

Development of a 3D micromagnetic numerical code

As the size of the magnetic object grows, the reversal process of the magnetization presents more complex, non-uniform magnetization configurations. These can not be determined analytically, thus requiring the numerical integration of the LLG equation. The problem complexity increases even more for 3D magnetic objects, which can not be approximated as thin films.

In this chapter we will present the development of a 3D numerical code for the efficient simulation of the magnetization reversal process of 3D magnetic nanostructures in presence of thermal effects. This code will be used in Chapter 5 to calculate the hysteresis losses of cylindrical and spherical permalloy nanostructures, in order to investigate their suitability for hyperthermia uses.

The numerical integration of the LLG equation can be computationally very demanding for multiple reasons related to the need of simulating phenomena at the exchange length scale (5-10 nm) as well as to the integral description of the magnetostatic field. As an example, the modelling of a permalloy cube with a 200 nm long side requires a spatial discretization $\Delta s \sim 5$ nm, in order to correctly calculate the exchange field, since the exchange length of the material is about 5 nm. Each side of the cube is then

discretized in 40 subdivisions, with a consequently total number of element $N = 64000$. The computation of the magnetostatic field being a long-range phenomenon requires the calculation of the interactions between each mesh element. In the above example we have to compute around 4×10^9 contributions, since they scale with N^2. Because these contributions have to be calculated at each time step, it is essential to implement an algorithm able to reduce the computational burden. To this aim, we have chosen to use the Fast Fourier Transform (FFT) for the determination of the magnetostatic field in the 3D code implementation, despite some of its drawbacks, such as the need to use a regular (structured) mesh. This type of mesh limits the accurate reconstruction of curved boundaries, which are approximated in a stair-case like way. Moreover, since the main goal of our work is the computation of the hysteresis loops of magnetic nanostructures, it is important to implement an efficient time-integration scheme, allowing a rapid convergence to equilibrium for a given applied field value. This task becomes particularly critical for irreversible jumps. For this reason we have opted for a time integration scheme based on the Cayley transform, which has proven to be very efficient in the calculation of equilibrium states [1, 2].

In the following sections we will describe the implementation of the 3D micromagnetic code, focusing on the used time integration scheme and on the calculation of the different terms of the effective field. In particular, the time integration is performed by means of a two-step time scheme based on the Cayley transform (see Fig. 3.1 and Fig. 3.2). The exchange field is calculated by means of a Finite Difference method, while the magnetostatic field is evaluated via an FFT based approach, as anticipated before. Furthermore, details are given about the computation of possible thermal noise contribution.

In the last part of the chapter, the developed 3D code is validated by comparison to other micromagnetic solvers, focusing on two of the standard reference problems proposed by the Micromagnetic Modeling Activity Group (μMAG), as part of the Center for Theoretical and Computational Materials Science (CTCMS) of the US National Institute of Standards and Technology (NIST) [3]. Moreover, we perform a direct comparison with

MuMax3 [4–6], a micromagnetic solver developed by the Ghent University.

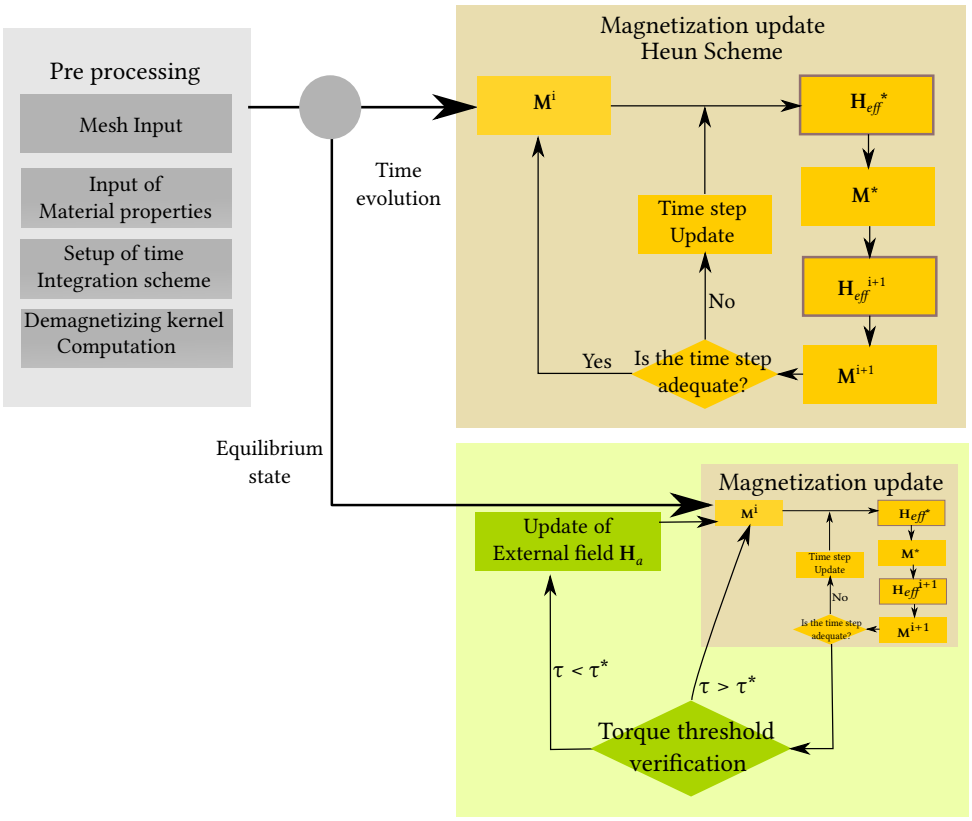

Figure 3.1: Scheme describing the structure of the 3D micromagnetic code. We identify two main blocks, a preprocessing one where we input the mesh, the properties of the materials, define the simulation parameters and compute the kernel necessary for the computation of the magnetostatic field. The second block comprehends the part of the solver for the evaluation of the effective field and the time integration algorithm (in the scheme we show the Heun adaptive solver), which are called at each time step. Two kind of simulations can be done. We can perform a time evolution analysis, where the applied field $\mathbf{H}_a$ is a function of time, and the simulation is performed for a given time interval, or we can search for the equilibrium points of the system. In this second case the applied field $\mathbf{H}_a$ is a discountinous piecewise constant function. For each value of applied field the simulation runs until a torque threshold is reached.

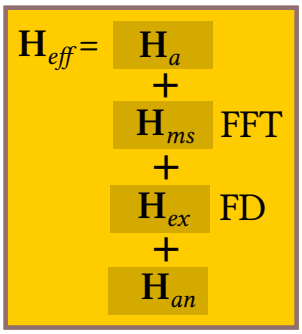

Figure 3.2: $\mathbf{H}_{eff}$ is the sum of four contributes:

- the applied field $\mathbf{H}_a$;
- the magnetostatic field $\mathbf{H}_{ms}$ (computed with an FFT algorithm);
- the exchange field $\mathbf{H}_{ex}$ (computed with a finite difference algorithm);
- the anisotropy field $\mathbf{H}_{an}$ (evaluated pointwise).

3.1 Time integration of the LLG equation

In this section we will address the time integration of the LLG equation. The spatial discretization of the LLG equation, by means of the Finite Difference approach, like in our 3D code, or by Finite Element techniques, leads to a system of ordinary differential equations (ODEs), with dimension equal to the number of mesh elements or nodes. The resulting ODE system has to be time integrated to calculate the magnetization dynamics. The discretized micromagnetic problem has very peculiar properties that must be taken into consideration in the choice of the time integration numerical solver. These features are listed in the following.

- The magnetization has constant magnitude $\forall t \in \mathbb{R}$ and $\forall \mathbf{r} \in \Omega$. Classical time stepping algorithms do not preserve this property, independently of the scheme order and of the time step [7]. Thus, classical Euler, Adam-Bashford, Runge-Kutta schemes [8] are not properly suitable. In many micromagnetic codes this problem is circumvented either re-normalizing the magnetization at each time step, or if $|\mathbf{M}| > M_S + \varepsilon$, with ε being a given tolerance [9, 10]. This approach is not without concerns, in fact the process of re-normalization is a numerical modification of the time evolution, and in some cases can have a strong effect on the magnetostatic field evaluation [1, 11] since

$$\nabla \cdot \left(M_S \frac{\mathbf{M}_{n+1}}{|\mathbf{M}_{n+1}|} \right) \neq \nabla \cdot \mathbf{M}_{n+1}. \tag{3.1}$$

Taking a closer look to standard integration algorithms with the following form (explicit methods):

$$\mathbf{u}(x, t + \Delta t) \approx \mathbf{u}(x, t) + F(\mathbf{u}(x, t), t, \Delta t), \tag{3.2}$$

the impossibility of these numerical schemes to preserve the magnetization module is obvious. In fact the expression of $F(\cdot, \cdot, \cdot)$, which may vary depending on the chosen scheme, clearly represents a translation of $\mathbf{u}(x, t)$ and not a rotation (Fig. 3.3), hence

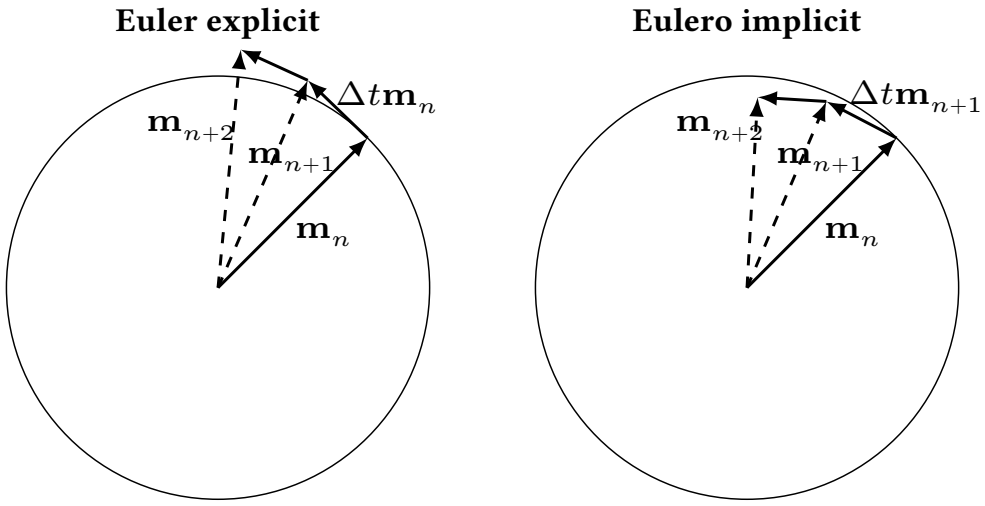

Figure 3.3: A simple example of how classic integration schemes do not preserve the vector module. In the simple case of a constant rotation, an explicit scheme will inevitably tend to generate an outward moving spiral instead of a circumference; conversely, an implicit scheme will produce an inward spiral trajectory.

this kind of schemes does not inherently preserve the magnetization amplitude. This type of behavior is also present in some implicit schemes such as the implicit Euler one (see Fig. 3.3).

- The LLG equation has a Lyapunov structure, that is, for a time-constant external field, the free energy functional decreases in time [12]. This means that the system tends to a stable equilibrium point, which is a minimum of the free energy. In general, classical integration schemes can preserve this property only when using very small time steps. The use of large time steps can lead to the occurrence of instability phenomena, for example causing a steady increase in the exchange energy [2]. This limitation on the step size can be very strong, greatly affecting the solution computational time.

- When the dissipation phenomena are neglected ($\alpha = 0$), we expect that the time integration algorithm is able to preserve the total energy, since the problem, in the case of no damping, is Hamiltonian (conservative).

In general, explicit methods do not guarantee that any of the above properties are satisfied, unless the used time step is extremely small. For what concerns the family of implicit methods, many of them have good stability performance, however they do not guarantee the norm preservation of the magnetization nor the energy conservation properties of the LLG equation. Moreover, in general implicit methods tend to be computationally heavy, requiring to solve large non-linear coupled systems of equations [13], therefore it is preferred to use semi-implicit methods [14].

The geometrical integrators are a family of solvers, which are able to preserve these properties and, before being applied in micromagnetics, they were used in many research fields in computational mechanics, where this kind of constraints appears [15–18]. In micromagnetics, geometrical methods were developed using semi-implicit algorithms and quasi-Newton method [13]. However, these methods require the implementation of iterative techniques; therefore, they need that, at each iteration, the effective field and thus the magnetostatic field are recalculated, resulting in very time-consuming operations.

In the following sub-sections we will introduce the explicit Cayley transform based method, which is implemented in our code [1, 2]. To this aim, one has to utilize the mathematical framework of the Lie Groups and of the Lie algebras. For completeness, a brief introduction to these mathematical concepts can be found in Appendix A.

3.1.1 Cayley transform based scheme

Let us rewrite the LLG equation (2.81) in a more general form:

$$\dot{\mathbf{M}}(\mathbf{r}, t) = \mathbf{A}(\mathbf{M}(\mathbf{r}, t)) \times \mathbf{M}(\mathbf{r}, t) \tag{3.3}$$

where $\mathbf{A}$ is a non linear operator containing both the effective field and the damping term of the LLG equation, i.e.

$$\mathbf{A} = \frac{\gamma}{1+\alpha^2}\left[\mathbf{H}_{\mathit{eff}} + \frac{\alpha}{M_S}\left(\mathbf{M}\times\mathbf{H}_{\mathit{eff}}\right)\right]. \tag{3.4}$$

For convenience, it is possible to introduce a generalization $\boldsymbol{\omega}$ of this non linear operator:

$$\boldsymbol{\omega}(\mathbf{M}) = \mathbf{A}(\mathbf{M}) + \sigma(\mathbf{M})\mathbf{M}. \tag{3.5}$$

In Eq.3.5 σ is an arbitrary scalar function, and since $\sigma(\mathbf{M})\mathbf{M}$ is parallel to the magnetization vector, this new term does not affect the dynamics of $\mathbf{M}$. Hence, we can substitute $\mathbf{A}$ with $\boldsymbol{\omega}$ in Eq.3.3.

By considering the mathematical framework provided in Appendix A about Lie algebras, one is now able to rewrite Eq. (3.3) in terms of a skew matrix using the properties of the underlying Lie Groups. This is done introducing a family of curves Q such that

$$Q(t) : \Omega \to SO(3) \;/\; \mathbf{M}(\mathbf{r},t) = Q(\mathbf{r},t)\mathbf{M}_0(\mathbf{r}), \quad \forall \mathbf{r}\in\Omega \tag{3.6}$$

with $\mathbf{M}_0(\mathbf{r})$ being the magnetization vector at the time instant $t = 0$.
From the mathematical passages contained in Appendix A we know that

$$\dot{\mathbf{M}}(t) = \dot{Q}(t)\mathbf{M}_0 \tag{3.7}$$

$$\dot{\mathbf{M}}(t) = skew[\xi(t)]\mathbf{M}(t), \tag{3.8}$$

$$\dot{\mathbf{M}}(t) = \xi(t)\times\mathbf{M}(t) \tag{3.9}$$

where $\xi(t) \in \mathbb{R}$ is a function that verifies the reletionship $\dot{Q}(t) = skew[\xi(t)]Q(t)$. Comparing this last equation with the original system described by Eq. (3.3) yields

$$\xi(t) = \boldsymbol{\omega}(\mathbf{M}(t)). \tag{3.10}$$

Using Eq. (3.8) and Eq. (3.5) one can define a family of ODEs

$$\dot{Q} = skew[\boldsymbol{\omega}(Q\mathbf{M}_0)]Q, \tag{3.11}$$

With this process, instead of searching directly for the vector field $\mathbf{M} \in \mathbb{R}^3$, we look for the family of rotations in $SO(3)$ describing the rotation of $\mathbf{M}$. Recurring to the geometric integration techniques developed for the Lie groups, it is possible to determine approximate discrete solution curves of these ODEs. In its generic form, an integrator of this kind can be written as [7, 19]

$$g_{n+1} = \exp(F(g_{n-p}, \dots, g_n, \Delta t))g_n. \tag{3.12}$$

Now the exponential mapping can be replaced by the Cayley transform

$$\text{cay}(\xi) = (I + skew[\xi/2])(I - skew[\xi/2])^{-1}, \tag{3.13}$$

which is a second order approximator of the exact exponential for the group $SO(3)$. It is important to notice that algorithms of any order can be built from the Cayley transform applied to matrix groups determined by quadratic constraint [11, 20]. Thus, the implementation of an opportune scheme using the Cayley transform allows us to solve:

$$Q_{n+1} = \text{cay}(F(\boldsymbol{\omega}(Q_n\mathbf{M}_0), \Delta t)Q_n \tag{3.14}$$

$$\mathbf{M}_{n+1} = Q_{n+1}\mathbf{M}_0 = \text{cay}(F(\boldsymbol{\omega}(\mathbf{M}_n), \Delta t)\mathbf{M}_n. \tag{3.15}$$

Another advantage of this implementation with the Cayley transform is that the image of a vector $\boldsymbol{\nu} \in \mathbb{R}^3$ under the action of $\text{cay}(\boldsymbol{\omega})$ takes the following simple form:

$$\text{cay}(\boldsymbol{\omega})\boldsymbol{\nu} = \boldsymbol{\nu} + \frac{1}{1 + ||\boldsymbol{\omega}/2||^2}\left[\boldsymbol{\omega} \times \boldsymbol{\nu} + \frac{1}{2}\boldsymbol{\omega} \times (\boldsymbol{\omega} \times \boldsymbol{\nu})\right] \tag{3.16}$$

It is now possible to introduce variants of the classical explicit Euler and Heun time-integrator schemes using the Cayley transform. In this way, these two methods preserve the properties of the LLG equation, independently of the time step, since now those are intrinsic properties of the integration scheme. In order to solve the ODEs in each discretization cell or i, j, k mesh element the system can be written as:

$$\mathbf{M}_{n+1}^{i,j,k} = \text{cay}\left(\Delta t \tilde{\boldsymbol{\omega}}\right) \mathbf{M}_{n}^{i,j,k}, \tag{3.17}$$

where, for the explicit first order Euler scheme:

$$\tilde{\boldsymbol{\omega}} = A(\mathbf{M}_{n}^{i,j,k}) + \sigma \mathbf{M}_{n}^{i,j,k}; \tag{3.18}$$

and for the second order Heun method:

$$\begin{cases} \tilde{\boldsymbol{\omega}} = \dfrac{1}{2}(\boldsymbol{\omega}_{*} + \boldsymbol{\omega}_{n}) \\ \boldsymbol{\omega}_{*} = A(\mathbf{M}_{*}^{i,j,k}) + \sigma \mathbf{M}_{*}^{i,j,k} \\ \mathbf{M}_{*} = \text{cay}(\Delta t \boldsymbol{\omega}_{n}) \mathbf{M}_{n}^{i,j,k} \end{cases} \tag{3.19}$$

3.1.2 Effects of term $\sigma\mathbf{M}$

In this section we take a closer look to the effects of the generalized operator we introduced previously, focusing on the effects of the term $\sigma(\mathbf{M})\mathbf{M}$ on hysteresis loop computation. In our implementation of the algorithm, $\sigma(\mathbf{M})$ is a constant in time and space equal to parameter σ. In the following part we discuss how, acting on this constant, we are able to speed up the computation of static hysteresis loops.

To explain the contribution of the term $\sigma\mathbf{M}$ to the magnetization dynamics, we focus the attention on a simplified case, where α is fixed to zero ($\mathbf{A} = \gamma\mathbf{H}_{\mathit{eff}}$) and the magnetization update is performed by means of the Euler algorithm (one-step method).

Considering the Euler method described in Eq. (3.18), using Eq. (3.16) and opportunely regrouping the terms we obtain:

$$\mathbf{M}_{n+1} - \mathbf{M}_n = \frac{\gamma \Delta t}{1 + \left\| \frac{\Delta t \left(\gamma \mathbf{H}_{eff_n} + \sigma \mathbf{M}_n \right)}{2} \right\|^2} \Bigg[\left(\mathbf{H}_{eff_n} \times \mathbf{M}_n \right) + \\ + \underbrace{\frac{1}{2} \Delta t \gamma \mathbf{H}_{eff_n} \times \left(\mathbf{H}_{eff_n} \times \mathbf{M}_n \right)}_{\text{numerical damping}} + \underbrace{\frac{1}{2} \Delta t \sigma \mathbf{M}_n \times \left(\mathbf{H}_{eff_n} \times \mathbf{M}_n \right)}_{\text{numerical damping}} \Bigg]. \tag{3.20}$$

In the above equation, the first term is the external product between $\mathbf{H}_{eff_n}$ and $\mathbf{M}_n$. This term describes the precessional motion of the magnetization vector via physical way. The second and third term assume instead the form of a damping. The second term comes from the numerical integration and is responsible of appreciable artificial damping phenomena only for high effective fields and large timestep Δt. The third term has also a numerical origin, and it is an increasing function of σ and time step Δt. The effect of this last term becomes significant when σ and γ are of the same order of magnitude and Δt is of the order of picoseconds.

Artificial damping phenomena have a strong impact on computational efficiency, influencing the time step number between two successive equilibrium states, the maximum step size able to guarantee the convergence of the solution, and the threshold defining the criterion of convergence to equilibrium [2]. As proposed in [2, 21], despite the time trajectories are modified, it is possible to exploit the additional damping phenomena introduced by the geometrical integrator in the magnetization time evolution, without altering the expected equilibrium state, to strongly reduce the computational time (see. Fig. 3.4). As shown in [2] the optimized combinations of parameters, e.g. ($\alpha = 0.1$, $\sigma = 4.5\gamma$) or ($\alpha = 0.03$), $\sigma = 9\gamma$, lead to a remarkable improvement in terms of computational efficiency.

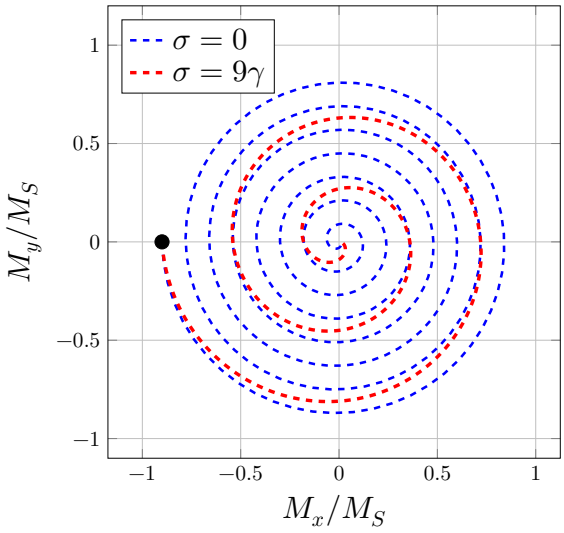

Figure 3.4: Representation of the influence of parameter σ on the magnetization trajectory in the plane (M_x, M_y) corresponding to a transition between two states, with $\alpha = 0.1$. The black dot is the starting point of the two solutions; it is clear that when $\sigma = 9\gamma$ there is an enhancement of damping phenomena, and a much quicker convergence to equilibrium.

3.1.3 Adaptive time stepping

To further increase the performance of the code, we implement an adaptive time integration scheme. The purpose of introducing an adaptive step size is to obtain a predetermined accuracy of the solution, reducing as much as possible the computational cost. Generally, in the calculation of static hysteresis loops, after the update of the external applied field, the solution can evolve through a series of rapid transients, where very small time steps are required, alternated with much smoother transients, where the time step can be increased, up to the final damping of the magnetization motion when approaching the equilibrium point, where the step size can be greatly increased [2]. The time reduction obtained in some cases can be in the order of tenths to hundredths times of the original computation time.

The parameter governing the process of time step adaptation is the local truncation error, or at least a good estimate of it, since the calculation of truncation error would require to know the exact solution at a given time instant. The simplest way to obtain

this estimate is to compare the numerical solution obtained with two successive steps to the numerical solution obtained with a single step corresponding to the double of the chosen step size. In details

$$\mathbf{M}_1(t + 2\Delta t) = \text{cay}\,(2\Delta t\tilde{\boldsymbol{\omega}})\,\mathbf{M}(t), \tag{3.21}$$

where $\mathbf{M}_1(t + 2\Delta t)$ is the solution obtained with a single step of length $2\Delta t$.

$$\mathbf{M}_*(t + \Delta t) = \text{cay}\,(\Delta t\tilde{\boldsymbol{\omega}})\,\mathbf{M}(t) \tag{3.22}$$

$$\mathbf{M}_2(t + 2\Delta t) = \text{cay}\,(\Delta t\tilde{\boldsymbol{\omega}})\,\mathbf{M}_*(t + \Delta t), \tag{3.23}$$

where $\mathbf{M}_2(t + 2\Delta t)$ is the solution obtained with two steps of length Δt.
In general, the local truncation error ε can be defined as the difference between the two computed solutions

$$\varepsilon = \mathbf{M}_1 - \mathbf{M}_2 \tag{3.24}$$

This method of estimation of the local truncation error would require an extra evaluation of the solution, introducing an heavy computational overhead at each time step. Since we have implemented the Euler-Heun integration scheme, which belongs to the family of Runge Kutta 1-2 methods, we choose a way of evaluating the error following the technique developed for the embedded Runge-Kutta methods. In this case, instead of computing a second solution by doubling the time step, the solutions obtained from two methods with a different accuracy order are compared. Recalling equations (3.17) and (3.19) we have that $\mathbf{M}_*$ is the solution of the Euler method and also the first step solution of the Heun integration scheme. The comparison of these two solutions does not require other evaluations, apart from the computation of the current error. Once the truncation error is obtained it is possible to estimate the correctness of the used time step. As shown in [20] the order of accuracy of a Cayley transform method is the same of the associated explicit method, therefore our truncation error is $\varepsilon = \mathcal{O}(\Delta t^2)$. Let ε_0

be our target accuracy and ε_* the truncation error corresponding to the time step Δt_* it is easy to obtain an estimate for Δt_0 as the time step required to achieve the target accuracy as

$$\Delta t_0 = \Delta t_* \left| \frac{\varepsilon_0}{\varepsilon_*} \right|^{\frac{1}{2}} \tag{3.25}$$

If the truncation error is smaller than the target accuracy the solution is stored and the estimate is used to reasonably increase the time step, without exceeding the desired accuracy; if the truncation error is larger the solution is discarded and recalculated using the corrected time step. The definition of the local truncation error is not an easy task and may depend on the peculiarity of the problem. In this case we choose

$$\varepsilon = \max_{i,j,k} |\boldsymbol{\tau}_{\text{high}}^{i,j,k} - \boldsymbol{\tau}_{\text{low}}^{i,j,k}| \Delta t \tag{3.26}$$

where $\boldsymbol{\tau}_{\text{high}}^{i,j,k}$ and $\boldsymbol{\tau}_{\text{low}}^{i,j,k}$ are respectively the torques $\mathbf{H}_{\mathit{eff}}^{i,j,k} \times \mathbf{M}^{i,j,k}$ obtained from the Heun and the Euler estimates. Using a cautelative approach the time step is adjusted introducing a precautionary factor equal to 0.8, moreover it is possible to specify an upper and a lower limit to the time step to ensure a better control of the magnetization time evolution, i.e.

$$\Delta t_0 = 0.8 \left| \frac{\varepsilon_0}{\varepsilon_*} \right|^{\frac{1}{2}} \Delta t_* \tag{3.27}$$

In the last section of this chapter we will show the performance of the adaptive time step solver comparing the relative solution with the one obtained with the maximum time-step achievable with the Euler and Heun algorithms.

3.2 Spatial Discretization of the LLG equation

In micromagnetic solvers, the most time-comsuming operation is the calculation of the magnetostatic field, being a long-range interaction. Over the years, many strategies and algorithms were developed to increase the efficiency of the computation of

this field. In general, Finite Element Methods (FEMs) are very accurate in the solution of problems with high gradient fields, and provide high flexibility in the reconstruction of shapes with curved boundaries, or complex 3D structures. Different approaches were implemented to solve the Poisson equation with FEMs in the whole space, like the coupling of FEMs with asymptotic boundary conditions [22], or the use of hybrid methods coupling FEMs to BEMs (Boundary Element Methods) for the solution of the open boundary problem [23, 24]. In the first case the precision of the solution depends on the size of the domain selected to solve the open boundary problem (magnetic object plus external amagnetic region) and on the order of the asymptotic boundary conditions. In the second case it is necessary to solve a large set of dense linear algebraic systems. Alternatively to the solution of the Poisson's equation with FEM-based techniques, it is possible to speed up the integration of the magnetostatic field using the properties of the Discrete Fourier Transform, implementing a Fast Fourier Transform (FFT) algorithm for the evaluation of the Green's integral [5, 25]. This method can lead to a good computational efficiency, however it introduces some limitations in the choice of the geometric discretization. The FFT methods require in fact a *structured regular grid*, which imposes strong limitations to the reconstruction of curved surfaces. In the development of our 3D code we chose to use this last approach because, when dealing with 3D structures, the dimension of the micromagnetic problem can grow very rapidly. Hence, we opted for greater computational efficiency at the expense of more flexibility in the accurate geometrical reconstruction of curved shapes.

The computational domain $\mathcal{D}$ is a regular prism composed of regularly placed parallelepiped shaped Finite Difference (FD) cells of size $\Delta_x \times \Delta_y \times \Delta_z$. This computational domain includes the ferromagnetic sample Ω. In each FD cell we define the corresponding material properties, i.e. the saturation magnetization M_S, the exchange constant k_{ex}, the magneto-crystalline anisotropy constants k_{an} and the easy/hard axes. The FD cells that do not correspond to a part of the magnetic sample have the free space properties (amagnetic regions). The total number of discretization FD cells is

$N = N_x \times N_y \times N_z$; in each cell the magnetization is assumed to be uniform with a value associated with the barycenter of the cell.

3.3 Effective field terms evaluation

In this section we present the spatial discretization of the effective field $\mathbf{H}_{eff}$, mainly focusing on the terms that are computationally heavy, discussing the techniques used to reduce the computational cost.

3.3.1 Exchange field

The exchange field introduced in Chapter 2, which describes the effects of the exchange interaction, has the following expression

$$\mathbf{H}_{ex} = \frac{2k_{ex}}{\mu_0 M_S^2}\Delta\mathbf{M}, \tag{3.28}$$

This quantity can be calculated using a standard finite difference scheme, which requires the use of structured meshes. In this case, we use a 6-neighbor approximation for the Laplacian operator [26], similarly to [27]. For each FD cell identified by the triplet (i, j, k) with $i, j, k = 1, \dots, N_{x,y,z}$ we have:

$$\begin{aligned} H_{ex_q}^{i,j,k} = \frac{2k_{ex}}{\mu_0 M_S^2}\Bigg(&\frac{1}{\Delta_x}(M_q^{i+1,j,k} + M_q^{i-1,j,k} - 2M_q^{i,j,k}) + \\ &+ \frac{1}{\Delta_y}(M_q^{i,j+1,k} + M_q^{i,j-1,k} - 2M_q^{i,j,k}) + \\ &+ \frac{1}{\Delta_z}(M_q^{i,j,k+1} + M_q^{i,j,k-1} - 2M_q^{i,j,k})\Bigg) \end{aligned} \tag{3.29}$$

for each component $q = x, y, z$. Special attention must be paid to the cell elements on the boundaries with a non magnetic material, where we have to enforce the Neumann condition (2.64). When the computation of the exchange field in a FD cell i, j, k located

on this type of boundary is performed, the terms in Eq. (3.29) that correspond to an outside cell are replaced with the value of the computation cell i, j, k, thus enforcing $\frac{\partial \mathbf{M}}{\partial \mathbf{n}}\big|_{\partial\Omega} = \mathbf{0}$.
Taking a look to the algorithm that evaluates $\mathbf{H}_{ex}$ it is clear that it scales as $\mathcal{O}(N)$, in fact the calculation of the Laplacian operator depends exclusively on local quantities.

3.3.2 Magneto-crystalline anisotropy field

The magneto-crystalline anisotropy field introduced in Chapter 2, which describes the role of the crystal lattice, as:

$$\mathbf{H}_{an} = \frac{1}{\mu_0 M_S} \frac{\partial \phi_{an}}{\partial \mathbf{m}}, \tag{3.30}$$

depends pointwise on $\frac{\partial \phi_{an}}{\partial \mathbf{m}}$, thus in each FD cell we can compute the anisotropy field value independently. The code is able to treat both uniaxial and cubic anisotropy. For the former, the expression (3.30) becomes

$$\mathbf{H}_{an} = \frac{2k_{an}}{\mu_0 M_S} (\mathbf{m} \cdot \mathbf{e}_{an}) \mathbf{e}_{an}. \tag{3.31}$$

where $\mathbf{e}_{an}$ is the unit vector along the uniaxial anisotropy direction.
Cubic anisotropy is more difficult to implement, because one must consider the relation between the lattice axes $(\mathbf{e}_1, \mathbf{e}_2, \mathbf{e}_3)$ orientation and the axes of the reference system $(\mathbf{u}_1, \mathbf{u}_2, \mathbf{u}_3)$. The cubic anisotropy energy density is, for a generic lattice not aligned with the reference system, defined as

$$\phi_{an}(\mathbf{m}) = K_1(\alpha_1^2\alpha_2^2 + \alpha_1^2\alpha_3^2 + \alpha_1^2\alpha_3^2) + K_2\alpha_1^2\alpha_2^2\alpha_3^2 + \ldots \tag{3.32}$$

with $\alpha_i = \mathbf{m}\cdot\mathbf{e}_i, i = 1, \dots, 3$. Applying the chain rule to Eq. (3.30) the generic anisotropy field component becomes

$$H_{an_i} = -\frac{1}{\mu_0 M_S}\frac{\partial \phi_{an}}{\partial \alpha_j}\frac{\partial \alpha_j}{\partial m_i} \tag{3.33}$$

The cubic anisotropy axes are expressed as functions of the cartesian axes

$$\mathbf{e} = \mathbf{Q}\mathbf{u} \tag{3.34}$$

It is easy to also show that

$$\mathbf{m} = \mathbf{Q}^T\boldsymbol{\alpha} \tag{3.35}$$

therefore

$$\frac{\partial \alpha_j}{\partial m_i} = \left[(\mathbf{Q}^T)^{-1}\right]_{ij} \tag{3.36}$$

From these equations it is now straightforward the implementation of Eq. (3.33) into the 3D code. Since the calculation of $\mathbf{H}_{an}$ in a FD cell requires no other input from any other cell of the computational domain, this calculation can be carried out in $\mathcal{O}(N)$ operations.

3.3.3 Magnetostatic field

The magnetostatic field introduced in Section 2.2.3 as

$$\mathbf{H}_{ms}(\mathbf{r}) = -\frac{1}{4\pi}\int_\Omega \nabla\left(\nabla'\frac{1}{|\mathbf{r}-\mathbf{r}'|}\cdot\mathbf{M}(\mathbf{r}')\right)dV'. \tag{3.37}$$

depends in each point $\mathbf{r}$ on the integral over the whole volume. Once fixed the spatial discretization, we aim at computing the value of $\mathbf{H}_{ms}(\mathbf{r})$ in the center $\mathbf{r}_i$ of each FD cell. Since for hypothesis we assume that, in each cell, the value of the magnetization is

constant, we can rewrite the above equation as a sum of integrals over each FD cell, as

$$\mathbf{H}_{ms}(\mathbf{r}_i) = -\frac{M_S}{4\pi} \sum_{\substack{j=1 \\ i \neq j}}^{N} \int_{\mathcal{V}_j} \nabla \left(\nabla \frac{1}{|\mathbf{r}_i - \mathbf{r}_j|} \right) d\mathcal{V}_j \cdot \mathbf{m}_j. \tag{3.38}$$

In this case $\mathbf{m}_j$ can be taken out from the integral on the volume $\mathcal{V}_j$ of each individual cell, where it is assumed to be constant. It is clear that, for each FD cell, the evaluation of the magnetostatic field requires $\mathcal{O}(N)$ operation, if a classic integration scheme is used. To derive the computational cost of the magnetostatic field evaluation on the total volume we multiply this estimate by the number of cells N, resulting in the total number of operations $\mathcal{O}(N^2)$.
In the following part we will illustrate how we can reduce this computational cost using the properties of the Discrete Fourier Transform (DFT), which can be used thanks to the opportune choice of structured geometrical discretization [6, 28]. Because of the very efficient numerical implementation of the DFT using the Fast Fourier Transform algorithm, this approach allows us a noticeable speed up of the calculations.

The basic idea behind the DFT procedure is that whenever a field f can be expressed as a discrete convolution between a Green's function g and a source s in the spatial domain for this specific case

$$f(\mathbf{r}_i) = \sum_{j=1}^{N} g(\mathbf{r} - \mathbf{r}_j) s(\mathbf{r}_j), \tag{3.39}$$

the Fourier transform $\hat{f}$ of the field f can be written as a scalar product of the transform of the source and of the Green's function in the spatial frequency domain, thanks to the properties of Fourier transform. This is of particular interest in our case since, for each of the N points or FD cells, the product can be easily computed in $\mathcal{O}(1)$ operations giving a total complexity for the evaluation of $\hat{f}$ in the order of $\mathcal{O}(N)$. With this technique, in the transformed space domain we are able to obtain the DFT of the function that we want to evaluate with a cost of $\mathcal{O}(N)$ instead of $\mathcal{O}(N^2)$ operations, required to

directly calculate the function in the spatial domain. Since the discrete transform can be computed by means of a family of well-known algorithms known as Fast Fourier Transforms that perform the transform in $\mathcal{O}(N\log N)$ operations [29], at the end we are able to lower the computational cost of the magnetostatic field evaluation to $\mathcal{O}(N) + \mathcal{O}(N\log N) \subseteq \mathcal{O}(N\log N)$ operations. Now, we will see how this approach can be applied to the micromagnetic problem and briefly illustrate the convolution theorem.

Convolution theorem

Let g and s be two integrable functions for which there exists the Fourier transform, the convolution theorem states that: *the transform of the convolution between g and s, $\mathfrak{F}(g*s)$, is equal to the pointwise product between the transform of $\mathfrak{F}(g)$ and the transform of $\mathfrak{F}(s)$*[30]. By definition, the Discrete Fourier Transform operates on a finite number of equispaced samples of a function in the "spatial domain", giving a same-length sequence of samples of a complex function in the "spatial frequency domain" with the following relation:

$$\hat{f}^k = \sum_{n=0}^{N-1} f^n \cdot e^{-\frac{2\pi i}{N}kn} \tag{3.40}$$

where $\hat{f}^k$, $k = 0, \dots, N-1$, is the series of complex coefficients, i.e. the Discrete Fourier Transform of the series f^k, $k = 0, \dots, N-1$. The inverse operation is given by:

$$f^n = \frac{1}{N}\sum_{k=0}^{N-1} \hat{f}^k \cdot e^{\frac{2\pi i}{N}kn} \tag{3.41}$$

The discrete form of the convolution theorem states:

Theorem 1. *If a signal s_j is periodic with period N, so that it is completely determined by the N values $s_0, \dots, s_{N-1}$, then its response function of finite duration N is related to the discrete Fourier transform pair*

$$f^j = \sum_{k=-N/2+1}^{N/2} g^{j-k}s^k \Leftrightarrow \hat{f}^n = \hat{g}^n\hat{s}^n, \tag{3.42}$$

where $\hat{g}^n$ $(n = 0, \dots, N-1)$ *is the Discrete Fourier Transform of* g^j*, while* $\hat{s}^n$, $(n = 0, \dots, N-1)$ *is the Discrete Fourier Transform of* s^k*.*

It is quite simple to extend these results to the three dimensional case. In the application it is important to notice that by its definition the DFT accurately reconstructs the sampled signal, but inherently assumes its periodicity, however our physical problem is not guaranteed to be periodic in any of the 3D directions. The convolution when performed with the DFT, if one does not take the proper precaution, will then force a periodic boundary condition into the problem. In order to avoid this imposition a zero-padding technique should be used. Zero-padding consists in extending the signal to be transformed with a sequence of zeros that must be at least as long as the signal itself. When performing the inverse DFT this buffer of zeros will guarantee that the physical data of the un-padded signal will not be affected by the periodicity condition. This procedure can be easily extended to the 3D case, supposing that the computational domain $\mathcal{D}$ is subdivided into $N_x \times N_y \times N_z$ cells. In order to perform the convolution, the input data will have, in the case of no periodicity in any of the three directions, size of $2N_x \times 2N_y \times 2N_z$ (after the introduction of zero-padding).

FFT method for magnetostatic field evaluation

The implemented FFT scheme is based on the direct evaluation of the components of the magnetostatic field. We chose this approach, instead of the evaluation of the magnetostatic potential and then of its derivatives, since even if it is computationally heavier and requires much more memory, it guarantees higher accuracy [31].
Let us consider the discretization of the domain $\mathcal{D}$ in $N_x \times N_y \times N_z$ rectangular prisms of size $\Delta_x, \Delta_y, \Delta_z$ with the faces parallel to the coordinate system axes. Each FD cell can be easily identified by the triplet i, j, k with $i = 1, \dots, N_x$, $j = 1, \dots, N_y$, $k = 1, \dots, N_z$. The source cell is identified by the triplet p, q, r defined in the same range of values.

With this notation Eq. (3.38) becomes

$$\mathbf{H}_{ms}^{p,q,r} = -\frac{M_S}{4\pi} \sum_{\substack{i=1 \\ i\neq p}}^{N_x} \sum_{\substack{j=1 \\ j\neq q}}^{N_y} \sum_{\substack{k=1 \\ k\neq r}}^{N_z} \int_{\mathcal{V}_{i,j,k}} \nabla \frac{\mathbf{r}_{p,q,r} - \mathbf{r}_{i,j,k}}{|\mathbf{r}_{p,q,r} - \mathbf{r}_{i,j,k}|^3} d\mathcal{V}_{i,j,k} \cdot \mathbf{m}_{i,j,k}. \tag{3.43}$$

which can be explicitly rewritten as a convolution product

$$\mathbf{H}_{ms}^{p,q,r} = \sum_{\substack{i=1 \\ i\neq p}}^{N_x} \sum_{\substack{j=1 \\ j\neq q}}^{N_y} \sum_{\substack{k=1 \\ k\neq r}}^{N_z} \mathbf{G}(\mathbf{r}_{p,q,r} - \mathbf{r}_{i,j,k}) \cdot \mathbf{m}_{i,j,k}, \tag{3.44}$$

where $\mathbf{G}(\mathbf{r})$ is the symmetric Green's tensor.

$$\mathbf{G}(\mathbf{r}) = \begin{pmatrix} g_{xx}(\mathbf{r}) & g_{xy}(\mathbf{r}) & g_{xz}(\mathbf{r}) \\ g_{xy}(\mathbf{r}) & g_{yy}(\mathbf{r}) & g_{yz}(\mathbf{r}) \\ g_{xz}(\mathbf{r}) & g_{yz}(\mathbf{r}) & g_{zz}(\mathbf{r}) \end{pmatrix} \tag{3.45}$$

The components of the tensor can be calculated via numerical integration or using the analytical formulation proposed by Nakatani [32], see Appendix (B). Transposing the results of theorem (1) to Eq. (3.44) it is possible to compute the convolution integral by applying the FFT to the magnetization vector and the Green tensor. Then, the integral becomes the simple product in the spatial frequency domain

$$\begin{aligned} \hat{\mathbf{H}}_{ms,x}^{i,j,k} &= \hat{g}_{xx}^{i,j,k} \hat{m}_x^{i,j,k} + \hat{g}_{xy}^{i,j,k} \hat{m}_y^{i,j,k} + \hat{g}_{xz}^{i,j,k} \hat{m}_z^{i,j,k} \\ \hat{\mathbf{H}}_{ms,y}^{i,j,k} &= \hat{g}_{xy}^{i,j,k} \hat{m}_x^{i,j,k} + \hat{g}_{yy}^{i,j,k} \hat{m}_y^{i,j,k} + \hat{g}_{yz}^{i,j,k} \hat{m}_z^{i,j,k} \\ \hat{\mathbf{H}}_{ms,z}^{i,j,k} &= \hat{g}_{xz}^{i,j,k} \hat{m}_x^{i,j,k} + \hat{g}_{yz}^{i,j,k} \hat{m}_y^{i,j,k} + \hat{g}_{zz}^{i,j,k} \hat{m}_z^{i,j,k} \end{aligned} \tag{3.46}$$

Now applying the inverse FFT to the three components of $\hat{\mathbf{H}}_{ms}$ it i possible to obtain the magnetostatic field in the spatial domain $\mathcal{D}$. This algorithm thus requires:

- once at the beginning of the computation

  1. the determination and the transformation of the Green kernel tensor, as

described in detail in Appendix C;

- for each magnetostatic field evaluation:

  2. the Fourier transformation of the three components of the magnetization;
  3. 9 multiplications of the transformed components of $\mathbf{m}$ by the transformed elements of the Green tensor;
  4. the anti-transformation of the result of the previous product to obtain the value of the magnetostatic field.

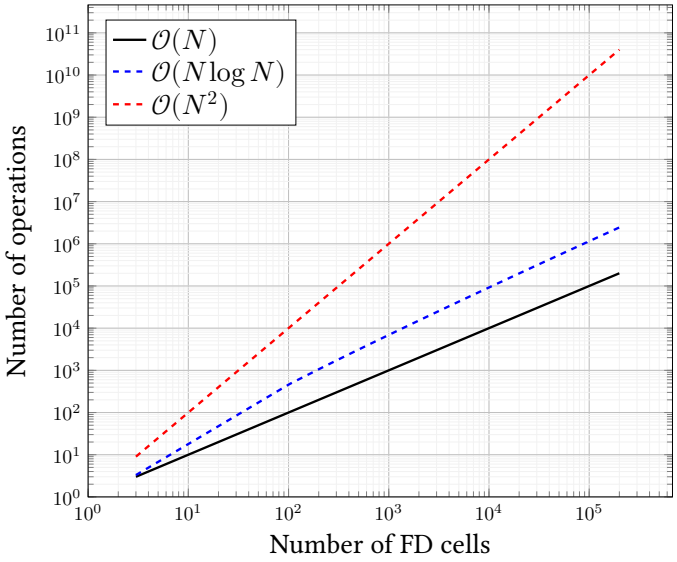

Figure 3.5: The graph reports a quick visual representation of the differences between algorithms presenting different scaling on a log-log scale. The more efficient algorithm scales as $\mathcal{O}(N)$, which means that its computational cost progresses linearly with the number of FD cells. In the micromagnetic code almost every type of computations present this cost. $\mathcal{O}(N^2)$ represents the scaling of an algorithm that implements the standard integration technique for the computation of the magnetostatic field. $\mathcal{O}(N \log N)$ is the scaling we can achieve using the FFT technique described in this section.

Many considerations can be done on the effectiveness of the algorithm. To have an immediate visual perception, Fig. 3.5 reports the graph that compares the number of operations requested to perform a task given the algorithm and the size of the processed data. It is evident that the scaling of the FFT algorithm $\mathcal{O}(N \log N)$ is much better when compared to the standard integration of a convolution product $\mathcal{O}(N^2)$. As N grows, the

performance benefit rapidly outweighs the computational cost of the determination of the Green kernel tensor at the beginning of the simulation. Further improvements can be obtained implementing Fast Multipole Techniques for the calculation of farther interactions, as shown in [33].

3.3.4 Thermal field

Thermal effects are considered following the Langevin approach: an isotropic, spatially and temporally uncorrelated Gaussian white-noise term is incorporated in the LLG equation. The introduction of the thermal field, described in Section 2.5, leads to a change in the equation properties and imposes the setting of proper procedures for the determination of the equilibrium points of the system. This is relevant for example when solving the LLG equation to compute the hysteresis loops of nanostructures. In the absence of thermal effects, the applied field is changed in discrete steps and the solution is computed up to the reaching of the equilibrium for that value of field amplitude. The reaching of the equilibrium is evaluated imposing a torque threshold on the system, that is, for each FD cell we have to verify that the maximum instantaneous local value of the torque

$$\tau = \frac{||\mathbf{M} \times \mathbf{H}_{eff}||}{M_S^2} \tag{3.47}$$

is lower than a fixed threshold τ^*, typically in the order of 10^{-8}. The inclusion of the thermal field does not allow us to reach the equilibrium, since the thermal noise continues to perturb the system. Since the criterion based on torque threshold can not be used, the simulation is performed leaving the magnetization to evolve over a defined time interval ΔT_{th} for each step of the external field, and after that, changing the applied field to the next value. As shown in [34, 35] the length of ΔT_{th} can affect the results of the simulations. Therefore ΔT_{th} should be long enough to guarantee that the time average of the thermal noise is equal to zero, and that the time interval is greater than the time required to achieve the full evolution of the magnetization for a specific applied field

value. One could get a good estimate of the minimum length of ΔT_{th} evaluating the time required to achieve the zero torque condition for the non stochastic LLG simulation ($T = 0$). In general, in micromagnetic studies, ΔT_{th} should be in the order of several nanoseconds to enable the determination of a reliable solution.
The thermal field was initially studied by Brown [36], which investigated the behavior of single domain particles and thermal switching phenomena. The theory presented by Brown can be also applied to micromagnetic simulations since each FD computational cell can be seen as a single domain particle. For practicality, we report the equation introduced in Section 2.5

$$\begin{aligned} &\langle \mathbf{H}_{th}(\mathbf{r},t)\rangle = 0 \\ &\left\langle H^i_{th}(\mathbf{r},t)\cdot H^j_{th}(\mathbf{r}',t')\right\rangle = 2D\delta_{ij}\delta(t-t')\delta(\mathbf{r}-\mathbf{r}') \end{aligned} \tag{3.48}$$

where D is equal to

$$D = \frac{\alpha k_B T}{\gamma \mu_0 M_S \Delta V} \tag{3.49}$$

being $\Delta V$the volume size of the FD cell, k_B the Boltzmann constant and $T$the absolute temperature. From the equations 3.48 the thermal field $\mathbf{H}_{th}$ is determined in such a way that:

- its average, taken over different stochastic realizations, vanishes in all spatial directions;
- the thermal fluctuations are uncorrelated in time and are uncorrelated at different spatial points of the finite difference mesh.

It is important to remember that the thermal field does not correspond to an actual magnetic field, and it is not derived from any energy functional. It is a mathematical abstraction inserted to reproduce the effects of thermal noise in the context of the stochastic processes theory. This is defined to verify the correct noise statistical properties.

The thermal field is computed as:

$$\mathbf{H}_{th}(\mathbf{r},t) = \boldsymbol{\eta}(\mathbf{r},t)\sqrt{\frac{2\alpha k_B T}{\gamma \mu_0 M_S \Delta V \Delta t}} \tag{3.50}$$

where $\boldsymbol{\eta}(\mathbf{r},t)$ is a stochastic vector with components that are Gaussian random numbers. These numbers are uncorrelated in space and time, and have zero mean value and dispersion equal to 1, Δt is the time step used in the integration of the LLG equation [9, 34, 35, 37]. In the solution of the stochastic LLG equation, one must keep in mind that each simulation is the realization of a stochastic process. Therefore, to estimate the correct value, one should run many simulations and average the results.

3.4 Validation of 3D micromagnetic code

In this section we validate and test the accuracy of the developed 3D FFT based micromagnetic code. The validation process is divided in three parts. In the first one standard reference micromagnetic problems proposed by NIST are considered, in the second part the results of a simple test case are compared with the results obtained with MuMax3, a well established micromagnetic code developed by Ghent University. In the last section we will present an analysis of the adaptive time stepping scheme, investigating the time step size that guarantees the numerical stability.

3.4.1 Test on μMag standard problems

The Micromagnetic Modeling Activity Group (μMAG), as part of the NIST Center for Theoretical and Computational Materials Science (CTCMS), developed a series of micromagnetic standard problems to allow researchers to compare computational techniques, identify problems, and detect programming bugs of micromagnetic codes [3]. Each problem is set to test a specific aspect of micromagnetic simulations. For our code standard problems #3 and #4 are the most suitable to perform the validation.

Standard problem #3

The standard problem #3 is aimed at the calculation of the single domain limit of a cubic magnetic particle. This is the size L of equal energy for the so-called flower state (which one may also call a splayed state or a modified single-domain state) on the one hand, and the vortex or curling state on the other hand. The aim is to find for which length expressed in units of the intrinsic length scale the transition happens. The intrinsic length scale is defined as

$$l_{ex} = (k_{ex}/K_m)^{1/2}, \tag{3.51}$$

where K_m is a magnetostatic energy density, $K_m = 1/2\mu_0 M_S^2$. The transition is expected to be found around $L = 8l_{ex}$. The problem is solved using a cubic grid with edge length around 1 nm. Simulations are performed in a range of sizes from 7.5 times to 9 times the exchange length. Setting M_S at 800 kA/m and α at 0.02 the other simulation parameters are fixed following the specifications of the standard problem, imposing uniaxial anisotropy with $k_{an} = 0.1K_m$, and with the easy axis directed along one of the principal axis of the cube. Each cube is initialized with a random distribution of the magnetization and relaxed to a quasi-zero torque equilibrium condition ($\tau^* = 10^{-8}$). We find three different ground states: flower state (a), twisted flower state (b) and vortex state (c). The results show that the ground state is the flower state for $L < 8.2l_{ex}$ (Fig. 3.6a), the twisted flower state for $8.2l_{ex} < L < 8.46l_{ex}$ and the vortex state for $L > 8.46l_{ex}$ (Fig. 3.6b). The transition at $L = 8.46l_{ex}$ is in line with the solutions posted on μMag site [3, 38] and presented in the validation of Mumax3 [5], which also shows the presence of the twisted flower state in a similar range of values.

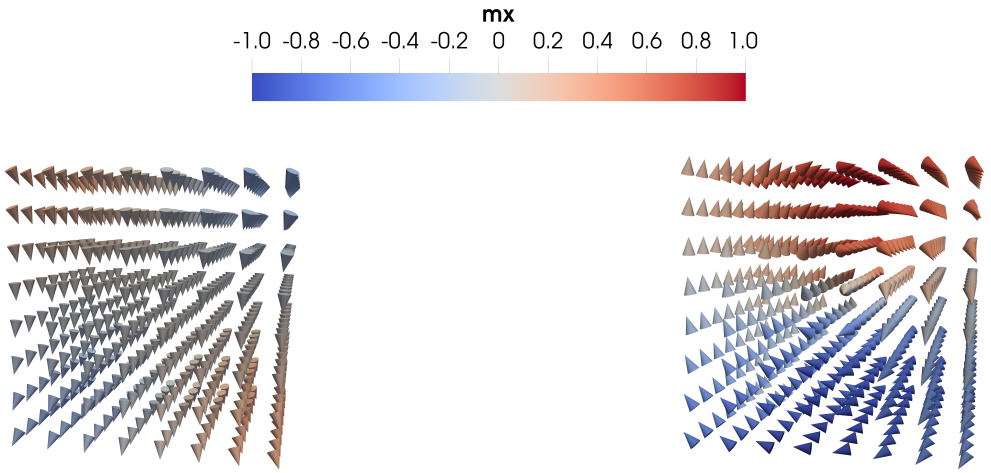

(a) Flower State ($L = 8.13 l_{ex}$)

(b) Vortex State ($L = 8.47 l_{ex}$)

Figure 3.6: Results of simulations for the μMag standard problem #3, showing the magnetization vector configuration for the transition values of single domain limit length. The color bar represents the x component of the normalized magnetization (p.u.).

Standard problem #4

Standard problem $\#4$ is focused on dynamic aspects of micromagnetic computations [39]. This problem tests the ability to correctly reproduce the reversal of the magnetization in a thin film, when a constant uniform field is applied nearly antiparallel to the initial direction of the magnetization.

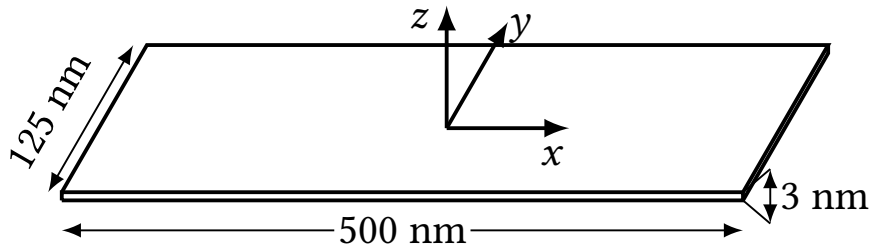

Figure 3.7: Scheme and dimensions of the thin film sample considered in the μMag standard problem #4.

The following material parameters are considered:

k_{ex} = 13 pJ/m;

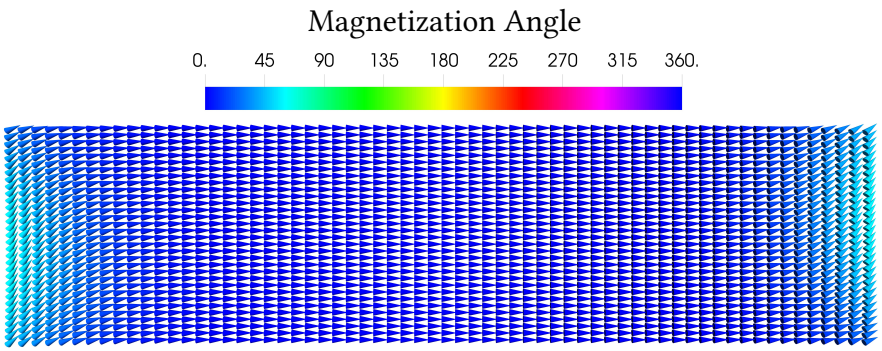

Figure 3.8: μMag#4 Initial magnetization configuration (s-state). The color bar represents the angle (in degrees) between the projection of the magnetization in the xy plane and the positive direction of the x axis.

M_S = 800 kA/m;

k_{an} = 0.0 Jm^{-3};

α = 0.02.

Starting from an initial s-state with zero field the time evolutions of the magnetization, as the system moves towards equilibrium in the new fields, are examined. The following values of the external field are applied:

Field 1: $\mu_0 H_x$=-24.6 mT, $\mu_0 H_y$= 4.3 mT, $\mu_0 H_z$= 0.0 mT which is a field approximately equal to 25 mT, directed 170° counterclockwise from the positive x axis;

Field 2: $\mu_0 H_x$=-35.5 mT, $\mu_0 H_y$=-6.3 mT, $\mu_0 H_z$= 0.0 mT which is a field approximately equal to 36 mT, directed 190° counterclockwise from the positive x axis.

The magnetization dynamics are calculated using different mesh sizes Δs ranging between 2 nm and 4 nm to verify mesh size independency of the solution. The results shown in Fig. 3.9 and Fig. 3.10 are obtained by using a mesh with $\Delta s = 3.125$ nm and a fixed time step $\Delta t = 0.1$ ps. It is verified that the choice of Δs does not affect the accuracy of the solution for the considered range of variables.

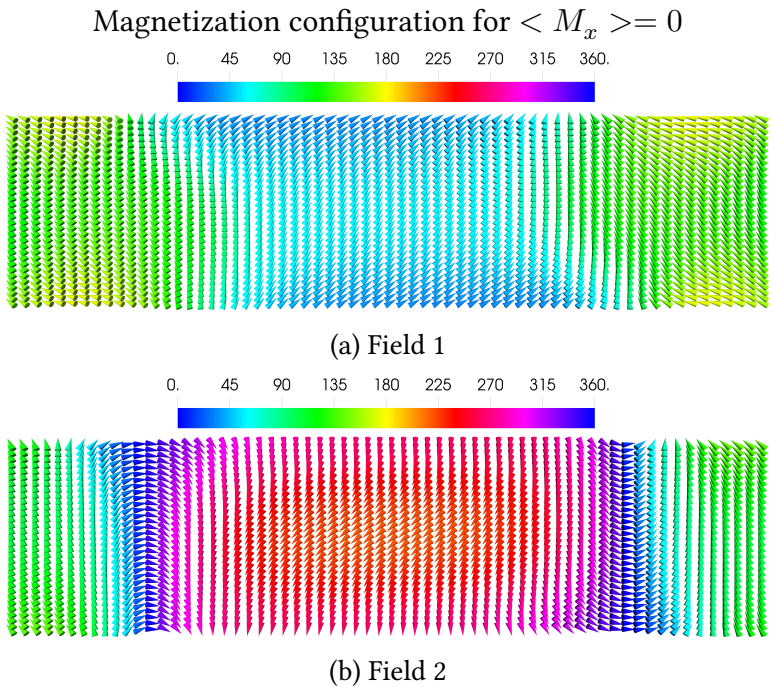

(a) Field 1

(b) Field 2

Figure 3.9: Comparison of magnetization reversal processes obtained with the two applied fields. The magnetization configurations are taken when the x-component of the spatially averaged magnetization first crosses zero. The color bar represents the angle (in degrees) between the projection of the magnetization in the xy plane and the positive direction of the x axis.

Figure 3.10 reports a comparison of the solutions available on the μMag site with the results obtained with our 3D code. We can see a good qualitative and quantitative agreement of the magnetization time evolutions when the two different fields are applied. From Fig. 3.9a and 3.9b, it is possible to observe the two different reversal phenomena of the magnetization. For the first applied field the magnetization reversal process proceeds by propagation of end domains towards the sample center, while for the second applied field the process is much more complex, involving the rotation of the end domains in one direction, while the magnetization in the center of the rectangular sample rotates in the opposite direction. This complex magnetization evolution causes the appearance of 360° domain walls, which later on collapse allowing the complete reversal of the magnetization [39]. From the plots of the average value of m_y in Fig. 3.10b emerges that the integration of the LLG equation, when the second field is applied, is

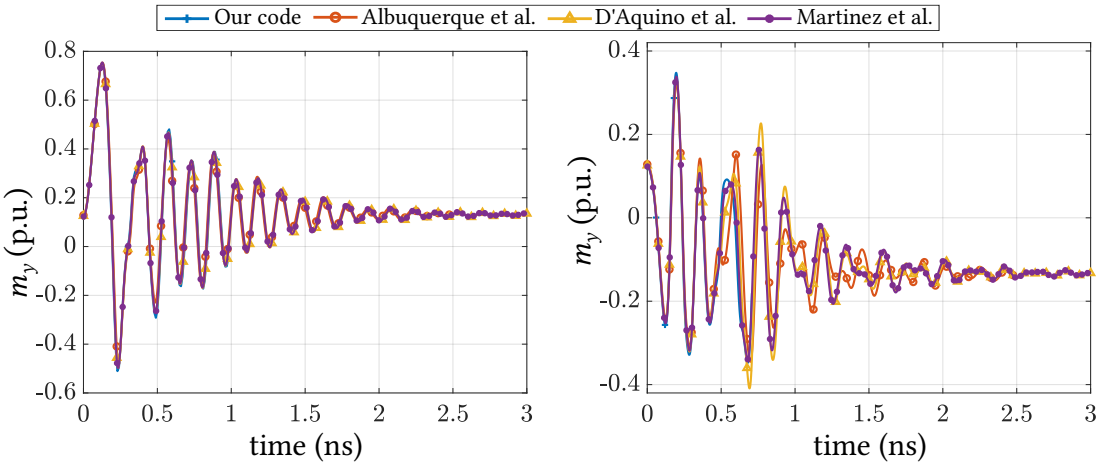

(a) Field 1

(b) Field 2

Figure 3.10: In the two plots we present the time evolution of the y-component of the spatially averaged magnetization, up to the reaching of the equilibrium, for the two different applied fields, comparing our results with different solutions submitted to μMag website.

more problematic, as it is demonstrated by the greater differences between the solutions computed with the different solvers. In fact, after 0.5 ns some differences appear between the values of magnetization computed by each solver. However, those differences later disappear and each method converges practically to the same value, finding the same equilibrium configuration. Finally we can conclude that the results obtained with our code are in full agreement with the other provided solutions.

3.4.2 Validation by comparison to MuMax3

Here we present the comparison between the solutions on a simple test case computed with MuMax3 [5] and our code. The full static hysteresis loop of a 100 nm diameter permalloy sphere is calculated. The same material parameters are used for both the solvers, namely:

k_{ex} = 13 pJ/m;

M_S = 860 kA/m;

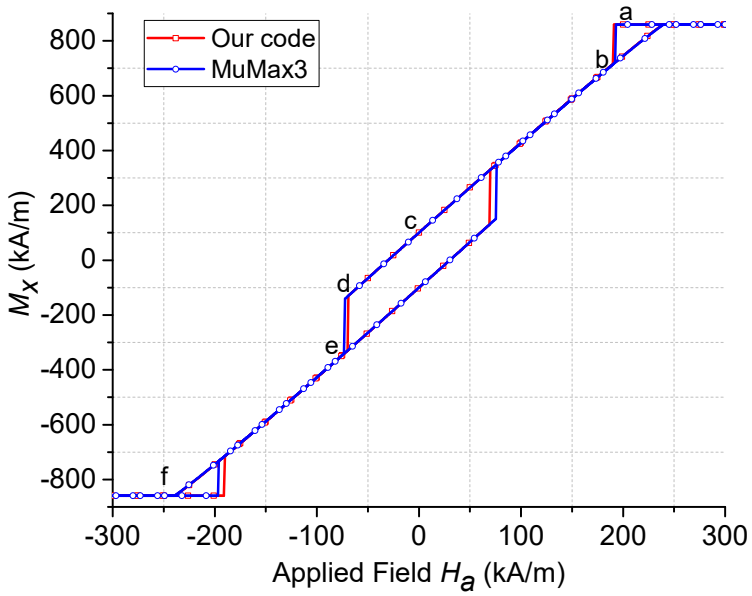

Figure 3.11: Comparison of the hysteresis loops of a permalloy sphere with diameter equal to 100 nm, calculated with our code (red line) and with MuMax3 (blue line).

k_{an} = 0.0 Jm^{-3};

α = 0.1.

The applied field is swept between 300 kA/m and -300 kA/m at 1kA/m step and applied along the x-axes. After each step of the applied field the magnetization is evolved until it reaches a torque equilibrium condition ($\tau < 10^{-6}$). The simulations are performed using the same spatial discretization in cubic elements with a side length of 3.125 nm. In our code we apply the Heun adaptive time integration algorithm based on the Cayley transform, setting $\sigma = 9\gamma$, and imposing a tolerance $\epsilon = 10^{-6}$. In MuMax3 we choose the Heun adaptive time integration scheme, imposing the same tolerance.

The calculated static hysteresis loops are shown in Fig. 3.11. First of all, the two solvers predict nearly the same fields for the irreversible jumps. Second, also the magnetization configuration at different equilibrium points, labelled with letters in Fig. 3.11, are very

similar. This is well demonstrated by the comparison reported in Fig. 3.12. We can appreciate a difference in the chirality of the vortex appearing after the first irreversible jump, this is due to the complete symmetry of the system; therefore both chirality directions are equally probable.

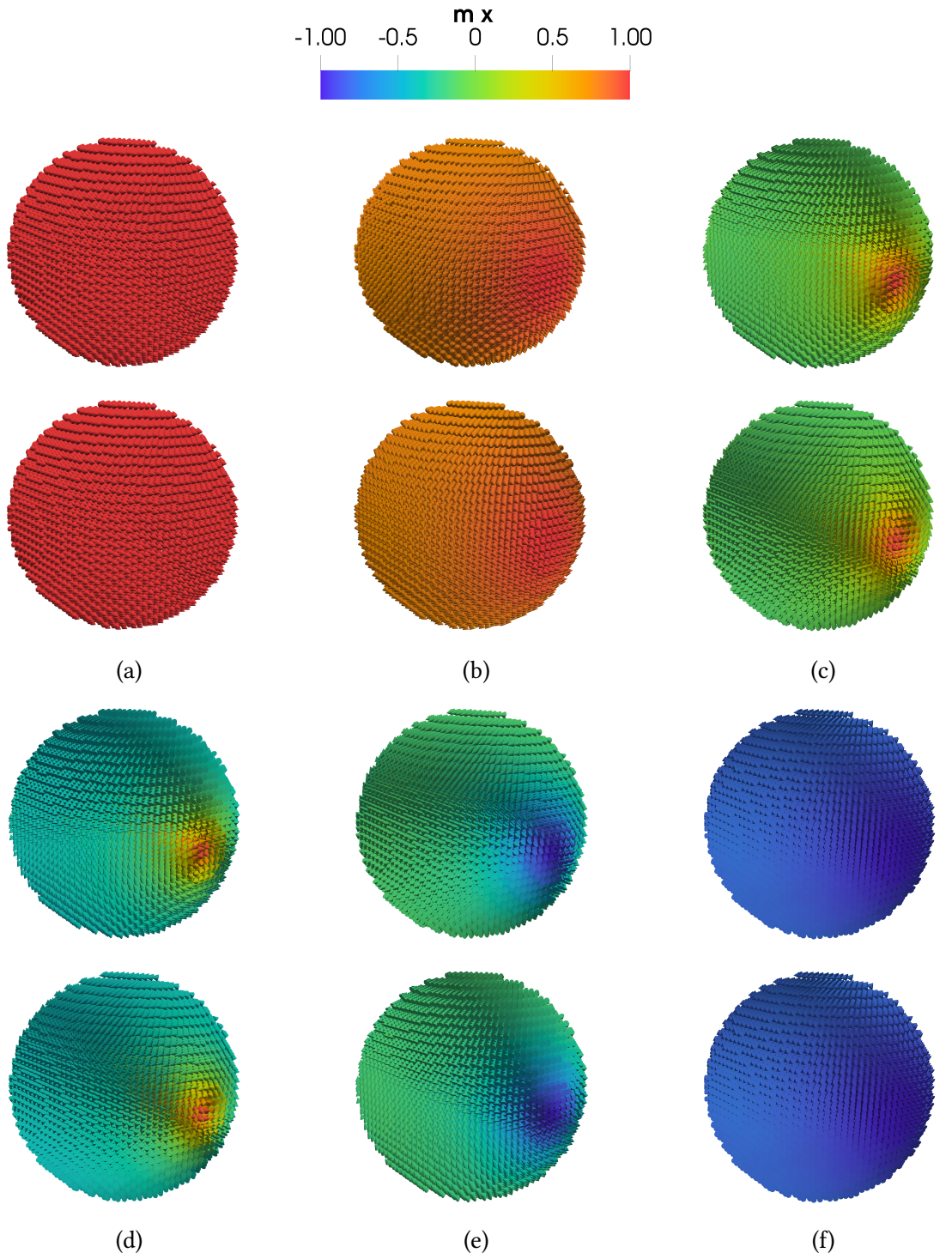

Figure 3.12: Comparison between the equilibrium magnetization configurations obtained with our code (1st and 3rd row) and MuMax3 solver (2nd and 4th row). The cones represent the magnetization direction while the color bar the x component of the normalized magnetization. The equilibrium points are indicated along the descending branches of the hysteresis loops in Fig. 3.11.

3.4.3 Analysis of the performance of the adaptive time stepping scheme

In this sub-section we provide a comparison between the three time stepping algorithms implemented in the 3D code: Euler, Heun, and Euler-Heun with adaptive time step. To perform this comparison we consider the same geometry, initial magnetization condition and applied field already used for the μMag reference problem #4. In this case, we apply the second field, which proved to generate a magnetization time evolution more complex to be reproduced by micromagnetic codes. The test is performed varying the time steps and looking for the maximum Δt able to guarantee the numerical stability and the convergence of the solution for both the Heun and the Euler algorithms coupled to the Cayley transform based scheme. The maximum time steps for Heun and Euler algorithms are then compared with the time dependent one for the Euler-Heun adaptive scheme. Specifically, we present a plot of the time steps Δt set by the algorithm when a reasonable truncation error tolerance is imposed.

	Δt (fs)	**Convergence**	**Number of time steps**
Euler	12.5	✓	400000
	25	×	200000
Heun	25	✓	200000
	50	✓	100000
	100	✓	50000
	150	✓	33333
	187	✓	26738
	200	×	25000
	Tolerance ϵ	**Convergence**	**Number of time steps**
Adaptive Euler-Heun	0.5×10^{-5}	✓	31500
	1×10^{-5}	✓	27190

Table 3.1: The table reports the number of time steps required by each algorithm to complete a 5 ns long simulation, and a checkmark when the algorithm is able to successfully compute the correct results. For the Euler and Heun algorithms we report the time step used in each simulation, for the Euler-Heun adaptive algorithm we indicate the used error threshold.

In Fig. (3.13) we report the time evolution of the spatially averaged value of the three components of the magnetization, using the three integration algorithms with different time steps. The graphs show that the Euler algorithm is accurate when the time step is in the order of 12.5 fs, but it becomes unstable when doubling the time step ($\Delta t = 25$ fs). Heun algorithm starts losing stability for Δt higher than 190 fs. The instability is also evident from the graph of the exchange energy in Fig. 3.14, where we can see a rapid increase in the exchange energy in correspondence of the time instant where the solution loses stability. The adaptive Euler-Heun implementation, as shown in the plot of time step in Fig. 3.15, presents a steep increase in the time step size around 0.25 ns from the beginning of the simulation, when the magnetization reversal happens, stabilizing around $\Delta t = 0.19$ ps when the magnetization starts precessing around the new equilibrium point. Even if the adaptive time step algorithm does not show a dramatic reduction in the number of necessary time steps, it has a comparable computational efficiency with the Heun algorithm when the latter uses the maximum allowable time step. The number of time steps necessary to complete the simulations are summarized in Tab. 3.1. Even if in this specific case we can not see a significative increase in performance comparing the Heun scheme with its time-adaptive counterpart, we want to point out that the time-adaptive step algorithm is able to guarantee a good level of performance without any effort for the user. Without a long process of trial and error to find the optimal time step for the Heun scheme, one would not obtain a priori the same computational efficiency of the adaptive solver.

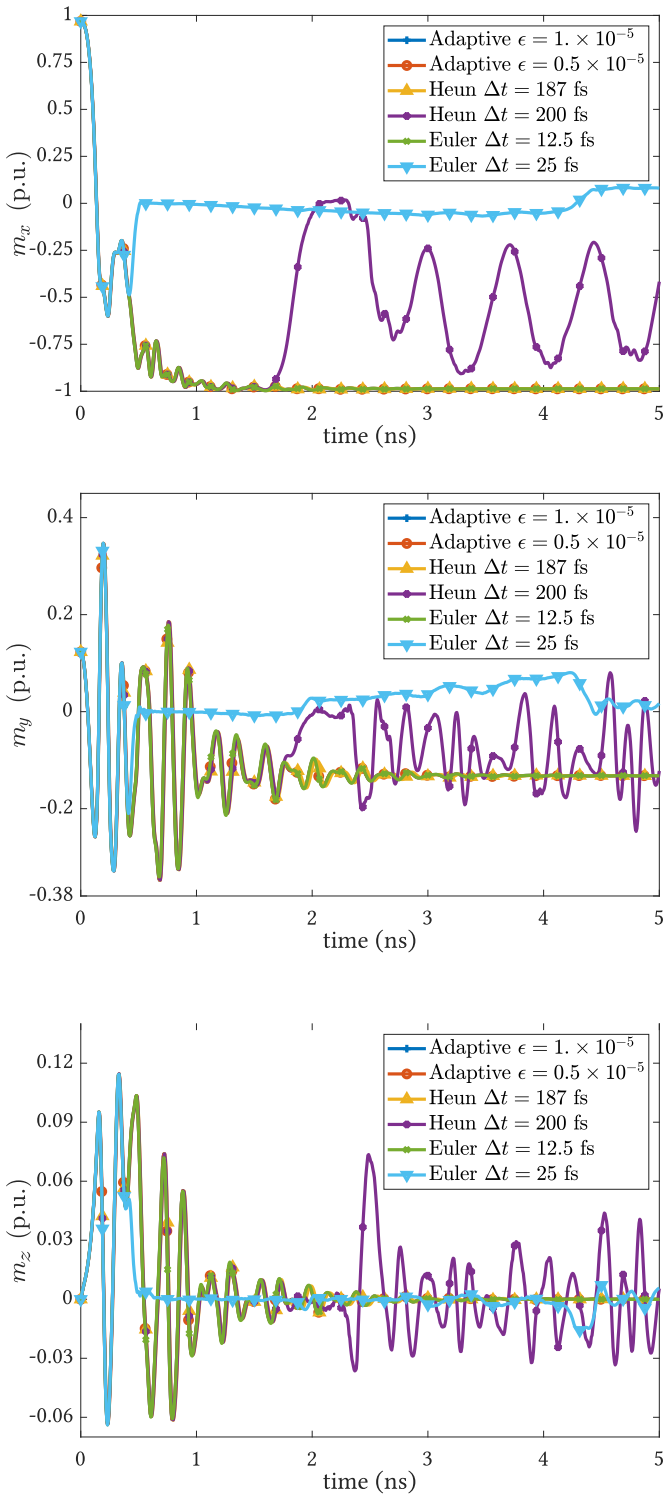

Figure 3.13: Comparison of the solutions for the μMag problem #4 (Field 2) obtained using different time integration algorithms and time steps. The graphs report the average values of the three components of the normalized magnetization.

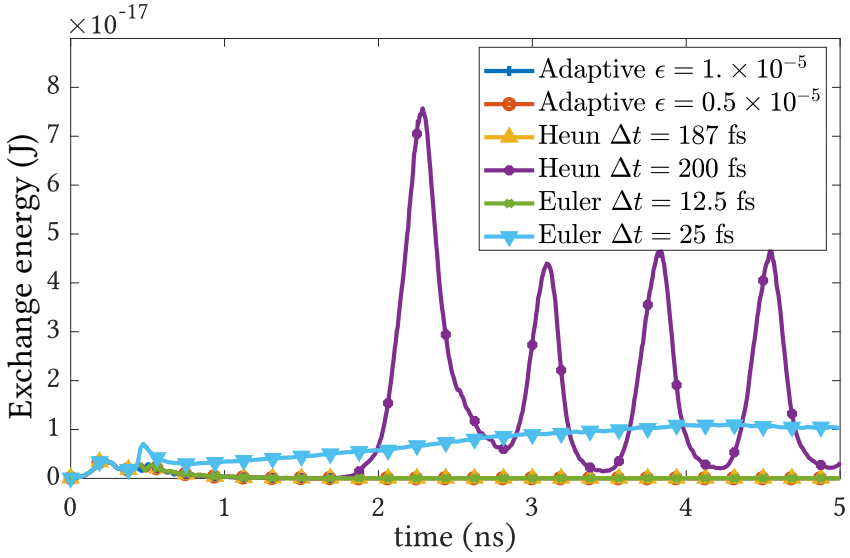

Figure 3.14: Comparison of the time evolution of the exchange energy, using different time steps and solvers. We can see that, for the unstable solutions (Euler $\Delta t = 25$ fs, Heun $\Delta t = 200$ fs), the exchange energy rapidly increases where the solution loses stability.

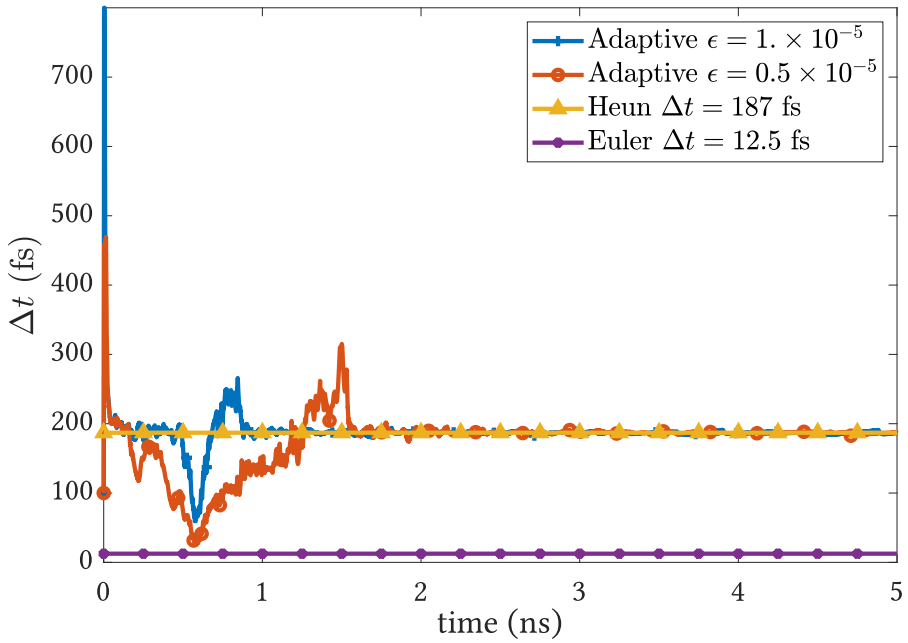

Figure 3.15: Comparison between the time steps used by different time-integration algorithms for the μMag problem #4 (Field 2).

3.5 Conclusions

In this chapter we presented the development of a 3D micromagnetic code able to efficiently simulate the magnetization dynamics of 3D objects. The integration of the LLG equation is particularly complex because of a number of factors: the magnetization is a norm conserving quantity, inducing a non convex constraint on the equation, moreover the equation has Lyapunov structure. In addition, the magnetostatic field being a long-range interaction is computationally heavy to integrate, and the description of quantum mechanics phenomena involved in the magnetization dynamics via the exchange field imposes a strong limit on the maximum size of the spatial discretization. Each aspect and the related computational challenges are analyzed in this chapter. To address these criticalities our code presents the features detailed in the following.

- The time integration scheme is based on a second order time-adaptive geometrical integrator using the Cayley transform, to guarantee the preservation of the constraint on the module of the magnetization.
- The magnetostatic field is calculated using a 3D-FFT algorithm to reduce the computational cost of this operation.
- The exchange field is calculated by means of a standard Finite Difference method.

The code is massively parallelized leveraging the high core count of Graphical Processing Units (GPUs). For what concerns the CPU part, the code is developed in FORTRAN, while the GPU parallelization is written in CUDA, a parallel computing platform and application programming interface (API) model created by Nvidia [40–42].
On the computational level GPUs can be much faster than CPUs, however the data transfer rate is considerably lower for GPUs, which can result in a significant bottleneck for high performance computing. Therefore, to optimize the computational speed of the simulations, we decided to perform all the calculations on the GPU to reduce at the bare minimum the data transfer between CPU and GPU. In our micromagnetic

code, after the initial setup, all the data are transferred to the GPU and transferred to the CPU only for the output to the data file. The developed 3D solver has been successfully tested on widely adopted micromagnetic standard problems, and it has been successfully applied to calculate the hysteresis loop of different 3D nanostructures, showing good performance and good accuracy in the reconstruction of the solutions.

References

[1] O. Bottauscio and A. Manzin. "Efficiency of the Geometric Integration of Landau–Lifshitz–Gilbert Equation Based on Cayley Transform". In: *IEEE Trans. Magn.* 47.5 (May 2011), pp. 1154–1157. ISSN: 0018-9464. DOI: 10.1109/TMAG.2010.2095831.

[2] A. Manzin and O. Bottauscio. "Connections between numerical behavior and physical parameters in the micromagnetic computation of static hysteresis loops". In: *J. Appl. Phys.* 108.9 (2010), p. 093917. DOI: 10.1063/1.3503873.

[3] *muMAG Micromagnetic Modeling Activity Group*. NIST. 2016. URL: https://www.ctcms.nist.gov/~rdm/mumag.org.html (visited on 01/07/2019).

[4] *mumax3 GPU-accelerated micromagnetism*. Ghent University. 2019. URL: http://mumax.github.io/ (visited on 01/07/2019).

[5] A. Vansteenkiste et al. "The design and verification of MuMax3". In: *AIP Adv.* 4.10 (2014). ISSN: 21583226. DOI: 10.1063/1.4899186.

[6] A. Vansteenkiste and B. V. De Wiele. "MUMAX: A new high-performance micromagnetic simulation tool". In: *J. Magn. Magn. Mater.* 323.21 (2011), pp. 2585–2591. ISSN: 03048853. DOI: 10.1016/j.jmmm.2011.05.037.

[7] A. Iserles et al. "Lie-group methods". In: *Acta Numerica* 9 (2000), pp. 215–365.

[8] W. Vetterling et al. *Numerical Recipes Example Book (C++): The Art of Scientific Computing*. Numerical recipes series. Cambridge University Press, 2002. ISBN: 9780521750349.

[9] J. Leliaert et al. "Fast micromagnetic simulations on GPU—recent advances made with mumax3". In: *J. Phys. D. Appl. Phys.* 51.12 (Mar. 2018), p. 123002. ISSN: 0022-3727. DOI: 10.1088/1361-6463/aaab1c.

[10] W. F. Brown. "Micromagnetics, Domains, and Resonance". In: *J. Appl. Phys.* 30.4 (1959), S62–S69. ISSN: 10897550. DOI: 10.1063/1.2185970.

[11] D. Lewis and N. Nigam. "Geometric integration on spheres and some interesting applications". In: *J. Comput. Appl. Math.* 151.1 (2003), pp. 141–170. ISSN: 03770427. DOI: 10.1016/S0377-0427(02)00743-4.

[12] P. Podio-Guidugli. "On dissipation mechanisms in micromagnetics". In: *Eur. Phys. J. B* 19.3 (Feb. 2001), pp. 417–424. ISSN: 1434-6028. DOI: 10.1007/s100510170318.

[13] M. D'Aquino, C. Serpico, and G. Miano. "Geometrical integration of Landau-Lifshitz-Gilbert equation based on the mid-point rule". In: *J. Comput. Phys.* 209.2 (2005), pp. 730–753. ISSN: 00219991. DOI: 10.1016/j.jcp.2005.04.001.

[14] X.-p. Wang, C. J. García-Cervera, and W. E. "A Gauss–Seidel Projection Method for Micromagnetics Simulations". In: *J. Comput. Phys.* 171.1 (July 2001), pp. 357–372. ISSN: 00219991. DOI: 10.1006/jcph.2001.6793.

[15] P. E. Crouch and R. Grossman. "Numerical integration of ordinary differential equations on manifolds". In: *J. Nonlinear Sci.* 3.1 (Dec. 1993), pp. 1–33. ISSN: 0938-8974. DOI: 10.1007/BF02429858.

[16] D. Lewis and J. C. Simo. "Conserving algorithms for the dynamics of Hamiltonian systems on lie groups". In: *J. Nonlinear Sci.* 4.1 (1994), pp. 253–299. ISSN: 09388974. DOI: 10.1007/BF02430634.

[17] H. Munthe-Kaas. "Lie-Butcher theory for Runge-Kutta methods". In: *BIT Numer. Math.* 35.4 (Dec. 1995), pp. 572–587. ISSN: 0006-3835. DOI: 10.1007/BF01739828.

[18] H. Munthe-Kaas. "Runge-Kutta methods on Lie groups". In: *BIT Numer. Math.* 38.1 (Mar. 1998), pp. 92–111. ISSN: 0006-3835. DOI: 10.1007/BF02510919.

[19] E. Celledoni, H. Marthinsen, and B. Owren. "An introduction to Lie group integrators – basics, new developments and applications". In: *Journal of Computational Physics* 257 (2014). Physics-compatible numerical methods, pp. 1040–1061. ISSN: 0021-9991. DOI: 10.1016/j.jcp.2012.12.031.

[20] F. Diele, L. Lopez, and R. Peluso. "The Cayley transform in the numerical solution of unitary differential systems". In: *Advances in Computational Mathematics* 8 (1998), pp. 317–334. ISSN: 10197168.

[21] O. Bottauscio and A. Manzin. "Critical aspects in micromagnetic computation of hysteresis loops of nanometer particles". In: 45.11 (2009), pp. 5204–5207. ISSN: 00189464. DOI: 10.1109/TMAG.2009.2031074.

[22] O. Bottauscio, M. Chiampi, and A. Manzin. "A finite element procedure for dynamic micromagnetic computations". In: *IEEE Trans. Magn.* 44.11 PART 2 (2008), pp. 3149–3152. ISSN: 00189464. DOI: 10.1109/TMAG.2008.2001666.

[23] T. R. Koehler. "Hybrid FEM - BEM method for fast micromagnetic calculations". In: *Phys. B Condens. Matter* 233.4 (1997), pp. 302–307. ISSN: 09214526. DOI: 10.1016/S0921-4526(97)00314-1.

[24] O. Bottauscio, M. Chiampi, and A. Manzin. "An edge element approach for dynamic micromagnetic modeling". In: *J. Appl. Phys.* 103.7 (2008), pp. 5–7. ISSN: 00218979. DOI: 10.1063/1.2830172.

[25] L. Exl and T. Schrefl. "Non-uniform FFT for the finite element computation of the micromagnetic scalar potential". In: *J. Comput. Phys.* 270 (2014), pp. 490–505. ISSN: 10902716. DOI: 10.1016/j.jcp.2014.04.013.

[26] M. Abramowitz, I. A. Stegun, and D. Miller. *Handbook of Mathematical Functions With Formulas, Graphs and Mathematical Tables (National Bureau of Standards Applied Mathematics Series No. 55)*. 1965. DOI: 10.1115/1.3625776.

[27] A. Vansteenkiste. "Dynamics of magnetic vortices in nanodots: experiment and simulation". PhD thesis. Ghent University, 2009.

[28] B. V. de Wiele. "Numerieke studie van magnetische processen : uitbreiding van de Landau-Lifshitz-Gilbert-aanpak van de nano- tot de microschaal". PhD thesis. Ghent University, 2010.

[29] J. W. Cooley and J. W. Tukey. "An Algorithm for the Machine Calculation of Complex Fourier Series". In: *Mathematics of Computation* 19.90 (1965), pp. 297–301. ISSN: 00255718, 10886842.

[30] R. Bracewell. *The Fourier Transform and Its Applications*. 3rd ed. McGraw-Hill series in electrical and computer engineering. Circuits and systems. McGraw Hill, 2000. ISBN: 9780073039381,0073039381.

[31] B. Van de Wiele et al. "On the accuracy of FFT based magnetostatic field evaluation schemes in micromagnetic hysteresis modeling". In: *J. Magn. Magn. Mater.* 322.4 (2010), pp. 469–476. ISSN: 03048853. DOI: 10.1016/j.jmmm.2009.09.077.

[32] Y. Nakatani, Y. Uesaka, and N. Hayashi. "Direct solution of the Landau-Lifshiftz-Gilbert equation for micromagnetics". In: *Jpn. J. Appl. Phys.* 28.12 (1989), pp. 2485–2507. ISSN: 0021-4922. DOI: 10.1143/JJAP.28.2485.

[33] B. Van de Wiele, F. Olyslager, and L. Dupré. "Application of the fast multipole method for the evaluation of magnetostatic fields in micromagnetic computations". In: *J. Comput. Phys.* 227.23 (2008), pp. 9913–9932. ISSN: 00219991. DOI: 10.1016/j.jcp.2008.08.003.

[34] E. Martinez et al. “Micromagnetic simulations with thermal noise: Physical and numerical aspects”. In: *J. Magn. Magn. Mater.* 316.2 SPEC. ISS. (2007), pp. 269–272. ISSN: 03048853. DOI: 10.1016/j.jmmm.2007.03.178.

[35] E. Martínez et al. “Minimizing cell size dependence in micromagnetics simulations with thermal noise”. In: *J. Phys. D. Appl. Phys.* 40.4 (2007), pp. 942–948. ISSN: 00223727. DOI: 10.1088/0022-3727/40/4/003.

[36] W. F. Brown. *Micromagnetics*. Interscience tracts on physics and astronomy. Interscience Publishers, 1963.

[37] J. Leliaert et al. “Adaptively time stepping the stochastic Landau-Lifshitz-Gilbert equation at nonzero temperature: Implementation and validation in MuMax 3”. In: *AIP Adv.* 7.12 (Dec. 2017), p. 125010. ISSN: 2158-3226. DOI: 10.1063/1.5003957.

[38] W. Rave, K. Fabian, and A. Hubert. “Magnetic states of small cubic particles with uniaxial anisotropy”. In: *J. Magn. Magn. Mater.* 190.3 (1998), pp. 332–348. ISSN: 0304-8853. DOI: 10.1016/S0304-8853(98)00328-X.

[39] R. D. McMichael et al. “Switching dynamics and critical behavior of standard problem No. 4”. In: *J. Appl. Phys.* 89.11 (2001), pp. 7603–7605. DOI: 10.1063/1.1355356.

[40] G. Ruetsch and M. Fatica. *CUDA Fortran for Scientists and Engineers: Best Practices for Efficient CUDA Fortran Programming*. 1st. San Francisco, CA, USA: Morgan Kaufmann Publishers Inc., 2013. ISBN: 0124169708, 9780124169708.

[41] *NVIDIA Cuda High Performance Computing*. NVIDIA. 2019. URL: https://developer.nvidia.com/hpc (visited on 01/07/2019).

[42] *CUDA C Programming Guide*. NVIDIA. 2018. URL: https://docs.nvidia.com/cuda/cuda-c-programming-guide/ (visited on 01/07/2019).

Chapter 4

2.5D micromagnetic solver for randomly distributed magnetic thin objects

The material presented in this chapter is submitted for publication on Journal of Magnetism and Magnetic materials.

Over the years a lot of efforts have been made to speed-up micromagnetic simulations, with the aim of efficiently modelling the magnetization evolution in samples with large size, i.e. higher than some microns. Several strategies were implemented to improve the efficiency of the calculation of the magnetostatic field, like Fast-Multipole methods [1–7], Fast Fourier Transform (FFT) techniques [8, 9] that we presented in the previous chapter and hybrid approaches combing FFT and multipole expansion [10, 11]. To accurately handle curved structures, finite-element solvers have also been developed, integrating the Poisson equation by means of Finite Element Method (FEM) or hybrid approaches that couple FEM with open boundary techniques, like the Boundary Element Method (BEM). Finally, particular attention has been paid to the development of parallelized micromagnetic solvers, which exploit massively parallel architectures.

These can be based on multiprocessor systems and, more recently, on graphical processing units (GPUs) [8, 12–18], like the 3D micromagnetic code presented in Chapter 3, which makes use of parallelization, via the implementation on a CPU-GPU-based system.

As we already discussed in the previous chapters, the spatial discretization of the LLG equation is a very critical task, whose complexity in terms of memory consumption and computation time increases when a high number of interacting magnetic nano-objects has to be modelled. This problem has to be faced when simulating large dot arrays for magnetic storage or magneto-logic devices [19–21], artificial spin-ice structures [22] and magnetic nano-systems for biomedical applications, like magnetic hyperthermia [23, 24]. In the last example, which is related to the objective of this thesis, the nano-objects can be randomly distributed in a 3D space (a biological fluid or a tissue) at locally elevated concentrations and with very different orientations with respect to the applied field. In this case, 3D-FFT techniques, as the one implemented in Chapter 3, cannot be applied, since they require structured meshes, which are not suitable for objects with complex shape and orientation not-aligned with mesh grid. For this specific case, neither the 3D FEM is suitable, since strongly irregular mesh elements should be employed to simultaneously discretize the ensemble of thin objects and the 3D medium where they are randomly distributed. Moreover, the solution accuracy and computational cost strongly depend on the size of the domain selected for approximating the open boundary problem and on the order of the asymptotic boundary conditions, if applied [25]. As a possible solution, we could combine two-dimensional (2D) FEM, for the discretization of the thin objects, with BEM, for the treatment of the surrounding non-magnetic medium. As pointed out in Chapter 3, the use of BEM leads to dense matrices and results in an additional computational complexity in the order of $\mathcal{O}(M^2)$, where M is the number of boundary nodes.

To face the above numerical problems, in this chapter we present a novel 2.5D GPU-parallelized micromagnetic solver, able to simulate a high number of interacting 2D

nano-objects, randomly distributed in a 3D space. Each nano-object is discretized with a non-structured mesh made of hexahedral elements, to well-reproduce complex shapes and very different mutual orientations. The exchange field is calculated with a finite difference approach able to handle non-structured meshes [26, 27], while the magnetostatic field is locally separated into two contributions: an internal and an external one. The internal term includes the interactions between magnetic spins in the hexahedra belonging to the same object. This is obtained by numerically solving the integral equation derived from Green's theorem application. The external term describes the inter-object magnetostatic interactions and it is determined by approximating the contribution from each mesh element as the stray field produced by a magnetic dipole [28, 29]. The time integration is performed by means of a norm-conserving scheme based on the Cayley transform and on the forward Euler method presented in Chapter 3; this scheme has been proven to be very efficient in the determination of the equilibrium states along hysteresis loops [30].

We investigate the performances of the developed 2.5D micromagnetic solver by analyzing the accuracy in the calculation of the external magnetostatic contribution and the computation cost per each time instant. The solver is validated by comparison to a reference code, where all the magnetostatic field terms are evaluated by numerically solving the Green's integral equation, as well as to a standard 3D-FFT code. As a final goal, we demonstrate the solver reliability by calculating the hysteresis loop of a high number of magnetic nanodots, strongly interacting and randomly oriented in the space.

4.1 Methodology

We consider a set of N equal 2D-approximable magnetic bodies (flat objects with uniform very low thickness t) distributed in the 3D space. Each object is discretized with the same mesh composed of T hexahedra with height fixed to t. In each hexahedron the magnetization vector $\mathbf{M}$ is assumed to be uniform. The time evolution is determined

under the assumption of no spatial variation along t, by solving the LLG equation (2.81). For the generic i-th hexahedron belonging to the n-th object it becomes:

$$\frac{\partial \mathbf{M}_{i,n}}{\partial t} = -\frac{\gamma}{(1+\alpha^2)}\mathbf{M}_{i,n} \times \mathbf{H}_{\mathit{eff}_{i,n}} - \frac{\gamma\alpha}{(1+\alpha^2)M_S}\mathbf{M}_{i,n} \times (\mathbf{M}_{i,n} \times \mathbf{H}_{\mathit{eff}_{i,n}}), \quad 1 \leq i \leq T,\ 1 \leq n \leq N \tag{4.1}$$

where M_S is the saturation magnetization, γ is the absolute value of the gyromagnetic ratio and α is the damping coefficient. The effective field $\mathbf{H}_{\mathit{eff}}$ is the sum of the applied field $\mathbf{H}_a$, the exchange field $\mathbf{H}_{ex}$, the magnetocrystalline anisotropy field $\mathbf{H}_{an}$ and the magnetostatic field $\mathbf{H}_{ms}$, which is in turn decomposed into an "internal" and an "external" term (Fig. 4.1). The internal term includes the magnetostatic contributions in the hexahedron of calculus due to the magnetic spins in all the other hexahedra belonging to the same object, namely

$$\mathbf{H}_{ms,\mathit{int}_{i,n}} = \frac{1}{4\pi}\sum_{\substack{j=1 \\ i\neq j}}^{T}\int_{\partial\Omega_j} \mathbf{M}_{j,n} \cdot \mathbf{n}_j \frac{(\mathbf{r}_{i,n} - \mathbf{r}_{j,n})}{|\mathbf{r}_{i,n} - \mathbf{r}_{j,n}|^3} ds, \quad 1 \leq i \leq T,\ 1 \leq n \leq N \tag{4.2}$$

where $\partial\Omega_j$ is the surface of the j-th hexahedron and $\mathbf{n}_j$ its normal unit vector, while $\mathbf{r}_{i,n}$ and $\mathbf{r}_{j,n}$ are the position vectors of the barycenters of the i-th and j-th hexahedra of the n-th object, respectively. The external term includes the magnetostatic contributions in the hexahedron of calculus due to the magnetic spins in the hexahedra belonging to all the other objects. This is approximated by associating each hexahedron with a magnetic dipole centred in its barycentre, namely

$$\mathbf{H}_{ms,\mathit{ext}_{i,n}} = \frac{1}{4\pi}\sum_{\substack{q=1 \\ q\neq n}}^{N}\sum_{j=1}^{T} \frac{3[\mathbf{m}_{j,q} \cdot (\mathbf{r}_{i,n} - \mathbf{r}_{j,q})](\mathbf{r}_{i,n} - \mathbf{r}_{j,q})}{|\mathbf{r}_{i,n} - \mathbf{r}_{j,q}|^5} - \frac{\mathbf{m}_{j,q}}{|\mathbf{r}_{i,n} - \mathbf{r}_{j,q}|^3}, \quad 1 \leq i \leq T,\ 1 \leq n \leq N \tag{4.3}$$

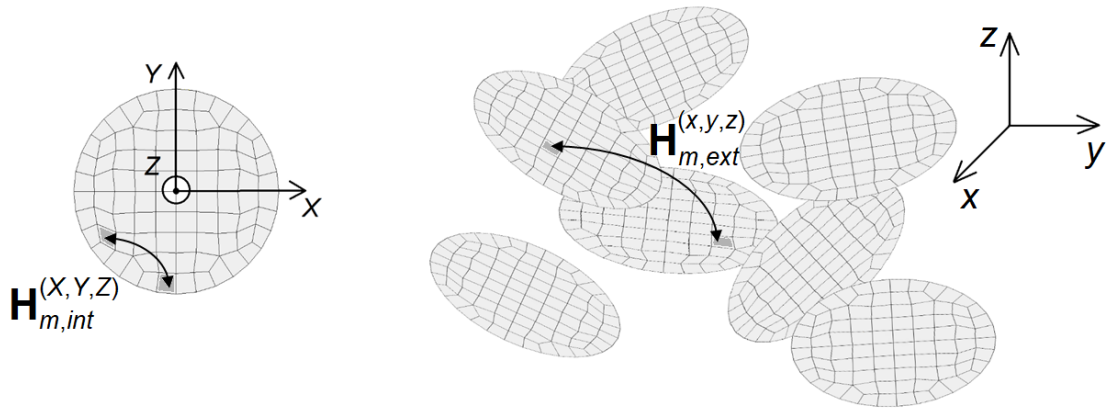

(a) (b)

Figure 4.1: (a) Schematic of the hexahedral mesh of a single object in coordinate system (X, Y, Z) (local reference frame) and representation of the interaction concurring to the internal magnetostatic field term. (b) Schematic of a 3D distribution of objects randomly arranged in coordinate system (x, y, z) (absolute reference frame) and representation of the interaction concurring to the external magnetostatic field term.

where $\mathbf{m}_{j,q}$ is the magnetic moment in the j-th hexahedron of the q-th object, equal to $\mathbf{M}_{j,q}\Delta V_j$, where ΔV_j is the volume of the j-th hexahedron.

4.1.1 Implementation

The developed 2.5D micromagnetic solver is composed of two main blocks. The first block, at the beginning, is related to the input of the geometry, the discretization mesh of a single object and the physical properties of the problem (pre-processing phase), followed by the calculation of the time-invariant system matrices for the exchange and internal magnetostatic fields. The second block is associated with the determination of the effective field contributions and the update of the magnetization at each time instant.

The first block starts with the input of the hexahedral mesh of a single object Ω in the local reference frame, i.e. the coordinate system (X, Y, Z), centered in the object barycenter and with Z-axis perpendicular to the object surface (Fig. 4.1a). Then, a 3D distribution of N objects is randomly generated in the absolute reference frame, i.e. the

coordinate system (x, y, z) (Fig. 4.1b), providing for each object the translation vector components (ΔX_n, ΔY_n, ΔZ_n) and the rotation (Euler) angles (ϕ_n, θ_n, ψ_n) for the transformation from (X, Y, Z) to (x, y, z). It results in

$$\begin{bmatrix} x \\ y \\ z \end{bmatrix} = \mathbf{R}_{\phi\theta\psi_n} \begin{bmatrix} X \\ Y \\ Z \end{bmatrix} + \begin{bmatrix} \Delta X_n \\ \Delta Y_n \\ \Delta Z_n \end{bmatrix}, \quad 1 \leq n \leq N \tag{4.4}$$

where $\mathbf{R}_{\phi\theta\psi_n}$ is the rotation matrix for the n-th object that is expressed in the Goldstein's notation

$$\mathbf{R}_{\phi\theta\psi_n} = \begin{bmatrix} \cos(\psi_n)\cos(\phi_n) - \cos(\theta_n)\sin(\phi_n)\sin(\psi_n) & -\sin(\psi_n)\cos(\phi_n) - \cos(\theta_n)\sin(\phi_n)\cos(\psi_n) & \sin(\theta_n)\sin(\phi_n) \\ \cos(\psi_n)\sin(\phi_n) + \cos(\theta_n)\cos(\phi_n)\sin(\psi_n) & -\sin(\psi_n)\sin(\phi_n) + \cos(\theta_n)\cos(\phi_n)\cos(\psi_n) & -\sin(\theta_n)\cos(\phi_n) \\ \sin(\theta_n)\sin(\psi_n) & \sin(\theta_n)\cos(\psi_n) & \cos(\theta_n) \end{bmatrix}. \tag{4.5}$$

After inputting the geometry, physical parameters ($\mathbf{M}_S$, exchange constant k_{ex} and magnetocrystalline properties) and source conditions (spatial-temporal distribution of $\mathbf{H}_a$), we calculate the time-invariant matrices $\mathbf{G}$ and $\mathbf{K}$ for the determination, in the local reference frame (X, Y, Z), of the internal magnetostatic and exchange fields, respectively. Matrices $\mathbf{G}$ and $\mathbf{K}$ are described later, in Subsections 4.1.2 and 4.1.3. The second block of the solver, detailed in Fig. 4.1b, involves the time integration of the LLG equation, which is performed by means of the Cayley transform and the forward Euler method as described in Section 3.1. At each time step, for each object, the magnetization at instant t_k is transformed from the absolute reference frame (x, y, z) to the local one (X, Y, Z). For the i-th hexahedron of the n-th object, it results

$$\mathbf{M}_{i,n}^{X,Y,Z}(t_k) = \mathbf{R}_{\phi\theta\psi_n}^{-1} \mathbf{M}_{i,n}^{x,y,z}(t_k), \; 1 \leq i \leq T, \; 1, \leq n \leq N. \tag{4.6}$$

Then, for each object, we first compute the internal term of the magnetostatic field and the exchange field in the local reference frame, by using the $3T \times 3T$ system matrices $\mathbf{G}$ and $\mathbf{K}$ calculated at the beginning and the spatial distribution of the magnetization

vector, expressed in the local reference frame. For the n-th object

$$\begin{cases} \mathbf{H}^{x,y,z}_{ms,int_{i,n}}(t_k) = \mathbf{GM}^{X,Y,Z}_{i,n}(t_k) \\ \mathbf{H}^{x,y,z}_{ex_{i,n}}(t_k) = \mathbf{KM}^{X,Y,Z}_{i,n}(t_k) \end{cases} 1, \leq n \leq N. \tag{4.7}$$

$\mathbf{K}$ is reduced to a matrix $\mathbf{K}^*$ with size $T \times T$, since the relative geometric contribution is the same for each component. Second, we transform the two fields from (X, Y, Z) to (x, y, z) by means of the rotation matrix, resulting in the following operations for the i-th hexahedron of the n-th object:

$$\begin{cases} \mathbf{H}^{x,y,z}_{ms,int_{i,n}}(t_k) = \mathbf{R}_{\phi\theta\psi_n}\mathbf{H}^{X,Y,Z}_{ms,int_{i,n}}(t_k) \\ \mathbf{H}^{x,y,z}_{ex_{i,n}}(t_k) = \mathbf{R}_{\phi\theta\psi_n}\mathbf{H}^{X,Y,Z}_{ex_{i,n}}(t_k) \end{cases}, \ 1 \leq i \leq T, \ 1, \leq n \leq N. \tag{4.8}$$

Then, by implementing equation (4.3), we determine $\mathbf{H}_{ms}$, i.e. the external term of the magnetostatic field, in the absolute reference frame (x, y, z). If present, we also calculate in (x, y, z) the magnetocrystalline anisotropy field and, by means of the Langevin approach, the thermal field (for more details see Section 2.5, Subsection 3.3.4 and related references). At the end, the effective field $\mathbf{H}^{x,y,z}_{eff}$ is determined, by summing all the field contributions obtained in coordinate system (x, y, z). Finally, we update the magnetization vector in (x, y, z) by means of the geometric time-integration scheme based on the Cayley transform, already presented in Chapter 3 for the 3D micromagnetic code.

4.1.2 System matrix for internal magnetostatic field

In this subsection we describe the $3T \times 3T$ system matrix $\mathbf{G}$ for the determination of the internal term of the magnetostatic field in the local reference frame (X, Y, Z), in accordance with Eq. (4.3). The geometric interaction between the generic i-th and j-th hexahedra in the reference object Ω leads to the following 3×3 symmetric sub-matrix

of $\mathbf{G}$

$$\mathbf{G}^{ij} = \begin{pmatrix} g^{ij}_{XX} & g^{ij}_{XY} & g^{ij}_{XZ} \\ g^{ij}_{YX} & g^{ij}_{YY} & g^{ij}_{YZ} \\ g^{ij}_{ZX} & g^{ij}_{ZY} & g^{ij}_{ZZ} \end{pmatrix} \tag{4.9}$$

where

$$g^{ij}_{pq} = \frac{1}{4\pi} \int_{\partial\Omega_j} n_{q_j} \frac{(p_{i,n} - p_{j,n})}{|\mathbf{r}_i - \mathbf{r}_j|^3} ds \tag{4.10}$$

for p and q equal to local system coordinates X, Y or Z. The numerical integration in Eq. (4.10) is performed by means of the Gaussian quadrature rules with 9 nodes.

4.1.3 System matrix for exchange field

In this subsection we describe the $T \times T$ system matrix $\mathbf{K}^*$ for the determination of the p-th component of the exchange field in the local reference frame (X, Y, Z) at instant t_k, defined as

$$H^{X,Y,Z}_{ex_p}(t_k) = k_{ex} \left[\frac{\partial^2 M^{X,Y,Z}_p(t_k)}{\partial X^2} + \frac{\partial^2 M^{X,Y,Z}_p(t_k)}{\partial Y^2} \right], \tag{4.11}$$

where $p = X, Y, Z$ and the derivative of $M^{X,Y,Z}_p(t_k)$ with respect to Z is assumed equal to zero, due to the thin-film approximation [26, 27].

The exchange field is here computed by means of a finite difference method suitable for non-structured meshes, thus allowing the accurate treatment of curved boundaries. Focusing on the XY-plane, the formulation is derived by approximating the magnetization vector by a second-order Taylor series expansion around the point of calculus (X_0, Y_0), namely

$$\begin{aligned} \mathbf{M}^{X,Y,Z} =& \mathbf{M}^{X,Y,Z}_0 + h\frac{\partial \mathbf{M}^{X,Y,Z}_0}{\partial X} + l\frac{\partial \mathbf{M}^{X,Y,Z}_0}{\partial Y} + \frac{h^2}{2}\frac{\partial^2 \mathbf{M}^{X,Y,Z}_0}{\partial X^2} \\ &+ \frac{l^2}{2}\frac{\partial^2 \mathbf{M}^{X,Y,Z}_0}{\partial Y^2} + \frac{hl}{2}\frac{\partial^2 \mathbf{M}^{X,Y,Z}_0}{\partial XY} + O(\Delta^3) \end{aligned} \tag{4.12}$$

where $h = X - X_0$, $l = Y - Y_0$ and $\Delta = \sqrt{h^2 + l^2}$.

By associating the points of calculus with the hexahedron barycenters, the five unknown derivatives in Eq. (4.12) can be obtained by considering the contributions from S surrounding hexahedra, where S is here assumed ~ 8 to avoid ill-conditioning. For hexahedra located at the object boundaries $\partial\Omega$, the boundary condition on $\mathbf{M}$

$$\left.\frac{\partial \mathbf{M}_0^{X,Y,Z}}{\partial \mathbf{n}}\right|_{\partial\Omega} = 0 \tag{4.13}$$

is imposed by introducing fictitious points outside Ω, replicating the magnetization value.

The five unknown derivatives of $\mathbf{M}$ in the generic i-th hexahedron of the n-th object can be determined via the minimization of the following norm

$$\begin{aligned}\mathfrak{F} = \sum_{j=1}^{S} \Bigg[\Bigg(\mathbf{M}_{i,n}^{X,Y,Z}(t_k) - \mathbf{M}_{j,n}^{X,Y,Z}(t_k) + h_{ij}\frac{\partial \mathbf{M}_{i,n}^{X,Y,Z}(t_k)}{\partial X} + l_{ij}\frac{\partial \mathbf{M}_{i,n}^{X,Y,Z}(t_k)}{\partial Y} + \\ + \frac{h_{ij}^2}{2}\frac{\partial^2 \mathbf{M}_{i,n}^{X,Y,Z}(t_k)}{\partial X^2} + \frac{l_{ij}^2}{2}\frac{\partial^2 \mathbf{M}_{i,n}^{X,Y,Z}(t_k)}{\partial Y^2} + \frac{h_{ij}l_{ij}}{2}\frac{\partial^2 \mathbf{M}_{i,n}^{X,Y,Z}(t_k)}{\partial XY} \Bigg) \frac{1}{\Delta_{ij}^3} \Bigg]^2, \\ 1 \leq i \leq T,\ 1, \leq n \leq N\end{aligned} \tag{4.14}$$

where $h_{ij} = X_i - X_j$, $l_{ij} = Y_i - Y_j$ and $\Delta_{ij} = \sqrt{h_{ij}^2 + l_{ij}^2}$. From

$$\frac{\partial \mathfrak{F}}{\partial \Delta \mathbf{M}_{i,n}^{X,Y,Z}(t_k)} = 0 \tag{4.15}$$

we derive a 5×5 algebraic system of equations for the generic p-component of $\mathbf{M}$, i.e.

$$\mathbf{C}\boldsymbol{\Delta}\mathbf{M}_{p_{i,n}}^{X,Y,Z}(t_k) = \mathbf{D},\ 1 \leq i \leq T,\ 1, \leq n \leq N, \tag{4.16}$$

where the transpose of vector $\mathbf{\Delta M}_{p_{i,n}}^{X,Y,Z}$ is equal to

$$\left[\frac{\partial M_{p_{i,n}}^{X,Y,Z}}{\partial X}, \frac{\partial M_{p_{i,n}}^{X,Y,Z}}{\partial Y}, \frac{\partial^2 M_{p_{i,n}}^{X,Y,Z}}{\partial X^2}, \frac{\partial^2 M_{p_{i,n}}^{X,Y,Z}}{\partial Y^2}, \frac{\partial^2 M_{p_{i,n}}^{X,Y,Z}}{\partial XY}\right] \tag{4.17}$$

In Eq. (4.16) 5×5 matrix $\mathbf{C}$ depends on the mesh geometry, being a function of the spatial coordinates of the hexahedra barycenters. The elements of $\mathbf{C}$ have the following expressions:

$$\begin{aligned} c_{m1} &= \sum_{j=1}^{S} \frac{2}{\Delta_j^3} h_j p_m \qquad & c_{m2} &= \sum_{j=1}^{S} \frac{2}{\Delta_j^3} l_j p_m \\ c_{m3} &= \sum_{j=1}^{S} \frac{h_j^2}{\Delta_j^3} p_m & c_{m4} &= \sum_{j=1}^{S} \frac{l_j^2}{\Delta_j^3} p_m \\ c_{m5} &= \sum_{j=1}^{S} \frac{2}{\Delta_j^3} h_j l_j p_m & m &= 1, \dots, 5 \end{aligned} \tag{4.18}$$

with

$$\begin{aligned} p_1 &= h_j \quad p_2 = l_j \qquad p_3 = \frac{h_j^2}{2} \\ p_4 &= \frac{l_j^2}{2} \quad p_5 = h_j l_j. \end{aligned} \tag{4.19}$$

The elements of $\mathbf{D}$ are defined as

$$\begin{aligned} d_1 &= -2 \sum_{j=1}^{S} \frac{(\mathbf{M}_i - \mathbf{M}_j)}{\Delta_j^3} h_j \qquad & d_2 &= -2 \sum_{j=1}^{S} \frac{(\mathbf{M}_i - \mathbf{M}_j)}{\Delta_j^3} l_j \\ d_3 &= -\sum_{j=1}^{S} \frac{(\mathbf{M}_i - \mathbf{M}_j)}{\Delta_j^3} h_j^2 & d_4 &= -\sum_{j=1}^{S} \frac{(\mathbf{M}_i - \mathbf{M}_j)}{\Delta_j^3} l_j^2 \\ d_5 &= -2 \sum_{j=1}^{S} \frac{(\mathbf{M}_i - \mathbf{M}_j)}{\Delta_j^3} h_j l_j \end{aligned} \tag{4.20}$$

By combining Eq. (4.11) and Eq. (4.16), for the generic i-th hexahedron in the reference object Ω we can derive the $T \times T$ system matrix $\mathbf{K}^*$.

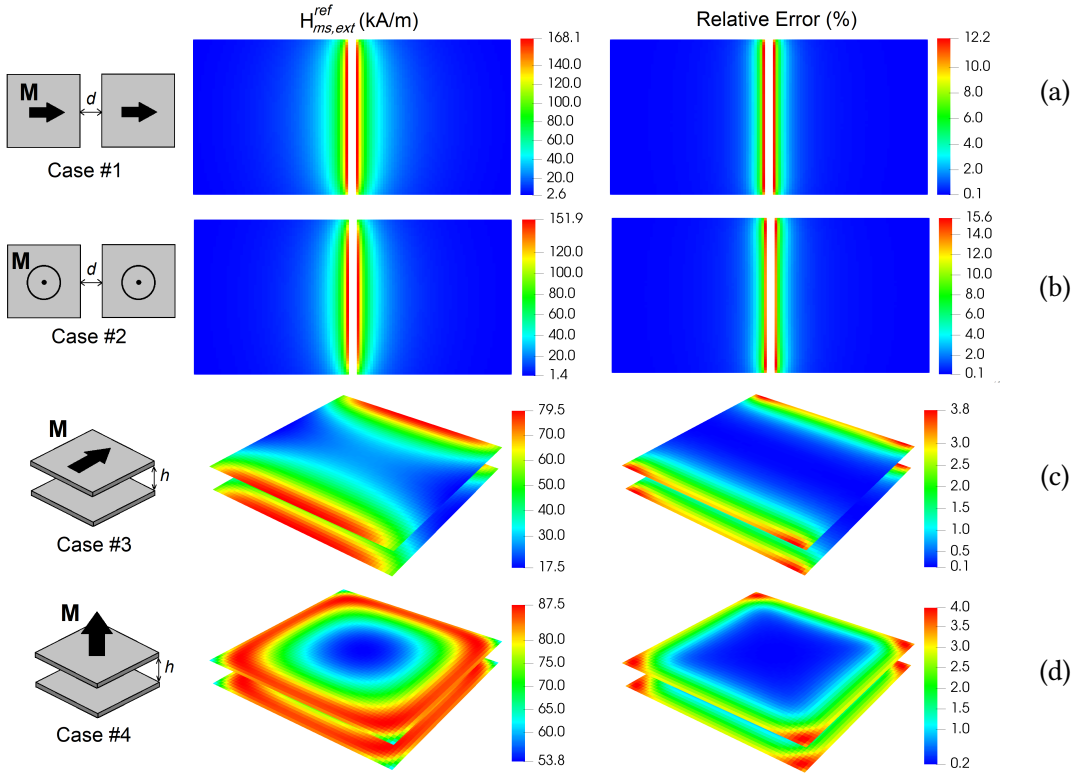

Figure 4.2: On the left: schematics of the analysed cases with indication of the magnetization spatial distribution. In the centre: maps of the module of the external magnetostatic field term calculated by solving Green's integral equation (reference solution). On the right: maps of the relative error of the external magnetostatic field, obtained by approximating each object as a collection of magnetic dipoles. In the reported results parameters d and h are fixed to 10 nm.

4.2 Analysis of accuracy

In the developed 2.5D micromagnetic solver, possible sources of inaccuracy are introduced in Eq. (4.3) when evaluating the external magnetostatic field term. This is caused by the approximation of the contribution from a single hexahedron as the stray field of a magnetic dipole, located at the hexahedron barycenter [28, 29].

We here investigate the loss of accuracy in the calculation of the inter-object magnetostatic interactions, by first considering a set of simple test cases with two interacting squared thin-films made of permalloy (saturation magnetization M_S of 860 kA/m, exchange constant k_{ex} of 13 pJ/m and negligile magnetocrystalline anisotropy). The features and main results of the analyzed cases are illustrated in Fig. 4.2. The reported

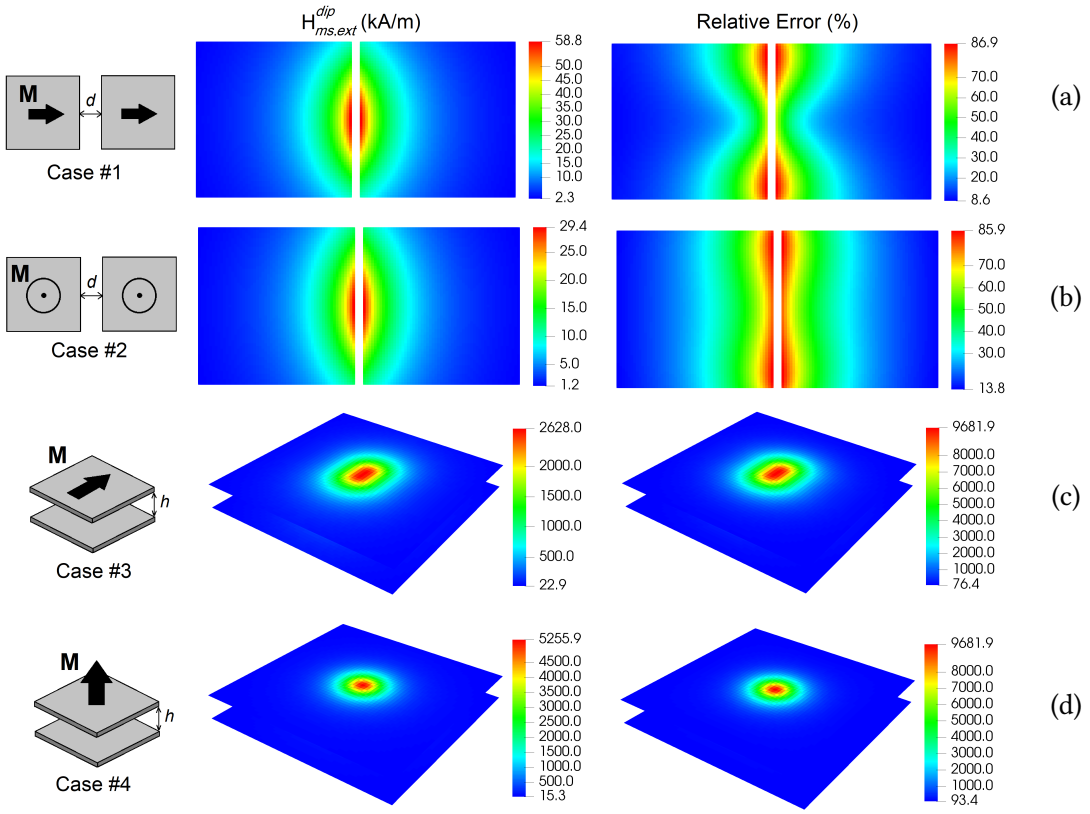

Figure 4.3: On the left: schematics of the analysed cases with indication of the magnetization spatial distribution. In the centre: maps of the module of the external magnetostatic field term calculated by approximating each object as a single magnetic dipole. On the right: maps of the relative error. In the reported results parameters d and h are fixed to 10 nm.

schemes depict the configuration of the magnetization, which is assumed to be uniformly distributed, with the same spatial orientation in the two films. In cases #1 and #2 the films are located in the xy-plane with a side-side distance d; in cases #3 and #4 the films are piled up with a face-face distance h. In cases #1 and #3 the magnetization lies in the xy-plane; in cases #2 and #4 it is orientated orthogonally to the film plane. The two squared films have a side of 200 nm and a thickness of 15 nm and are discretized with a structured mesh whose size in the xy-plane is fixed to ~ 3.5 nm.

Figure 4.2 also reports the maps of the module of the external magnetostatic field term, calculated by setting parameters d and h at 10 mm. Contextually, it shows the maps of

the relative error, which is determined in the following way

$$E(\mathbf{r}) = \frac{\left|\mathbf{H}^{ref}_{ms,ext}(\mathbf{r}) - \mathbf{H}_{ms,ext}(\mathbf{r})\right|}{\left|\mathbf{H}^{ref}_{ms,ext}(\mathbf{r})\right|} 100. \tag{4.21}$$

In Eq. (4.21) $\mathbf{H}^{ref}_{ms,ext}(\mathbf{r})$ is the reference solution, which is obtained by using the same approach adopted for the evaluation of the internal magnetostatic field term, calculating Green integrals via Gaussian quadrature rules with 9 nodes.

The highest relative errors are found for cases #1 and #2 in proximity to the adjacent sides, where peak errors in the order of 12% and 16% are encountered for #1 and #2, respectively (see Figs. 4.2a and 4.2b). The relative errors strongly decay by moving from the film side, going down 1% for distances from the boundary higher than 40 nm. Moreover, the peak values reduce to about 1% by increasing parameter d to 50 nm. Maximum errors in the order of 4% are found for cases #3 and #4, when $h = 10$ nm (see Figs. 4.2c and 4.2d). They reduce to less than 1% when $h = 50$ nm.

As a second test, we compare the above solutions with the one obtained by approximating the external magnetostatic field term as the interaction between objects represented by a unique magnetic dipole, centered in the object barycenter. It results in

$$\mathbf{H}^{dip}_{ms,ext_{i,n}} = \frac{1}{4\pi} \sum_{\substack{q=1 \\ q \neq n}}^{N} \frac{3[\tilde{\mathbf{m}}_q \cdot (\mathbf{r}_{i,n} - \tilde{\mathbf{r}}_q)](\mathbf{r}_{i,n} - \tilde{\mathbf{r}}_q)]}{|\mathbf{r}_{i,n} - \tilde{\mathbf{r}}_q|^5} - \frac{\mathbf{m}_q}{|\mathbf{r}_{i,n} - \tilde{\mathbf{r}}_q|^3}, \tag{4.22}$$
$$1 \leq i \leq T,\ 1 \leq n \leq N$$

where $\tilde{\mathbf{m}}_q$ is the magnetic moment of the q-th object and $\tilde{\mathbf{r}}_q$ the vector position of its barycenter. As can be seen in Fig. 4.3a for case #1 and $d = 10$ nm, this strong approximation leads to a significant increase in the relative errors. In particular, they reach peak values in the order of 85% when $d = 10$ nm and 50 % when $d = 50$ nm, for cases #1 and #2. Very critical issues arise for cases # 3 and #4 (Fig. 4.3c, 4.3d), due to the appearance of quasi-singularity in proximity to the position of the magnetic dipole that

approximates the contribution of an object to external magnetostatic field term. When $h = 10$ nm, for points located within 20 nm from the object barycenter the error tends practically to infinite.

As a third test, we analyze how the error introduced in the evaluation of the external magnetostatic field propagates during the solution of the LLG equation in a specified time interval. To this aim, we calculate the time evolution of the magnetization after the application of a uniform dc magnetic field, with amplitude variable between zero and 100 kA/m. The reference solution is obtained by calculating the external magnetostatic field term via Green integral evaluation. The damping coefficient α is fixed to 0.1, the time step to 50 fs and parameter σ in Eq. (3.5) to zero.

In the first and second tests, the geometrical configuration and the initial magnetization state correspond to case #1, with $d = 10$ nm and the external field applied along negative x-axis (inset of Fig. 4.4a). Figure 4.4a shows the relative error in the average value of the x-component of the magnetization at the equilibrium state reached at the end of the time evolution, as a function of the applied field amplitude. The errors are reported for the solutions obtained by approximating the external magnetostatic field term as in Eq. (4.3) (each hexahedron contributes as a dipole) and as in Eq. (4.22) (each object contributes as a dipole). For H_a = 0, an error higher than 4 % is found for the object-dipole approximation, while the hexahedron-dipole approximation implemented in the 2.5D code leads to an error of 0.5 %. This decreases to 0.004 % when H_a = 100 kA/m.

In the third test, the geometrical configuration and the initial magnetization state correspond to case #4, with $h = 10$ nm and the external field applied along negative z-axis (inset of Fig. 4.4b). In this case, the hexahedron-dipole approximation is responsible for an error of about 0.1 %, while the object-dipole approximation does not guarantee the reaching of the equilibrium state, also for large external fields, due to the appearance of quasi-singularities. This is well depicted by Fig. 4.4b, which reports the time evolution of the average value of the z-component of the magnetization when H_a = 100 kA/m, for the reference and the two approximated solutions. From the above analysis, it is

clear that the object-dipole approximation is inadequate in the calculation of hysteresis loops, since in presence of very close objects it introduces such strong errors to not permit the reaching of equilibrium states.

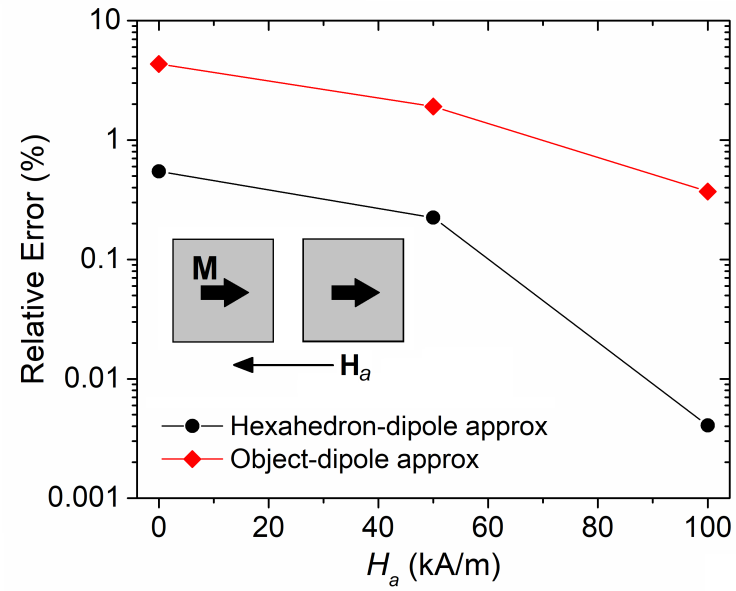

(a)

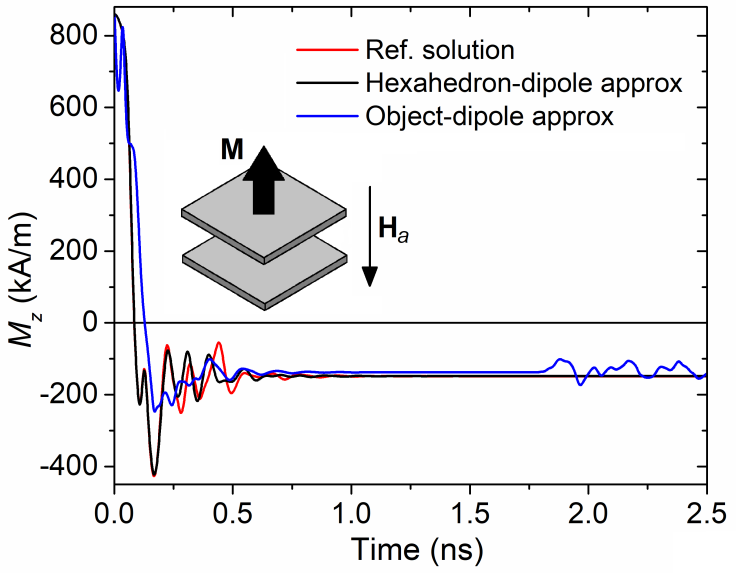

(b)

Figure 4.4: The insets in (a) and (b) show the geometrical configuration, the initial uniform magnetization state and the direction of the external field. (a) Relative error in the average value of the x-component of the magnetization at the equilibrium state reached after the application of a uniform dc field (along negative x-axis) with variable amplitude H_a. The solutions are calculated with the hexahedron-dipole and object-dipole approximations, for $d = 10$ nm. (b) Time evolution of the z-component of the magnetization in presence of a uniform dc field with $H_a = 100$ kA/m, applied along negative z-axis. The solutions calculated for $h = 10$ nm with the hexahedron-dipole and object-dipole approximations are compared to the reference one, obtained via Green integral evaluation

4.3 Analysis of computation time

We here investigate the computational cost of the developed 2.5D solver, highlighting its advantages when compared to a standard approach, where all the magnetostatic interactions are calculated via Green integration. The study is performed on a variable number N of objects, discretized with a fixed mesh composed of 1000 hexahedra. The algorithm can be split in two main blocks, a preliminary one, where the local time-invariant system matrices $\mathbf{G}$ and $\mathbf{K}^*$ are calculated and permanently transferred to GPU, and a second one, where the LLG equation is solved at each time instant.

The computation time for the first block, which involves the determination of the exchange and internal magnetostatic field matrices in the local reference frame (equal for each object), does not depend on N, but only on the number T of hexahedra. The assembly of the exchange field matrix $\mathbf{K}^*$ requires a negligible computation time, 5000 times smaller than the one necessary to build the Green tensor $\mathbf{G}$ for the internal magnetostatic field term.

The non-dependence on N represents a great advantage in terms of computational efficiency and memory requirement. If we consider a standard approach, where the entire Green tensor is calculated at the beginning, we have to evaluate a total of $9N^2 \times T^2$ matrix elements, compared to a number of $9T^2$ elements for the developed 2.5D algorithm. This poses limits to the maximum number of objects that can be handled with a standard approach, e.g. with a GPU card NVIDIA Quadro K6000 we can treat up to 15 objects, considering the additional storage of the exchange field matrix. In this case, the total time to assemble the entire Green tensor is roughly 200 times larger than the one required for the matrix for the only internal magnetostatic field term.

The computation time for the second block is analysed in Fig. 4.5, which shows the time required for the calculation of the exchange field and of the internal and external magnetostatic field terms and for the update of the magnetization per each time instant.

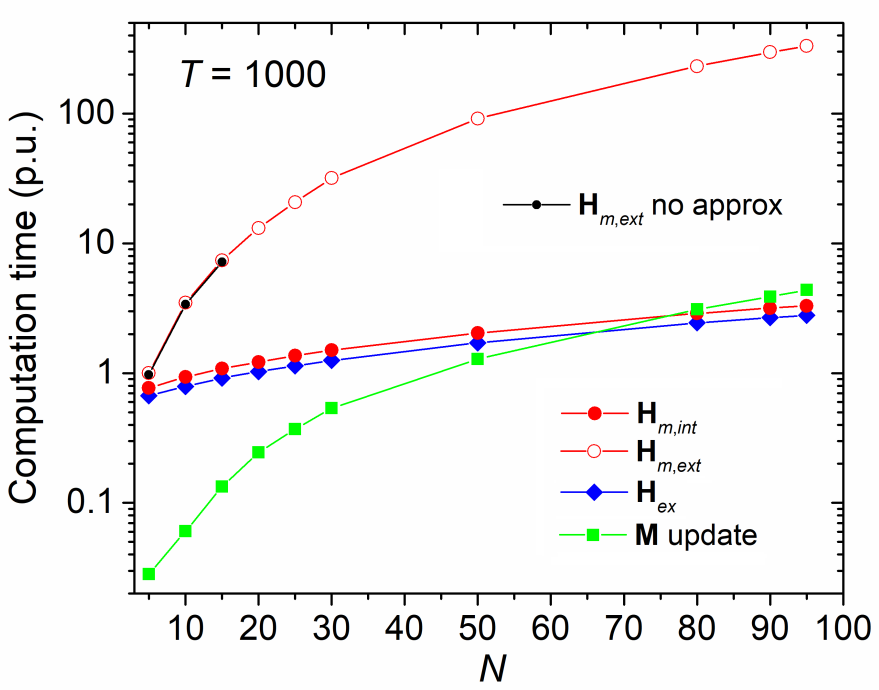

Figure 4.5: Analysis of the computation time for distributions of N objects (discretized with 1000 hexahedra), separately considering the calculation of the exchange field and of the internal and external magnetostatic field terms and the update of magnetization at each time instant. The time required for the evaluation of the external magnetostatic field term without approximation is also reported for comparison, up to N = 15. The computation time contributions are normalized to the time needed to calculate the approximated external magnetostatic field with $N = 5$.

The computation time contributions, normalized to the time needed to calculate the external magnetostatic field with $N = 5$, are registered under the condition of optimal data transfer to GPU.

The most time-consuming task is the evaluation of the external magnetostatic field term $\mathbf{H}_{ms,ext}$, which is directly computed in the absolute reference frame. For each of the $N \times T$ mesh elements (hexahedra), this consists in summing the dipole contributions from all the mesh elements belonging to the other $(N-1)$ objects. As demonstrated by Fig. 4.5, the computation time of this operation is a quadratic function of N. A similar computation time is obtained with the standard approach (non-approximated calculation of $\mathbf{H}_{ms,ext}$), up to the admissible number of objects ($N = 15$), since the geometric contributions have been already computed and stored in the preliminary part of the

algorithm. With the used hexahedron-dipole approximation, described by Eq. (4.3), we can operate entirely in the GPU with a much larger number of objects (up to 95 with the NVIDIA Quadro K6000), without incurring in the bottleneck of the data transfer bandwidth between CPU and GPU.

A strong reduction in the computational cost of the inter-object magnetostatic interaction can be obtained by approximating the contribution from each object as the stray field of a single dipole, as described by Eq. (4.22). The reason is that in this case for each of the $N \times T$ mesh elements (hexahedra) we have to sum only $(N-1)$ contributes. This effectively improves the scaling, which passes from $\mathcal{O}(N^2T^2)$ to $\mathcal{O}(N^2T)$, but as shown in the previous subsection the introduced approximation is not acceptable in terms of accuracy.

Concerning the computation of the internal magnetostatic field term $\mathbf{H}_{ms,int}$ and of the exchange field $\mathbf{H}_{ex}$, which is performed in the local reference frame, we find a linear scaling with N. The operation of rotation of the fields from the local to the absolute reference frames concurs with a marginal cost.

Finally, we analyze the computation time necessary to calculate the effective field in the absolute reference frame (sum of the different field contributions) and to update the magnetization according to the Cayley transform based scheme. A quadratic dependence on N is found; this time is negligible for low numbers of objects, becoming comparable to the one required for calculating the exchange and the internal magnetostatic fields for $N > 50$.

4.4 Application to 3D distributions of objects

In the following subsections we will illustrate three different applications of the developed 2.5D micromagnetic code. In the first one we compare the accuracy and the computational efficiency of the 2.5D code to the ones of the 3D FFT implementation. To do this task the objects are distributed in the space, but mutually parallel. In this

specific case the 3D micromagnetic code can reconstruct the geometry providing a reliable solution for the comparison with the results of the 2.5D micromagnetic code. In the second subsection we perform a comparative test with the 3D code, showing its drawbacks in a simple case, where two thin films are oriented at 45° in the 3D space. In the third subsection we test the 2.5D micromagnetic code in the evaluation of the hysteresis loops of 3D randomly orientated objects.

4.4.1 Test case with a 3D distribution of thin objects mutually parallel

In this subsection we apply the 2.5D micromagnetic solver to calculate the hysteresis loops of ensembles of magnetic thin objects distributed in a 3D medium, but mutually parallel. The considered objects are circular nanodots made of permalloy, with diameter of 200 nm and thickness of 20 nm. For these samples, it is expected that the magnetization reversal process occurs via the nucleation, transverse motion and expulsion of a vortex [31].

We consider a set of nanodots with the same orientation in the space, assuming that they lie parallel to the xy-plane of the absolute reference frame. In this case, it is possible to compare the solution calculated with the 2.5D solver with the one obtained with the 3D-FFT code, where the magnetostatic field is computed via an FFT approach based on the discrete convolution theorem 1 described in Chapter 3 and the exchange field with a standard finite difference method. The application of the 3D-FFT code, which implements the same time-integration scheme of the 2.5D solver, requires the use of a structured mesh and the discretization of the volume containing all the objects. The 2.5D solver is more flexible, needing as an input the mesh of a single nanodot, which is non-structured to accurately reproduce the dot curved boundaries and thus avoid the introduction of fictitious shape anisotropy effects. The solutions are obtained by setting the damping coefficient α at 0.1, the parameter σ in Eq. (3.5) at 5γ and the time step at

1 ps, according to the analysis reported in Ref. [32].

Figure 4.6a shows the hysteresis loops of a distribution of 30 nanodots with a volume

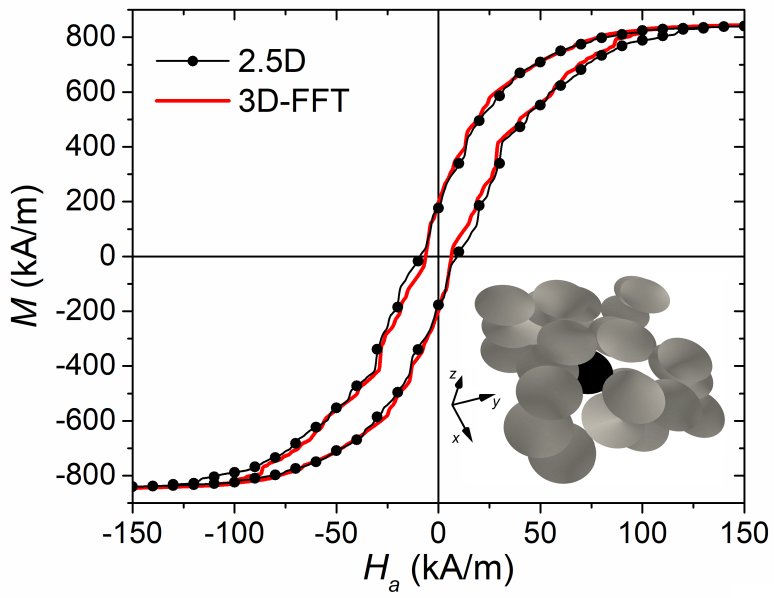

(a)

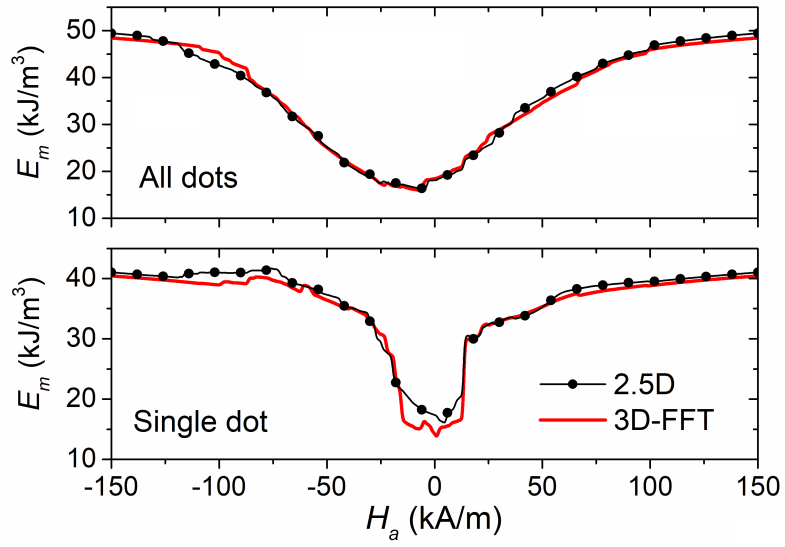

(b)

Figure 4.6: (a) Comparison of the hysteresis loops calculated with the 2.5D and the 3D-FFT solvers, in the case of a distribution of 30 permalloy nanodots lying parallel to the xy-plane of the absolute reference frame (inset). The nanodot diameter is 200 nm and the thickness is 20 nm; the external field is applied along x-axis. (b) Comparison of the magnetostatic energy for the entire set of nanodots (top) and for a single nanodot (bottom), coloured in black in the distribution in the inset of (a).

concentration of 25% (see inset), comparing the results obtained with the 2.5D and the 3D-FFT solvers. The volume concentration is defined as the ratio V_{dots}/V_{system}, where V_{dots} is the volume of a nanodot multiplied by the number of nanodots and V_{system} is the minimum volume of the 3D domain containing all the nanodots. The 2.5D code solution is calculated with a spatial discretization size Δs of 6.25 nm in the film plane, while the 3D-FFT code one is determined on a $800 \times 800 \times 160$ nm^3 volume, by fixing Δs to 6.25 nm along x- and y-axes and to 5 nm along z-axis. Figure 4.6b compares the different solvers in the computation of the specific magnetostatic energy for the entire ensemble of nanodots and for a single nanodot, coloured in black in the distribution in the inset of Fig. 4.6a.

Overall, a good agreement is reached between the results obtained with the 2.5D and the 3D-FFT solvers. The small discrepancies are mainly attributable, for the 2.5D code, to the approximation of the interdot magnetostatic interactions and, for the 3D-FFT code, to the staircase reconstruction of the dot circular edges, responsible for the introduction of pinning sites for the nucleation of vortexes. These lead to a non-synchronous field-evolution of the magnetization inside the dots, as demonstrated by the comparison of the maps in Fig. 4.7, which shows the magnetization configurations at different equilibrium points along the descending branch of the hysteresis loops, for H_a equal to 20 kA/m (4.7a), zero (4.7b) and −50 kA/m (4.7c). At the beginning of the reversal process, the maps calculated with the 2.5D and the 3D-FFT codes are very similar; at remanence, deviations appear for certain dots, due to variations in the computation of the external magnetostatic field term and in the dot mesh. As a consequence, the reversal mechanism of some dots could be different, with possible non-occurrence of vortex state. Anyway, the 2.5D solver is able to predict the global behaviour of the ensemble of nanodots, with a reliable determination of the hysteresis loop and of the energy terms. Finally, its advantages in terms of computational efficiency with respect to the 3D-FFT code become evident for lower concentrations of objects, since in this case the 3D-FFT solver has to manage a larger portion of non-magnetic region. As an example, for an

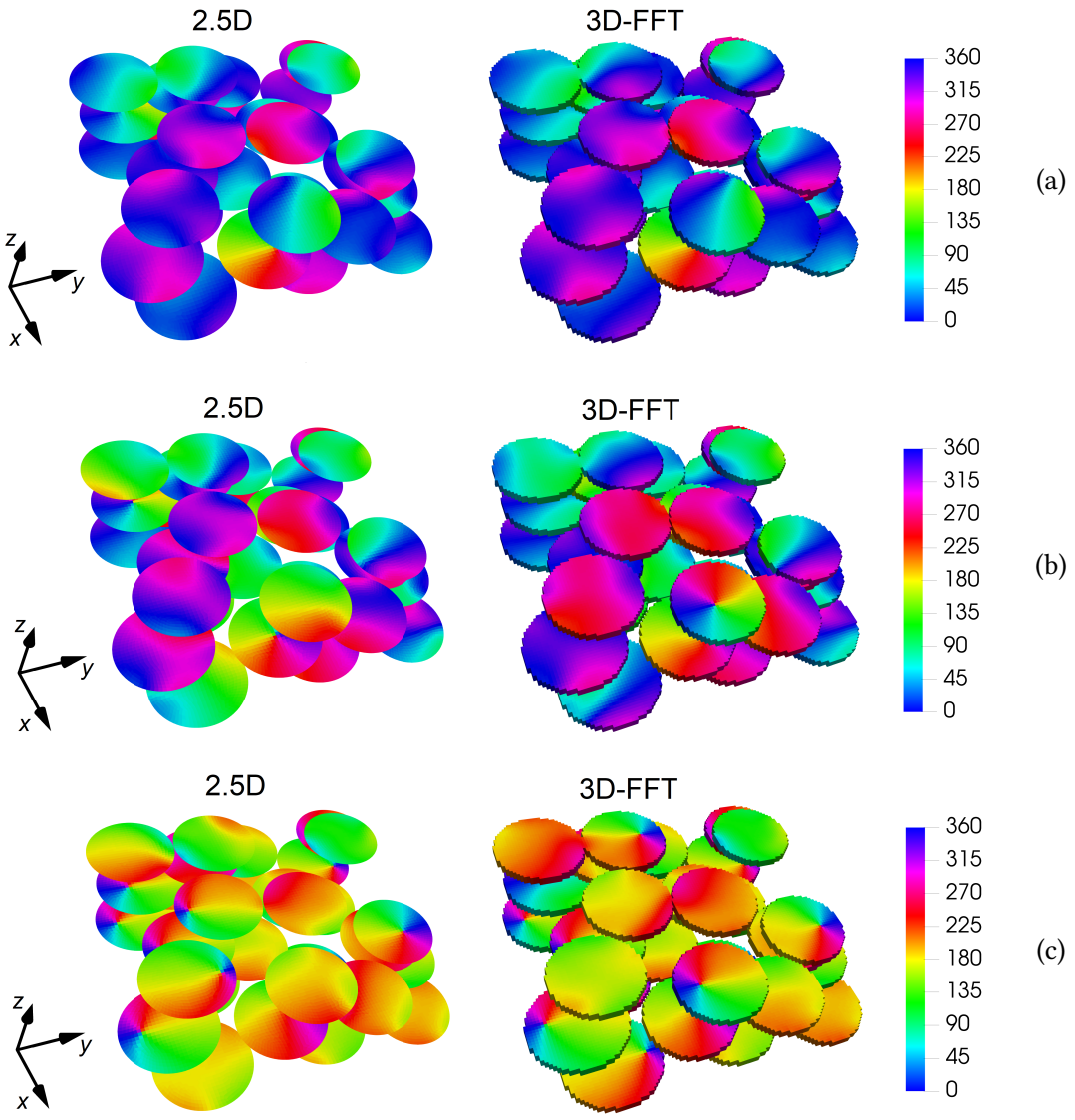

Figure 4.7: Magnetization configurations calculated with the 2.5D (left) and the 3D-FFT (right) solvers at different equilibrium points along the descending branch of the hysteresis loops in Fig. 4.6a. The maps are reported for H_a equal to 20 kA/m (a), zero (b) and −50 kA/m (c), considering an external field applied along x-axis. The colour bar represents the angle, in degrees, between magnetization component in the xy-plane and x-axis.

occupied volume 10 times larger than the previously considered one and for the same number of nanodots ($N = 30$) , the computation time increases of a factor 6 for the 3D-FFT code, remaining unvaried for the 2.5D code. For the small volume ($800 \times 800 \times 160$

nm^3), the computation time of the 2.5D code is 2 times higher than the one of the 3D-FFT code, while for the large volume the computation time of the 2.5D code is a third of the one of 3D-FFT code.

4.4.2 Test case highlighting the drawbacks of 3D-FFT micromagnetic code

In this subsection we will show how strong inaccuracies arise when applying 3D-FFT micromagnetic codes to the solution of even simple problems, where structured meshes do not appropriately reproduce the object shape (e.g. for objects not aligned with mesh grid). As an example, we calculate the hysteresis loop of a thin permalloy square (200 nm size and 15 nm thickness) for two equivalent configurations in terms of object-applied field orientation. The two considered cases are illustrated in the schematic of Fig. 4.8a. Given a common absolute reference frame (x, y, z), in case #1 the film is orientated parallel to the xy-plane and the external field is applied along a direction that forms an angle of 45° with the x-axis. In case #2, the film is inclined of 45° with respect to the xy-plane and the external field is aligned with the x-axis. Figure 4.8b reports the hysteresis loops for the two analyzed cases, calculated with the 2.5D solver as well as with the 3D-FFT code described in Chapter 3 and used in the previous tests. Even if from physical and geometrical point of view the two problems are equivalent, very different results are obtained with the 3D-FFT code when adopting, for both cases, a mesh aligned with the reference frame (x, y, z). The reason is that in case #2 the use of 3D-FFT code forces to reconstruct the object edges and faces with a staircase function, introducing fictitious shape anisotropy effects. As a consequence, for a spatial discretization Δs of 5 nm (see the bottom of Fig. 4.8a), strong discrepancies are found between the solutions of problems #1 and #2 computed with the 3D-FFT code. On the contrary, the two solutions are identical when using the 2.5D solver, since the same discretization mesh is employed, apart from a rotation with respect to the reference frame.

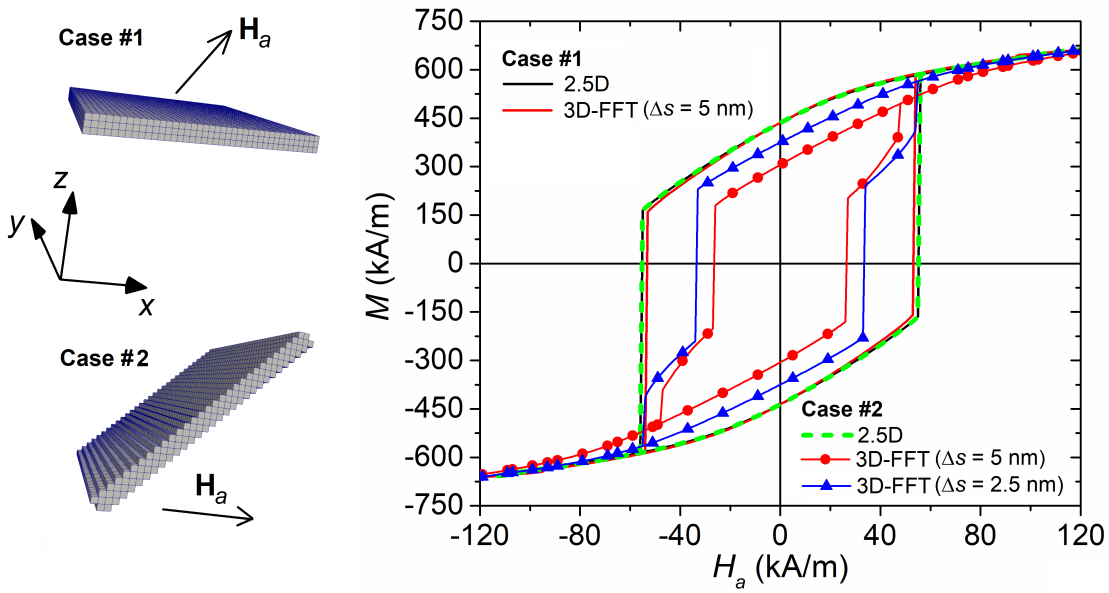

(a) (b)

Figure 4.8: (a) Schematics of the two considered cases with a permalloy thin film (size of 200 nm and thickness of 15 nm) inclined of 45° with respect to the applied field $\mathbf{H}_a$. (b) Hysteresis loops for the two cases calculated with both the 2.5D solver and a 3D-FFT code that uses a structured mesh aligned with the reference frame (x, y, z). The 2.5D code solutions are calculated with a spatial discretization size Δs of 5 nm in the film plane, while the 3D-FFT code ones by fixing Δs to 5 nm (as shown in the schematics) and to 2.5 nm.

As expected, these solutions practically coincide with the one of problem #1 calculated with the 3D-FFT code. Finally, it is interesting to note that with a finer mesh ($\Delta s = 2.5$ nm) the solution of problem #2 calculated with the 3D-FFT code is a bit closer to the other three ones, but strong discrepancy remains. Moreover, the computational cost rises dramatically, due to the increase in the FFT matrix size (including the contributions also from non-magnetic hexahedra) and the simultaneous reduction in the time step that guarantees numerical stability. For a single object, these criticalities can be avoided by generating a mesh aligned with the object itself. However, these strong limitations of 3D-FFT solvers cannot be bypassed when one has to handle multiple objects, like thin films, with different spatial orientations in a 3D medium.

4.4.3 Test case with 3D random distributions of thin objects

In the case analyzed in Subsection 4.4.1, staircase reconstruction is imposed by the 3D-FFT code only to the dot circular edges, while dot faces are flat. Severe criticalities occur for random spatial distributions, where the thin-film objects can have different orientations with respect to the structured mesh axes. As described in the previous subsection for a simple test case, when the objects are not aligned with the mesh grid, fictitious shape anisotropies are introduced due to the staircase reconstruction of faces. This leads to strong inaccuracies, which increase with the misalignment with respect to the mesh and can be reduced only by considering very small spatial discretization sizes. In the following, we demonstrate the capability of the 2.5D code to reliably reproduce the behaviour of random distributions of thin-film objects. To test the accuracy, in Fig. 4.9a we compare the solutions obtained with the solver, as described in Section 4.1, and without introducing approximations in the evaluation of the external magnetostatic field term. The analysis is performed by calculating the hysteresis loop of a distribution of 5 permalloy nanodots (diameter of 200 nm and thickness of 20 nm), differently orientated in the space and with a minimum (maximum) barycentre distance of 120 nm (300 nm). Very small differences are found, demonstrating the high-order approximation introduced by equation Eq. (4.3) and confirming the conclusions of Refs. [28, 29]. To test the efficiency of the 2.5D code, in the same figure we report the hysteresis loop calculated for a random distribution of 45 nanodots, with a volume concentration of 25%. Figure 4.9b reports the map of the relative magnetization configuration at remanence, well illustrating how the magnetostatic interactions and the different orientations with respect to the applied field lead to a non-synchronous evolution of the magnetization in the nanodots.

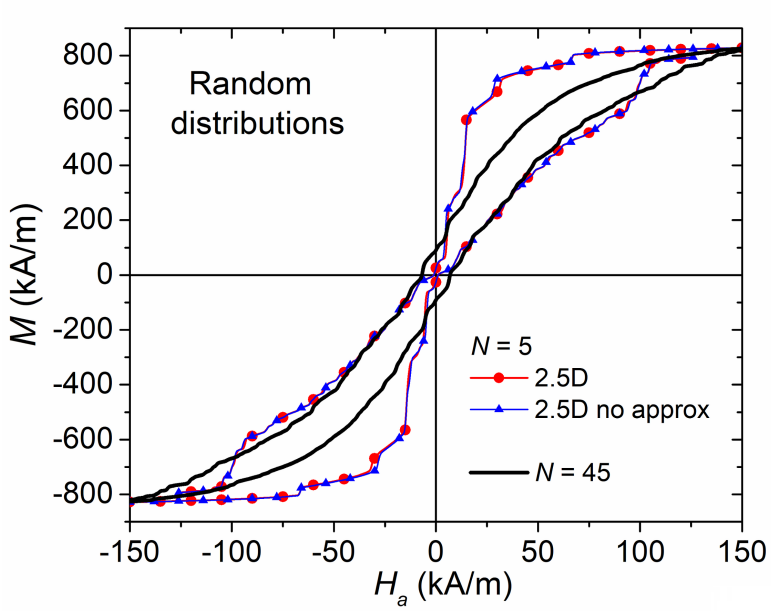

(a)

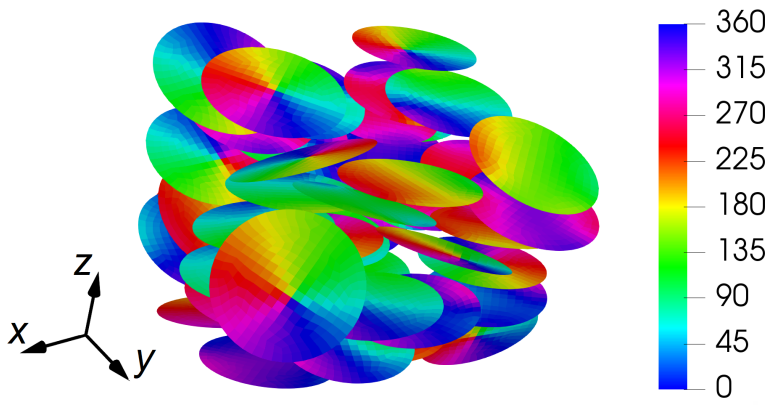

(b)

Figure 4.9: (a) Hysteresis loops calculated with the 2.5D solver for two random distributions of permalloy nanodots, with N equal to 5 and 45. The solution obtained for $N = 5$ is compared to the one where the external magnetostatic field term is not approximated and is determined via Green integration. (b) Magnetization configuration calculated at remanent state for the case with $N = 45$. The colour bar represents the angle, in degrees, between magnetization component in the xy-plane and x-axis (direction of application of the external field).

4.5 Conclusions

We have developed a 2.5D micromagnetic solver that is able to efficiently simulate the magnetization dynamics in 3D distributions of magnetic thin-film objects, randomly arranged in a non-discretized space. Thanks to the integration of a finite difference method for the exchange field calculation on non-structured meshes, objects with complex shape can be easily handled, without the introduction of fictitious shape anisotropy effects. Moreover, the mesh element-dipole approximation introduced in the evaluation of the inter-object magnetostatic interactions permits to efficiently simulate large numbers of objects, with strong reductions in the computation time needed to assemble Green tensor as well as in memory requirements.

The developed 2.5D solver has been successfully applied to calculate the hysteresis loop of a high number of strongly interacting magnetic circular nanodots, with different orientations in the space and with respect to the applied field. The analysis has put in evidence the great advantages of the 2.5D code in comparison to standard 3D-FFT solvers, which are typically used for the simulation of large samples. In this case, the use of non-structured meshes does not allow to accurately treat problems with thin objects having complex shape and not aligned with mesh grid. Moreover, the need to discretize the non-magnetic medium surrounding the objects affects in a strong way the computational efficiency, while with the 2.5D solver the computational cost does not vary with the extension of the volume where the objects are distributed.

As further developments, the 2.5D solver can be generalized to enable the handling of different types of objects, with variable size and shape. In this case, the preliminary block of the algorithm would involve the calculation of more time-invariant matrices for the internal magnetostatic field term and the exchange field, one for each type of object.

References

[1] B. Van de Wiele, F. Olyslager, and L. Dupré. "Application of the fast multipole method for the evaluation of magnetostatic fields in micromagnetic computations". In: *J. Comput. Phys.* 227.23 (2008), pp. 9913–9932. ISSN: 00219991. DOI: 10.1016/j.jcp.2008.08.003.

[2] Y. Takahashi et al. "Micromagnetic simulation by using the fast multipole method specialized for uniform brick elements". In: *J. Appl. Phys.* 105.7 (2009), pp. 1–4. ISSN: 00218979. DOI: 10.1063/1.3068012.

[3] D. M. Apalkov and P. B. Visscher. "Fast multipole method for micromagnetic simulation of periodic systems". In: *IEEE Transactions on Magnetics* 39.6 (Nov. 2003), pp. 3478–3480. ISSN: 0018-9464. DOI: 10.1109/TMAG.2003.819461.

[4] C. Seberino and H. N. Bertram. "Concise, efficient three-dimensional fast multipole method for micromagnetics". In: *IEEE Trans. Magn.* 37.3 (2001), pp. 1078–1086. ISSN: 00189464. DOI: 10.1109/20.920479.

[5] P. Palmesi et al. "Highly parallel demagnetization field calculation using the fast multipole method on tetrahedral meshes with continuous sources". In: *J. Magn. Magn. Mater.* 442 (2017), pp. 409–416. ISSN: 03048853. DOI: 10.1016/j.jmmm.2017.06.128.

[6] A. Manzin and O. Bottauscio. "Multipole expansion technique for the magnetostatic field computation in patterned magnetic films". In: *J. Appl. Phys.* 111.7 (2012). ISSN: 00218979. DOI: 10.1063/1.3677770.

[7] A. Manzin and O. Bottauscio. "A Micromagnetic Solver for Large-Scale Patterned Media Based on Non-Structured Meshing". In: *IEEE Trans. Magn.* 48.11 (Nov. 2012), pp. 2789–2792. ISSN: 0018-9464. DOI: 10.1109/TMAG.2012.2195648.

[8] A. Vansteenkiste et al. "The design and verification of MuMax3". In: *AIP Adv.* 4.10 (2014). ISSN: 21583226. DOI: 10.1063/1.4899186.

[9] L. Exl and T. Schrefl. "Non-uniform FFT for the finite element computation of the micromagnetic scalar potential". In: *J. Comput. Phys.* 270 (2014), pp. 490–505. ISSN: 10902716. DOI: 10.1016/j.jcp.2014.04.013.

[10] H. H. Long et al. "Fast fourier transform on multipoles for rapid calculation of magnetostatic fields". In: *IEEE Trans. Magn.* 42.2 (2006), pp. 295–300. ISSN: 00189464. DOI: 10.1109/TMAG.2005.861505.

[11] Z. J. Liu et al. "A fast Fourier transform on multipole algorithm for micromagnetic modeling of perpendicular recording media". In: *J. Appl. Phys.* 99.8 (2006), pp. 8–11. ISSN: 00218979. DOI: 10.1063/1.2169501.

[12] M. Donahue. "Parallelizing a Micromagnetic Program for Use on Multiprocessor Shared Memory Computers". In: *IEEE Trans. Magn.* 45.10 (Oct. 2009), pp. 3923–3925. ISSN: 0018-9464. DOI: 10.1109/TMAG.2009.2023866.

[13] Shaojing Li, B. Livshitz, and V. Lomakin. "Graphics Processing Unit Accelerated O(N) Micromagnetic Solver". In: *IEEE Trans. Magn.* 46.6 (June 2010), pp. 2373–2375. ISSN: 0018-9464. DOI: 10.1109/TMAG.2010.2043504.

[14] O. Bottauscio and A. Manzin. "Parallelized micromagnetic solver for the efficient simulation of large patterned magnetic nanostructures". In: *J. Appl. Phys.* 115.17 (2014), p. 17D122. DOI: 10.1063/1.4862379.

[15] A. Kakay, E. Westphal, and R. Hertel. "Speedup of FEM Micromagnetic Simulations With Graphical Processing Units". In: *IEEE Trans. Magn.* 46.6 (June 2010), pp. 2303–2306. ISSN: 0018-9464. DOI: 10.1109/TMAG.2010.2048016.

[16] J. Leliaert et al. "Fast micromagnetic simulations on GPU—recent advances made with mumax3". In: *J. Phys. D. Appl. Phys.* 51.12 (Mar. 2018), p. 123002. ISSN: 0022-3727. DOI: 10.1088/1361-6463/aaab1c.

[17] L. Lopez-Diaz et al. "Micromagnetic simulations using Graphics Processing Units". In: *J. Phys. D. Appl. Phys.* 45.32 (Aug. 2012), p. 323001. ISSN: 0022-3727. DOI: 10.1088/0022-3727/45/32/323001.

[18] S. Fu et al. “Finite-Difference Micromagnetic Solvers With the Object-Oriented Micromagnetic Framework on Graphics Processing Units”. In: *IEEE Trans. Magn.* 52.4 (Apr. 2016), pp. 1–9. ISSN: 0018-9464. DOI: 10.1109/TMAG.2015.2503262.

[19] G. Barrera et al. “Magnetization switching in high-density magnetic nanodots by a fine-tune sputtering process on a large-area diblock copolymer mask”. In: *Nanoscale* 9.43 (2017), pp. 16981–16992. ISSN: 2040-3364. DOI: 10.1039/C7NR04295G.

[20] S. Louis et al. “Bias-free spin-wave phase shifter for magnonic logic”. In: *AIP Advances* 6.6 (June 2016), p. 065103. ISSN: 2158-3226. DOI: 10.1063/1.4953395.

[21] A. Manzin et al. “Influence of lattice defects on the ferromagnetic resonance behaviour of 2D magnonic crystals”. In: *Sci. Rep.* 6.1 (Apr. 2016), p. 22004. ISSN: 2045-2322. DOI: 10.1038/srep22004.

[22] Y.-L. Wang et al. “Rewritable artificial magnetic charge ice”. In: *Science* 352.6288 (May 2016), pp. 962–966. ISSN: 0036-8075. DOI: 10.1126/science.aad8037.

[23] Y. Yang et al. “Orientation Mediated Enhancement on Magnetic Hyperthermia of Fe3O4 Nanodisc”. In: *Advanced Functional Materials* 25.5 (2015), pp. 812–820. DOI: 10.1002/adfm.201402764.

[24] K. Simeonidis et al. “In-situ particles reorientation during magnetic hyperthermia application: Shape matters twice”. In: *Sci. Rep.* 6.October (2016), pp. 1–11. ISSN: 20452322. DOI: 10.1038/srep38382.

[25] O. Bottauscio, M. Chiampi, and A. Manzin. “A finite element procedure for dynamic micromagnetic computations”. In: *IEEE Trans. Magn.* 44.11 PART 2 (2008), pp. 3149–3152. ISSN: 00189464. DOI: 10.1109/TMAG.2008.2001666.

[26] O. Bottauscio and A. Manzin. “Spatial Reconstruction of Exchange Field Interactions With a Finite Difference Scheme Based on Unstructured Meshes”. In: *IEEE Trans. Magn.* 48.11 (Sept. 2012), pp. 3250–3253. ISSN: 0018-9464. DOI: 10.1109/TMAG.2012.2197738.

[27] T. Liszka and J. Orkisz. "The finite difference method at arbitrary irregular grids and its application in applied mechanics". In: *Computers & Structures* 11.1-2 (Feb. 1980), pp. 83–95. ISSN: 00457949. DOI: 10.1016/0045-7949(80)90149-2.

[28] J. van Opheusden and E. Reuvekamp. "Computer simulation of a thin magnetic film with vertical anisotropy". In: *J. Magn. Magn. Mater.* 88.1-2 (July 1990), pp. 247–259. ISSN: 03048853. DOI: 10.1016/S0304-8853(97)90034-2.

[29] E. Boerner and H. Bertram. "Dynamics of thermally activated reversal in nonuniformly magnetized single particles". In: *IEEE Trans. Magn.* 33.5 (1997), pp. 3052–3054. ISSN: 00189464. DOI: 10.1109/20.617841.

[30] A. Manzin and O. Bottauscio. "Connections between numerical behavior and physical parameters in the micromagnetic computation of static hysteresis loops". In: *J. Appl. Phys.* 108.9 (2010), p. 093917. DOI: 10.1063/1.3503873.

[31] V. Novosad et al. "Nucleation and annihilation of magnetic vortices in sub-micron permalloy dots". In: *IEEE Trans. Magn.* 37.4 (July 2001), pp. 2088–2090. ISSN: 00189464. DOI: 10.1109/20.951062.

[32] O. Bottauscio and A. Manzin. "Efficiency of the Geometric Integration of Landau–Lifshitz–Gilbert Equation Based on Cayley Transform". In: *IEEE Trans. Magn.* 47.5 (May 2011), pp. 1154–1157. ISSN: 0018-9464. DOI: 10.1109/TMAG.2010.2095831.

Chapter 5

Influence of shape, size and magnetostatic interactions on the hyperthermia properties of permalloy nanostructures

The material presented in this chapter is published in
Scientific Reports 9 (6591):1-12, April 2019

In this chapter we present a parametric analysis of permalloy nanostructures with variable shape (disk, cylinder and sphere) for possible application in magnetic hyperthermia, exploiting hysteresis losses for the heat release. The study is performed by varying the aspect ratio and the size of the nanostructures (up to some hundreds of nanometres), with the aim of finding the optimal conditions that enable the maximization of their specific heating capabilities. At the same time, the parameters are tuned to guarantee negligible magnetic remanence and fulfilment of biophysical limits on the product of frequency and applied field amplitude, to avoid aggregation phenomena and intolerable resistive heating. Hysteresis losses, which are the main heating contribution for the

considered magnetic nanostructures, are calculated by integrating the Landau-Lifshitz-Gilbert (LLG) Eq. (2.81), with the inclusion of thermal noise effects. The attention is first focused on disk-shaped nanostructures. For this shape we present a detailed comparison between micromagnetic simulations and experimental results, obtained on nanodisks still attached on the lithography substrate (2D array form) as well as dispersed in ethanol solution (free-standing). This analysis enables us to investigate the role of magnetostatic interactions between nanodisks (diameters ranging from 270 nm to 680 nm) and to individuate an optimal concentration for the maximization of heating capabilities. Finally, we study the magnetization reversal process and the hysteresis properties of permalloy nanocylinders (diameter between 150 nm and 600 nm, thickness from 30 nm up to 150 nm) and permalloy nanospheres (size between 100 nm and 300 nm), to provide insights on the best combination of geometrical parameters for the design of novel hyperthermia mediators.

The chapter is organized as detailed in the following.

- In the first section we will give a brief description of the production technique of permalloy nanodisks, of the characteristics of the samples we modeled and of the measurements performed on the samples.
- The second section is devoted to a brief discussion on the numerical approaches used to perform the different kind of simulations.
- The third section describes the numerical analysis of the fabricated samples and a comparison to the experimental results.
- In the fourth section we present the parametric study showing the effects of shape and size of nano-structures on the hysteresis losses.

5.1 Experimental methodology

In this section we describe the fabrication process of nanodisks and the adopted measurement technique. The preparation of nanodisks and the measurements were performed at the Istituto Nazionale di Ricerca Metrologica (INRIM), in Torino, by the group leaded by Dr. Paola Tiberto and, in particular, by Dr. Marco Coïsson, Ms Federica Celegato and Dr. Gabriele Barrera.

5.1.1 Sample fabrication and dimensional characterization

Disk-shaped permalloy nanostructures are prepared by means of a bottom-up nanolithography technique based on the self-assembling of polystyrene nanospheres[1, 2].The nanofabrication procedure consists in sputtering a continuous thin film of permalloy on a Si substrate, coated with a layer of optical resist. Successively, a monolayer of polystyrene nanospheres is deposited on the permalloy film and properly reduced in diameter by plasma etching in Ar^+. The polystyrene nanospheres are then used as a hard mask for sputter etching with Ar^+ ions the exposed areas of permalloy. Subsequently, the hard mask is removed by sonication in deionised water, resulting in a 2D array of permalloy nanodisks on the resist layer surface. Finally, the nanodisks are detached from the substrate, by chemically dissolving the underlying resist.

Samples of three sizes were prepared. The sizes depend on the initial diameter of the polystyrene nanospheres used for the lithographic mask (nominal values of 300 nm, 500 nm and 800 nm) and on the duration of plasma etching process. The dimensional characterization is performed in an intermediate stage of the fabrication process, when the nanodisks are still attached on the substrate, forming a 2D array with quasi-hexagonal lattice. The diameter distribution is derived by analysing a set of Scanning Electron Microscopy (SEM) images of different areas of the 2D arrays (top of Fig. 5.1), by means of *ImageJ* software [3]. Image processing enables us to obtain the statistical distributions of the nanodisk diameters (bottom of Fig. 5.1), corresponding to mean diameters

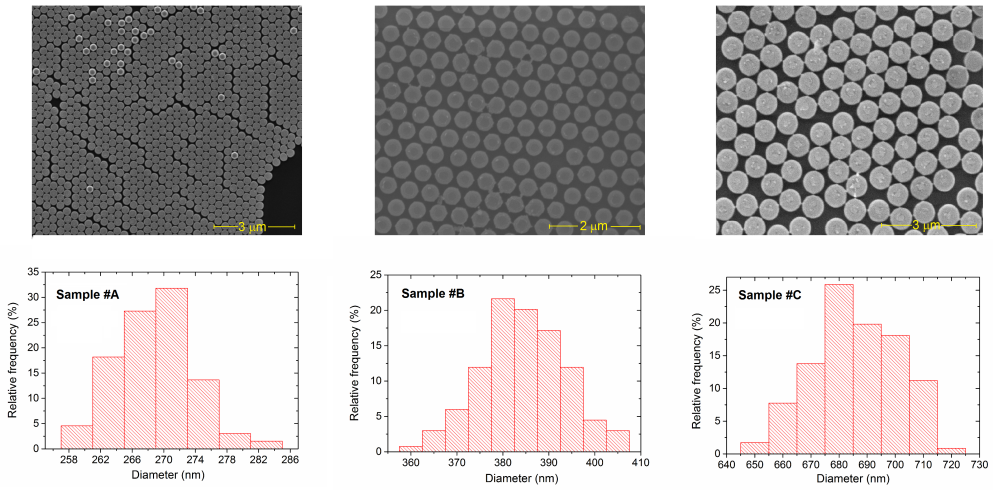

Figure 5.1: Top: Scanning electron microscopy (SEM) images of permalloy nanodisk arrays prepared by self-assembling of polystyrene nanospheres with initial diameter of 300 nm (sample #A), 500 nm (sample #B) and 800 nm (sample #C). Bottom: graphs of the statistical distribution of nanodisk diameters. All samples have an average thickness of 30 nm.

of 270 nm (sample #A), 380 nm (sample #B) and 680 nm (sample #C), and relative standard deviations of 5 nm, 9 nm and 14 nm. Via SEM image analysis we also determine the centre-to-centre distance among disks, which results to be in the order of 300 nm (sample #A), 480 nm (sample #B) and 780 nm (sample #C). For all the samples, the thickness of the nanodisks is 30 ± 1.5 nm, as derived from a priori calibration of the sputter deposition of permalloy film.

5.1.2 Details of hysteresis loop measurements

First, measurement were performed on disk-shaped permalloy nanostructures in the 2D array form, a stage where their spatial distribution can be easily reproduced in the modelling analysis. Static hysteresis loops are obtained in a temperature range from 10 K to 300 K, in order to extrapolate the temperature dependence of saturation magnetization, remanent magnetization and coercive field. This characterization is done by means of an ultra-sensitive alternating-gradient field magnetometer (AGFM) equipped

with a liquid-He continuous flow cryostat.

Second, the room-temperature hysteresis loop of free-standing nanodisks in ethanol suspension is measured by using a Vibrating-Sample Magnetometer (VSM). The ferrofluid is placed within a sample holder suitable for VSM.

Microstructure and, consequently, magnetic properties of the sputtered permalloy films and of the derived nanodisks strongly depend on the deposition conditions (e.g. working gas pressure and substrate temperature) [4]. In particular, high deposition pressures can induce porosity or void structure leading to a variation in the film density, which results lower than the bulk one [5, 6]. As a consequence, also the saturation magnetization of the thin films and of the derived nanodisks is decreased with respect to the nominal bulk value (in the order of 800 kA/m for permalloy) [7]. For this reason, an experimental characterization of the saturation magnetization of a permalloy continuous film is performed. The continuos thin film has a thickness comparable to the one of the layers used for the nanodisk production and it is obtained with the same deposition parameters. The saturation magnetization measured at 300 K results to be ~ 570 kA/m: this value is set as a reference for both hysteresis loop measurements and micromagnetic modelling.

5.2 Micromagnetic modelling methodology

The micromagnetic modelling of permalloy nanostructures is performed by numerically integrating the LLG equation 2.81. For the simulations the damping coefficient is fixed to 0.02, and the magnetocrystalline anistropy is assumed to be negligible for permalloy. Where required, the thermal field $\mathbf{H}_{th}$ is included following the descriptions provided in Section 2.5 and Subsection 3.3.4.

The update of the LLG equation is performed by means of the norm-conserving time integration scheme described in Chapter 3. To speed up the computation, we calculate the effective field terms with different parallelized solvers, depending on the sample spatial

arrangement (2D array form or 3D random distribution) and on the nanostructure type (2D-approximable or 3D).

For the nanodisks arranged in 2D arrays we adopt a GPU parallelized micromagnetic solver, which uses a Fast-Multipole based approach for the computation of the magnetostatic field. This code, developed by Dr. Oriano Bottauscio and Dr. Alessandra Manzin, was proven to be very efficient in the simulation of large-scale films composed of different unit cells [8–11].For the nanodisks randomly distributed we use the 2.5D code described in Chapter 4. For 3D nanostructures, the solutions are calculated via the 3D-FFT micromagnetic code described in Chapter 3.

5.3 Experimental and modelling analysis of nanodisks

We focus here on disk-shaped nanostructures with expected vortex based magnetization switching [12], analysing how hysteresis losses can be tuned by varying nanodisk diameter. Both experimental and modelling results are presented.

5.3.1 Analysis of nanodisks arranged in 2D array form

Figure 5.2a reports a set of static hysteresis loops measured at different temperatures (from 10 K to 300 K) for sample #B in the 2D array form. At very low temperatures, we find high coercive field and remanent magnetization values, rapidly decreasing between 10 K and 20 K. Above 20 K the two quantities keep decreasing, but at a much slower rate. As shown in Fig. 5.2b, also the saturation magnetization M_S reduces with temperature; at 300 K M_S is decreased of about 15% compared to the measurement at 10 K (570 kA/m versus 670 kA/m). The value of M_S at low temperature, which results less than the nominal one, is well justified by the reduction in the sputtered permalloy density (6.19 g/cm^3 versus 8.72 g/cm^3).

After this preliminary experimental study, we compare the static hysteresis loops measured at 300 K to the calculated ones, for all the three samples in the 2D array form

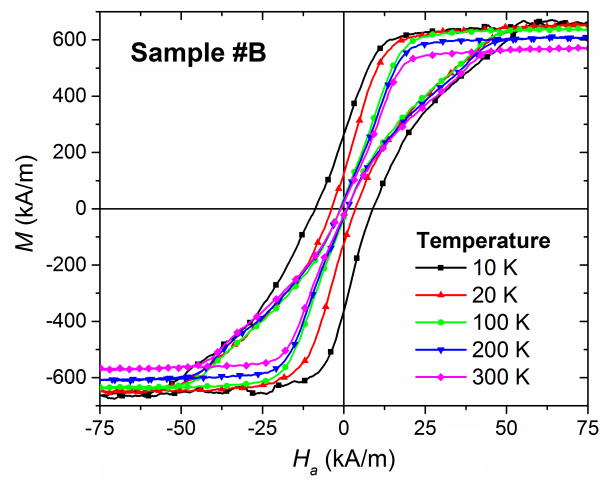

(a)

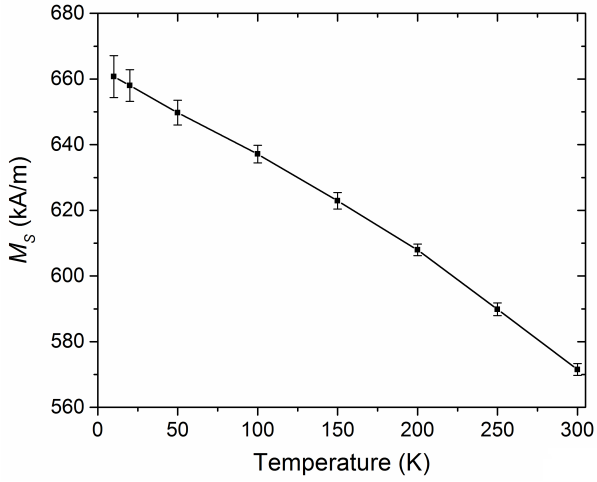

(b)

Figure 5.2: (a) Hysteresis loops of sample #B (mean disk diameter of 380 nm) in 2D array form, measured at different temperatures from 10 K to 300 K, for a field applied in the xy-plane along the x-axis. (b) Saturation magnetization versus temperature for sample #B, from experimental characterization.

(see the top of Fig. 5.3). In the micromagnetic simulations, which include thermal noise effects, the nanodisk arrays are described as ordered patterns with hexagonal packing, considering the disk mean diameter and the mean centre-to-centre distance extracted from SEM images. The numerical results are obtained with the following material properties: saturation magnetization of 570 kA/m (from experimental characterization); exchange constant of 13 pJ/m; zero magnetocrystalline anisotropy.

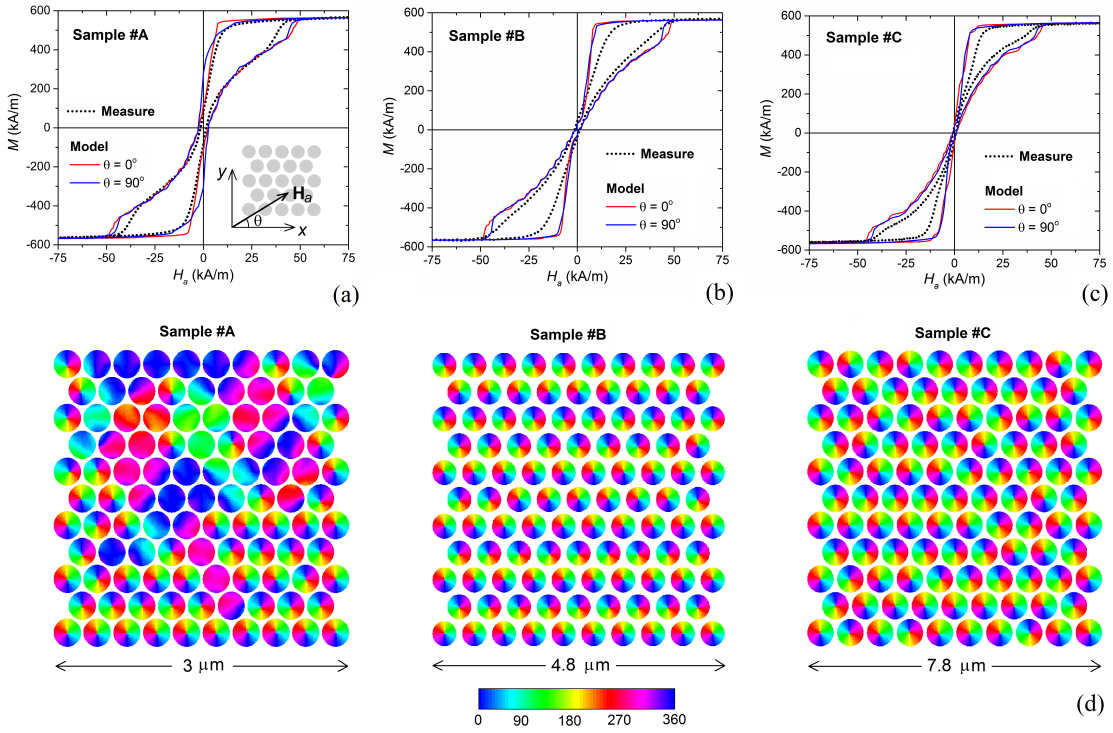

Figure 5.3: Top: Comparison between measured and calculated hysteresis loops of the disk-shaped nanostructures in 2D array form at the temperature of 300 K. Simulation results are obtained by applying the external field both along x axis ($\theta = 0°$) and y-axis ($\theta = 90°$) directions (inset on top-left). Bottom: calculated magnetization configurations at remanence for external field applied along x-axis (the color bar represents the angle, in degrees, between magnetization vector and x-axis). The results are reported in the following order: on the left: sample #A (mean disk diameter $d = 270$ nm); in the center: sample #B ($d = 380$ nm); on the right: sample #C ($d = 680$ nm).

As demonstrated by Fig. 5.3, modelling results are in good agreement with experimental ones for all the considered samples, with a reliable prediction of the magnetization reversal process. Small discrepancies in vortex nucleation and expulsion fields can be explained by moderate patterning imperfections in the fabricated samples, which are characterized by edge roughness and variations in nanodisk diameter and reciprocal distance, as shown by the SEM images in Fig. 5.1. This stochastic distribution of defects can facilitate the transition between states, due to the creation of artificial pinning and depinning sites for vortexes. As a consequence, vortex nucleation and expulsion result

to be anticipated in the measured loops. Moreover, magnetization transitions are more gradual, due to the non-synchronous nucleation and expulsion of vortexes, caused by the random distribution of pinning/depinning sites. Additionally, patterning imperfections lead to an isotropic behavior, strongly mitigating the influence of hexagonal lattice on shape anisotropy.

The role of microstructure lattice can be evinced by modelling results, which are obtained under the assumption of ordered patterns. Modelled sample #A, for which the minimum distance δ between nanodisk boundaries is fixed to 30 nm, shows a weak geometrical six-fold anisotropy with easy and hard axes alternating every 30°, as demonstrated by the comparison of the hysteresis loops calculated along the expected hard and easy axes. These correspond to angular field orientations θ equal to 0° (x-axis) and 90° (y-axis), respectively, and to geometrically equivalent directions, shifted in multiples of 60° (see the inset in Fig. 5.3, top-left). Due to the magnetostatic interactions between nanodisks, we find non-negligible values for the remanent magnetization and the coercive field, higher when $\theta = 90°$. This effect can be seen also in the corresponding measured loop. The collective switching behavior is confirmed by the equilibrium magnetization state calculated at remanence (Fig. 5.3, bottom-left, for $\theta = 0°$). In particular, not all the nanodisks are in the vortex state, due to non-synchronous vortex nucleation, which results to be spread over a large field interval around zero. Moreover, in some nanodisks vortex nucleation is inhibited and magnetization reversal takes place via the formation of C-state, as a consequence of the mutual interaction with neighbouring nanodisks.

Modelled samples #B and #C (δ = 100 nm) have a more isotropic behavior tending towards the one of single disk, with remanent magnetization and coercive field close to zero and limited differences between the two considered field orientations. In particular, the behavior tends towards the one of the single disk, with synchronous magnetization switching. This is illustrated by the equilibrium magnetization states calculated at remanence when $\theta = 0°$, shown in Fig. 5.3 (bottom-centre for sample #B and bottom-right

for sample #C). In particular, at zero field all the nanodisks are in vortex state, with more centred vortex for sample #B, which is characterized by a higher ratio of centre-to-centre distance to diameter (reduced intensity of magnetostatic interactions).
For both measurements and simulations, hysteresis losses reduce with the nanodisk diameter increase. In particular, the measured specific energy losses are about 20 kJ/m^3 for sample #A, 16 kJ/m^3 for sample #B and 10 kJ/m^3 for sample #C. The calculated energy losses are moderately higher, being approximately 27 kJ/m^3 for sample #A, 25 kJ/m^3 for sample #B and 20 kJ/m^3 for sample #C (average of data obtained with $\theta = 0°$ and $\theta = 90°$).

5.3.2 Analysis of free-standing nanodisks

After the analysis of nanodisks in the 2D array form, we investigate the behavior of free-standing nanodisks dispersed in a liquid medium, focusing on sample #C (mean diameter of 680 nm). During the hysteresis loop measurement, the nanodisks do not deposit on the bottom of the sample holder and remain suspended in the solution with a random spatial distribution, thanks to the dynamic nature of the VSM technique. The resulting room-temperature loop, reported in Fig. 5.4a, presents a more gradual reversal than the loop for the corresponding sample in the 2D array form (Fig. 5.3, top-right). In this case, it is not possible to identify vortex nucleation/expulsion transitions, since magnetization switching in the nanodisks is not synchronous (vortex are generated and expelled at different applied fields). This is a consequence of the magnetostatic interactions between nanodisks as well as of the variation in the angular orientation of the nanodisks with respect to the applied field direction. The local misalignment between the nanodisk plane and the field affects the loop shape, since the reduction in the in-plane field component requires the application of fields with larger amplitudes to enable both vortex nucleation and expulsion.
The experimental behavior can be well interpreted by means of micromagnetic simulations. These are performed by randomly distributing the nanodisks in the 3D space with

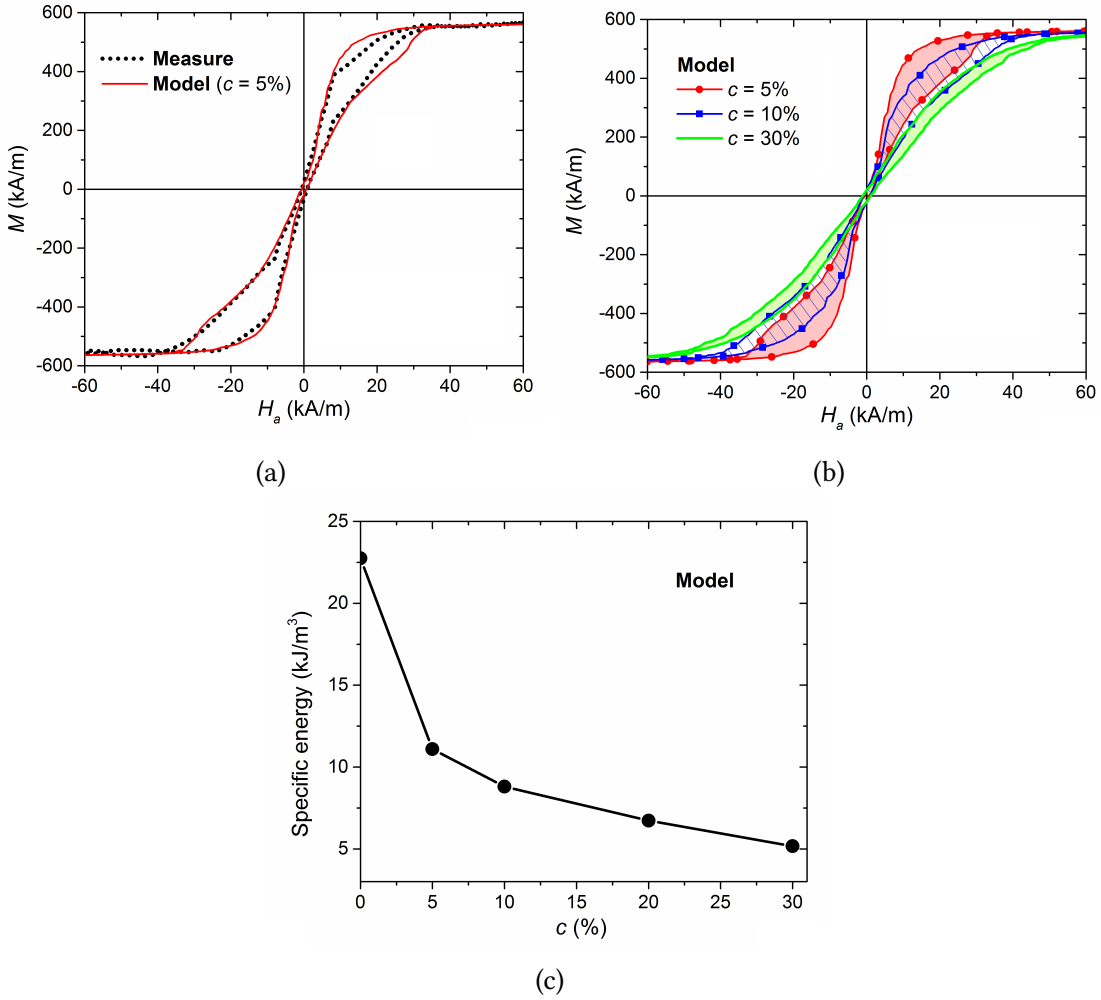

Figure 5.4: (a) Comparison of room-temperature measured hysteresis loop of ∼680 nm diameter nanodisks suspended in ethanol solution with the loop calculated at 300 K for a volume concentration of 5%. (b) Comparison of simulated hysteresis loops for different nanodisk concentrations ranging from 5% to 30%. (c) Specific energy losses calculated as a function of nanodisk concentration. All the numerical results are obtained by fixing the nanodisk diameter to 680 nm.

different volume concentrations (from 5% up to 30%) and setting the temperature at 300 K. Very diluted systems are also simulated, considering a single nanodisk. The volume concentration c is defined as the ratio $V_{\text{nanodisks}}/V_{\text{system}}$, where $V_{\text{nanodisks}}$ is the volume of a nanodisk multiplied by the number of nanodisks and V_{system} is the minimum volume of the 3D domain containing all the nanodisks.

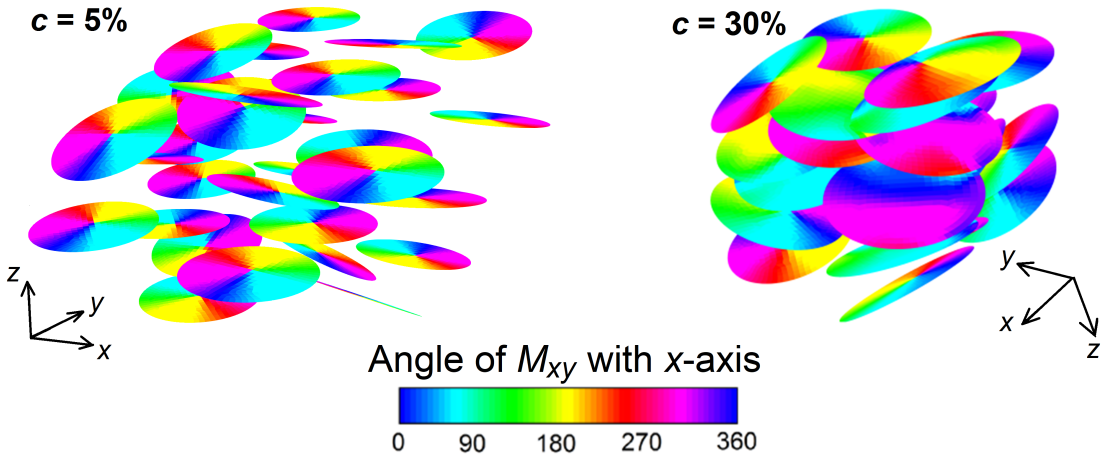

Figure 5.5: Calculated magnetization configurations at remanence for external field applied along x-axis (the colour bar represents the angle, in degrees, between magnetization component in the xy-plane and x-axis). The reported results refer to the case of 680 nm diameter nanodisks randomly distributed in a 3D domain with volume concentrations of 5% (left) and 30% (right). The temperature is set at 300 K.

A good agreement with measurements is obtained when c is around 5%, as demonstrated by the comparison reported in Fig. 5.4a. The measured specific energy losses are about 8 kJ/m^3, while the calculated ones are in the order of 11 kJ/m^3. This energy amount can be obtained by applying a sufficient high field, in the order of 40 kA/m, which guarantees to reach quasi-saturation state. Regarding biophysical constraints [13, 14], the above field amplitude is acceptable if we assume as a limit $H_a \times f \leq 5 \times 10^9$ Am^{-1}s^{-1} and as a maximum frequency 125 kHz. A good metric to evaluate the power generated is the specific loss power (SLP):

$$\mathrm{SLP} = \mu_0 f \rho^{-1} \oint \mathbf{M} \cdot d\mathbf{H} \tag{5.1}$$

where ρ is the density of the material. In this case, a SLP in the order of 150-200 W/g can be obtained. The estimated value is in line with the results in the review article by Angelakeris [15], considering that the reported data were obtained with a product $H_a \times f$ that exceeds more than twice the limit of 5×10^9 Am^{-1}s^{-1}. Very high values, up to $\sim$5 kW/g, were found for iron oxide nanodisks, under the exposure to an external field

with amplitude of 47.8 kA/m and frequency of 488 kHz [16]. However, a non-negligible remanence magnetization value, around 100 kA/m, is observed.

As shown in Fig. 5.4b, the increase in c leads to an enhancement of the magnetostatic interactions, resulting in a wider spread of vortex nucleation/expulsion fields. This causes an increment of the saturation field, thus limiting the maximum acceptable frequency to avoid intolerable resistive heating. Moreover, it has a detrimental effect on the specific energy losses, which reduce from $\sim$23 kJ/m^3 for extremely diluted systems (negligible magnetostatic interactions) up to $\sim$5 kJ/m^3 for concentrations around 30% (Fig. 5.4c). Thus, high volume concentrations lead to a strong reduction in the heating efficiency, with negative repercussions for hyperthermia applications.

The obtained result is in agreement with the conclusions of Haase and Nowak, which investigated the effects of magnetostatic interactions for increasing concentrations of magnetic nanoparticles [17]. Similar findings were reported by Martinez-Boubeta et al. [18], when studying the influence of concentration on the heating properties of iron oxide nanocubes in aqueous solutions. Analogously, Guibert et al. [19] observed that the specific loss power of iron oxide nanoparticles strongly decreases when moving from well-dispersed systems to large and dense aggregates. Moreover, in the study of multi-core iron oxide nanoparticles, Blanco-Andujar et al. [20] found that the core-to-core magnetostatic interaction can adversely affect magnetic heating properties.

The influence of nanodisk concentrations on magnetization reversal processes is finally investigated, by analysing the evolution of magnetization configuration at successive equilibrium points along the descending branch of the hysteresis loops. The obtained results, reported in Fig. 5.6 for volume concentrations of 5% and 30%, demonstrate that the nucleation and expulsion of vortexes are not synchronous, due to both magnetostatic interactions and local misalignment with the applied field. This effect results amplified for the highest concentration, leading to a remanent state where not all the nanodisks are in the vortex configuration, as can be seen in Fig. 5.5.

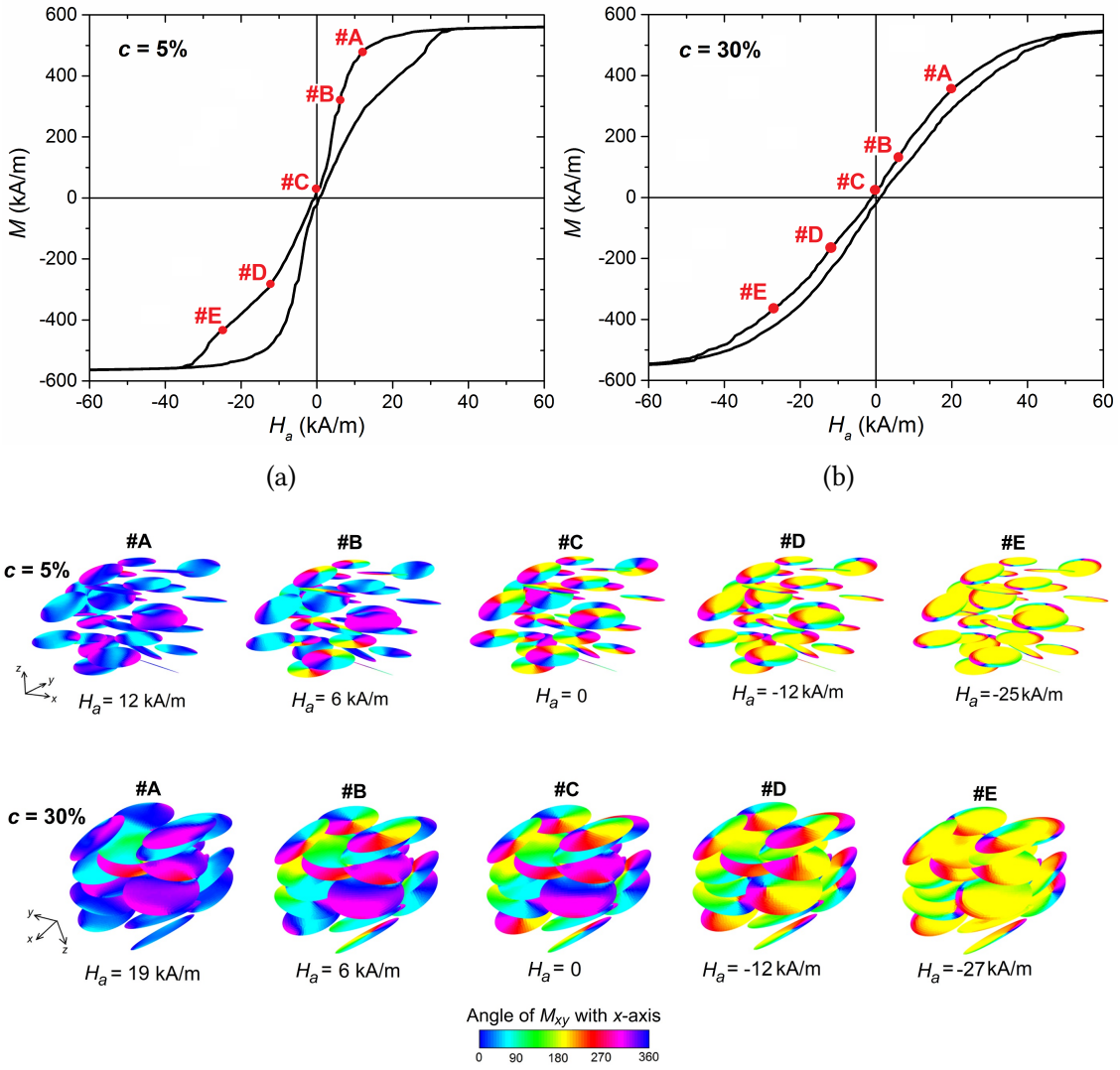

Figure 5.6: Evolution of equilibrium states #A, #B, #C, #D and #E along the descending branch of the hysteresis loops of 680 nm diameter permalloy nanodisks randomly distributed in a 3D domain with two volume concentrations, namely 5% (top) and 30% (down). The hysteresis loops, reported on the top with the indication of the analysed equilibrium states, are calculated by applying the external field along the x-axis and by setting the temperature at 300 K. The colour bar represents the angle, in degrees, between magnetization component in the xy-plane (M_{xy}) and x-axis.

5.4 Parametric analysis of the role of nanostructure size and shape

By means of micromagnetic modelling, we here determine the hysteresis losses of permalloy nanostructures with different shape (disk, cylinder or sphere) and variable size in the sub-micrometer range. The aim is to find optimal geometrical properties for hyperthermia applications, reaching a compromise between the maximization of the produced heat and the fulfilment of biophysical constraint on the applied field. The simulations are performed considering the nominal value of magnetization saturation for permalloy (800 kA/m) [7] and including the effects of thermal noise, fixing the temperature to 300 K.

First, we calculate the hysteresis loops of nanocylinders with diameters d ranging from 150 nm to 600 nm and variable thickness t starting from 30 nm. The field is applied in the plane perpendicular to the nanocylinder axis. For all the considered geometrical parameters, the nucleation of an out-of-plane vortex (with core perpendicular to the applied field axis) is expected [12, 21].

As shown in Fig. 5.7a, which reports the results obtained for $d = 300$ nm, the loop shape is strongly influenced by t. Its increase leads to a rise in out-of-plane vortex nucleation and expulsion fields, as a consequence of the reduction in shape anisotropy, typical of disk geometry [22]. For high values of t, e.g. $t = 150$ nm, the quasi-saturation state with in-plane magnetization is no more energetically favored. In this case, the out-of-plane vortex configuration is stable for a very large field range, leading to a dominant reversible behavior and thus to a small loop area (see Fig. 5.8). The magnetization reversal starts with the formation of a third-order buckle state [12], which evolves into a vortex lying in the plane perpendicular to the applied field and with core moment pointing in the field direction. At the first irreversible jump, occurring at $\sim$110 kA/m, the in-plane vortex transforms into a vortex with out-of-plane core and magnetization rotating in the plane orthogonal to the nanocylinder axis. Along the reversible part of the loop,

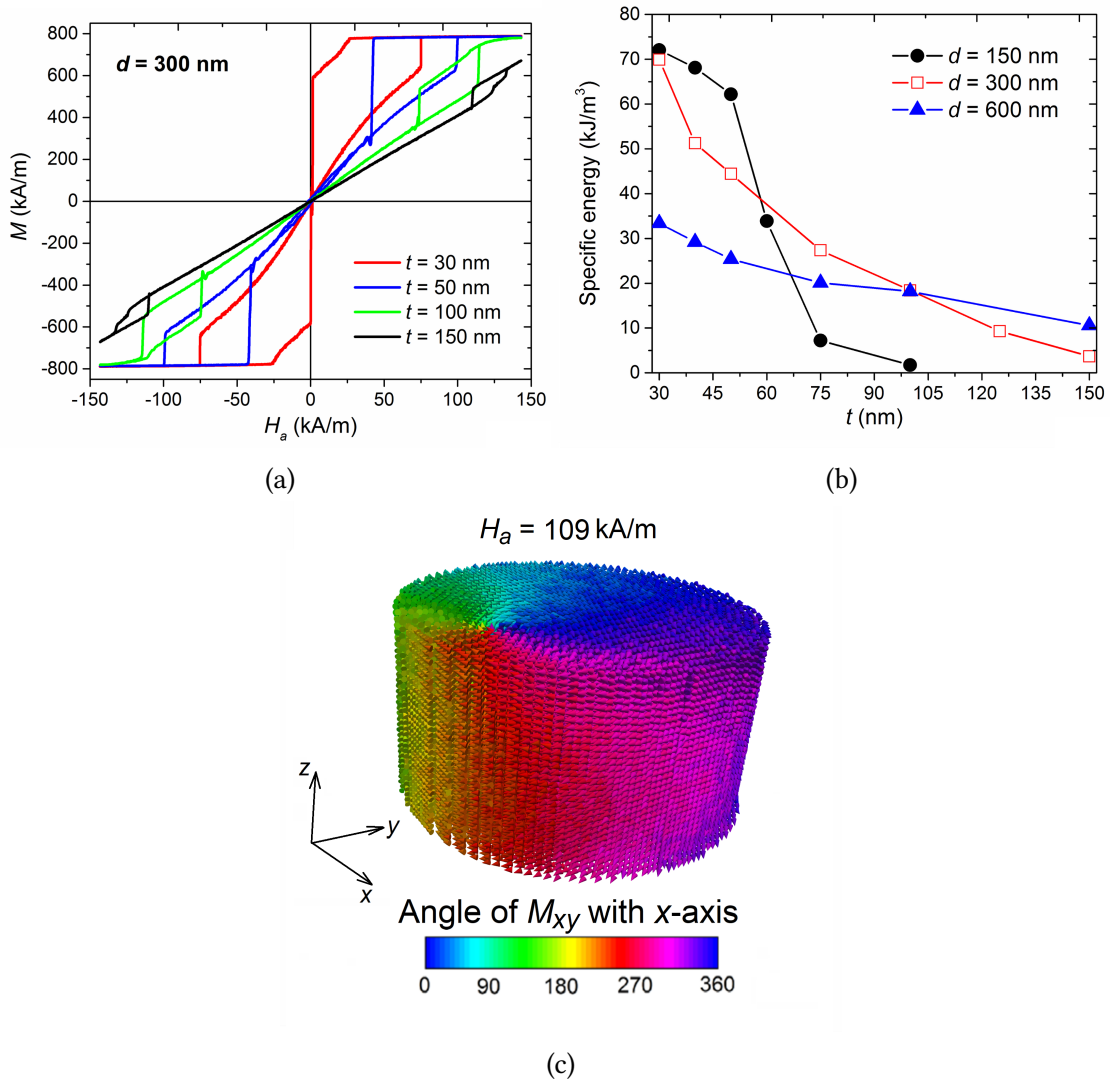

Figure 5.7: (a) Comparison of hysteresis loops calculated as a function of thickness t ranging from 30 nm to 150 nm, for nanocylinders with diameter d equal to 300 nm. The external field is applied orthogonally to the cylinder axis and the temperature is set at 300 K. (b) Specific energy losses calculated as a function of nanocylinder thickness for diameter d equal to 150 nm, 300 nm and 600 nm. (c) Case $d = 300$ nm and $t = 150$ nm: magnetization configuration showing the out-of-plane vortex that forms immediately after the first irreversible jump. The colour bar represents the angle, in degrees, between magnetization component in the xy-plane and x-axis (applied field direction).

this out-of-plane vortex moves orthogonally to the applied field up to the opposite side, where it is expelled around -117 kA/m, evolving again into a third-order buckle state. The final irreversible jump, occurring at about -125 kA/m, corresponds to the shift of

the buckle state towards the direction of the applied field. At remanence, the magnetization rotates symmetrically around the nanocylinder axis, resulting in a negligible moment [23]. The evolution of magnetization configuration at successive equilibrium points along the descending branch of the hysteresis loop is illustrated in Fig. 5.9. Figure 5.7b shows the magnetic state, with out-of-plane vortex, which forms after the first irreversible jump (equilibrium point #B).

When increasing t, we observe a reduction in the hysteresis loop area and a rise in out-of-plane vortex nucleation and expulsion fields also for nanocylinder diameters equal to 150 nm and 600 nm. The calculated loops are reported in Fig. 5.10.

The behavior of specific energy losses as a function of geometrical parameters d and t is depicted in Fig. 5.7c. The graph puts in evidence how the increase in d and t diminishes hyperthermia efficiency; the highest energy value, in the order of 72 kJ/m^3, is obtained for d = 150 nm and t = 30 nm. For the specific case of d = 150 nm, we observe a slight decrease in the hysteresis losses when varying t from 30 nm to 50 nm, followed by an abrupt reduction between 50 nm and 75 nm, due to the weakening of shape anisotropy. Very low hysteresis losses are found for diameters higher than 100 nm, similarly to what happens for d = 300 nm and t = 150 nm.

For the nanocylinders with d equal to 300 nm and 600 nm the specific energy losses decrease more gradually with t, due to the higher aspect ratio d/t. However, for t = 30 nm, the doubling of d from 300 nm to 600 nm causes the halving of the produced heat.

Hysteresis losses can be maximized by applying sufficiently large fields, which enable out-of-plane vortex expulsion and, thus, the reaching of quasi-saturation state. Moreover, loop areas can be amplified by reducing vortex nucleation fields and by increasing vortex expulsion fields as much as possible. At the same time, the nanostructures should be properly designed to avoid too high vortex expulsion fields, whose application at the frequencies typical for hyperthermia could lead to intolerable resistive heating.

To further investigate the suitability of permalloy nanocylinders for magnetic hyper-

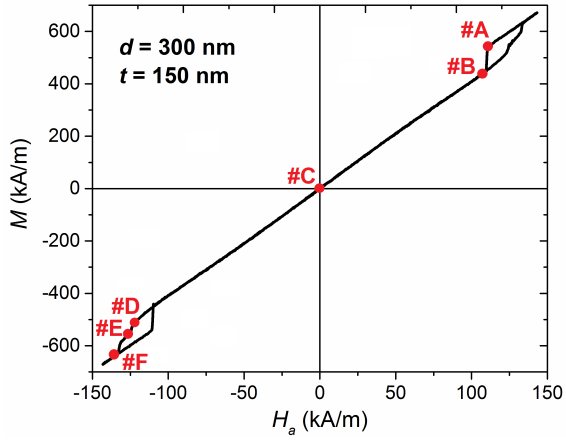

Figure 5.8: Hysteresis loop of a permalloy nanocylinder with a diameter of 300 nm and a thickness of 150 nm. The loop is calculated by applying the external field along the x-axis and by setting the temperature to 300 K

thermia, in Fig. 5.11 we report out-of-plane vortex nucleation and expulsion fields versus thickness for the diameters of 150 nm (Fig. 5.11a), 300 nm (Fig. 5.11b) and 600 nm (Fig. 5.11c). For the 150 nm diameter cylinders with t ranging from 30 nm to 100 nm, the nucleation field rises from ∼20 kA/m up to ∼110 kA/m, rapidly increasing between 50 nm and 75 nm, in correspondence with the abrupt reduction in energy losses (Fig. 5.7c). The out-of-plane vortex expulsion field slightly increases, varying from ∼90 kA/m to ∼120 kA/m. For t in the order of 90-100 nm, the last irreversible jump does not correspond to the expulsion of the out-of-plane vortex, but to the transition to a third-order buckle state, as described for d = 300 nm and t = 150 nm. For the 600 nm diameter cylinders, the out-of-plane vortex expulsion and nucleation fields increase nearly at the same rate and, consequently, hysteresis losses reduce more gradually with t.

When t is in the order of 100 nm, between quasi-saturation and out-of-plane vortex nucleation there is an intermediate state, characterized by a double-vortex configuration, illustrated in Fig. 5.13. Considering the biophysical constraint $H_a \times f \leq 5 \times 10^9$ $\mathrm{Am^{-1}s^{-1}}$, the high expulsion fields reported in Fig. 5.11 strongly impact on the largest acceptable value for f. This should be in the order of 50 KHz, resulting in a maximum allowable field around 100 kA/m. To satisfy the above requirement, we should opt for

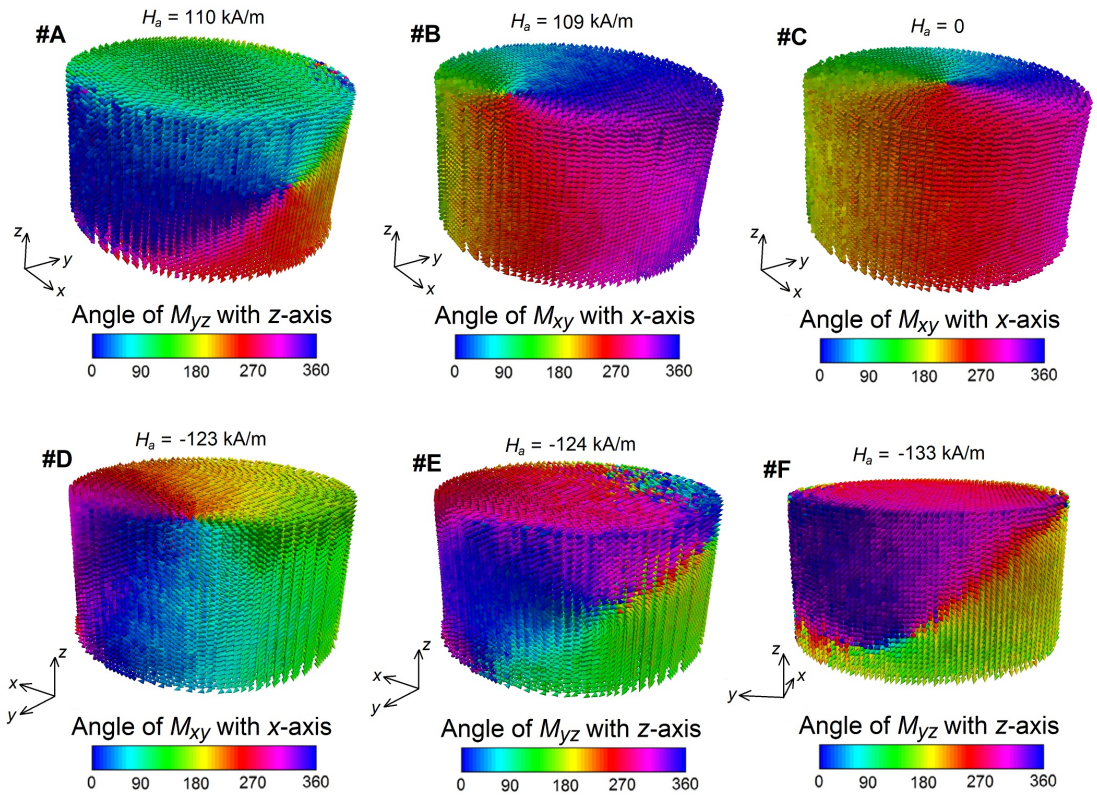

Figure 5.9: Evolution of equilibrium states #A, #B, #C, #D, #E and #F along the descending branch of the hysteresis loop of a permalloy nanocylinder with a diameter of 300 nm and a thickness of 150 nm. The colour bars represent the angle,in degrees, between the indicated in-plane magnetization components and axes. Depending on the equilibrium state, the 3D view is varied to better illustrate the magnetization spatial distribution. The magnetization reversal starts with the formation of a third-order buckle state, which evolves into an in-plane vortex (#A). At the first irreversible jump, the in-plane vortex transforms into a vortex with out-of-plane core (#B). Along the reversible part of the loop, this out-of-plane vortex moves orthogonally to the applied field up to the opposite side (#D), where it is expelled, evolving into a third-order buckle state (#E). The final irreversible jump corresponds to the shift of the buckle state towards the direction of the applied field (#F).

nanocylinders with limited thickness, e.g., when d = 150 nm (300 nm), t should be lower than 40 nm (50 nm). It follows that disk-shaped nanostructures with a diameter of few hundred nanometres (less than 300 nm) could be the optimal solution in terms of both energy release and fulfilment of the applied field constraint. In this case, an SLP value higher than 400 W/g can be obtained. Finally, we investigate the suitability of permalloy nanospheres for hyperthermia applications, focusing on diameters d in the range from

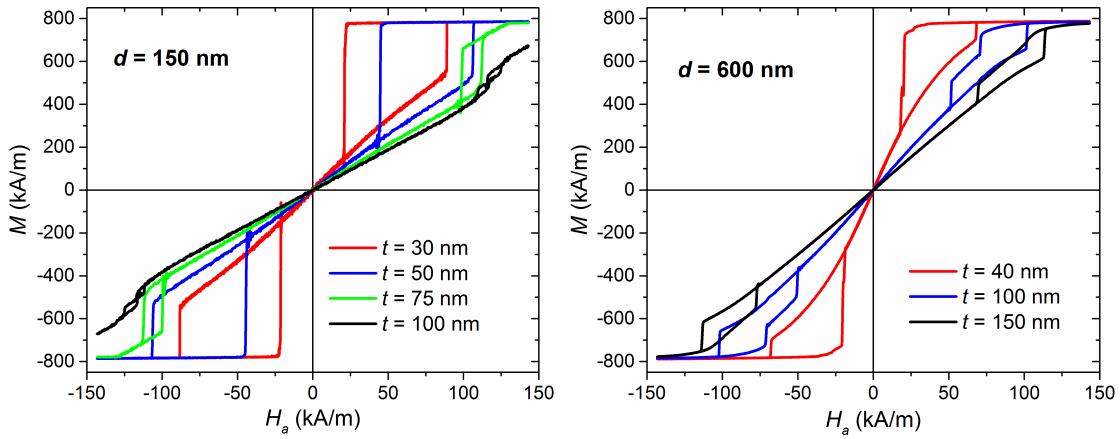

(a) (b)

Figure 5.10: Comparison of hysteresis loops calculated as a function of thickness t for nanocylinders with diameter d equal to 150 nm (a) and 300 nm (b). The simulations are performed by setting the temperature at 300 K.

100 nm to 300 nm (see the hysteresis loops in Fig. 5.12a). For these nanostructures, vortex nucleation and thus saturation condition can be reached at very large fields, higher than 150 kA/m. For lower fields, the reversal mechanism is almost entirely a reversible process. As illustrated for $d = 150$ nm in Fig. 5.14, the magnetization prevalently rotates around the applied field axis, with the exception of the centred vortex core, which results aligned with the external field [24]. Also at remanence (Fig. 5.12b for $d = 150$ nm), the vortex core contributes with a non-negligible magnetic moment, maintaining its orientation up to the irreversible jump. Here, the magnetization in the vortex core switches, following the new direction of the applied field. The field inversion gives rise to a hysteresis loop symmetric around zero, whose size depends on the nanosphere diameter. In particular, remanent magnetization and irreversible jump field reduce by increasing d (Fig. 5.12a). This strongly impacts on the specific energy losses, which diminish from $\sim$65 kJ/m^3 to $\sim$7 kJ/m^3 when reducing the nanosphere diameter from 100 nm to 300 nm.

Moreover, it is interesting to note that the change in the nanosphere size has a weak effect on the diameter of the vortex core (d_{core}), which results to be in the order of 40

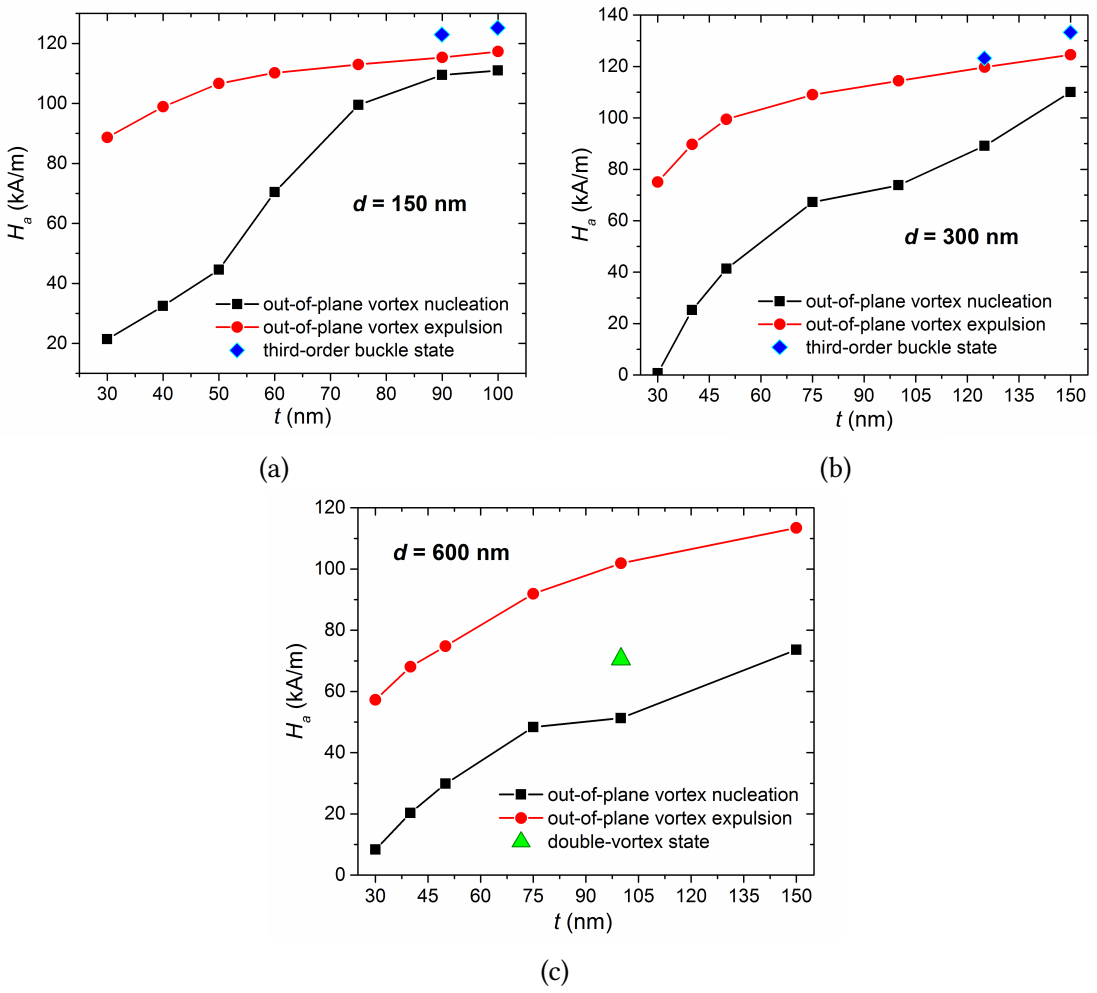

Figure 5.11: Out-of-plane vortex nucleation and expulsion fields versus thickness t, extracted from the hysteresis loops of the nanocylinders with diameter equal to (a) 150 nm, (b) 300 nm and (c) 600 nm, calculated at 300 K. The reported values are obtained by averaging the data obtained along the descending and ascending hysteresis loop branches. In (a) and (b) the blue rhombic markers reported for high values of t correspond to the field of the last irreversible jump, which is not characterised by the out-of-plane vortex expulsion, but to the transition to a third-order buckle state. In (c) the green triangle marker at t = 100 nm corresponds to the field at which the transition to double-vortex configuration takes place.

nm. This explains the decreasing behavior of specific energy losses versus d, which can be interpolated by a function $f(d) = ad_{core}^2/d^2$, where a is a constant parameter. This means that the energy release (in joules) rises linearly with d.

As a negative aspect, non-zero remanent moment can lead to undesirable aggregation

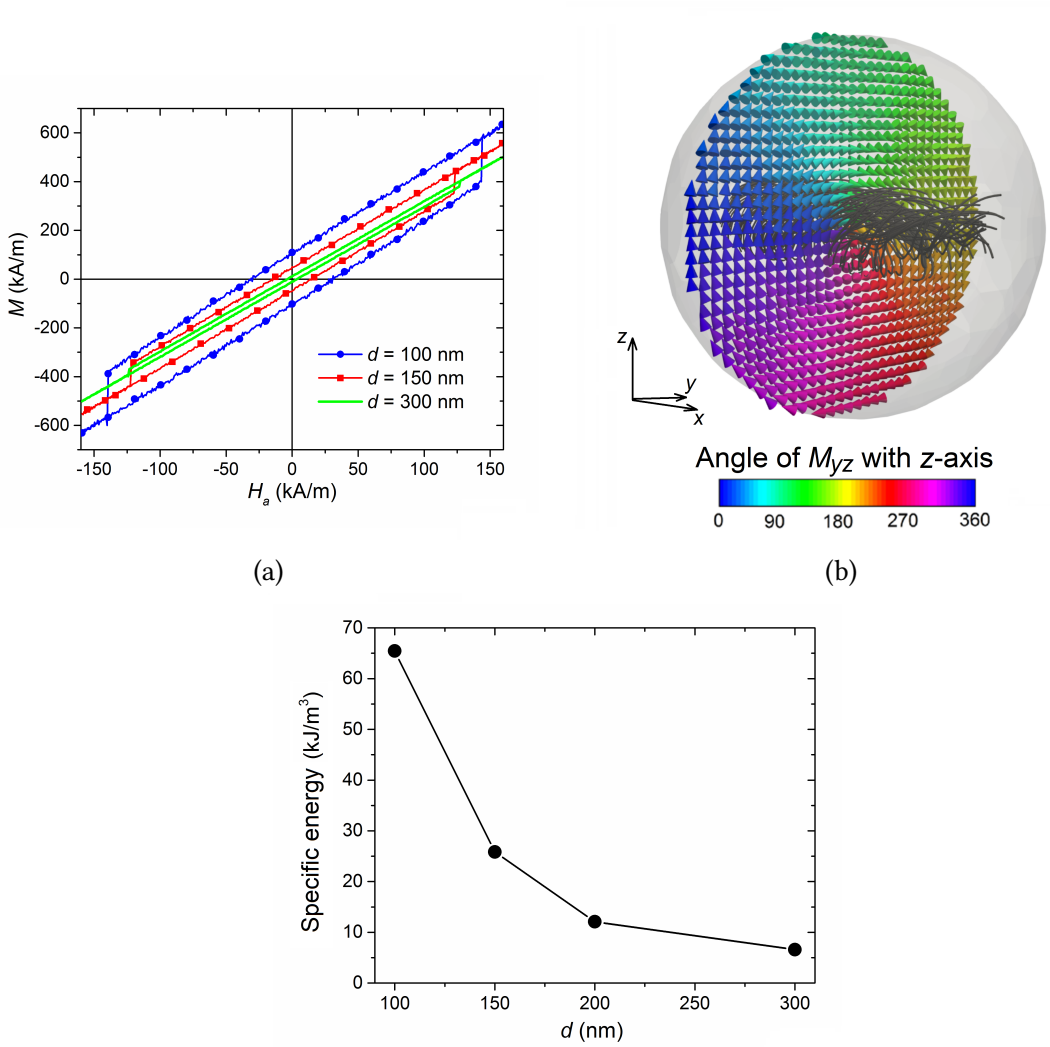

Figure 5.12: (a) Comparison of the calculated hysteresis loops for nanospheres with diameter d ranging from 100 nm to 300 nm. The simulations are performed by fixing the temperature to 300 K. (b) Remanence magnetization configuration for the nanosphere with diameter equal to 150 nm. The external field is applied along x-axis. Magnetization vector distribution is reported for the central yz-plane. The colour bar represents the angle, in degrees, between magnetization component in the yz-plane and z-axis; the streamlines describe the vortex core. (c) Specific energy losses calculated as a function of nanosphere diameter d.

phenomena. Moreover, the use of nanospheres poses criticalities concerning the fulfilment of the biophysical constraint $H_a \times f \leq 5 \times 10^9$ Am^{-1}s^{-1}. Due to the high

irreversible fields, which result to be larger than 100 kA/m, only frequencies with inadequate value for hyperthermia applications could be applied. At the same time, if we reduce H_a below 100 kA/m, the reversal process becomes entirely reversible, without hysteresis effects and, consequently, with no energy release.

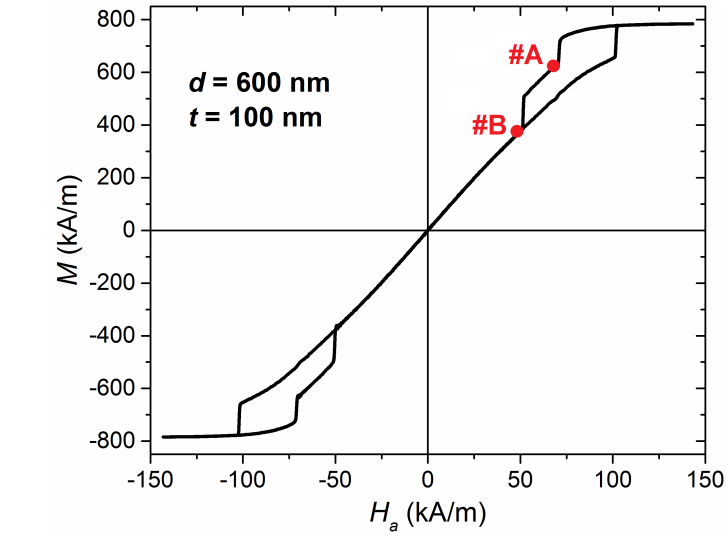

(a)

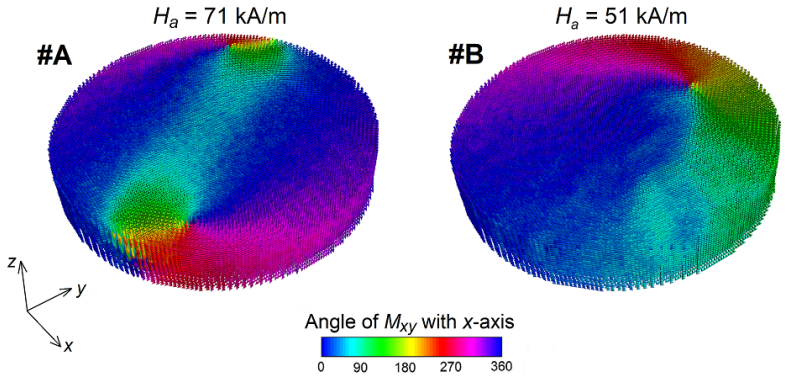

(b)

Figure 5.13: (a) Hysteresys loop of a permalloy nanocylinder with diamenter of 600 nm and thickness of 100 nm, calculated by setting the temperature to 300 K. (b)Magnetization configurations at the equilibrium states immediately after the first irreversible jump (left) and the second one (right) for the considered permalloy nanocylinder. The colour bar represents the angle, in degrees, between magnetization component in the xy-plane (M_{xy}) and x-axis.

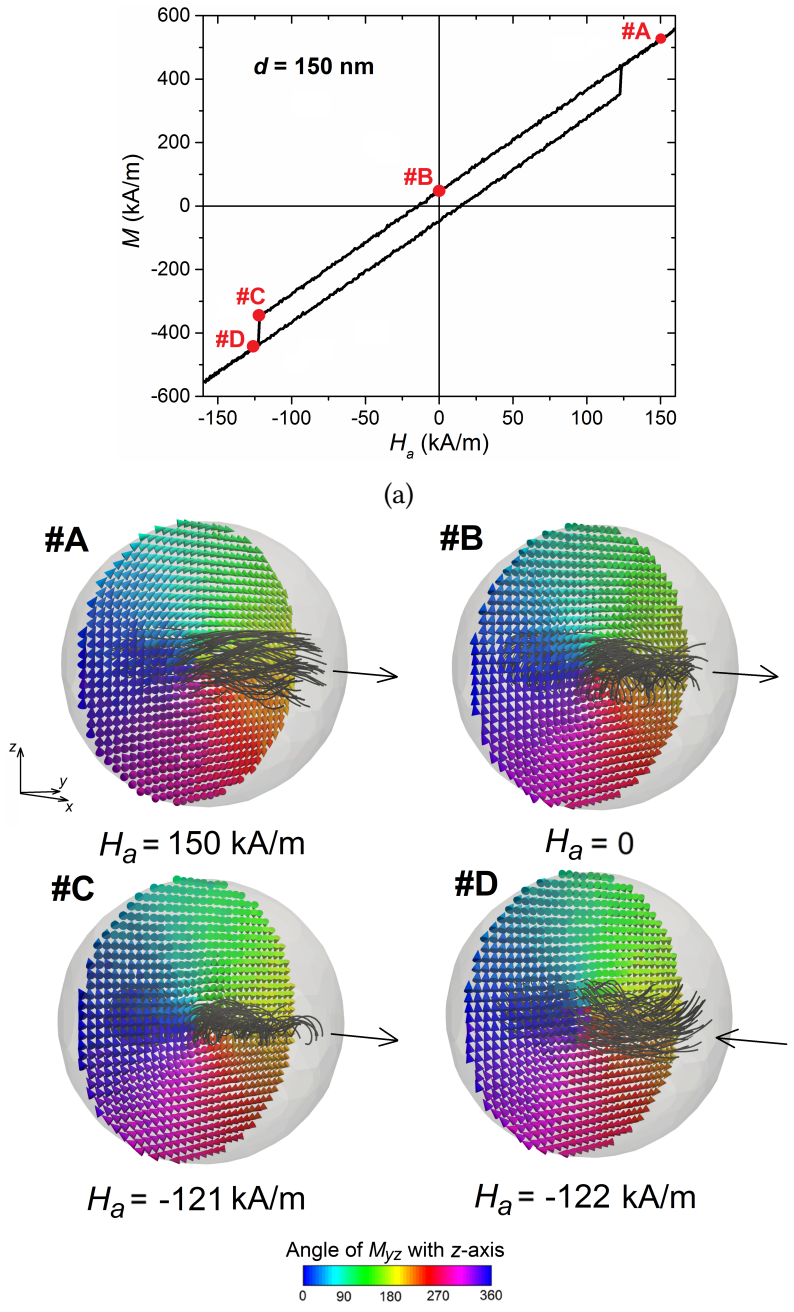

Figure 5.14: (a) Minor hysteresis loop of a permalloy nanosphere with diameter equal to 150 nm. The hysteresis loop is calculated by applying the external field along the x-axis and by setting the temperature at 300 K. (b) Evolution of equilibrium states #A, #B, #C and #D along the descending branch of the hysteresis loop of the considered nanosphere. Magnetization vector distribution is reported for the central yz-plane. The colour bar represents the angle, in degrees, between magnetization component in the yz-plane (M_{yz}) and z-axis. The streamlines represent the vortex core, whose magnetization orientation is described by the arrow. The magnetic configurations on the bottom refer to the equilibrium states before (left) and after (right) the irreversible jump, which leads to the inversion of the vortex core magnetization.

5.5 Conclusions

One of the issues of magnetic hyperthermia is the large quantity of magnetic nanomaterials required to release sufficient heat to the treated area and then generate an appreciable increment of temperature. Disk-shaped nanostructures can be a valid alternative to SPIONs, due the possibility of producing energy via hysteresis losses. However, their synthesis via nanolithography processes can be a very time-consuming and costly task, which needs to be addressed by proper design and optimization stages.

The study here reported, focused on permalloy nanostructures, has demonstrated how micromagnetic simulations can be an efficient way to support fabrication steps in the engineering of optimized heating agents. First, micromagnetic modelling has enabled us to perform an extensive parametric investigation of the influence of nanostructure geometrical properties on the amount of heat generated via hysteresis losses. Second, it has provided useful information on the type of magnetization configuration at remanence and on its implications in particle aggregation phenomena. Third, it has allowed us to explore magnetization reversal processes and to determine saturation fields, which are required to obtain major hysteresis loops and thus maximize hysteresis losses. Regarding this last aspect, caution has been paid to not exceed acceptable biophysical limits for the maximum applicable field at a given frequency, focusing on the well-known constraint $H_a f \leq 5 \times 10^9$ $\mathrm{Am^{-1}s^{-1}}$.

With the aim of reaching a compromise between heat maximization and biophysical limit fulfilment, we have investigated permalloy nanostructures with different shapes (disk, cylinder and sphere) and dimensions, ranging up to some hundreds of nanometres. For all the analyzed nanostructures, the magnetization reversal takes place via the nucleation, motion and expulsion of a vortex.

Regarding disk-/cylinder-shaped nanostructures, we have observed that the optimal heating performances can be obtained with limited diameters and thicknesses, lower than 300 nm and 50 nm, respectively. Specific energy losses higher than 70 $\mathrm{kJ/m^3}$ have

been predicted for nanodisks with a diameter of 150 nm and a thickness of 30 nm. This data corresponds to an SLP value of ∼400 W/g, obtainable under the exposure to an external field with a frequency of 50 kHz and an amplitude of 100 kA/m.

The increase in diameter and thickness leads to a reduction in the specific energy losses. Moreover, for thicknesses in the order of 100-150 nm, we have observed a strong increment of the vortex nucleation and expulsion fields, with a negative impact on the fulfilment of biophysical limits with adequate frequencies for hyperthermia applications. At remanence, all the analyzed disk-/cylinder-shaped nanostructures are characterized by an out-of-plane vortex state with negligible magnetic moment and thus reduced possibility of aggregation. Concerning nanospheres, we have predicted high specific energy losses (∼65 kJ/m^3) for diameters in the order of 100 nm, but in this case it is required to apply fields larger than 130 kA/m and a non-negligible magnetic moment is observed. Moreover, the increase in nanosphere diameter leads to a strong reduction in the hysteresis losses, with very low contribution for sizes higher than 300 nm.

Finally, by means of a combined modelling and experimental analysis we have studied how magnetostatic interactions influence hysteresis losses, focusing on 30 nm thick nanodisks with diameters between 270 nm and 680 nm. For the nanodisks dispersed in ethanol solution, we have found that the nucleation and expulsion of vortexes are not synchronous, also due to the local misalignment with the applied field direction. Moreover, we have observed that the increment of volume concentration can be detrimental for specific energy losses, which halve when increasing the nanodisk concentration from 5% to 30%.

References

[1] P. Tiberto et al. “Ni80Fe20 nanodisks by nanosphere lithography for biomedical applications”. In: *J. Appl. Phys.* 117.17 (2015). ISSN: 10897550. DOI: 10.1063/1.4913278.

[2] G. Barrera et al. “Surface modification and cellular uptake evaluation of Au-coated Ni80Fe20nanodiscs for biomedical applications”. In: *Interface Focus* 6.6 (2016). ISSN: 20428901. DOI: 10.1098/rsfs.2016.0052.

[3] C. A. Schneider, W. S. Rasband, and K. W. Eliceiri. “NIH Image to ImageJ: 25 years of Image Analysis HHS Public Access”. In: *Nat. Methods* 9.7 (2012), pp. 671–675. ISSN: 1548-7105. DOI: 10.1038/nmeth.2089.

[4] J. A. Thornton. “The microstructure of sputter-deposit coating.” In: *J. Vac. Sci. Technol. A* 11.4 (1986), pp. 3059–3065.

[5] J. H. Thomas. “Effect of pressure on dc planar magnetron sputtering of platinum”. In: *J. Vac. Sci. Technol. A* 21.3 (2003), pp. 572–576. ISSN: 0734-2101. DOI: 10.1116/1.1564027.

[6] K. Robbie et al. “Fabrication of thin films with highly porous microstructures”. In: *J. Vac. Sci. Technol. A* 13.3 (1995), pp. 1032–1035. ISSN: 0734-2101. DOI: 10.1116/1.579579.

[7] R. A. McCurrie. *Structure and Properties of Ferromagnetic Materials*. Academic Press, London, 1994, p. 300. ISBN: 9780124824959.

[8] A. Manzin and O. Bottauscio. “A Micromagnetic Solver for Large-Scale Patterned Media Based on Non-Structured Meshing”. In: *IEEE Trans. Magn.* 48.11 (Nov. 2012), pp. 2789–2792. ISSN: 0018-9464. DOI: 10.1109/TMAG.2012.2195648.

[9] O. Bottauscio and A. Manzin. “Efficiency of the Geometric Integration of Landau–Lifshitz–Gilbert Equation Based on Cayley Transform”. In: *IEEE Trans. Magn.* 47.5 (May 2011), pp. 1154–1157. ISSN: 0018-9464. DOI: 10.1109/TMAG.2010.2095831.

[10] O. Bottauscio and A. Manzin. “Parallelized micromagnetic solver for the efficient simulation of large patterned magnetic nanostructures”. In: *J. Appl. Phys.* 115.17 (2014), p. 17D122. DOI: 10.1063/1.4862379.

[11] A. Manzin and O. Bottauscio. "Multipole expansion technique for the magnetostatic field computation in patterned magnetic films". In: *J. Appl. Phys.* 111.7 (2012). ISSN: 00218979. DOI: 10.1063/1.3677770.

[12] J. Ha, R. Hertel, and J. Kirschner. "Micromagnetic study of magnetic configurations in submicron permalloy disks". In: *Phys. Rev. B* 67.22 (2003), p. 224432. ISSN: 0163-1829. DOI: 10.1103/PhysRevB.67.224432.

[13] W. J. Atkinson, I. A. Brezovich, and D. P. Chakraborty. "Usable Frequencies in Hyperthermia with Thermal Seeds". In: *IEEE Trans. Biomed. Eng.* BME-31.1 (1984), pp. 70–75. ISSN: 15582531. DOI: 10.1109/TBME.1984.325372.

[14] R. Hergt and S. Dutz. "Magnetic particle hyperthermia-biophysical limitations of a visionary tumour therapy". In: *J. Magn. Magn. Mater.* 311.1 SPEC. ISS. (2007), pp. 187–192. ISSN: 03048853. DOI: 10.1016/j.jmmm.2006.10.1156.

[15] M. Angelakeris. "Magnetic nanoparticles: A multifunctional vehicle for modern theranostics". In: *Biochim. Biophys. Acta - Gen. Subj.* 1861.6 (2017), pp. 1642–1651. ISSN: 18728006. DOI: 10.1016/j.bbagen.2017.02.022.

[16] X. L. Liu et al. "Magnetic Vortex Nanorings: A New Class of Hyperthermia Agent for Highly Efficient in Vivo Regression of Tumors". In: *Adv. Mater.* 27.11 (2015), pp. 1939–1944. ISSN: 15214095. DOI: 10.1002/adma.201405036.

[17] C. Haase and U. Nowak. "Role of dipole-dipole interactions for hyperthermia heating of magnetic nanoparticle ensembles". In: *Phys. Rev. B - Condens. Matter Mater. Phys.* 85.4 (2012), pp. 2–6. ISSN: 10980121. DOI: 10.1103/PhysRevB.85.045435.

[18] C. Martinez-Boubeta et al. "Learning from nature to improve the heat generation of iron-oxide nanoparticles for magnetic hyperthermia applications". In: *Sci. Rep.* 3.May 2014 (2013). ISSN: 20452322. DOI: 10.1038/srep01652.

[19] C. Guibert et al. “Magnetic fluid hyperthermia probed by both calorimetric and dynamic hysteresis measurements”. In: *J. Magn. Magn. Mater.* 421 (2017), pp. 384–392. ISSN: 03048853. DOI: 10.1016/j.jmmm.2016.08.015.

[20] C. Blanco-Andujar et al. “High performance multi-core iron oxide nanoparticles for magnetic hyperthermia: Microwave synthesis, and the role of core-to-core interactions”. In: *Nanoscale* 7.5 (2015), pp. 1768–1775. ISSN: 20403372. DOI: 10.1039/c4nr06239f.

[21] M. Goiriena-Goikoetxea et al. “Magnetization reversal in circular vortex dots of small radius”. In: *Nanoscale* 9.31 (2017), pp. 11269–11278. ISSN: 20403372. DOI: 10.1039/c7nr02389h.

[22] X. Zhou et al. “Axially and radially quantized spin waves in thick permalloy nanodots”. In: *Phys. Rev. B - Condens. Matter Mater. Phys.* 92.5 (2015), pp. 1–5. ISSN: 1550235X. DOI: 10.1103/PhysRevB.92.054401.

[23] K. Y. Guslienko et al. “Giant moving vortex mass in thick magnetic nanodots”. In: *Sci. Rep.* 5 (2015), pp. 1–8. ISSN: 20452322. DOI: 10.1038/srep13881.

[24] R. P. Boardman et al. “Micromagnetic simulation studies of ferromagnetic part spheres”. In: *J. Appl. Phys.* 97.10 (2005), pp. 3–6. ISSN: 00218979. DOI: 10.1063/1.1850073.

Chapter 6

A detailed parametric analysis of permalloy nanodisks

In the last decade, magnetic nanostructures and in particular magnetic nanodisks and nanorings obtained a lot of interest in cancer treatment, for both hyperthermia based therapies and induced cell apoptosis with the mechanical stimulation of cell membranes [1–3].

From the analysis shown in Chapter 5, permalloy nanodisks emerged as a very promising candidate candidate for magnetically mediated hyperthermia, to be used in alternative to standard iron oxide nanoparticles. In fact, they present optimal properties for this application, for instance:

- they can have a large hysteresis loop for opportune values of thickness and diameter, and thus release a large amount of heat due to hysteresis losses;
- at remanence, they present a magnetization vortex configuration, which enables to limit the stray field and the mutual magnetostatic interactions, thus preventing the aggregation and creation of clusters of nanodisks;
- for opportune values of diameter and thickness, they require relatively small field amplitudes to generate consistent hysteresis losses.

In this chapter, micromagnetic modeling is applied to find the optimal combination of geometrical parameters for hyperthermia application, when using permalloy nanodisks. In particular, we perform a detailed parametric analysis by varying disk diameter (100-800 nm) and thickness (15-30 nm), to find the optimal conditions for the maximization of the specific heating capabilities.

Before that, we evaluate the mechanical behavior of the nanodisks in a physiological medium with the physical properties of blood . This aspect is very important to correctly estimate the heating capability of nanostructures. On the one hand, we want to evaluate possible mechanical contribution to the heat generation, due to possible friction effects. On the other hand, since the characteristic hysteresis loop of a nanodisk greatly depends on its shape anisotropy, it depends also on the relative orientation between the disk plane and the applied field [4, 5]. Therefore, we verified the ability of nanodisks to reorient along the direction of the applied magnetic field, depending on the viscosity and density of the medium where they are distributed.

Many different factors can affect the hysteresis losses and change the heating efficiency of nanodisks, hence, a simple investigation of the geometrical parameters is not sufficient. Since the goal is to understand how this kind of nanostructures will actually behave when used for hyperthermia treatment, one should consider also other effects, such as the influence of the environment temperature and the magnetostatic interactions. Regarding this last effect, the analysis of the individual behavior of nanodisks is not sufficient, therefore we have to study their collective performance as ensembles of nanodisks, evaluating the influence of nanodisks concentration on the produced heat.

Another possible contribution to the heat generation of ferromagnetic nanostructures excited by an alternating magnetic field may come from eddy currents. Hence, we analyzed the induction of eddy currents in nanodisks, considering an external field with frequency in the order of 100 kHz.

Eddy currents can also be generated by the applied field directly into the tissues. It is very important to prevent the non-selective heating of both cancerous and healthy

tissue due to these induced currents. To begin with, one can consider that, for a cylindrical tissue sample, the heating power produced per unit volume by eddy currents can be expressed as

$$P = \sigma_{tissue}(\pi\mu_0)^2(H_a f)^2 r^2 \tag{6.1}$$

where σ_{tissue} is the electrical conductivity of the tissue, H_a is the field amplitude, f is the field frequency, and r is the radial distance from the cylinder axis [6]. In 1984, the upper value of 4.85×10^8 $\mathrm{Am^{-1}s^{-1}}$ was assumed as the acceptable threshold for the field-frequency product $H_a \times f$ to avoid intolerable resistive heating. This is known as the Atkinson-Brezovich limit and was determined by exposing for more than an hour the thorax of a number of volunteers to a RF magnetic field (f = 13.56 MHz) generated by a single-turn induction coil [6]. For a smaller size of the exposed body region and considering the variation of σ_{tissue} with frequency and tissue properties, this critical product may be exceeded. Accordingly, a less rigid criterion, $H_a \times f \leq 5 \times 10^9 \mathrm{Am^{-1}s^{-1}}$, was proposed by R. Hergt and S. Dutz in 2007 [7]. This is the biological constraint that we considered as an acceptable limit for the applied field parameters in the analysis performed in Chapter 5. Successive in vivo experimental analyses demonstrated the possibility of overcoming this threshold of more than one order of magnitude, maintaining eddy current effects below safe and tolerable limits. In [8], breast and pancreatic tumors in mice were successfully treated with superparamagnetic iron oxide nanoparticles exposed to magnetic fields with H_a = 15.4 kA/m and f =435 kHz. Anyway, the proper selection of suitable nanostructures for hyperthermia applications must consider this biological limits.

6.1 Analysis of nanodisk oscillation in a fluid

In this section we present the study of the mechanical behavior of magnetic nanodisks in a fluid with the physical properties (density and viscosity) of blood. This is a crucial analysis, since the hysteretic properties of the nanodisks greatly depend on

their shape anisotropy. The reciprocal orientation between the nanodisks and the applied field can have a relevant effect on the hysteresis loop shape and area, with a consequent important impact on the heating efficiency. Consequently, we want to understand the possibility of nanodisks to be re-oriented along the direction of the applied alternating magnetic field.

To this aim, we start with a very simple model to analyze the time scale of the eventual re-orientation phenomena in a fluid. The analysis is based on the momentum balance equation. For simplicity, we do not consider the whole range of kinds of motions and of rotations that a nanodisk can have in a fluid. Instead, we focus on the time evolution of the rotation angle identified by the intersection between the plane of the disk and the plane normal to the applied field and passing through the center of the disk. The disk position can be easily represented as a function of the angle θ between the planes. We know from the angular momentum equation that

$$\frac{d\mathbf{L}}{dt} = \boldsymbol{\tau}, \tag{6.2}$$

for a rigid body with a fixed axes of rotation passing by its center of mass, under the effect of a torque τ. In particular

$$\frac{d\mathbf{L}}{dt} = I\frac{d\boldsymbol{\omega}}{dt}. \tag{6.3}$$

where I is the moment of inertia and $\boldsymbol{\omega}$ is the angular velocity. The torque $\boldsymbol{\tau}$ applied on the magnetic nanodisk, under the effect of an applied field $\mathbf{H}_a$, is defined as

$$\boldsymbol{\tau} = \mathbf{m} \times \mathbf{H_a} + \boldsymbol{\tau}_D + \boldsymbol{\tau}_B \tag{6.4}$$

where $\mathbf{m}$ is the magnetic moment of the nanodisk, $\boldsymbol{\tau}_D$ is the dynamic drag torque and $\boldsymbol{\tau}_B$ is a stochastic Brownian contribution. Thus

$$I\frac{d\boldsymbol{\omega}}{dt} = \mathbf{m} \times \mathbf{H} + \boldsymbol{\tau}_D + \boldsymbol{\tau}_B. \tag{6.5}$$

For the dynamic drag torque we use an analytical approximation calculated for circular disks, as presented in the work of Brenner [9]. It results in

$$\boldsymbol{\tau}_D = -\mu \boldsymbol{\Omega}_R \cdot \boldsymbol{\omega}, \tag{6.6}$$

where μ is the viscosity of the fluid and $\boldsymbol{\Omega}_R$ is a constant dyadic depending only on the shape of the particle and the location of it center of rotation. For a thin omogeneous disk rotating around its center of mass it has the following form:

$$\boldsymbol{\Omega}_R = \mathbb{I}\frac{32}{3}d^2 \tag{6.7}$$

where d is the diameter of the disk and $\mathbb{I}$ is the identity 3×3 matrix.
In our simplified model (as described by the schematic Fig. 6.1) we assume that the magnetization of the nanodisk can be modeled as a dipolar magnetic moment placed in the disk barycenter. Moreover, we assume that the rotation axis γ is coincident with the coordinate y-axis, and we assume that the particle is able to rotate only around this fixed axis, leading to the simple equations:

$$\begin{aligned} \boldsymbol{\omega}(t) &= \omega(t)\hat{\mathbf{j}} \\ \frac{d\theta}{dt} &= \omega(t) \end{aligned} \tag{6.8}$$

From the micromagnetic simulation of nanodisks oriented along different angles and interested by different field values, we took the volume averaged total magnetization. Interpolating in time we reconstruct a function representing the magnetic moent $\mathbf{m}(\theta(t), |\mathbf{H}(t)|)$ to be used in the mechanical problem.
The simulations are performed by using an algorithm developed ad hoc. In particular we vary disk size, the field frequency (from 1kHz to 500kHz), the field amplitude from 1 kA/m to 100kA/m, and the fluid viscosity ν to simulate different fluids (water

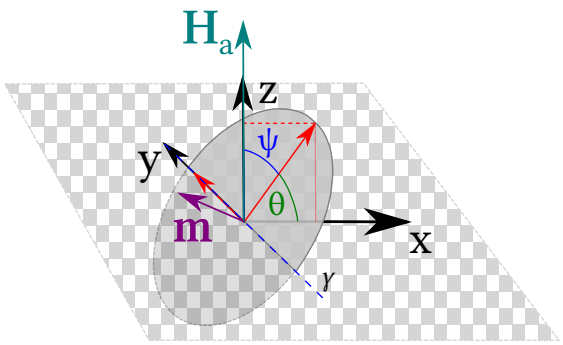

Figure 6.1: Description of of the system: γ is the rotation axis of the nanodisks, the applied field $\mathbf{H}_a$ is directed along the z axis, $\psi = 90 - \theta$ is the angle between the positive direction of the applied field and the versor lying in the plane of the disk perpendicular to the rotation axis γ. ψ is equal to 0 when the disks is oriented parallele to the field and equal to 90 when orthogonal to the applied field.

0.894×10^{-3} kg/ms, blood 0.58×10^{-1} kg/ms). For the simulations "in blood", the parameters are obtained from literature [10–12] assuming a Newtonian behavior.

In the following we report a significant example of the simulated data, where the nanodisk is initially placed almost perpendicular to a field of low amplitude (20 kA/m) at different frequencies, considering the viscosity of blood (Fig. 6.2) as well as of water (Fig. 6.3). From the analysis of the results, the nanodisks are able to re-orientate along the principal direction of the applied field in an average time Δt smaller than oner tenth of a second for every combination of field frequency, field amplitude, starting position and viscosity of the fluid.

Being the estimated Δt much lower than the average duration of the hyperthermia treatment (from30 to 60 minutes), for measurements in a liquid media we can expect that the nanodisks will be oriented in a small range of angles around the direction of the applied field.

From micromagnetic simulation we know that the reduction of hysteresis losses is very limited when the nanodisks are almost parallel to the applied field (see Subsection 6.2.3). This explains the difference found in measurements when considering nanodisk suspended in a fluid or blocked in a gel matrix, mimicking a tissue [5].

However, later evidence suggested that, when internalized in the tumor environment, adhesion phenomena to the cellular membrane and inclusion in endosomes through

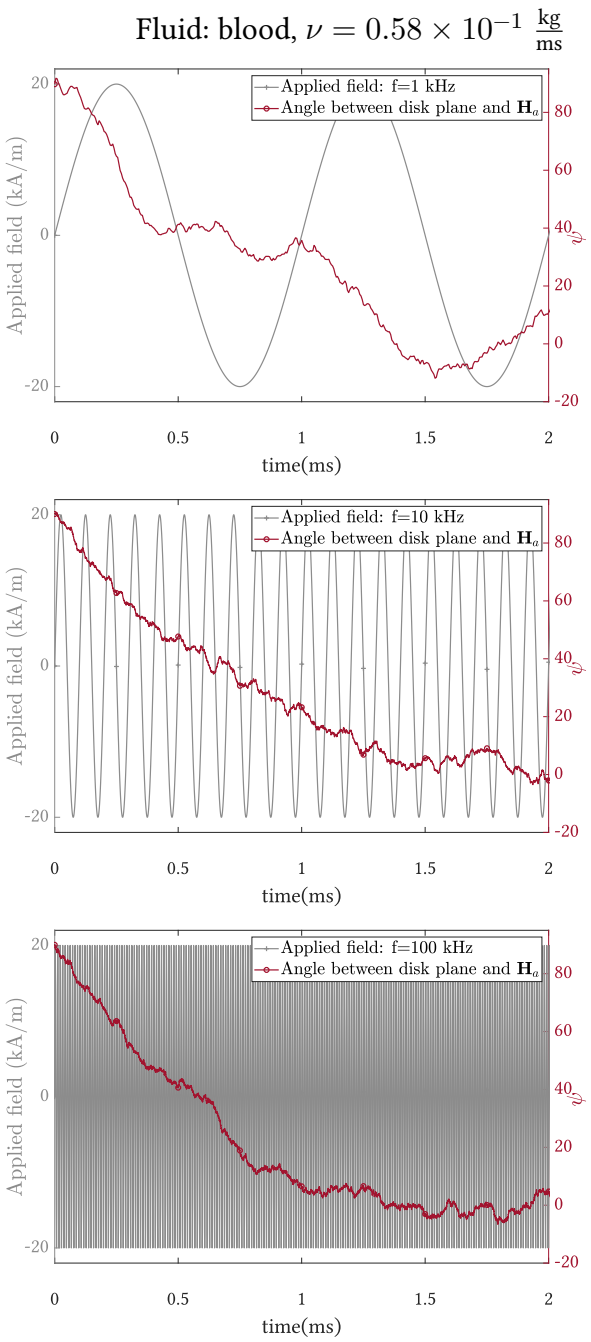

Figure 6.2: The plots report the angle $\psi = 90° - \theta$ between the disk plane and the applied AC magnetic field direction. This angle is equal to 0 when the disk and the field are parallel, while it is equal to 90° when the field is normal to the plane of the disk. The plots show the time evolution of the angle ψ for a disk with diameter of 200 nm and a thickness of 30 nm, floating in thick blood $\nu = 0.58 \times 10^{-1}$ $\frac{kg}{ms}$) with a field with $|\mathbf{H}|_{max} = 20$ kA/m and (a) $f = 1$ kHz, (b) $f = 10$ kHz, (c) $f = 100$ kHz

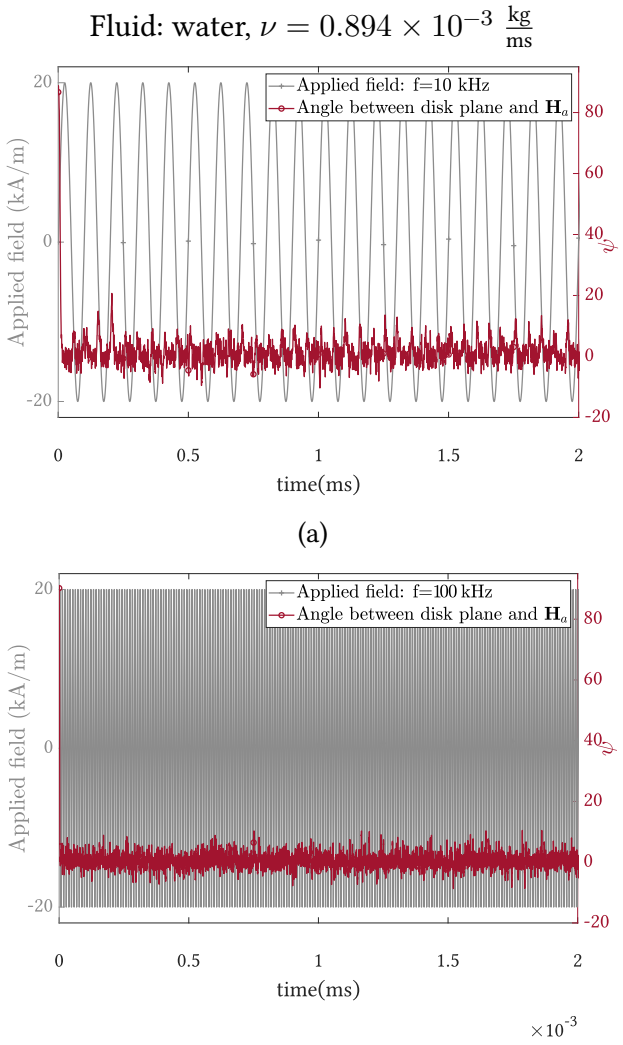

Figure 6.3: The plots report the angle $\psi = 90° - \theta$ between the disk plane and the applied AC magnetic field direction. This angle is equal to 0 when the disk and the field are parallel, while it is equal to 90° when the field is normal to the plane of the disk. The plots show the time evolution of the angle ψ for a disk with diameter of 200 nm and a thickness of 30 nm, floating in water ($\nu = 0.894 \times 10^{-3}$ $\frac{kg}{ms}$) with a field with $|\mathbf{H}|_{max} = 20$ kA/m and (a) $f = 10$ kHz, (b) $f = 100$ kHz.

endocytosis can block the nanostructures in place preventing their re-orientation [13–15].

6.2 Parametric analysis focused on a single nanodisk

We start analyzing the influence of the geometrical parameters of the nanodisks, which can be controlled in the production phase. Subsequently, we study the effects of ambient temperature on the magnetization reversal process and the relative orientation with respect to the applied feld. The possible contribution from eddy current heating is also investigated.

6.2.1 Analysis of the effect of size on the hysteresis losses

In this subsection we present an extensive parametric analysis of permalloy nanodisks, analyzing the effect on the hysteresis losses due to change in size. We performed different simulations on permalloy nanodisks varying the diameter and the thickness of the disk. To correctly evaluate the effect of size excluding other effects, we decided to start studying an isolated nanodisk, excited with a magnetic field applied parallel to the plane of the disk and first neglecting the effect of the temperature. Keeping fixed the properties of the material ($M_S = 860$ kA/m, $k_{ex} = 13$ pJ/m^3, $k_{an} = 0$ jm^{-3}), we computed the hysteresis loop by means of the 3D micromagnetic code developed in this thesis.

The effects of geometrical properties on the hysteresis loop shape are depicted in Fig. 6.4a and 6.4c, which respectively report the loops calculated for different diameters (d = 150 nm, 300 nm and 650 nm) fixing the thickness t to 15 nm, and for different thicknesses (t = 15 nm, 20 nm and 30 nm) fixing d to 400 nm. Apart for the case with d = 150 nm and t = 15 nm, each loop branch is characterized by two irreversible jumps, corresponding to vortex nucleation and annihilation, connected through a reversible part dominated by vortex translation along a direction perpendicular to the applied field direction. At remanence, a negligible average magnetization is found, with the vortex pinned at the nanodisk center. The evolution of magnetic state is clearly illustrated by the magnetization maps reported in Fig.6.4d, calculated for d = 400 nm and t = 15 nm. When d

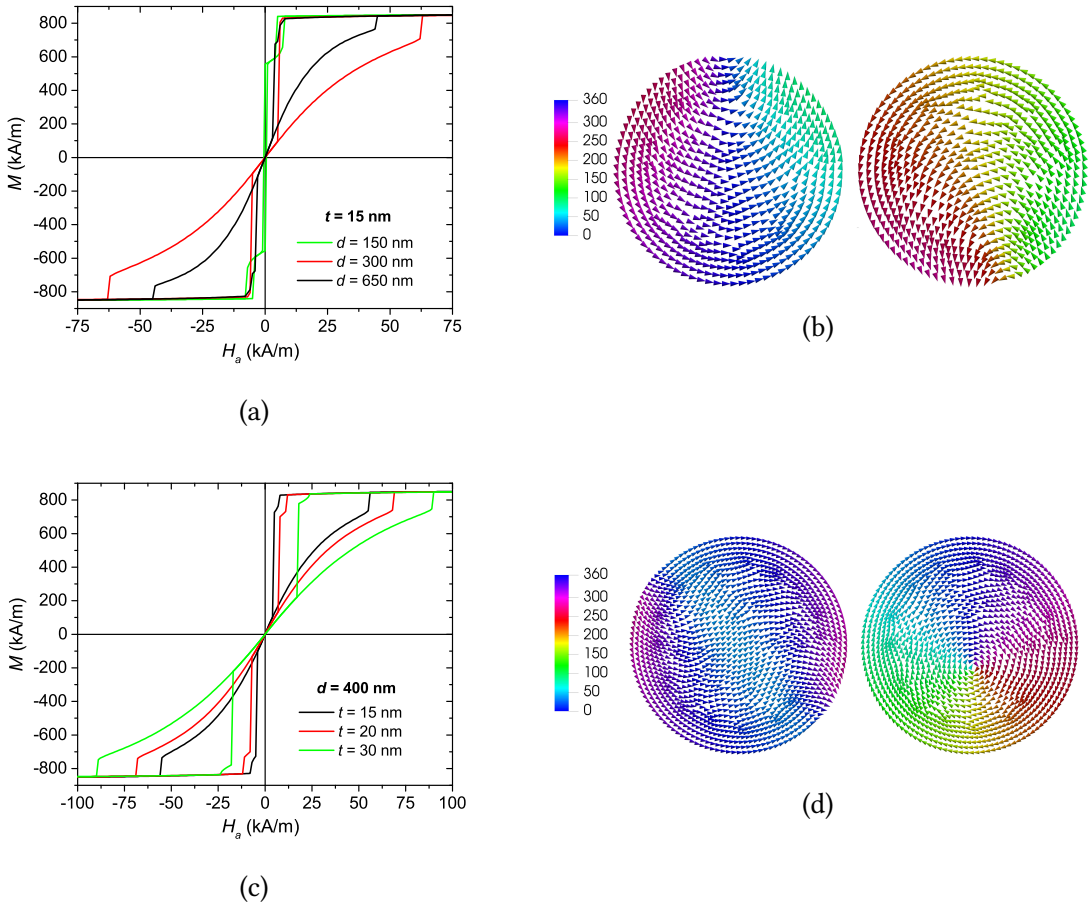

Figure 6.4: The plots (a) and (c) show the computed hysteresis loops for nanodisks with variable size. In plot (a) we report the comparison between permalloy nanodisks of the same thickness ($t = 15$ nm) for different diameters (d = 150 nm, 300 nm and 650 nm). In plot (c) we fixed the diameter to 400 nm and vary the thickness (t = 15 nm, 20 nm and 30 nm). (To allow a higher readability of the plots we choose to not include all the calculated loops, the intermediate values fit well in the trend we described). Images (b) and (d) illustrate the magnetization distribution of two nanodisks before and after an irreversible jump around the remanence state. Figure (b) corresponds to the complete reversal of the magnetization for the case with d = 150 nm and t = 15 nm. . Figure (d) shows the nucleation of the vortex in the case of d= 400 nm and t = 15 nm, common to all the other reported loops.

= 150 nm and t = 15 nm, the magnetization reversal occurs at zero applied field with an irreversible jump between two C-states, leading to a negligible loop area (see Fig. 6.4b). Figure 6.4 well demonstrates that, in the case of vortex formation, wider hysteresis loops can be obtained by reducing nanodisk diameter and/or increasing nanodisk thickness. The latter is true for thicknesses up to around 40 nm. As shown in Chapter 5,

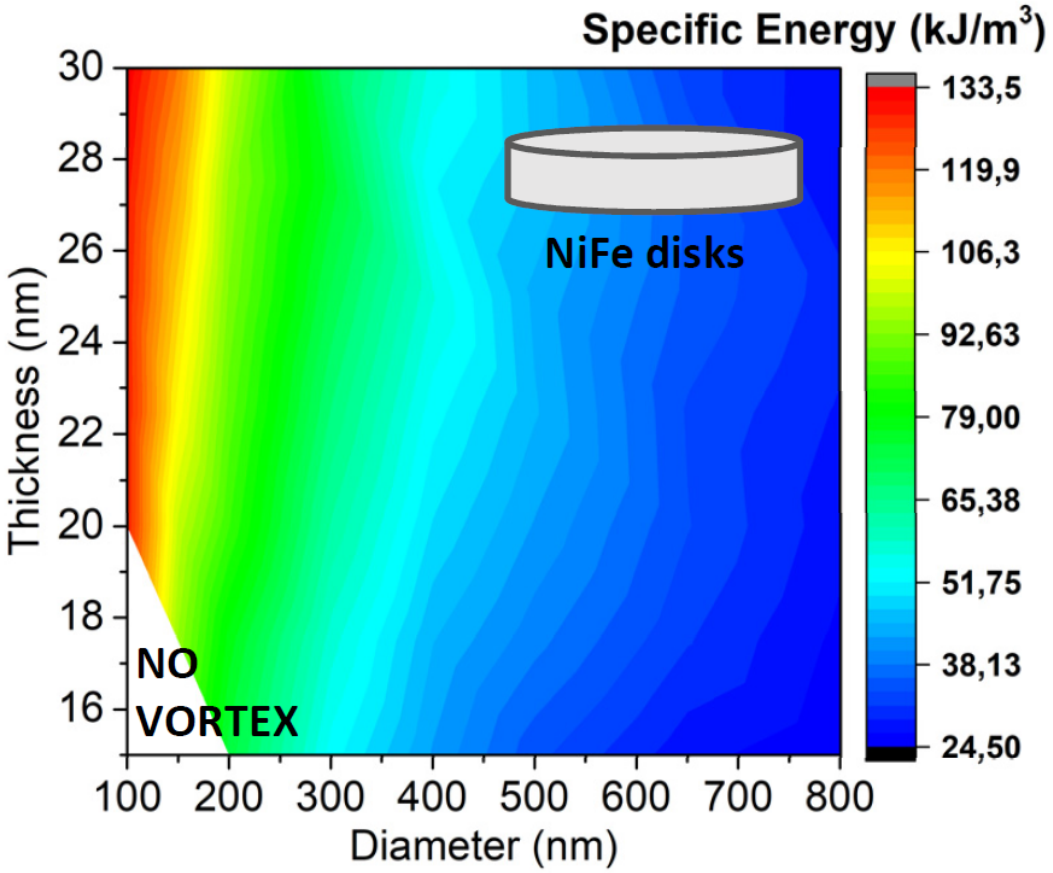

Figure 6.5: Phase diagram representing the specific energy in kJ/m^3 produced by permalloy nanodisks with different thickness and diameter. The white area represents the combination of geometrical parameter for which the magnetization reversal process takes place following *Stoner-Wohlfarth* model, , thus leading to negligible hysteresis losses.

when transitioning from a thin disk to a cylinder, the hysteresis losses start to decrease again. The above conditions lead to greater heating capabilities, as shown by Fig. 6.5, which reports the specific energy losses, calculated as a function of parameters d and t:

$$E = \mu_0 \int_{loop} \mathbf{H}_a \cdot d\mathbf{M} \tag{6.9}$$

The data are plotted only for the cases characterized by vortex nucleation, confirming, for the considered values of d and t, the classification of remanent states reported in the phase diagram of Ref. [1].

To maximize the hysteresis losses, the amplitude of the external field should be large enough to enable the saturation of the nanodisks. For the major loops, the estimated losses vary from ∼25 kJ/m^3 (case with d = 800 nm and t = 15 nm) to ∼135 kJ/m^3 (case with d = 100 nm and t = 30 nm). These data correspond to a heating efficiency or specific loss power (SLP) of 287 W/g and 1552 W/g, respectively, when considering an AC external field with a frequency of 100 kHz and a value of 8.72 g/cm^3 for the mass density of permalloy.

For the considered geometrical properties, it is worth noting that saturating conditions can be obtained by applying external fields with quite large estimated amplitudes, ranging from ∼40 kA/m for d = 800 nm and t = 15 nm up to ∼120 kA/m for d = 150 nm and t = 30 nm. This can impact on the maximum field frequency that can be selected for safe in vivo treatment, in order to prevent the non-selective heating of both cancerous and healthy tissue due to the generation of eddy currents as discussed at the beginning of this chapter and in Chapter 5.

6.2.2 The effects of ambient temperature

It should be remarked that the results reported in Fig. 6.4 have been calculated by neglecting thermal noise and by assuming ideal material and geometrical properties (absence of defects) for the considered nanodisks. If we include thermal agitation effects, introduced in the simulations via a Langevin approach (see Section 3.3.4), we can observe a modification of the hysteresis loop, with a significant decrease in the field corresponding to vortex annihilation and, consequently, in the saturation field. Thermal noise can moderately impact also on the vortex nucleation field, which can be randomly reduced or amplified. The influence of temperature on hysteresis loops is illustrated in Fig. 6.6, referring to nanodisks with a thickness of 30 nm and a diameter ranging from 100 nm to 800 nm. Each new loop has been calculated by setting the temperature at (320 K), a value that is expected to be reached during a standard hyperthermia session, and

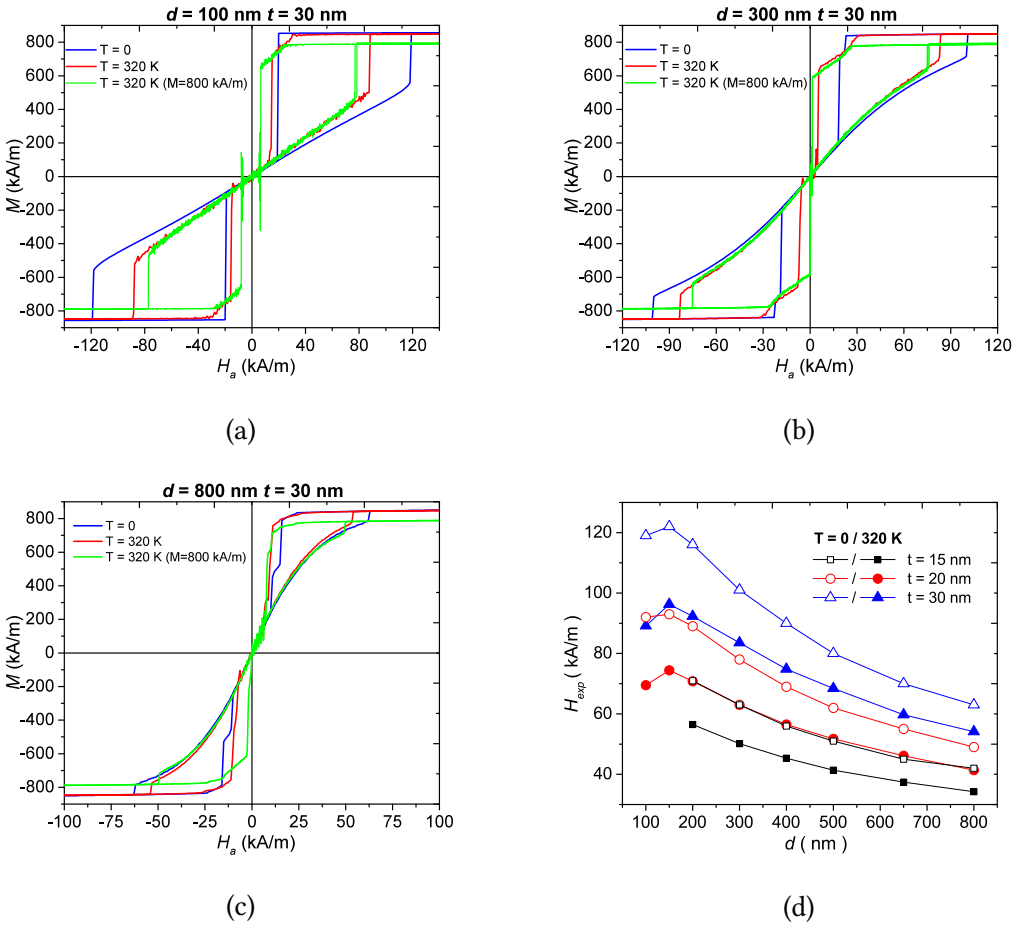

Figure 6.6: Comparison of the hysteresis loops of nanodisks, calculated neglecting thermal effects and setting the temperature at 320 K. At 320 K two sets of simulations are performed: one with the standard value of M_S of 860 kA/m and one using the corrected value of 800 kA/m obtained from Eq. 6.10. In (a) d = 100 nm, t = 30 nm; (b) d = 300 nm, t = 30 nm; (c) d =800 nm, t = 30 nm; (d) Diagram showing the behavior of the vortex expulsion field H_{ex} as function of d, for the temperature T equal to zero or to 320 K.

by extracting the average curves over 20 stochastic realizations. The saturation magnetization at 320 K has been fixed to 800 kA/m, according to the following law:

$$M_S(T) = M_{S_0}(1 - bT^{3/2} - cT^{5/2} - aT^2) \tag{6.10}$$

derived from the classical spin-wave theory [16, 17]. We consider the parameter values reported in [16], namely $a = 0.19 \times 10^{-7}$ K^{-2}, $b = 0.88 \times 10^{-5}$ K$^{-3/2}$ and

$c = 0.09 \times 10^{-7}$ $K^{-5/2}$. Figure 6.6d compares the values of the vortex annihilation field determined with and without thermal effects inclusion, for the entire considered ranges of thickness and diameter.

It is worth noting that the role of temperature is higher for the nanodisks with smaller diameter and larger thickness, and reduces with the diameter increase. The highest annihilation field, 122 kA/m, obtained with zero temperature when d = 150 nm and t = 30 nm, decreases up to 96 kA/m. As a conclusion, thermal effects favor the vortex annihilation enabling to reach saturation with strongly reduced fields. Anyway, the impact on the hysteresis losses is limited, with a weak decrease, e.g. for the major loops, the estimated losses vary from 18.8 kJ/m^3 (instead of 24.9) (case with d = 800 nm and t = 15 nm) to ∼93 kJ/m^3 (instead of 132.9 kJ/m^3) (case with d = 100 nm and t = 30 nm). These data correspond to a heating efficiency or specific loss power (SLP) of 287 W/g and 1552 W/g, respectively, when considering an AC external field with a frequency of 100 kHz and a value of 8.72 g/cm^3 for the mass density of permalloy. This enables to obtain SLP values similar to the ones previously estimated, but with reduced applied fields.

6.2.3 Study of the influence of the angular orientation with respect to the applied field

The previous results shown in this chapter have been obtained by applying the external field in the nanodisk plane. As explained in Section 6.1 and reported in literature, we can expect that the nanostructures dispersed in a tissue will not be all aligned with the field, presenting a local variation in the orientation with respect to the field. Even if in a fluid magnetic nanodisks can be re-oriented along the direction of the applied field, in a tissue because of adhesion or internalization phenomena within the cellular environment, they are presumably not free to rotate. Since the nanodisks present a strong shape anisotropy it is interesting to see how they perform in terms of heat generation when the field is applied at different angles. This study is necessary to obtain a realistic

estimate of the heat production for the development of therapeutic plans.

Here, we investigate the effects of the inclination of the external field with respect to the nanodisk plane, evaluating the vortex nucleation and vortex expulsion fields, H_{nuc} and H_{exp}, as a function of field application angle θ (see inset in Fig. 6.7b). Figure 6.7a shows the results obtained for a nanodisk with d = 150 nm and t = 25 nm, also considering the influence of temperature. The increase in θ leads to an amplification of both H_{nuc} and H_{exp}. In particular, H_{nuc} varies moderately when θ is in the range of 0-40°, with a steep rise for values of θ larger than 80°, due to the relative reduction in the external field component lying in the nanodisk plane.

When disregarding thermal effects, the simulations predict a value of ∼390 kA/m for θ = 85°, resulting in a practical infinite amplitude when the external field is applied orthogonally to the nanodisk surface. Regarding H_{exp}, it increases more smoothly with θ, reaching a value of ∼430 kA/m for θ = 85°.

The specific energy losses gradually reduce as the angle increases up to around $\sim 60°$ as shown by Fig. 6.7b, drastically decaying when reaching $\theta \sim 80°$. This fact emerges also looking at the hysteresis loops reported in Fig. 6.8 for a field with a maximum amplitude of 150 k/Am, neglecting thermnal effects. The reversible part of the loop gradually increases as the field rotates away from the disk plane and, for this value of field, already at 55° we are not able to achieve the irreversible jumps giving a negligible contribute to the losses.

Therefore, the choice of the applied field, when imagining an ensemble of randomly oriented nanodisks, affects also the overall number of disks generating heat. Remembering the $H_a \times f$ limits, developing an hyperthermia protocol, it is important to choose the amplitude of the field to balance the reduction in losses due to the effect of the angle (for low values of the applied field) or the reduction in losses due to a smaller operative frequency, when choosing high fields to maximize the losses of disks not aligned with the field.

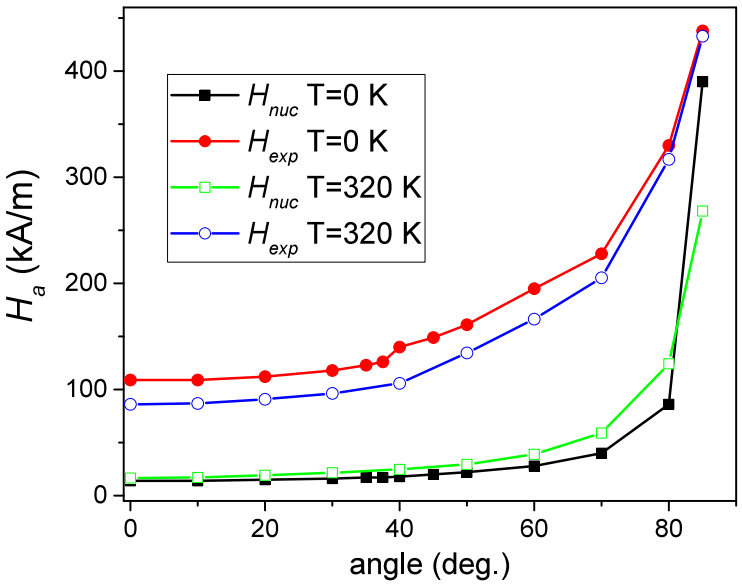

(a)

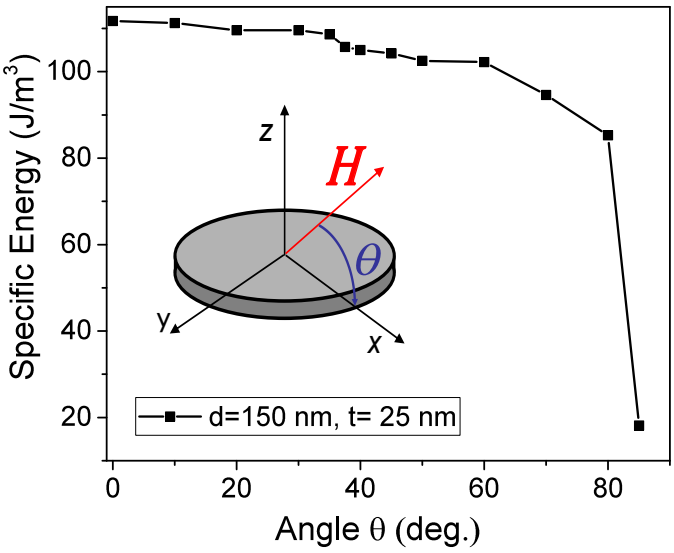

(b)

Figure 6.7: (a) Effect of the field orientation on H_{nuc} and H_{exp} of nanodisk (the angular orientation is depicted in the schematic). We report the data for the disk with $d = 150$ nm and $t = 25$ nm without and with the inclusion of thermal effects ($T = 320$ K).). (b) Graph that shows the behaviour of the hysteresis losses as a function of the orientation of the field ($\theta = 0°$ when the field is applied in the plane of the disk and $\theta = 90°$ when the field is applied orthogonal to the plane of the disk), highlighting a sharp decay above 80°

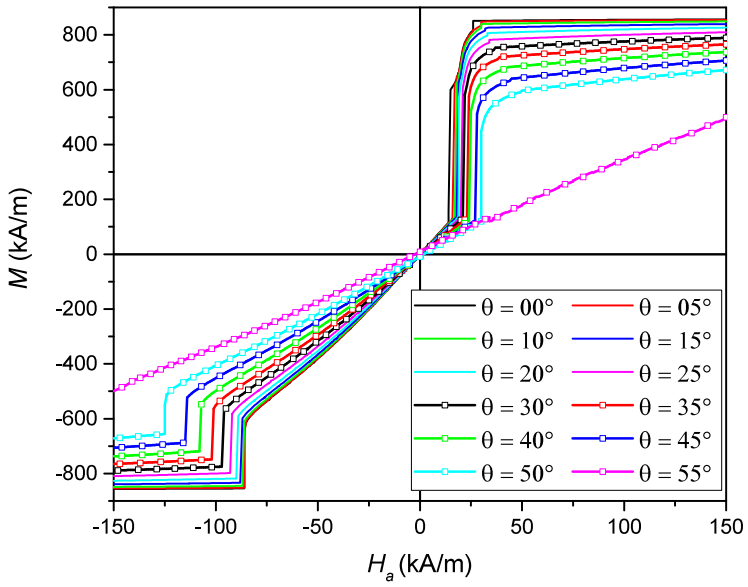

Figure 6.8: The graphs report the descending branch of the hysteresis loops for a nanodisk with $d = 150$ nm and $t = 30$ nm for different angular orientations of the applied field. The component of the magnetization M is taken parallel to the applied field H_a. For value of $\theta \geq 55°$ limiting the applicable field to 150 kA/m the vortex is not expelled, therefore we have an almost entirely reversible motion of the vortex with negligible losses.

6.2.4 Eddy current heating

For a frequency of 100 kHz of the AC applied field, the time scale of magnetization dynamics is much shorter than the one of electromagnetic field diffusion. In the studied examples, the largest duration of magnetization relaxation processes towards equilibrium, at a specific field level, is in the order of a few tens of nanoseconds, for irreversible jumps. This means that hysteresis losses can be determined by calculating quasi-static hysteresis loops, and thus decoupling spin dynamics from eddy current phenomena. As a first approximation, eddy current losses can be estimated via analytical modelling.

For the case corresponding to maximal heat generation via eddy current effects (external field perpendicular to nanodisk surface), the heating power can be expressed as

$$P = \frac{\pi \hat{H}_a x}{\sigma} \frac{ber_0(x)ber_0'(x) + bei_0(x)bei_0'(x)}{ber_0^2(x) + bei_0^2(x)} \tag{6.11}$$

where

$$x = \frac{d}{2}\sqrt{2\pi f \sigma \mu_r \mu_0}. \tag{6.12}$$

In Eq. (6.11) $\hat{H}_a$ is the amplitude (peak value) of the AC external field, σ is the electrical conductivity and is the relative magnetic permeability of the disk material.
From a preliminary analysis the eddy current contribution can be considered negligible, for the nanodisks in the studied range of sizes, when considering a maximum field of 100 kA/m and a frequency of 100 kHz.

6.3 Study of ensambles of nanodisks: the effect of concentration and magnetostatic interactions

As explained in Section 6.1 and reported in literature, we can expect that, when applied in hyperthermia therapy, because of the immobilization in the cellular or extracellular environment, the magnetic nanostructures are not able to re-orientate with the applied field, resulting dispersed in the target tissue with a random spatial distribution. Therefore, it is crucial to estimate the heat production in the case of 3D ensembles of nanodisks, which mutually interact by means of magnetostatic interactions and present different orientation with respect to the applied field. A fundamental parameter that governs the produced heat is the nanodisk concentration.
To analyze the influence of the above factors, different sets of randomly distributed

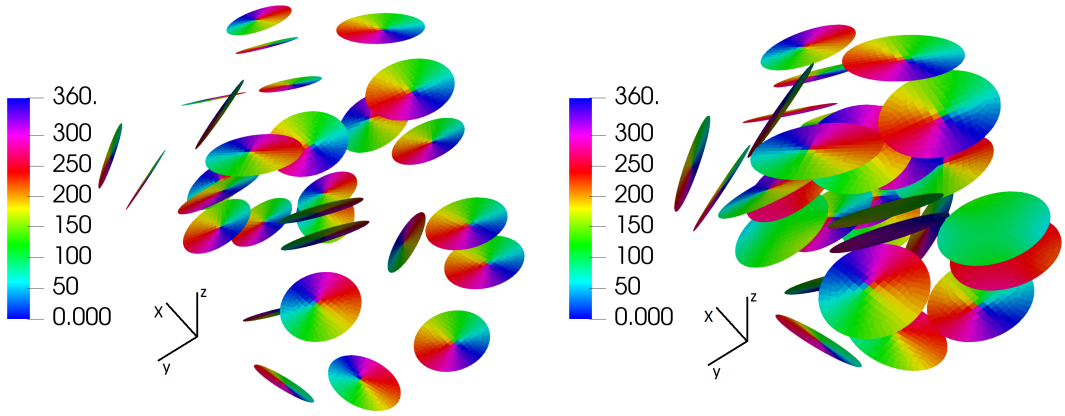

(a) (b)

Figure 6.9: We report two examples of random distribution of nanodisks ($d = 150$ nm $t = 25$ nm). For the distribution (a) the volume concentration c is equal to 1%, for (b) it is equal to 20%. The colors rapresent the angle between the projection of the magnetization vector on the plane xy and the direction of the applied magnetic field, evaluated at the remanence. We can notice that in case (b) not all the nanodisks show the vortex configuration.

nanodisks were generated using an algorithm developed ad hoc to avoid shape overlapping andcompenetration . Each distribution is made of one kind of nanodisks, randomly placed in space and randomly oriented following a uniform probability density function. The study is focused on nanodisks with diameter of 150 nm and thickness of 25 nm. Each distribution, of which we report two examples with the relative remanent magnetization configurations in Fig. 6.9 was generated with at a given volume concentration in Fig. 6.9 was generated with at a given volume concentration c. The volume concentration c is defined as the ratio $V_{\text{nanodisks}}/V_{\text{system}}$, where $V_{\text{nanodisks}}$ is the volume of a nanodisk multiplied by the number of nanodisks and V_{system} is the minimum volume of the 3D domain containing all the nanodisks. Simulations were performed for different concentration values, from $\sim 0.5\%$ up to $\sim 30\%$.

The results are shown in Fig. 6.10,which reports the hysteresis loops computed for 4 random distributions of nanodisks also including thermal effects, averaged over 20 stochastic simulations. We can observe that as the concentration increases the hysteresis loops appear smoother, with smaller area and with nucleation and expulsion field spread over a wider range of values. Only for values of $c < 2\%$ the loops have still sharp

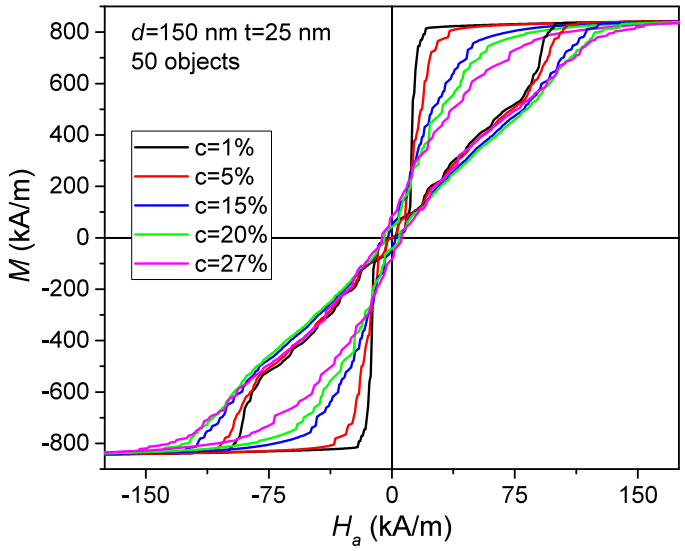

Figure 6.10: Hysteresis loops obtained for stochastic distributions 50 of nanodisks ($d = 150$ nm, $t = 25$ nm) considering different values of concentration.

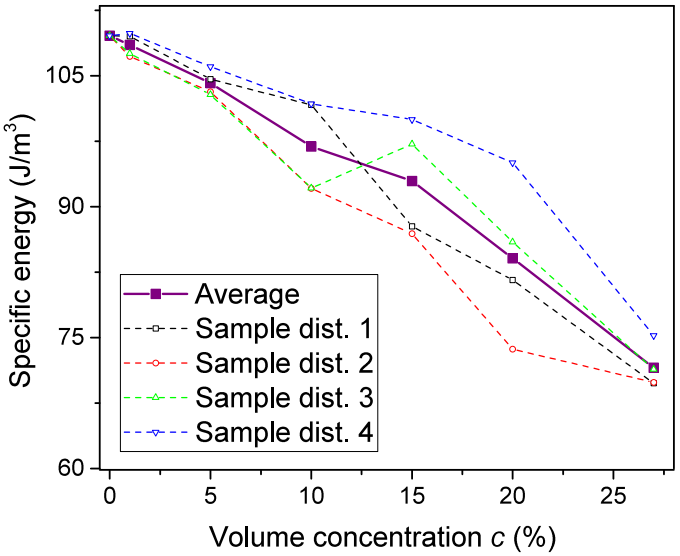

Figure 6.11: Plot of the trend of specific energy per unit volume of ferromagnetic material. In purple we report the average on different distributions of nanodisks. The other lines represent the behaviour of 4 different random distributions with 50 nanodisks.

irreversible jump transition.This effect is due to the magnetostatic interaction between nanodisks and to variable orientation with respect to the applied field.
The magnetostatic interactions are stronger for high values of concentration, since in this case the distance between nanodisks is smaller. For elevated concentrations, we cannot individuate anymore a specific expulsion and nucleation field in the loop, since the nanodisks in the distribution have different H_{nuc} and H_{exp}.
These changes in the shape of the hysteresis loops reflects in the heating performance of the nanodisks. Figure 6.11 clearly shows that the specific energy losses (per volume of magnetic material) is smaller when the concentration is higher, tending towards the value of isolated disks only for very small concentrations.
As a second aspect, in our simulations, we pushed the fields over therapeutic reasonable limits to obtain the full hysteresis loop. However, in a realistic therapeutic application, the amplitude of the field has to be lower. In this case we expect a further reduction in the energy losses, since the field is not able to induce irreversible jumps in all the nanodisks in the distribution. Therefore, some nanodisks will show only reversible motion of the vortex, giving a negligible contribution to the hysteresis losses. The studied effects give us two indications for the hyperthermia application: one is that increasing the concentration of nanostructures per unit volume of treated region does not have, even in principle, a linear effect on the heat generation. The other one is that the aggregation and local clustering of nanodisks may have a strong negative effect on the ability of the nanostructures to produce heat.

6.4 Conclusions

In this chapter we provide an extensive analysis of the heating performance of permalloy nanodisks for possible application in magnetic hyperthermia. We extensively evaluated the influence of parameters and phenomena that can strongly affect the heat generation of such nanostructures. The idea is to be able to provide a reliable estimate

of the losses, to be potentially used as a source in bio-heat dissipation simulations based on the Penn's equation and on the use of anatomical virtual models. Thanks to this work we are able to identify the optimal size for the nanodisks from a heat generation point of view ($d \sim 150$ nm and $t \sim 30$ nm). Given the area and irreversible jump fields of the hysteresis loops for the considered nanodisks we are able to obtain, from the biological limit to the $H_a \times f$ product, the requirement for the exciting field in terms of amplitude and frequency. From the study of the effects of temperature, angular orientation with respect to the field and concentration, we can rescale the expected heat generation of these nanostructures when used in hyperthermia treatment.

References

[1] J. Ha, R. Hertel, and J. Kirschner. "Micromagnetic study of magnetic configurations in submicron permalloy disks". In: *Phys. Rev. B* 67.22 (2003), p. 224432. ISSN: 0163-1829. DOI: 10.1103/PhysRevB.67.224432.

[2] E. A. Vitol, V. Novosad, and E. A. Rozhkova. "Microfabricated magnetic structures for future medicine: from sensors to cell actuators". In: *Nanomedicine* 7.10 (Oct. 2012), pp. 1611–1624. ISSN: 1743-5889. DOI: 10.2217/nnm.12.133.

[3] M. Angelakeris. "Magnetic nanoparticles: A multifunctional vehicle for modern theranostics". In: *Biochim. Biophys. Acta - Gen. Subj.* 1861.6 (2017), pp. 1642–1651. ISSN: 18728006. DOI: 10.1016/j.bbagen.2017.02.022.

[4] D.-H. Kim et al. "Biofunctionalized magnetic-vortex microdiscs for targeted cancer-cell destruction". In: *Nature Materials* 9 (Nov. 2009). Article, p. 165.

[5] K. Simeonidis et al. "In-situ particles reorientation during magnetic hyperthermia application: Shape matters twice". In: *Sci. Rep.* 6.October (2016), pp. 1–11. ISSN: 20452322. DOI: 10.1038/srep38382.

[6] W. J. Atkinson, I. A. Brezovich, and D. P. Chakraborty. "Usable Frequencies in Hyperthermia with Thermal Seeds". In: *IEEE Trans. Biomed. Eng.* BME-31.1 (1984), pp. 70–75. ISSN: 15582531. DOI: 10.1109/TBME.1984.325372.

[7] R. Hergt and S. Dutz. "Magnetic particle hyperthermia-biophysical limitations of a visionary tumour therapy". In: *J. Magn. Magn. Mater.* 311.1 SPEC. ISS. (2007), pp. 187–192. ISSN: 03048853. DOI: 10.1016/j.jmmm.2006.10.1156.

[8] S. Kossatz et al. "High therapeutic efficiency of magnetic hyperthermia in xenograft models achieved with moderate temperature dosages in the tumor area". In: *Pharm. Res.* 31.12 (2014), pp. 3274–3288. ISSN: 1573904X. DOI: 10.1007/s11095-014-1417-0.

[9] H. Brenner. "the Stokes Resistance of an Arbitrary Particle .2. an Extension". In: *Chem. Eng. Sci.* 19.9 (1964), pp. 599–629. ISSN: 00092509. DOI: 10.1016/0009-2509(64)85051-X.

[10] D. Klatt et al. "Noninvasive assessment of the rheological behavior of human organs using multifrequency MR elastography: A study of brain and liver viscoelasticity". In: *Phys. Med. Biol.* 52.24 (2007), pp. 7281–7294. ISSN: 00319155. DOI: 10.1088/0031-9155/52/24/006.

[11] S. M. Abe Hiroyuki, Hayashi Kozaburo. *Data Book on Mechanical Properties of Living Cells, Tissues, and Organs*. Vol. 53. 1989, p. 160. ISBN: 9788578110796. DOI: 10.1017/CBO9781107415324.004.

[12] O. K. Baskurt. *Handbook of hemorheology and hemodynamics*. Vol. 69. 2007, pp. 1–455. ISBN: 9781586037710.

[13] S. Dutz et al. "Magnetic multicore nanoparticles for hyperthermia-influence of particle immobilization in tumour tissue on magnetic properties". In: *Nanotechnology* 22.26 (2011). ISSN: 09574484. DOI: 10.1088/0957-4484/22/26/265102.

[14] R. Di Corato et al. “Magnetic hyperthermia efficiency in the cellular environment fordifferent nanoparticle designs”. In: *Biomaterials* 35.24 (2014), pp. 6400–6411. ISSN: 18785905. DOI: 10.1016/j.biomaterials.2014.04.036.

[15] L. Beola et al. “A Roadmap to the Standardization of In Vivo Magnetic Hyperthermia”. In: *Nanomater. Magn. Opt. Hyperth. Appl.* Elsevier, 2019, pp. 317–337. ISBN: 9780128139288. DOI: 10.1016/B978-0-12-813928-8.00012-0.

[16] C. Luo et al. In: *J. Magn. Magn. Mater.* 374 (2015), pp. 711–715. ISSN: 0304-8853. DOI: 10.1016/j.jmmm.2014.09.014.

[17] J. Tejada et al. “Phenomenological study of the amorphous $Fe_{80}B_{20}$ ferromagnet with small random anisotropy”. In: *Phys. Rev. B* 42 (1 July 1990), pp. 898–905. DOI: 10.1103/PhysRevB.42.898.

Chapter 7

Study of bi-component magnetic nanodisks for potential application in magnetic storage

The material presented in this chapter is submitted for publication on Applied Physics letters.

In the last decades, magnetic nanodisks have been extensively studied by means of both experimental and modeling analysis, also for their potential application in advanced sensor technologies, magnetologic devices and high density storage media [1]. In this framework, the nucleation of vortex state in magnetic nanodisks is a topic of intensive research, due to its possible implementation in data storage and specifically in non-volatile magnetic random access memories (MRAMs). Two units of information can be stored in a single nanodisk, exploiting either vortex polarity (up/down orientation of the magnetization in the vortex core) or chirality (clockwise/counterclockwise rotational direction of the magnetization) [2].

Despite the technological potentiality of magnetic vortices, the control of their topological properties still remains a challenging issue [3]. Different solutions based on broken

rotational symmetry were proposed to tailor vortex chirality and possibly polarity, like the use of asymmetric dots with a flattened edge [4–6] or regular polygonal nanomagnets with an odd number of sides [7–9]. Alternatively, "Pac-Man"-like nanodots can be considered to obtain specific chirality and polarity states without the application of out-of-plane magnetic fields for setting vortex core polarity [10].

Recently, the simultaneous definition of chirality and polarity was achieved in nanodots with modulated or tapered thickness, by simply changing the in-plane applied field direction [11, 12]. Thickness-modulated disks in the form of a permalloy lens on top of a disk made of the same material were also proposed to control the vortex core location and vortex chirality depending on the magnetostatic interactions between the two regions [13]. At the same time, static and dynamic control of both polarity and chirality was demonstrated for a vortex confined in a magnetic tunnel junction by using resonant excitation with an rf current [14].

Broken symmetry can be also achieved by means of bi-component disks (made of two magnetic materials); as an example, angle deposition and lift-off processes were employed to fabricate bi-component dots consisting of a crescent of iron and a lens of permalloy [15]. Their hysteresis loop, measured with MOKE technique, is characterized by a three-step switching, corresponding respectively to magnetization switching in the permalloy lens, and to vortex nucleation and expulsion in the iron crescent. This result opens up the possibility of finely controlling vortex core position, by simply varying the relative dimensions of the two regions constituting bi-component magnetic nanostructures.

In this chapter, we investigate bi-component magnetic nanodisks with geometrical configuration similar to the one proposed by Shimon et al. [15], to explore the possibility of tuning the chirality and stability of vortex, as well as its nucleation and expulsion, by means of the local shape anisotropies at the interface between the two materials. The analysis is performed from a micromagnetic numerical point of view, calculating the static hysteresis loops of disks arranged in both single and 2D array configurations.

The latter case is considered to study the effects of magnetostatic interactions between disks on vortex stability.

7.1 Numerical methodology and parameter setting

The simulations of the nanodisks for the two considered arrangements (single and 2D array) are performed by using a parallelized micromagnetic code previously developed by Dr. Oriano Bottauscio and Dr. Alessandra Manzin. This code was designed to efficiently solve the Landau-Lifshitz-Gilbert equation in samples with complex patterning and heterogeneous composition [16, 17]. The code implements a norm-conserving scheme based on Cayley transform and Heun method for the magnetization update as described in Chapter 3 and in References [18, 19]. Moreover, it uses a finite difference technique for the exchange field evaluation on unstructured meshes, thus enabling the accurate treatment of curved boundaries [20]. For the 2D array arrangement, periodic boundary conditions are introduced on the edges of the array unit cell [21, 22].
Regarding the parameter setting, the numerical analysis focuses on 20 nm thick nanodisks with diameter d =300 nm and composed of two magnetic regions, namely a lens of permalloy (saturation magnetization M_S of 860 kA/m, exchange constant k_{ex} of 13 pJ/m and negligible magnetocrystalline anisotropy) and a crescent of iron (M_S = 1700 kA/m, k_{ex} = 21 pJ/m and cubic magnetocrystalline anisotropy with constant equal to 48 kJ/m^3). The reversal mechanism is studied for different fractions of the two constituents, by shifting the position of the permalloy-iron interface. In particular, we vary parameter w, which corresponds to the distance between the interface and the disk left boundary, from 60 nm to 240 nm (see inset of Fig. 7.1a).

7.2 Analysis of single bi-component nanodiks

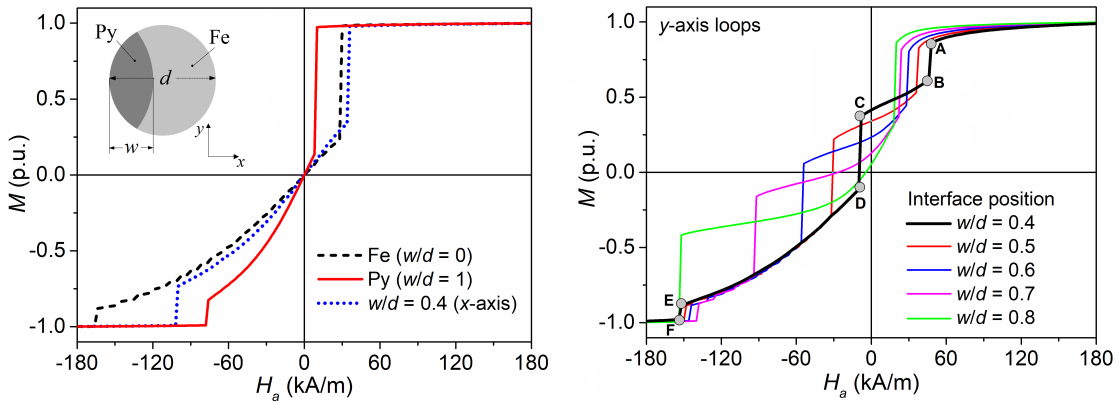

(a) (b)

Figure 7.1: (a) Descending branches of the hysteresis loops of single homogeneous permalloy and iron nanodisks, compared to the x-axis loop of a bi-component nanodisk with w/d = 0.4. Inset: schematic of the bi-component nanodisk composed of a lens of permalloy, with thickness w, and a crescent of iron. (b) Descending branches of the y-axis hysteresis loops versus parameter w. Magnetization is normalized to saturation value.

The single bi-component disks are characterized by a strong shape anisotropy, as demonstrated by the differences in the descending branches of the static hysteresis loops calculated for different values of parameter w along the directions orthogonal (x-axis) and parallel (y-axis) to the interface. The x-axis loops are similar to the ones of the entirely homogeneous disks, with two irreversible jumps corresponding to vortex nucleation and expulsion, connected through a reversible part dominated by vortex shift along vertical direction. At remanence, a negligible average magnetization is always found (Fig. 7.1a). As shown in Fig. 7.1b, the y-axis loops are generally characterized by three irreversible jumps; the magnetization configurations immediately before and after the jumps are reported in Fig. 7.2a for w/d = 0.7. The first jump (from equilibrium point #A to #B) corresponds to evolution from C-state to vortex nucleation, occurring always in permalloy lens at an internal point located between the disk left boundary and the permalloy-iron interface. Between the first and second irreversible jump (from equilibrium point #B to #C) the vortex moves reversibly along the x-axis up to the interface.

The second jump (from equilibrium point #C to #D) is associated with vortex horizontal motion from the interface to an internal point located between the interface and the disk right boundary. Between the second and third irreversible jump (from equilibrium point #D to #E) the vortex moves reversibly along the x-axis up to a position close to the disk right boundary. The third jump (from equilibrium point #E to #F) corresponds to vortex expulsion, occurring always in iron region. When w/d = 0.8, the magnetization reversal is characterized by only two irreversible jumps, with the second jump directly associated with evolution from vortex anchored to the interface to vortex expulsion. In these cases, equilibrium points #D and #E are not present.

As illustrated in Fig. 7.2b, for the y-axis loops the spatial position u of the vortex at

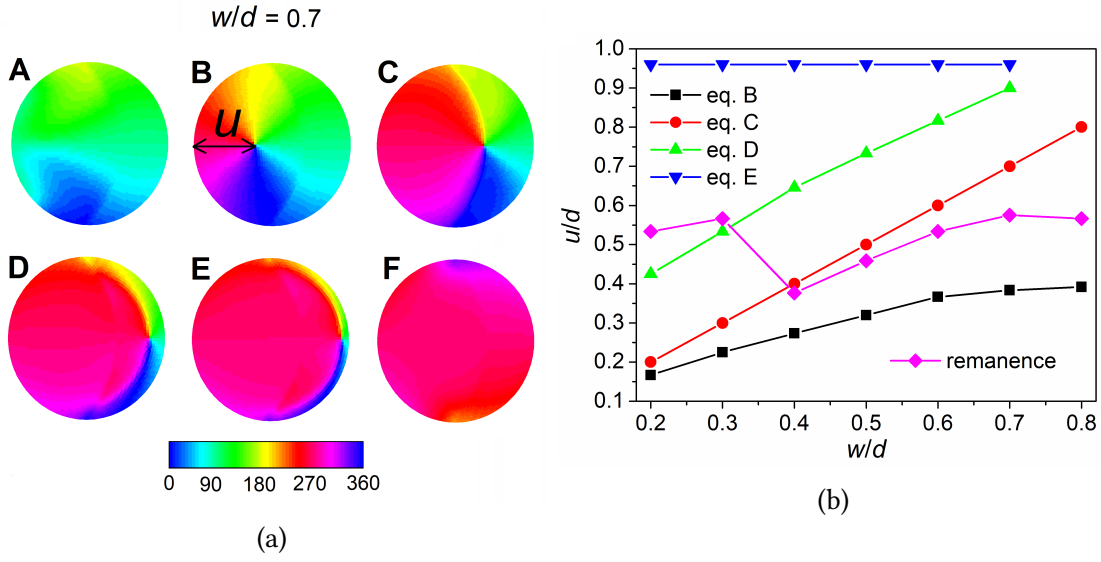

Figure 7.2: (a) Magnetization configurations at the equilibrium points along y-axis hysteresis loop descending branch Fig. 7.1b, calculated for w/d = 0.7. The color bar represents the angle, in degrees, between magnetization vector and x-axis. (b) Vortex spatial position (u/d) versus parameter w/d for remanence state and equilibrium points #B, #C, #D and #E. Parameter u describes the distance of vortex core from the disk left boundary

equilibrium points #B, #C, #D and #E is a function of parameter w, coinciding with w for point #C. For point #B, there is a linear dependence on w up to w/d = 0.6, reaching a plateau for larger values; for point #D the linear dependence extends up to w/d = 0.7 and for point #E u is nearly constant, in the order of $0.96d$. It results that for the

reversal mechanism along y-axis it is possible to monitor the vortex position inside the disk and control both vortex nucleation and expulsion, which respectively occur in the permalloy lens and at the opposite iron boundary for all the considered values of w.

The reason why the vortex enucleates first in the permalloy lens and then evolves with

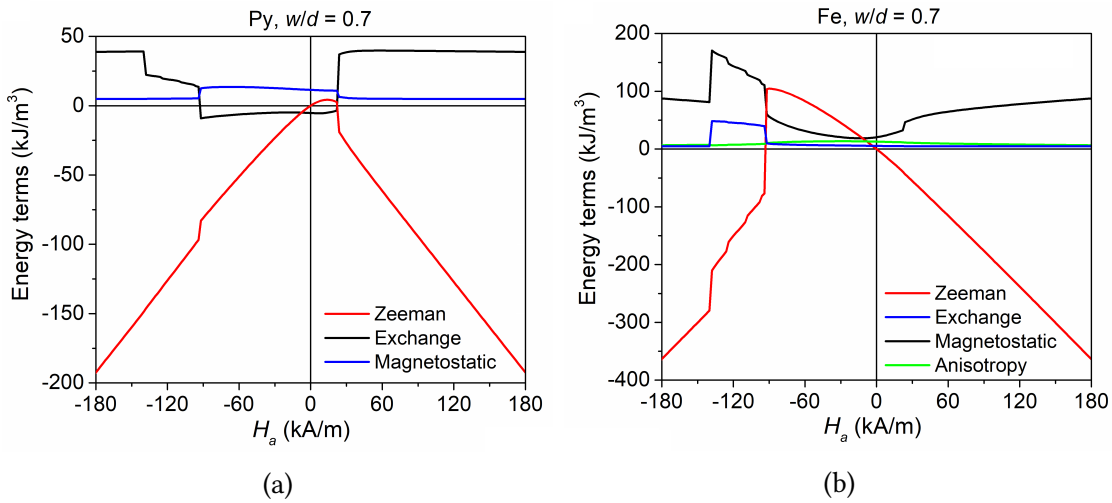

Figure 7.3: Zeeman, exchange, magnetostatic and anisotropy (when present) energy densities versus applied field for (a) permalloy lens and (b) iron crescent, calculated for w/d = 0.7. The energy term evolution is evaluated along the y-axis loop descending branch.

a stepped motion with well-defined positions can be understood by analyzing the energy density terms versus the applied field, separately calculated for the two magnetic regions (Fig. 7.3 for w/d = 0.7). Before the first irreversible jump, the magnetization curls forming a C-state, which will govern the chirality of the successive vortex. In particular, the magnetization mainly curls in the permalloy region and rotates internally following the shape of the permalloy-iron interface: this will always lead to a counterclockwise (CCW) chirality when the field is swept from positive to negative values and to a clockwise (CW) chirality for the opposite branch of the hysteresis loop. The C-state formation is accompanied by a reduction in magnetostatic energy in the iron crescent and in a slight increase in the same energy term in the permalloy lens, as a consequence of the generation of magnetic poles along the disk left boundary (Fig. 7.4).

Contemporary, magnetic poles appear at the permalloy-iron interface. The vortex nucleation during the first irreversible jump leads to a strong reduction in the magnetostatic energy in the permalloy lens, thanks to the disappearance of the lateral magnetic poles. At the irreversible jump end (equilibrium point #B), the vortex locates internally to the permalloy lens at a position that enables to reduce as much as possible the magnetostatic volume integral in the permalloy region. Contextually, also the magnetostatic energy in the iron region decreases, due to the greater curling of the magnetization caused by vortex closure. Finally, the vortex formation is accompanied by a steep increase in the exchange and Zeeman energies in the permalloy lens.

Between the first and second irreversible jump, there is an ulterior reduction in the magnetostatic energy in permalloy, since the vortex motion towards the interface contributes to a greater alignment of the magnetization with the magnetostatic field. At the end of the second irreversible jump (equilibrium point #D) the magnetization in permalloy is completed. This leads to an increment of the relative magnetostatic energy, since magnetostatic field and magnetization become antiparallel. In the iron crescent there is a reduction in the magnetostatic energy due to the presence of the vortex, which remains anchored to a position that allows the minimization of the magnetostatic volume integral. At the same time, the exchange energy increases (decreases) in iron (permalloy) with an amount larger in permalloy, due to its higher exchange constant.

Between the second and third irreversible jump, the magnetostatic energy increases both in permalloy and iron regions, since with the vortex motion towards the disk right boundary there is an enlargement of the areas where magnetization and magnetostatic field are antiparallel. At the end of the third irreversible jump (equilibrium point #F), the C-state forms again, leading to an increment of the magnetostatic energy in the permalloy lens, due to magnetic pole generation, and to a reduction in the same energy term in iron, consequent to a greater magnetization curling.

It is also interesting to point out that for disks with exchanged features (lens in iron and crescent in permalloy) the vortex shows a CW chirality when the field is swept

from positive to negative values and a CCW chirality for the opposite hysteresis loop branch (schematic in Fig. 7.5). The vortex chirality is driven again by the previous C-state configuration, which mainly curls in the permalloy region and follows internally the permalloy-iron interface (Fig. 7.6). In addition, also in this case the C-state governs the formation site of the vortex, which appears always in permalloy and then moves towards iron region.

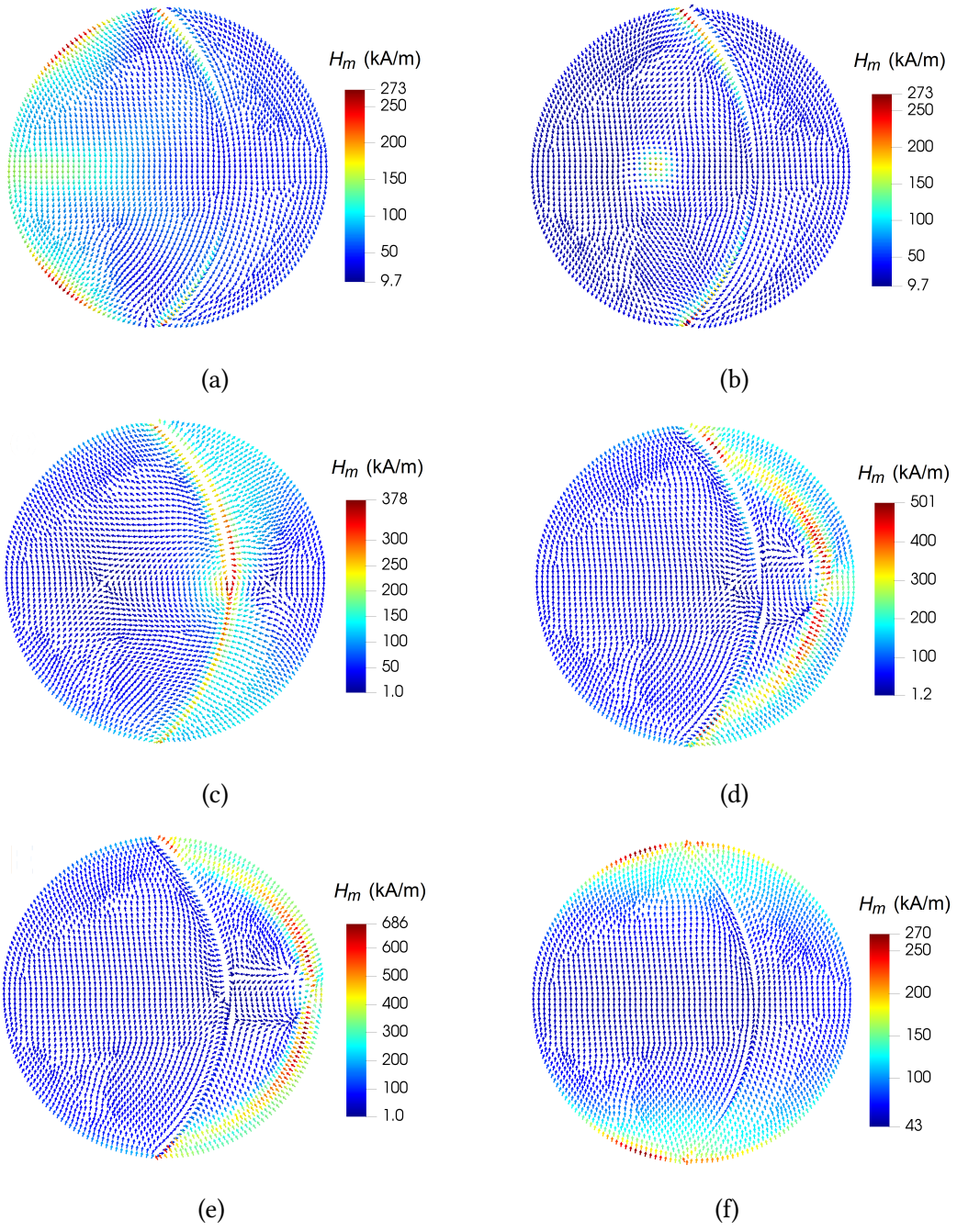

Figure 7.4: Spatial distributions of the magnetostatic field at the equilibrium points along y-axis hysteresis loop descending branch (Fig. 7.1b) , calculated for w/d = 0.7. The color bars represent the amplitude of the magnetostatic field, while the arrows indicate its direction.

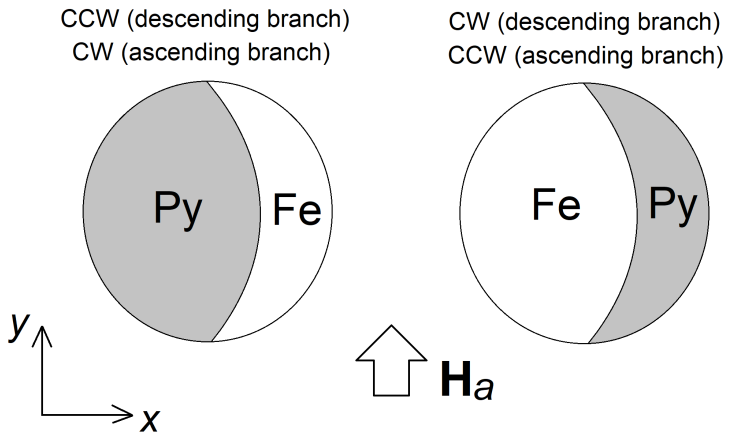

Figure 7.5: Schematic of vortex chirality as a function of nanodisk geometrical configuration and y-axis applied field direction (ascending or descending hysteresis loop branch). For the bi-component disk with permalloy lens and iron crescent (left) the chirality is CCW for the descending branch (from positive to negative field) and CW for the ascending branch (from negative to positive field). For the structure with iron lens and permalloy crescent (right) the chirality is CW for the descending branch and CCW for the ascending branch.

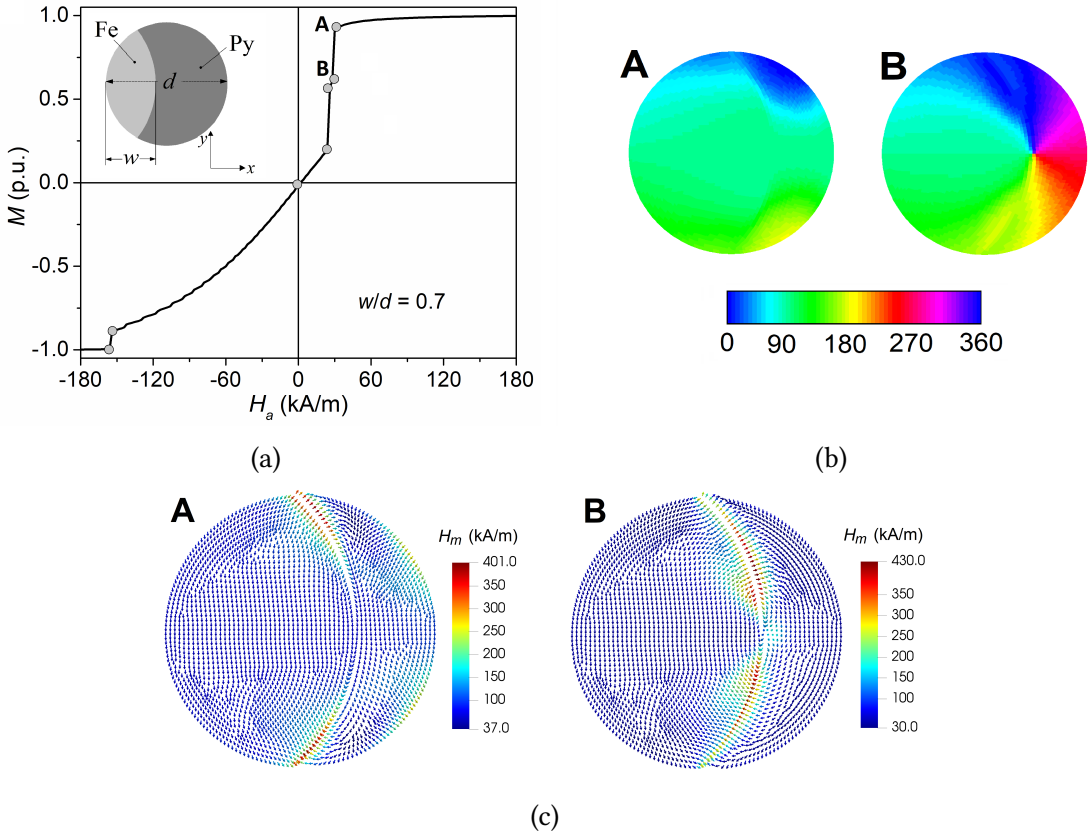

Figure 7.6: (a) Descending branch of the y-axis hysteresis loop of a bi-component nanodisk with iron lens and permalloy crescent (inset), calculated for w/d = 0.7. (b) Magnetization configurations at the equilibrium points #A and #B; the color bar represents the angle, in degrees, between magnetization vector and x-axis. The map at equilibrium point #A illustrates C-state formation, with the magnetization that mainly curls in the permalloy region and follows internally the permalloy-iron interface. This results in a CW rotation of the magnetization and thus in a vortex with CW chirality (equilibrium point #B). (c) Spatial distributions of the magnetostatic field at the same equilibrium points; the color bars represent the amplitude of the magnetostatic field, while the arrows indicate its direction. The C-state is associated with the generation of magnetic poles along the disk right boundary (permalloy side). Contemporary, magnetic poles appear at the permalloy-iron interface. The vortex nucleation during the first irreversible jump leads to a strong reduction in the magnetostatic energy in the permalloy crescent, thanks to the disappearance of the lateral magnetic poles (on the right boundary).

7.3 Analysis of bi-material nanodisks arranged in 2D array form

As illustrated in Fig. 7.1b for the disks with permalloy lens and iron crescent, the shape of the y-axis loops is strongly influenced by parameter w, whose variation leads to a modulation of the applied field range between vortex nucleation and expulsion, thus affecting vortex stability. A more stable vortex state is found for w/d = 0.2-0.5, corresponding to a larger field interval between nucleation and expulsion. This feature can be exploited in 2D arrays where the magnetostatic interactions between disks can cause a detriment of vortex stability. To analyze this effect, we have calculated the y-axis loops of strongly packed disks, with a spacing s (distance between boundaries) equal to 30 nm and 50 nm. Some of the results obtained for s = 30 nm are shown in Fig. 7.7, which reports the hysteresis loops of 2D arrays of both homogeneous disks (made of permalloy or iron) and bi-component disks with $w/d = 0.5$. It is important to note that also when tightly packed, the loop shape of the considered bi-component disks is slightly altered with respect to single disk case. As a consequence, also the remanence magnetization

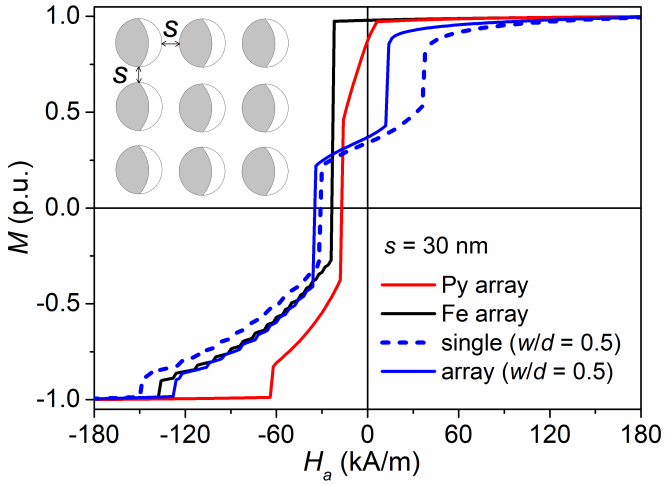

Figure 7.7: Influence of interdisk magnetostatic coupling on the shape of the hysteresis loop of 2D arrays, when considering an interdisk spacing s of 30 nm. The graph compares the results obtained for homogeneous disks to the ones of bi-component disks with w/d = 0.5. Magnetization is normalized to saturation value.

is weakly modified when passing from single to 2D array arrangement, as summarized in Fig. 7.8a. On the contrary, it results strongly altered for the case of 2D arrays made of homogeneous disks: for both homogeneous iron disks ($w/d = 0$) and homogeneous permalloy disks ($w/d = 1$) the remanent magnetization is very close to saturation value. For the bi-component nanodisks we see from the same plot that the vortex magnetization configuration at remanence is preserved in the range $w/d = [0.2 - 0.7]$ for an interdisk distance of 50 nm (blue zone) and in the range $w/d = [0.4 - 0.6]$ for an interdisk distance of 30 nm (red zone). This behavior is well described in Fig. 7.8a, which shows the remanent magnetization configurations for $w/d = 0.3$ calculated for the single nanodisk and for the two considered distances s. From top to bottom, the isolated disk presents the typical vortex configuration, for $s = 50$ nm we still have a vortex configuration displaced towards the disk left side because of the magnetostatic interactions that cause a delay on the vortex motion, for $s = 30$ nm the vortex state disappears. We can conclude that, for very low inter-disk spacing, the vortex state at zero field remains practically unperturbed only for bi-component arrays with $w \sim d/2$ (see Fig. 7.8).

This behavior, showing higher vortex stability, is further confirmed by the data shown in Fig. 7.9, which illustrates the influence of parameter w and inter-disk spacing s on vortex nucleation and expulsion fields and on the amplitude ΔH of the field interval between vortex nucleation and expulsion. In particular,when w/d = 0.2-0.5, the reduction in inter-disk spacing has a moderate effect on ΔH, which is characterized by a relative small decrease, confirming the high vortex stability also for strongly packed systems. On the contrary, this field range is strongly reduced for arrays composed of homogenous disks; as an example, when s = 30 nm, ΔH reduces by 50% for iron disks. For permalloy disks the reduction is lower, in the order of 20%, but in this case the vortex stability is reduced also for the single case, being characterized by a a low value of ΔH.

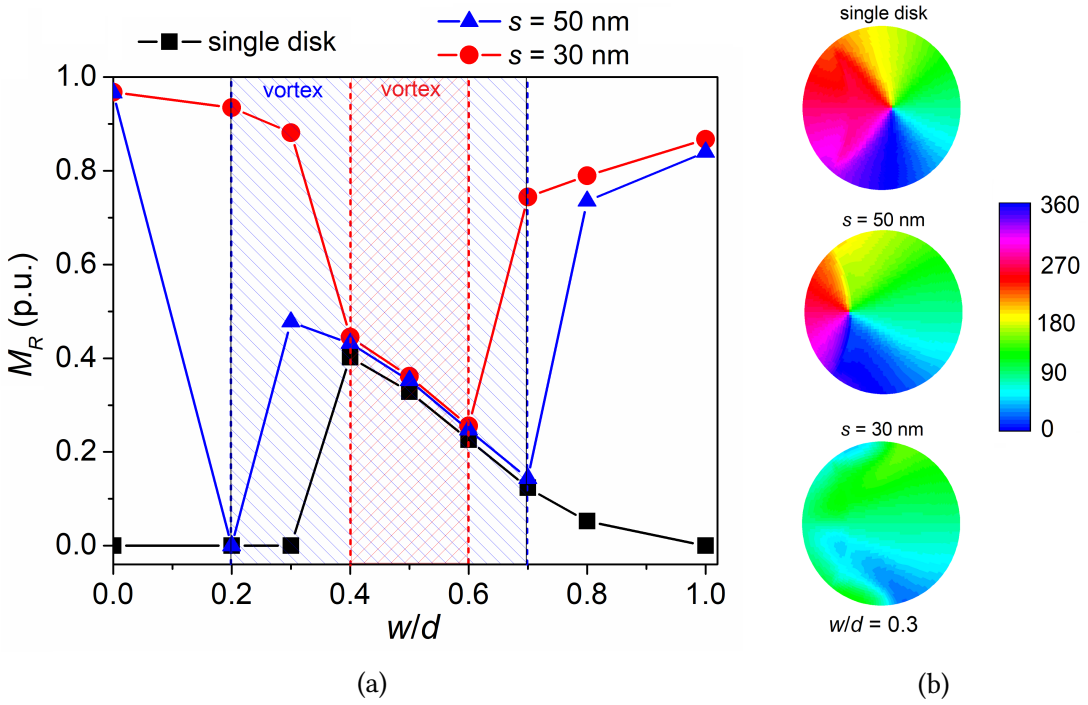

Figure 7.8: (a) Influence of interdisk magnetostatic coupling on the remanent magnetization value. The graph compares the results obtained for single disks to the ones of 2D arrays with s fixed to 30 nm and 50 nm. (b) Remanence magnetization configurations for single nanodisks (top) and 2D arrays with s equal to 50 nm (center) and 30 nm (bottom), setting w/d at 0.3. The color bar represents the angle, in degrees, between magnetization vector and x-axis.

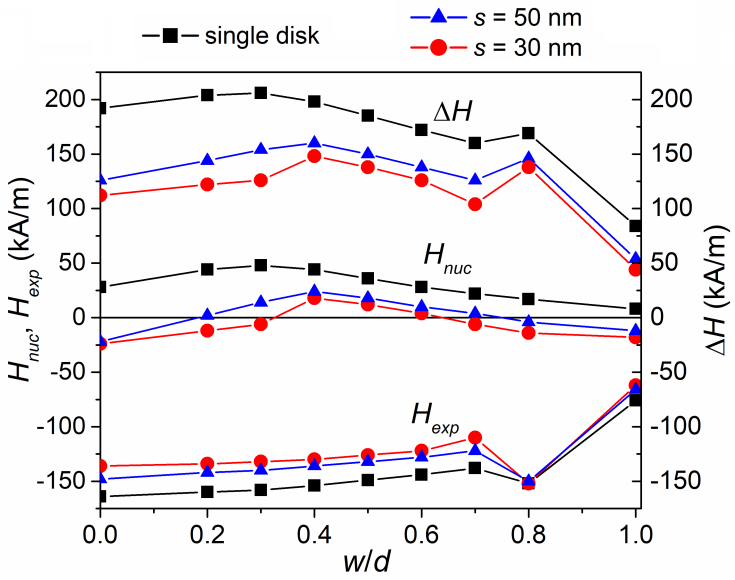

Figure 7.9: Effect of parameter w and interdisk spacing s on vortex nucleation field H_{nuc}, vortex expulsion field H_{exp} and amplitude ΔH of the field interval between vortex nucleation and expulsion.

7.4 Conclusions

In this chapter we proposed a detailed analysis of the effects of the shape anisotropy of bi-component nanodisks on vortex nucleation, chirality and stepped motion. In particular, we showed how the local shape anisotropies arising at the two-material interface influence the curling of the magnetization, which is enforced to rotate orthogonally to the interface to reduce magnetostatic energy, enabling the control of vortex chirality. This happens when the switching field is applied parallel to the interface. Moreover, these nanodisks present high vortex stability when disposed in bi-dimensional arrays, when compared to the mono-material counterparts.

Another advantage regards the possibility of monitoring the vortex position inside the disk through the intermediate irreversible jump and the associated vortex anchorage to the interface.

All these properties make bi-material nanodisks a potential candidate as magnetic recording units for MRAM devices. The ability of controlling the chirality is a very suitable feature for the application in magnetic recording, allowing the development of systems for the single bit storage. Moreover, the large vortex stability in closed pack arrays allows the development of densely packed memories, with elevated storage capacities.

References

[1] J. W. Lau and J. M. Shaw. "Magnetic nanostructures for advanced technologies: fabrication, metrology and challenges". In: *J. Phys. D. Appl. Phys.* 44.30 (July 2011), p. 303001. DOI: 10.1088/0022-3727/44/30/303001.

[2] R. Hertel. "Vortex states à la carte". In: *Nat. Nanotechnol.* 8.5 (May 2013), pp. 318–320. ISSN: 1748-3387. DOI: 10.1038/nnano.2013.81.

[3] Y. Zheng and W. J. Chen. "Characteristics and controllability of vortices in ferromagnetics, ferroelectrics, and multiferroics". In: *Reports on Progress in Physics* 80.8 (June 2017), p. 086501. DOI: 10.1088/1361-6633/aa5e03.

[4] R. K. Dumas et al. "Chirality control via double vortices in asymmetric Co dots". In: *Phys. Rev. B* 83 (6 Feb. 2011), p. 060415. DOI: 10.1103/PhysRevB.83.060415.

[5] M. Schneider, H. Hoffmann, and J. Zweck. "Magnetic switching of single vortex permalloy elements". In: *Appl. Phys. Lett.* 79.19 (2001), pp. 3113–3115. DOI: 10.1063/1.1410873.

[6] T. Kimura et al. "Vortex motion in chilarity-controlled pair of magnetic disks". In: *Appl. Phys. Lett.* 90.13 (2007), p. 132501. DOI: 10.1063/1.2716861.

[7] M. Jaafar et al. "Control of the chirality and polarity of magnetic vortices in triangular nanodots". In: *Phys. Rev. B* 81 (5 Feb. 2010), p. 054439. DOI: 10.1103/PhysRevB.81.054439.

[8] S. Yakata et al. "Control of vortex chirality in regular polygonal nanomagnets using in-plane magnetic field". In: *Appl. Phys. Lett.* 97.22 (2010), p. 222503. DOI: 10.1063/1.3521407.

[9] Y. Wen et al. "Fast and controllable switching the circulation and polarity of magnetic vortices". In: *J. Magn. Magn. Mater.* 370 (2014), pp. 68–75. ISSN: 0304-8853. DOI: 10.1016/j.jmmm.2014.06.049.

[10] V. Cambel and G. Karapetrov. "Control of vortex chirality and polarity in magnetic nanodots with broken rotational symmetry". In: *Phys. Rev. B* 84 (1 July 2011), p. 014424. DOI: 10.1103/PhysRevB.84.014424.

[11] S. Agramunt-Puig et al. "Controlling vortex chirality and polarity by geometry in magnetic nanodots". In: *Appl. Phys. Lett.* 104.1 (2014), p. 012407. DOI: 10.1063/1.4861423.

[12] V. Uhlír et al. “Dynamic switching of the spin circulation in tapered magnetic nanodisks”. In: *Nature Nanotechnology* 8 (Apr. 2013). Article, 341 EP -. DOI: 10.1038/nnano.2013.66.

[13] G. Shimon, A. O. Adeyeye, and C. A. Ross. “Magnetic vortex dynamics in thickness-modulated $Ni_{80}Fe_{20}$ disks”. In: *Phys. Rev. B* 87 (21 June 2013), p. 214422. DOI: 10.1103/PhysRevB.87.214422.

[14] A. S. Jenkins et al. “Controlling the chirality and polarity of vortices in magnetic tunnel junctions”. In: *Appl. Phys. Lett.* 105.17 (2014), p. 172403. DOI: 10.1063/1.4900743.

[15] G. Shimon, A. O. Adeyeye, and C. A. Ross. “Reversal mechanisms of coupled bi-component magnetic nanostructures”. In: *Appl. Phys. Lett.* 101.8 (2012), p. 083112. DOI: 10.1063/1.4747446.

[16] A. Manzin and O. Bottauscio. “A Micromagnetic Solver for Large-Scale Patterned Media Based on Non-Structured Meshing”. In: *IEEE Trans. Magn.* 48.11 (Nov. 2012), pp. 2789–2792. ISSN: 0018-9464. DOI: 10.1109/TMAG.2012.2195648.

[17] O. Bottauscio and A. Manzin. “Parallelized micromagnetic solver for the efficient simulation of large patterned magnetic nanostructures”. In: *J. Appl. Phys.* 115.17 (2014), p. 17D122. DOI: 10.1063/1.4862379.

[18] A. Manzin and O. Bottauscio. “Connections between numerical behavior and physical parameters in the micromagnetic computation of static hysteresis loops”. In: *J. Appl. Phys.* 108.9 (2010), p. 093917. DOI: 10.1063/1.3503873.

[19] O. Bottauscio and A. Manzin. “Efficiency of the Geometric Integration of Landau–Lifshitz–Gilbert Equation Based on Cayley Transform”. In: *IEEE Trans. Magn.* 47.5 (May 2011), pp. 1154–1157. ISSN: 0018-9464. DOI: 10.1109/TMAG.2010.2095831.

[20] O. Bottauscio and A. Manzin. "Spatial Reconstruction of Exchange Field Interactions With a Finite Difference Scheme Based on Unstructured Meshes". In: *IEEE Trans. Magn.* 48.11 (Sept. 2012), pp. 3250–3253. ISSN: 0018-9464. DOI: 10.1109/TMAG.2012.2197738.

[21] O. Bottauscio, M. Chiampi, and A. Manzin. "Micromagnetic numerical analysis of magnetization processes in patterned ferromagnetic films". In: *J. Appl. Phys.* 105.7 (2009), p. 07D530. DOI: 10.1063/1.3072376.

[22] A. Manzin and O. Bottauscio. "Micromagnetic modelling of the anisotropy properties of permalloy antidot arrays with hexagonal symmetry". In: *J. Phys. D. Appl. Phys.* 45.9 (Feb. 2012), p. 095001. DOI: 10.1088/0022-3727/45/9/095001.

Chapter 8

Conclusions

In this thesis the hysteretic behavior of magnetic nanostructures has been studied in connection with magnetically mediated hyperthermia therapies. The analysis has been performed by means of a numerical modeling approach, based on the micromagnetic theory and, specifically, on the Landau-Lifshitz-Gilbert equation, which describes the magnetization dynamics at a sub-micrometric length scale.

The main objective of the study has been to investigate the magnetization reversal processes, remanent state and hysteresis losses of magnetic nanostructures, in order to find efficient heat mediators, which can be used in alternative to SPIONs. Initially, we have analyzed the hyperthermia properties of permalloy nanodisks, conducting a detailed modeling study supported by experimental results (measured hysteresis loops) obtained on nanodisks in an intermediate stage of the fabrication process (attached on the substrate) as well as on free-standing nanodisks (dispersed in solution). Permalloy nanodisks showed some interesting properties for our application beyond their ability to generate a large amount of heat, due to the wide area of the hysteresis loop. In particular, they present a vortex remanence configuration, which is very advantageous for hyperthermia application, since it is able to minimize particle-particle magnetic interaction at zero field, greatly reducing the risk of aggregation and favoring a uniform

dispersion in the target tissue. The results of the comparison with the experimental results prove the ability of our numerical models to accurately reconstruct the magnetic properties of these nanostructures in real operative conditions.

To further expand our analysis it was necessary to develop specific micromagnetic numerical tools able to evaluate the heating efficiency of thin-film like nanostructures randomly dispersed in a 3D medium (2.5D code) as well as to model three-dimensional nanostructures (3D code). Thanks to the flexibility of the developed numerical tools, we were able to perform a comparison between nanodisks, nano-cylinders and nanospheres, assessing their hysteretic and heating properties, as a function of size. From the results of the detailed simulation analysis, nanodisks emerge as the nanostructures with the most suitable properties for hyperthermia. Nanocylinders, as an intermediate solution between nanospheres and nanodisks, did not show relevant advantages neither in terms of heating performance nor in terms of fulfillment of the biological constraints on the applied field parameters. Nanospheres proved to be good heat generators, in some case with performance comparable to nanodisks, but they require very high AC fields to achieve the same amount of losses. Nanodisks provide an elevated loss contribution, and a vortex remanence configuration (not present in the nanospheres and in the thick nanocylinders).

Focusing on nanodisks, an extensive parametric analysis has been performed analyzing the effect on the hysteresis loop of thickness (15-30 nm) and diameter (100-800 nm), trying to find the optimal parameters that maximize the loop area, without increasing too much the vortex expulsion field and thus the saturation field. Further analysis with the help of the 2.5D code allowed us to investigate how the hysteresis losses are affected by different parameters, like the local concentration of nanostructures, their mutual magnetostatic interactions and their relative orientation with the applied field, which can be strongly variable in a real distribution. This analysis enabled us to simulate more realistic hyperthermia conditions, trying to mimic the stochastic dispersion of nanomaterials in a tissue or in a biological fluid. All the above parameters not only concur to modify

the area of the hysteresis loop, but also its shape and the values of the fields necessary to reach the irreversible jumps, which govern vortex nucleation and expulsion.
One of the critical aspect of our analysis depends on the limits imposed by the biological application. Losses due to hysteresis are significant only if certain values of the applied field, corresponding to the irreversible jumps in the hysteresis loop, are reached. Hence, it derives the need to characterize accurately the hysteresis loops of the nanostructures. In literature, there is not yet a consensus on the actual limitation of the range of applicable fields for this application. This is because depending on the treated region and the kind of applicator (focusing the field around the region of interest, or investing the whole body) this limit can vary substantially. Since the heat deposition in the tissue depends also on the magnetic field applied to the nanostructures, a direct comparison between data find in literature is often difficult. In fact, right now, one of the major problems that the scientific community working on in vivo magnetic hyperthermia faces is the difficulty to compare results from different laboratories, as little attention has been paid to the standardization of protocols.
Computational simulated models of in vivo heat dissipation will be essential for the development of more reliable, tumor specific, personalized and efficient treatment planning. The data on the specific losses obtained in this thesis can be used as input parameters for this kind of models, which are based on the bioheat or Pennes equation. Assuming a distribution of nanoparticles into the tumor, it will be possible to analyze the variation of temperature in the tissues. From this simulation, one can obtain important data regarding the duration of the treatment necessary to heat the cancerous tissue, or evaluate if the administered dose of nanostructures in a particular location of the tumor is sufficient to reach the therapeutic temperature, possibly enhancing the efficacy of the treatments.
In the last part of the thesis, we focus the attention on another technical application of magnetic nanodisks, presenting a study on the control of the vortex chirality in bimaterial (iron-permalloy) nanodisks. This study is of interest for its potential application

in high-density magnetic recording, where nanostructures showing stable vortex state at remanence can be used as units for bit storage. In this case the bit is coded by the chirality of the vortex. We show how bi-component nanodisks, through the application of a magnetic field parallel to the material interface, allow us the control of the nucleation of the vortex (always occurring in permalloy region), its motion up to the expulsion site and its chirality. Moreover, by studying both single and 2D array arrangements of nanodisks, it is possible to identify the optimal fraction of materials to obtain better vortex stability as well as to control the minimum field value necessary to change the vortex chirality.

Appendix A

Lie algebras and geometrical integrators

Let us analyze the generalized version of the LLG equation (2.81) as rewritten in Chapter 3:

$$\dot{\mathbf{M}}(\mathbf{r},t) = \mathbf{A}(\mathbf{M}(\mathbf{r},t)) \times \mathbf{M}(\mathbf{r},t) \tag{A.1}$$

From the form of the equation it is easy to verify the following constraint:

$$||\mathbf{M}(\mathbf{r},t)|| = \text{const.} \;\; \forall t \in \mathbb{R}, \;\; \forall \mathbf{r} \in \Omega \tag{A.2}$$

This constraint on the module of $\mathbf{M}$ can be reformulated with the following geometrical interpretation:

$$\mathbf{M}(\mathbf{r},t) : \Omega \rightarrow S^2 \;\; \forall t \tag{A.3}$$

which means that the magnetization is able to evolve only on a sphere (S^2 in the case of a problem in $\mathbb{R}^3$). Therefore, the evolution of $\mathbf{M}$ can be described as a rotation. Since $SO(3)$ is the group of all rotations around the origin of three-dimensional Euclidean space $\mathbb{R}^3$ under the operation of composition, any given point belonging to S^2 can be mapped in any other point of S^2 with a rotation of $SO(3)$. Thus, there exists a time

dependent curve that, for every point in the domain Ω, associates the rotation in $SO(3)$ [1, 2], satisfying

$$Q(t) : \Omega \rightarrow SO(3) \ / \ \mathbf{M}(\mathbf{r}, t) = Q(\mathbf{r}, t)\mathbf{M}_0(\mathbf{r}), \quad \forall \mathbf{r} \in \Omega \tag{A.4}$$

where $\mathbf{M}_0(\mathbf{r})$ is the magnetization vector at time instant $t = 0$. Within this space setting, Lie Groups and Lie Algebras are the mathematical tools necessary to understand the problem properties and derive the time-integration scheme. Let us now introduce some definitions of space and groups that we will use in the derivation of the method.

Definition A.1. A Lie algebra $\mathfrak{g}$ is a vector space over a field $\mathbb{F}$, where it is defined a bilinear operation$[\cdot, \cdot]$ verifying the following properties:

- **bilinearity**: $[ax + by, z] = a[x, z] + b[y, z]$, $\forall a, b \in \mathbb{R}$ and $x, y, z \in \mathfrak{g}$
- **alternativity**: $[x, x] = 0 \ \forall x \in \mathfrak{g}$
- **Jacoby identity**: $[x, [y, z]] + [z, [x, y]] + [y, [z, x]] = 0 \ \forall x, y, z \in \mathfrak{g}$
- **anticommutativity**: $[x, y] = -[y, x] \ \forall x, y \in \mathfrak{g}$

Definition A.2. A Lie Group is a differentiable manifold G that is also a group, such that the group product

$$G \times G \longrightarrow G$$

and the inverse map $g \rightarrow g^{-1}$ are differentiable.

Definition A.3. A matrix Lie Group is a closed subgroup of the invertible matrices. It is possible to prove that a matrix Lie Group is also a Lie Group.

Property A.1. Let G be a matrix Lie group. Then the Lie algebra of G, denoted $\mathfrak{g}$, is the set of all matrices X such that e^{tX} is in G for all real numbers t.

It is easy to verify that $\mathbb{R}^3$ with its classic vector product is a Lie algebra. The group $SO(3)$ is a matrix Lie Group (namely the group of 3×3 orthogonal matrices with

determinant equal to one), therefore it is a Lie Group and it is possible to define a Lie Algebra on it. It is possible to prove, by using the property (A.1), that the Lie Algebra of $SO(3)$, denoted as $\mathfrak{so}(3)$, is the set of the 3×3 antisymmetric matrices with the following operation, as

$$[X, Y] = XY - YX \quad \forall X, Y \in \mathfrak{so}(3). \tag{A.5}$$

Moreover, we have that between the Lie algebra on $\mathbb{R}^3$ and $\mathfrak{so}(3)$ there exists an isomorphism, which can be written as

$$\begin{aligned} skew : \mathbb{R}^3 &\longrightarrow \mathfrak{so}(3) \\ \boldsymbol{\xi} &\longmapsto skew[\boldsymbol{\xi}] \end{aligned} \tag{A.6}$$

$$skew[\boldsymbol{\xi}] = \begin{pmatrix} 0 & -\xi_3 & \xi_2 \\ \xi_3 & 0 & -\xi_1 \\ -\xi_2 & \xi_1 & 0 \end{pmatrix} \tag{A.7}$$

If we consider the curve $Q(t) \in SO(3)$, it is possible to obtain an expression for its derivative using the orthogonality property

$$Q(t)Q(t)^T = I$$

Now, the calculation of the derivative on both sides of the equation leads to

$$\dot{Q}Q^T + (\dot{Q}Q^T)^T = 0 \tag{A.8}$$

Therefore $\dot{Q}Q^T$ is an antisymmetric matrix. Right multiplying both sides of the last equation by Q yields

$$\dot{Q} = (\dot{Q}Q^T)Q. \tag{A.9}$$

Because $\dot{Q}Q^T$ is a skew matrix and there exists the isomorphism (A.6) it is possible to

find a function $\xi(t) \in \mathbb{R}$ such that:

$$\dot{Q}(t) = skew[\xi(t)]Q(t). \tag{A.10}$$

Looking now at the initial problem formulated in Eq.(A.4) and differentiating it, one has

$$\dot{\mathbf{M}}(t) = \dot{Q}(t)\mathbf{M}_0. \tag{A.11}$$

Performing the opportune substitution, replacing the expression of $\dot{Q}(t)$ from equation (A.10) in equation (A.11) leads to:

$$\dot{\mathbf{M}}(t) = skew[\xi(t)]\mathbf{M}(t) \tag{A.12}$$

$$\dot{\mathbf{M}}(t) = \xi(t) \times \mathbf{M}(t) \tag{A.13}$$

With the presented results we can explain the connection between our constrained problem in $\mathbb{R}^3$ and the family of curves in $SO(3)$. Starting from here, it is possible to derive a variety of geometrical integrators. In our micromagnetic codes we chose to use the Cayley transform, as detailed in Chapter 3.

[1] D. Lewis and N. Nigam. "Geometric integration on spheres and some interesting applications". In: *J. Comput. Appl. Math.* 151.1 (2003), pp. 141–170. ISSN: 03770427. DOI: 10.1016/S0377-0427(02)00743-4.

[2] D. Lewis and J. C. Simo. "Conserving algorithms for the dynamics of Hamiltonian systems on lie groups". In: *J. Nonlinear Sci.* 4.1 (1994), pp. 253–299. ISSN: 09388974. DOI: 10.1007/BF02430634.

Appendix B

Green tensor computation

In the following we present the Green tensor elements for the direct computation of the magnetostatic field, according to the formulation proposed by Nakatani [1]

B.1 Nakatani analytical formulas

$$g_{xx}(I,J,K) = \sum_{i=0}^{1}\sum_{j=0}^{1}\sum_{k=0}^{1}(-1)^{i+j+k}\tan^{-1}\left|\frac{\left(K+k-\frac{1}{2}\right)\left(J+j-\frac{1}{2}\right)\delta z\delta y}{r_{i,j,k}\left(I+i-\frac{1}{2}\right)\delta x}\right| \tag{B.1}$$

$$g_{yy}(I,J,K) = \sum_{i=0}^{1}\sum_{j=0}^{1}\sum_{k=0}^{1}(-1)^{i+j+k}\tan^{-1}\left|\frac{\left(K+k-\frac{1}{2}\right)\left(I+i-\frac{1}{2}\right)\delta z\delta x}{r_{i,j,k}\left(J+j-\frac{1}{2}\right)\delta y}\right| \tag{B.2}$$

$$g_{zz}(I,J,K) = \sum_{i=0}^{1}\sum_{j=0}^{1}\sum_{k=0}^{1}(-1)^{i+j+k}\tan^{-1}\left|\frac{\left(I+i-\frac{1}{2}\right)\left(J+j-\frac{1}{2}\right)\delta x\delta y}{r_{i,j,k}\left(K+k-\frac{1}{2}\right)\delta z}\right| \tag{B.3}$$

$$g_{xy}(I,J,K) = \sum_{i=0}^{1}\sum_{j=0}^{1}\sum_{k=0}^{1}(-1)^{i+j+k}\log\left|\left(K+k-\frac{1}{2}\right)\delta z + r_{i,j,k}\right| \tag{B.4}$$

$$g_{yz}(I,J,K) = \sum_{i=0}^{1}\sum_{j=0}^{1}\sum_{k=0}^{1}(-1)^{i+j+k}\log\left|\left(I+i-\frac{1}{2}\right)\delta x + r_{i,j,k}\right| \tag{B.5}$$

$$g_{xz}(I,J,K) = \sum_{i=0}^{1}\sum_{j=0}^{1}\sum_{k=0}^{1}(-1)^{i+j+k}\log\left|\left(J+j-\frac{1}{2}\right)\delta y + r_{i,j,k}\right| \tag{B.6}$$

$$r_{i,j,k} = \sqrt{\left(I+i-\frac{1}{2}\right)^2\delta x^2 + \left(J+j-\frac{1}{2}\right)^2\delta y^2 + \left(K+k-\frac{1}{2}\right)^2\delta z^2} \tag{B.7}$$

B.2 Green surface integral

The integral used to compute the magnetostatic field in Eq. 3.38 becomes using the Gauss theorem :

$$\mathbf{H}_{ms}(\mathbf{r}_i) = -\frac{M_s}{4\pi}\sum_{\substack{j=1\\ i\neq j}}^{N}\int_{\partial\mathcal{V}'}\frac{\mathbf{r}_i-\mathbf{r}_j}{|\mathbf{r}_i-\mathbf{r}_j|^3}\cdot\mathbf{n}dS. \tag{B.8}$$

The component of the green tensor can be easily computed as

$$\begin{aligned} g_{xx}(I,J,K) = \int_{-1}^{1}\int_{-1}^{1}&\frac{I+1}{[(I+1)^2+(J+\eta)^2+(K+\zeta)^2]} \\ &-\frac{I-1}{[(I-1)^2+(J+\eta)^2+(K+\zeta)^2]}d\eta d\zeta, \end{aligned} \tag{B.9}$$

$$\begin{aligned} g_{yy}(I,J,K) = \int_{-1}^{1}\int_{-1}^{1}&\frac{J+1}{[(I+\xi)^2+((J+1)^2+(K+\zeta)^2]} \\ &-\frac{J-1}{[(I+\xi)^2+(J-1)^2+(K+\zeta)^2]}d\xi d\zeta, \end{aligned} \tag{B.10}$$

$$\begin{aligned} g_{zz}(I,J,K) = \int_{-1}^{1}\int_{-1}^{1}&\frac{K+1}{[(I+\xi)^2+(J+\eta)^2+(K+1)^2]} \\ &-\frac{K-1}{[(I+\xi)^2+(J+\eta)^2+(K-1)^2]}d\xi d\eta, \end{aligned} \tag{B.11}$$

$$g_{xy}(I,J,K) = \int_{-1}^{1}\int_{-1}^{1} \frac{J+\eta}{[(I+1)^2+(J+\eta)^2+(K+\zeta)^2]} - \frac{J+\eta}{[(I-1)^2+(J+\eta)^2+(K+\zeta)^2]} d\eta d\zeta, \tag{B.12}$$

$$g_{xz}(I,J,K) = \int_{-1}^{1}\int_{-1}^{1} \frac{K+\zeta}{[(I+1)^2+(J+\eta)^2+(K+\zeta)^2]} - \frac{K+\zeta}{[(I-1)^2+(J+\eta)^2+(K+\zeta)^2]} d\eta d\zeta, \tag{B.13}$$

$$g_{yz}(I,J,K) = \int_{-1}^{1}\int_{-1}^{1} \frac{K+\zeta}{[(I+\xi)^2+(J+1)^2+(K+\zeta)^2]} - \frac{K+\zeta}{[(I+\xi)^2+(J-1)^2+(K+\zeta)^2]} d\xi d\zeta, \tag{B.14}$$

[1] Y. Nakatani, Y. Uesaka, and N. Hayashi. "Direct solution of the Landau-Lifshiftz-Gilbert equation for micromagnetics". In: *Jpn. J. Appl. Phys.* 28.12 (1989), pp. 2485–2507. ISSN: 0021-4922. DOI: 10.1143/JJAP.28.2485.

Appendix C

3D Code Kernel

```
MODULE NAKATANIFUNCTIONS

USE GLOBALS
USE PRECISION

CONTAINS

ATTRIBUTES(GLOBAL) SUBROUTINE CUDANAKATANI_KERNELXX(KXXRd,nx,ny,nz,dx,dy,dz)


        integer(4), value :: nx,ny,nz


        real(dp), value :: dx,dy,dz


        real(dp), device :: KXXRd(0:2*nx-1,0:2*ny-1,0:2*nz-1)
        integer :: i,j,k,L,M,N,ii,jj,kk


    i=(blockIdx%x-1)*blockDim%x+(threadIdx%x-1)
        j=(blockIdx%y-1)*blockDim%y+(threadIdx%y-1)
```

```
        k=(blockIdx%z-1)*blockDim%z+(threadIdx%z-1)

        if (i<(2*nx) .and. j<(2*ny) .and. k<(2*nz) ) then
        ii=i
        if (i>nx) ii=i-2*nx
        jj=j
        if (j>ny) jj=j-2*ny
        kk=k
        if (k>nz) kk=k-2*nz
        DO L=0,1
                DO M=0,1
                        DO N=0,1
                        jpowicu=1.0_dp
                        if(mod(L+M+N,2)==1) jpowicu=-1.0_dp

                         KXXRD(i,j,k)=KXXRD(i,j,k)+(jpowicu) * atan (((kk+N- 0.50
                             _dp) * (jj + M - 0.50_dp) * dz * dy / (sqrt(((ii+L
                             -0.50_dp)*dx)**2 + ((jj+M-0.50_dp)*dy)**2 + ((kk+N
                             -0.50_dp)*dz)**2) * (ii + L - 0.50_dp) * dx)))

                        ENDDO
                ENDDO
        ENDDO
end if
END SUBROUTINE

ATTRIBUTES(GLOBAL) SUBROUTINE CUDANAKATANI_KERNELXY(offset,KXYRd,nx,ny,nz,dx,dy,
    dz)

        integer, value :: offset,nx,ny,nz
        real(dp), value :: dx,dy,dz
        real(dp), device :: KXYRd(0:2*nx-1,0:2*ny-1,0:2*nz-1)
        integer :: i,j,k,L,M,N,ii,jj,kk
```

```
        i=(blockIdx%x-1)*blockDim%x+(threadIdx%x-1)
        j=(blockIdx%y-1)*blockDim%y+(threadIdx%y-1)
        k=(blockIdx%z-1)*blockDim%z+(threadIdx%z-1)

        if (i<(2*nx) .and. j<(2*ny) .and. k<(2*nz) ) then
        ii=i
        if (i>nx) ii=i-2*nx
        jj=j
        if (j>ny) jj=j-2*ny
        kk=k
        if (k>nz) kk=k-2*nz

        DO L=0,1
                DO M=0,1
                        DO N=0,1
                        jpowicu=1.0_dp
                        if(mod(L+M+N,2)==1) jpowicu=-1.0_dp
                         KXYRd(i,j,k)=KXYRd(i,j,k)+(jpowicu)*log((kk+N-0.50_dp)*
                             dz+sqrt(((ii+L-0.50_dp)*dx)**2 + ((jj+M-0.50_dp)*dy)
                             **2 +((kk+N-0.50_dp)*dz)**2))
                        ENDDO
                ENDDO
        ENDDO
        !if (i>nx .or. j>ny .or. k>nz) KXYRD(i,j,k)=-1.0_dp*KXYRd(i,j,k)
        KXYRD(i,j,k)=-KXYRd(i,j,k)
        end if

END SUBROUTINE

ATTRIBUTES(GLOBAL) SUBROUTINE CUDANAKATANI_KERNELYY(offset,KYYRd,nx,ny,nz,dx,dy,
    dz)

        integer, value :: offset,nx,ny,nz
```

```
        real(dp), value :: dx,dy,dz
        integer, value :: offset
        real(dp), device :: KYYRd(0:2*nx-1,0:2*ny-1,0:2*nz-1)
        integer :: i,j,k,L,M,N,ii,jj,kk
        i=(blockIdx%x-1)*blockDim%x+(threadIdx%x-1)
        j=(blockIdx%y-1)*blockDim%y+(threadIdx%y-1)
        k=(blockIdx%z-1)*blockDim%z+(threadIdx%z-1)



        if (i<(2*nx) .and. j<(2*ny) .and. k<(2*nz) ) then
        ii=i
        if (i>nx) ii=i-2*nx
        jj=j
        if (j>ny) jj=j-2*ny
        kk=k
        if (k>nz) kk=k-2*nz
        DO L=0,1
                DO M=0,1
                        DO N=0,1
                        jpowicu=1.0_dp
                        if(mod(L+M+N,2)==1) jpowicu=-1.0_dp
                         KYYRD(i,j,k)=KYYRD(i,j,k)+(jpowicu) * atan ((kk+N- 0.50
                             _dp) * (ii + L - 0.50_dp) * dz * dx / (sqrt(((ii+L
                             -0.50_dp)*dx)**2 + ((jj+M-0.50_dp)*dy)**2 + ((kk+N
                             -0.50_dp)*dz)**2) * (jj + M - 0.50_dp) * dx))
                        ENDDO
                ENDDO
        ENDDO


        end if

END SUBROUTINE
```

```
ATTRIBUTES(GLOBAL) SUBROUTINE CUDANAKATANI_KERNELYZ(offset,KYZRd,nx,ny,nz,dx,dy,
    dz)

        integer, value :: offset,nx,ny,nz
        real(dp), value :: dx,dy,dz
        integer, value :: offset
        real(dp), device :: KYZRd(0:2*nx-1,0:2*ny-1,0:2*nz-1)
        integer :: i,j,k,L,M,N,ii,jj,kk
        i=offset+(blockIdx%x-1)*blockDim%x+(threadIdx%x-1)
        j=(blockIdx%y-1)*blockDim%y+(threadIdx%y-1)
        k=(blockIdx%z-1)*blockDim%z+(threadIdx%z-1)
        if (i<(2*nx) .and. j<(2*ny) .and. k<(2*nz) ) then
        ii=i
        if (i>nx) ii=i-2*nx
        jj=j
        if (j>ny) jj=j-2*ny
        kk=k
        if (k>nz) kk=k-2*nz
        DO N=0,1
                DO M=0,1
                        DO L=0,1
                        jpowicu=1.0_dp
                        if(mod(L+M+N,2)==1) jpowicu=-1.0_dp
                         KYZRd(i,j,k)=KYZRd(i,j,k)+((jpowicu) * log (((ii+L- 0.50
                             _dp) * dx + sqrt(((ii+L-0.50_dp)*dx)**2 + ((jj+M
                             -0.50_dp)*dy)**2 + ((kk+N-0.50_dp)*dz)**2) )))
                        ENDDO
                ENDDO
        ENDDO
        KYZRd(i,j,k)=-KYZRd(i,j,k)
        end if
END SUBROUTINE
```

```
ATTRIBUTES(GLOBAL) SUBROUTINE CUDANAKATANI_KERNELZZ(offset,KZZRd,nx,ny,nz,dx,dy,
    dz)

        integer, value :: offset,nx,ny,nz
        real(dp), value :: dx,dy,dz
        integer, value :: offset
        real(dp), device :: KZZRd(0:2*nx-1,0:2*ny-1,0:2*nz-1)
        integer :: i,j,k,L,M,N,ii,jj,kk
        i=offset+(blockIdx%x-1)*blockDim%x+(threadIdx%x-1)
        j=(blockIdx%y-1)*blockDim%y+(threadIdx%y-1)
        k=(blockIdx%z-1)*blockDim%z+(threadIdx%z-1)

        if (i<(2*nx) .and. j<(2*ny) .and. k<(2*nz) ) then
        ii=i
        if (i>nx) ii=i-2*nx
        jj=j
        if (j>ny) jj=j-2*ny
        kk=k
        if (k>nz) kk=k-2*nz
        DO L=0,1
                DO M=0,1
                        DO N=0,1
                        jpowicu=1.0_dp
                        if(mod(L+M+N,2)==1) jpowicu=-1.0_dp
                         KZZRD(i,j,k)=KZZRD(i,j,k)+(jpowicu) * atan (((ii+L- 0.50
                             _dp) * (jj + M - 0.50_dp) * dx * dy / (sqrt(((ii+L
                             -0.50_dp)*dx)**2 + ((jj+M-0.50_dp)*dy)**2 + ((kk+N
                             -0.50_dp)*dz)**2) * (kk + N - 0.50_dp) * dz)))
                        ENDDO
                ENDDO
        ENDDO
        end if

END SUBROUTINE
```

```
ATTRIBUTES(GLOBAL) SUBROUTINE CUDANAKATANI_KERNELXZ(offset, KXZRd,nx,ny,nz,dx,dy,
    dz)

        integer, value :: offset,nx,ny,nz
        real(dp), value :: dx,dy,dz
        integer, value :: offset
        real(dp), device :: KXZRd(0:2*nx-1,0:2*ny-1,0:2*nz-1)
        integer :: i,j,k,L,M,N,ii,jj,kk
        i=offset+(blockIdx%x-1)*blockDim%x+(threadIdx%x-1)
        j=(blockIdx%y-1)*blockDim%y+(threadIdx%y-1)
        k=(blockIdx%z-1)*blockDim%z+(threadIdx%z-1)

        if (i<(2*nx) .and. j<(2*ny) .and. k<(2*nz) ) then
        ii=i
        if (i>nx) ii=i-2*nx
        jj=j
        if (j>ny) jj=j-2*ny
        kk=k
        if (k>nz) kk=k-2*nz
        DO L=0,1
                DO M=0,1
                        DO N=0,1
                        jpowicu=1.0_dp
                        if(mod(L+M+N,2)==1) jpowicu=-1.0_dp
                         KXZRd(i,j,k)=KXZRd(i,j,k)+((jpowicu) * log (abs((jj+M-
                             0.50_dp) * dy + sqrt(((ii+L-0.50_dp)*dx)**2 + ((jj+M
                             -0.50_dp)*dy)**2 + ((kk+N-0.50_dp)*dz)**2) )))
                        ENDDO
                ENDDO
        ENDDO
        KXZRd(i,j,k)=-KXZRd(i,j,k)
        end if
END SUBROUTINE
```

```
END MODULE NAKATANIFUNCTIONS

MODULE DEMAGCUDAFUNCTIONS
USE PRECISION
USE CUDAFOR
CONTAINS



ATTRIBUTES(GLOBAL) SUBROUTINE CUDANAKATANI_ZEROPAD(Kd,nx,ny,nz)

        integer, value :: offset,nx,ny,nz
        real(dp) :: Kd(0:2*nx-1,0:2*ny-1,0:2*nz-1)
        integer :: i,j,k,L,M,N,ii,jj,kk
        i=(blockIdx%x-1)*blockDim%x+(threadIdx%x-1)
        j=(blockIdx%y-1)*blockDim%y+(threadIdx%y-1)
        k=(blockIdx%z-1)*blockDim%z+(threadIdx%z-1)
        if (i<(2*nx) .and. j<(2*ny) .and. k<(2*nz) ) then
                Kd(i,j,nz)=0
                Kd(nx,j,k)=0
                Kd(i,ny,k)=0
        end if
END SUBROUTINE

ATTRIBUTES(GLOBAL) SUBROUTINE CUDAFFT_SCALING(Kd,nx,ny,nz,scale)

        integer, value :: offset,nx,ny,nz
        real(dp), value :: scale
        complex(dp) :: Kd(0:nx,0:2*ny-1,0:2*nz-1)
        integer :: i,j,k,L,M,N
        i=(blockIdx%x-1)*blockDim%x+(threadIdx%x-1)
        j=(blockIdx%y-1)*blockDim%y+(threadIdx%y-1)
        k=(blockIdx%z-1)*blockDim%z+(threadIdx%z-1)
```

```
        if (i<(nx+1) .and. j<(2*ny) .and. k<(2*nz) ) then
                Kd(i,j,k)=Kd(i,j,k)*scale
        end if
END SUBROUTINE

ATTRIBUTES(GLOBAL) SUBROUTINE CUDACONVOLUTION_KERNEL(HDEM,MI,KII,MJ,KIJ,MK,KIK,nx
    ,ny,nz)
        USE GLOBALS
        integer, value :: offset,nx,ny,nz
        complex(dp) :: HDEM(0:nx,0:2*ny-1,0:2*nz-1)
        complex(dp) :: MI(0:nx,0:2*ny-1,0:2*nz-1),KII(0:nx,0:2*ny-1,0:2*nz-1)
        complex(dp) :: MJ(0:nx,0:2*ny-1,0:2*nz-1),KIJ(0:nx,0:2*ny-1,0:2*nz-1)
        complex(dp) :: MK(0:nx,0:2*ny-1,0:2*nz-1),KIK(0:nx,0:2*ny-1,0:2*nz-1)
        integer :: i,j,k, n(3)

        i=(blockIdx%x-1)*blockDim%x+(threadIdx%x-1)
        j=(blockIdx%y-1)*blockDim%y+(threadIdx%y-1)
        k=(blockIdx%z-1)*blockDim%z+(threadIdx%z-1)
        if(i<(nx+1) .and. j<2*ny .and. k<2*nz) then

        HDEM(i,j,k)= (MI(i,j,k)*KII(i,j,k)) + (MJ(i,j,k)*KIJ(i,j,k)) + (MK(i,j,k)
            *KIK(i,j,k))
        endif
END SUBROUTINE

ATTRIBUTES(GLOBAL) SUBROUTINE CUDACONVOLUTION_KERNEL_streamed(HDEM,MI,KII,MJ,KIJ,
    MK,KIK,nx,ny,nz,offset)
        USE GLOBALS
        integer, value :: offset,nx,ny,nz
        complex(dp) :: HDEM(0:nx,0:2*ny-1,0:2*nz-1)
        complex(dp) :: MI(0:nx,0:2*ny-1,0:2*nz-1),KII(0:nx,0:2*ny-1,0:2*nz-1)
        complex(dp) :: MJ(0:nx,0:2*ny-1,0:2*nz-1),KIJ(0:nx,0:2*ny-1,0:2*nz-1)
        complex(dp) :: MK(0:nx,0:2*ny-1,0:2*nz-1),KIK(0:nx,0:2*ny-1,0:2*nz-1)
        integer :: i,j,k, n(3)
```

```
        i=(blockIdx%x-1)*blockDim%x+(threadIdx%x-1)
        j=(blockIdx%y-1)*blockDim%y+(threadIdx%y-1)
        k=offset+(blockIdx%z-1)*blockDim%z+(threadIdx%z-1)
        if(i<(nx+1) .and. j<2*ny .and. k<2*nz) then

        HDEM(i,j,k)= (MI(i,j,k)*KII(i,j,k)) + (MJ(i,j,k)*KIJ(i,j,k)) + (MK(i,j,k)
            *KIK(i,j,k))
        endif
END SUBROUTINE

END MODULE

MODULE REDUCTIONCUDA
USE PRECISION
USE CUDAFOR
CONTAINS



ATTRIBUTES(GLOBAL) SUBROUTINE CUDASUMVAL(Matrix,log2,n)

        integer, value :: n, log2
        integer :: Matrix(0:n-1)
        integer :: i
        i=(blockIdx%x-1)*blockDim%x+(threadIdx%x-1)
        if (i<n/2) then
                Matrix(i)=Matrix(i)+Matrix(i+n/2)
        end if
         CALL SYNCTHREADS()
END SUBROUTINE

ATTRIBUTES(GLOBAL) SUBROUTINE MATRIXDIFF(Matrix11,Matrix12,Matrix13,Matrix21,
    Matrix22,Matrix23,err,n2,nx,ny,nz)
```

```
        integer, value :: nx,ny,nz, n2
        real(dp) :: Matrix11(0:nx-1,0:ny-1,0:nz-1)
        real(dp) :: Matrix21(0:nx-1,0:ny-1,0:nz-1)
        real(dp) :: Matrix12(0:nx-1,0:ny-1,0:nz-1)
        real(dp) :: Matrix22(0:nx-1,0:ny-1,0:nz-1)
        real(dp) :: Matrix13(0:nx-1,0:ny-1,0:nz-1)
        real(dp) :: Matrix23(0:nx-1,0:ny-1,0:nz-1)
        real(dp) :: err(0:n2-1)
        integer :: i,j,k
        i=(blockIdx%x-1)*blockDim%x+(threadIdx%x-1)
        j=(blockIdx%y-1)*blockDim%y+(threadIdx%y-1)
        k=(blockIdx%z-1)*blockDim%z+(threadIdx%z-1)

        if(i<nx .and. j<ny .and. k<nz) then
                err(i+j*nx+k*nx*ny)= (Matrix11(i,j,k)-Matrix21(i,j,k))**2+(
                    Matrix12(i,j,k)-Matrix22(i,j,k))**2+(Matrix13(i,j,k)-Matrix23
                    (i,j,k))**2
        endif
         CALL SYNCTHREADS()
end subroutine

ATTRIBUTES(GLOBAL) SUBROUTINE CUDAMAXVAL(Matrix,log2,n)

        integer, value :: n, log2
        real(dp) :: Matrix(0:n-1)
        integer :: i
        i=(blockIdx%x-1)*blockDim%x+(threadIdx%x-1)
        if (i<n/2) then
                if(Matrix(i+n/2).ge.Matrix(i))then
                 Matrix(i)=Matrix(i+n/2)
                end if
        end if
         CALL SYNCTHREADS()
END SUBROUTINE
```

```
END MODULE
```